Interféromètre atomique en rotation pour l'accélérométrie quantique embarquée

Quentin d'Armagnac de Castanet

THÈSE PRÉSENTÉE

POUR OBTENIR LE GRADE DE

DOCTEUR

DE L'UNIVERSITÉ DE BORDEAUX

Ecole Doctorale des Sciences Physiques et de l'Ingénieur

Spécialité Lasers, Matière et Nanosciences

Par **Quentin d'ARMAGNAC de CASTANET**

Rotating Atom Interferometer for Onboard Quantum Accelerometry

Interféromètre Atomique en Rotation pour l'Accélérométrie Quantique Embarquée

Sous la direction de : **Baptiste BATTELIER**

Soutenue le 23 Novembre 2023

Devant le jury composé de :

M. Florian SCHRECK	Professeur	University of Amsterdam	Président du jury
M. Fabien BRETENAKER	Directeur de Recherche	LuMIn	Rapporteur
M. Ernst M. RASEL	Professeur	Institute of Quantum Optics	Rapporteur
M. Quentin BEAUFILS	Ingénieur de Recherche	LNE-SYRTE	Examinateur
M. Alexandre GAUGUET	Maître de Conférences	LCAR	Examinateur
M. Philippe BOUYER	Professeur	University of Amsterdam	Membre Invité
M. Vincent MÉNORET	Ingénieur	Exail Quantum Systems	Membre Invité
M. Baptiste BATTELIER	Ingénieur de Recherche	LP2N	Directeur de thèse

Interféromètre atomique en rotation pour l'accélérométrie quantique embarquée

Résumé : Les systèmes de navigation inertielle intègrent les mesures de triades d'accéléromètres et gyromètres afin de déterminer leur position, mais la trajectoire déterminée est typiquement limitée par le biais variable dans le temps de ces capteurs inertiels. D'autre part, l'exploitation de la physique quantique a permis le développement d'interféromètres à ondes de matière, sensibles aux effets inertiels grâce à la masse des atomes. Lorsqu'ils sont en chute libre, leur trajectoire grandement prévisible permet une mesure absolue avec une exactitude et une stabilité remarquables. De considérables développements techniques ont permis le transfert technologique de gravimètres quantiques vers l'industrie, réalisant des mesures de longue durée en statique. Cependant, l'utilisation de capteurs à atomes froids pour la navigation et le positionnement nécessite de répondre à certains enjeux scientifiques et technologiques afin d'être compatible avec les applications embarquées tels que la compacité, la continuité de mesure et le fonctionnement dans des environnements difficiles.

Le laboratoire commun iXAtom (Exail/LP2N) vise à construire une nouvelle génération de capteurs inertiels de haute performance grâce à l'hybridation d'accéléromètres et de gyromètres classiques avec des capteurs quantiques basés sur l'interférométrie à ondes de matière. L'hybridation d'un interféromètre à atomes froids multi-axe séquentiel avec une triade d'accéléromètres classiques a permis d'augmenter la bande passante et la dynamique de mesure sans souffrir de la contrainte liée à la dérive du biais des accéléromètres mécaniques. Par ailleurs, cette hybridation inclut une correction de la phase laser en temps réel, permettant de reconstruire les franges atomiques brouillées par des vibrations parasites. En ce qui concerne les rotations de l'instrument au cours d'un interféromètre, leur compensation demeure l'enjeu principal restant à aborder pour réaliser un capteur solidaire d'un véhicule puisqu'elles entraînent une réduction de la visibilité des franges atomiques couplée à un brouillage du déphasage interférométrique.

Le travail de cette thèse porte sur la résolution de la dégradation des performances de l'accéléromètre hybride induite par les rotations. Une étude théorique a permis d'établir un modèle de la chute de contraste entraînée par des vitesses angulaires ainsi que des déphasages parasites résultant de la trajectoire complexe du nuage atomique dans le référentiel tournant du faisceau laser. Finalement, un système de compensation des rotations en temps réel utilise la mesure de vitesses angulaires par des gyroscopes à fibre optique afin de piloter une plateforme rotative piézo-électrique et ainsi stabiliser l'orientation du faisceau laser dans le référentiel externe dans le but de préserver le contraste des franges interférométriques et d'accroître la plage de mesure de l'interféromètre atomique tournant. Une rectification du modèle théorique prenant en compte la rotation du laser et l'hybridation avec les accéléromètres classiques permet de reconstruire les franges atomiques et de recouvrer la mesure inertielle, ouvrant la voie à l'accélérométrie hybride embarquée non stabilisée.

Mots-clés : Capteurs Quantiques, Interférométrie Atomique, Accélérométrie, Capteurs Inertiels, Hybridation Classique-Quantique

---

Laboratoire Photonique, Numérique et Nanosciences
UMR 5298 LP2N, 33400 Talence, France.

Rotating atom interferometer for onboard quantum accelerometry

Abstract: Classical inertial navigation systems integrate inertial measurements from triads of accelerometers and gyroscopes to determine their position, but the computed trajectory is typically limited by the intrinsic time-varying bias of these inertial sensors. In addition, the exploitation of quantum physics led to the development of matter-wave interferometers, sensitive to inertial effects due to the mass of the atoms. While they are free-falling, their highly predictable trajectory allows for an absolute measurement with outstanding accuracy and stability. Substantial technical developments have allowed bringing quantum gravimeters to the market, enabling static, long-term measurements. Nevertheless, the use of cold-atom sensors for navigation and positioning still requires addressing many scientific and technological challenges to be compatible with onboard applications such as compactness, measurement continuity and operation in the presence of strong vibrations and rotations.

The Joint Laboratory iXAtom aims at building a new generation of high-end inertial sensors through the hybridization of classical accelerometers and gyroscopes with quantum sensors based on matter-wave interferometry. The full hybridization of a sequential multi-axis cold-atom interferometer with a triad of classical accelerometers allowed increasing the bandwidth and dynamic range while overcoming the usual limitation due to the bias drift of the mechanical accelerometers. Moreover, this hybridization technique features a real-time correction of the laser phase which allows reconstructing the atomic fringes scrambled by parasitic vibrations. As regards the rotations of the instrument throughout an interferometer, their compensation remains the next major issue to tackle for strapdown applications as they induce a drastic reduction of the atomic fringes' visibility coupled to a scrambling of the interferometric phase shift.

This thesis work focuses on the mitigation of the rotation-induced performance deterioration of the hybrid accelerometer. Through a theoretical investigation, a model for both the angular velocity-dependent decay of the fringes contrast and the systematic phase shift arising from the complex trajectory of the atomic cloud in the rotating frame of the interrogation laser is established. A real-time rotation compensation system, employing the measurement of the rotation rate with high-end fiber-optic gyroscopes to drive a piezo-actuated tip-tilt platform, has been implemented to stabilize the orientation of the interrogation laser in the external frame in order to preserve the contrast of the atomic interference pattern and extend the measurement range of the rotating atom interferometer. A rectification of the theoretical model accounting for the rotation of the laser as well as the hybridization with the classical accelerometers enables reconstructing the atomic fringes and retrieving the inertial measurement, paving the way for strapdown onboard hybrid accelerometry.

Keywords: Quantum Sensors, Atom Interferometry, Accelerometry, Inertial Sensing, Classical-Quantum Hybridization

---

Laboratoire Photonique, Numérique et Nanosciences
UMR 5298 LP2N, 33400 Talence, France.

Remerciements

Les travaux de thèse présentés dans ce manuscrit ont été menés au sein de l'équipe iXAtom, fruit de la collaboration entre le Laboratoire Photonique, Numérique et Nanosciences (LP2N) et de l'entreprise Exail, précédemment iXblue. L'attribution d'une bourse CIFRE par l'Association Nationale de la Recherche et de la Technologie (ANRT) m'a permis de réaliser mon doctorat dans ce contexte singulier, à mi-chemin entre académie et industrie, et je les en remercie. J'entends souvent que la thèse est un long chemin de croix rempli de stress, de dépression et de frustration, et je mentirais en disant que chaque journée n'a été que succès et optimisme. Cependant, j'ai eu la chance de m'épanouir dans cette aventure autant que faire se peut et à l'heure du bilan, je ne retiens que des bons moments. Ceci je le dois aux innombrables personnes avec qui j'ai eu la chance de faire un bout de chemin, plus ou moins long, et que j'aimerais prendre le temps de remercier comme il se doit.

Je souhaite avant tout exprimer ma gratitude envers mon directeur de thèse **Baptiste Battelier**, tant il a été essentiel pour moi comme pour MAQS tout au long de ce chemin. Certes, je n'avais pas tout à fait envisagé d'entamer une thèse de physique expérimentale par neuf mois de programmation FPGA, de toutes façons je n'avais aucune idée de ce que ça pouvait bien être. Ajoutant à cela le contexte épidémique et une équipe vidée de ses membres, le temps passé seul devant un ordinateur aurait pu rapidement devenir infernal si tu n'avais pas réussi à dégager du temps chaque jour pour venir discuter. Ta disponibilité, ta bienveillance, ta générosité au moment de partager ta passion de la physique, ta patience lors de discussions parfois animées avec la personne têtue et bornée que je peux être, ont été autant de facteurs cruciaux dans mon épanouissement personnel et scientifique. Tu es je crois le meilleur directeur que j'aurais pu espérer avoir et je suis fier de pouvoir dire que tu es pour beaucoup dans ma volonté de poursuivre ma carrière dans la recherche. J'ai également pu bénéficier de l'arrivée de **Vincent Ménoret**, à mi-chemin de mon doctorat, qui a représenté un encadrant supplémentaire pour moi tout simplement formidable. Habitué à l'équipe AQG qui était déjà une machine bien huilée, tu t'es adapté à notre fonctionnement plus rustique tout en apportant ta vision du projet avec fraîcheur et enthousiasme. Ta bonne humeur, ton humour et ta gentillesse ont généré beaucoup d'animation dans le couloir et ont grandement contribué à rendre mon séjour chez iXAtom aussi agréable qu'il l'a été. Pour tout cela je souhaite te remercier, et oui c'était une blague ne t'inquiète

pas je continuerai de rentrer tes paniers de légumes pendant mon postdoc. J'aimerais également remercier **Philippe Bouyer** pour avoir créé et porté ce projet avec un engouement inépuisable, pour les discussions toujours passionnantes et les anecdotes amusantes sur la vie dans un laboratoire. Merci également à **Fabien Napolitano** et **Henri Porte** d'avoir permis à ce laboratoire commun de voir le jour, ainsi qu'à **Bruno Desruelles** et **Cédric Majek** d'avoir cru en ce projet au moment d'en reprendre successivement la responsabilité du côté d'Exail.

Merci à l'ensemble des membres de mon jury de thèse pour l'intérêt porté à mes travaux. Merci en particulier au président de ce jury **Florian Schreck**, à **Fabien Bretenaker** et **Ernst M. Rasel** pour avoir accepté la tâche de rapporteurs ainsi qu'à mes deux examinateurs **Quentin Beaufils** et **Alexandre Gauguet**. Je vous remercie pour le temps consacré à la relecture d'un manuscrit pas toujours très digeste, les discussions enthousiasmantes à l'issue de ma soutenance et la bienveillance dont vous avez fait preuve à mon égard.

Je remercie chaleureusement les gens qui m'ont accompagné au quotidien dans le labo pour mettre les mains dans le cambouis, à commencer par **Brynle** qui m'a accueilli lors de mes deux premiers mois et m'a appris tout ce qu'il pouvait en un temps (très) limité. Ta pédagogie m'a permis la meilleure intégration possible, et j'ai pris beaucoup de plaisir à travailler avec toi, aussi court fût-ce. Vient ensuite mon acolyte **Simon** qui avait déjà la tâche pénible de s'occuper de moi en stage, mais a tout de même accepté de revenir me prêter main forte à l'issue de sa thèse. Je garde en mémoire l'émotion de notre premier Batman en rotation, ton fameux porc aux kiwis et ta reprise de "Sweet Home Alabama" après le mélange douteux de Patxaran et de Chartreuse. Je remercie enfin "El Doctor" **Vincent** pour les moments de rigolade comme de sérieux, pour tout ce que tu m'as transmis au cours de cette demi-thèse, pour les pages Wikipédia pas toujours pertinentes et pour les journées interminables à tourner cette manipe en louchant sur le vernier. Ta sympathie et tes goûts musicaux particulièrement raffinés font de toi un collègue absolument génial, même si t'aimes pas les "japonaiseries". Je souhaite enfin bon courage à **Cyrille** pour la suite de l'aventure. Même si tu n'es pas arrivé au moment le plus rigolo avec une expérience qui mourait à petit feu, la motivation et l'optimisme que tu as très vite montré m'ont assuré qu'il n'y a aucun souci à se faire pour l'avenir de la manipe. Une pensée particulière pour **Romain** que je ne remercierai jamais assez pour l'héritage laissé sur l'étude de la compensation des rotations, pour m'avoir pré-mâché le travail avec une merveille de document explicatif de près de cinquante pages, pour s'être rendu disponible même en période de rédaction et pour la mémorable partie de rugby-piscine dont on n'a jamais vraiment compris les règles qu'on a nous-mêmes inventé sur le moment. Enfin,

je souhaite remercier **Pierrick**, **Baptiste**, **Théo** et **Camille** qui m'ont apporté une aide et des conseils précieux à chaque fois que je les ai sollicités.

La physique n'a pas toujours été une évidence pour moi, c'est pourquoi je souhaite témoigner ma profonde gratitude aux deux professeurs sans qui je n'en serais probablement pas là aujourd'hui. Merci tout d'abord à **Francis Lavernhe** pour m'avoir communiqué toute sa passion dans un domaine pour lequel je n'avais ma foi aucune appétence particulière. Merci également à **Simon Bernon** pour m'avoir introduit au monde chaleureux des atomes froids à un moment où je désespérais de trouver une voie qui saurait me garder captivé aussi longtemps. Votre pédagogie et votre ferveur dans l'enseignement ont grandement façonné mon parcours scolaire, et je ne pourrais être plus reconnaissant qu'à l'issue d'une expérience aussi intense.

Je tiens à remercier tous les gens que cette thèse m'a permis de rencontrer, à commencer par **Paul**, **JB**, **Dylan**, **Géovan**, **Célia** et l'ensemble du Cold Atoms in Bordeaux. Je souhaite bon courage à **Élise**, **Malo**, **Mathias**, **Luc** et tous les autres doctorants avec qui j'ai eu le plaisir de partager de bons moments autour d'un café ou d'une bière. Merci à l'ensemble de l'équipe Quantum Systems d'Exail, et en particulier à **Bruno** pour sa sympathie et pour avoir pris le temps de partager avec moi son expertise des horloges atomiques, sans qui je n'aurais peut-être pas décroché le postdoc de mes rêves. Enfin, je remercie le service administratif du LP2N ainsi que notre mécano **Philippe** et nos électroniciens **Jean-Hugues** et **Arnaud**, qui ne ménagent pas leurs efforts pour permettre à chaque équipe d'évoluer dans les meilleures conditions possibles.

J'éprouve une reconnaissance toute particulière envers mes plus proches amis **Nano**, **Amber**, **Elliott**, **Marie**, **Louej**, **Cerise**, **Raph** et tous ceux qui sont restés dans les bons comme les mauvais moments, au fil des années et malgré la distance parfois grandissante. Merci à tous les copains du Rugby Club Cadaujacais pour la famille que j'ai trouvé en vous rejoignant et pour l'exutoire que vous m'avez offert pendant ces trois années, sur et en dehors du terrain. Thank you to **Sanket** for the inspiring conversations about physics and every other stuff, I am proud of you as a ~~horse~~ human being and am glad to share your friendship, even separated by an ocean.

J'aimerais profiter du dernier paragraphe de cette section pour remercier l'ensemble de ma famille à qui je dois tout, "last but not least" comme on dit. En particulier merci au frérot "El Bonfo", le meilleur ami et colocataire qui soit. Après mille aventures et un quart de vie commune tu es sans doute celui qui me connait le mieux au monde, les bons comme les mauvais côtés. Merci d'avoir toujours été là, je souhaite à chacun d'avoir un Bonf dans sa vie et j'aime à croire que je suis une meilleure personne depuis

que je te connais. Merci à mon Pâton pour ton soutien indéfectible toutes ces années. Je me sens chanceux d'avoir cette relation avec toi, j'espère être toujours là pour toi comme tu l'as été pour moi et je vous souhaite le meilleur à toi, Ray et le petit monstre. Merci aux Dardars pour avoir toujours cru en moi et mis en œuvre tous les efforts du monde pour que je puisse faire ce que je voulais. Merci pour votre amour, merci pour votre confiance, merci pour le foyer chaleureux dans lequel vous avez toujours veillé à ce qu'on grandisse. Enfin je remercie Luisa, la plus belle rencontre de ma vie survenue au cours de cette thèse, pour cette dernière année riche en émotions. Merci pour ta confiance, merci pour le réconfort que me procure chaque instant passé avec toi, merci pour la personne merveilleuse que tu es. Merci d'être entrée dans ma vie, puisses-tu ne jamais en sortir.

Contents

Introduction

In March 1905, Albert Einstein publishes a revolutionary paper recommending that light is not a continuous wave but instead consists of localized particles, later called photons, declaring that "when a light ray is spreading from a point, the energy is not distributed continuously over ever-increasing spaces, but consists of a finite number of energy quanta that are localized in points in space, move without dividing, and can be absorbed or generated only as a whole" [Einstein 1905]. Following this idea, Louis de Broglie formulates the hypothesis of a wave associated with every particle of matter in 1923 [de Broglie 1923], paving the way for the fundamental concept of quantum mechanics known as the wave-particle duality which states that quantum entities exhibit particle or wave properties according to the experimental circumstances. The de Broglie hypothesis of matter waves led to define a wavelength associated with each particle of matter, equal to the Planck constant h divided by the momentum of the particle. Furthermore, using the equipartition theorem relating the temperature of a system to its average energy, it was then possible to calculate the wavelength associated with each particle in an atomic gas raised at a temperature $\mathcal{T}$ which is inversely proportional to the square-root of the mass of the considered atom times its temperature. Nevertheless, for a thermal gas of atoms at a temperature of three hundred Kelvin, this wavelength lies between ten and eleven orders of magnitude below the meter and the wide velocity distribution of the gas strongly limited the achievable fraction of an atomic ensemble which can be coherently manipulated.

Half a century later, the trapping and cooling of atoms using the radiation pressure force exerted by a laser beam tuned to an atomic resonance was simultaneously theorized by two groups in 1975 [Wineland and Dehmelt 1975; Hänsch and Schawlow 1975] before its first experimental demonstration on neutral atoms in 1982 [Phillips and Metcalf 1982]. Further reduction of the atomic ensemble's temperature being desirable and laser technologies gaining in stability and linewidth, new techniques were developed allowing to reach temperatures below the Doppler cooling limit [Dalibard and Cohen-Tannoudji 1989; Chu et al. 1985] and below the one-photon recoil energy [Aspect et al. 1988; Boiron et al. 1995] down to the order of the microkelvin. This drastic reduction of the gas' temperature equating to a diminution of its velocity distribution set the ground for new exciting experiments and in particular matter-wave interferometry. The assumption made for this last proposition was that if particles exhibit a wave behavior

at a wavelength which can be manipulated with narrow lasers or radio-frequency radiations, it should in principle be possible to exploit their quantum properties and have an atom coherently interfering with itself. Much as their optical counterparts, splitting and recombining electromagnetic waves to measure a path difference between the traveling waves, cold-atom interferometers use light pulses to coherently split and recombine atomic wave packets to measure the difference between the trajectories of the two — or more — arms. One of the major distinctions with optical interferometers is that the path difference in matter-wave interferometers is related to inertial effects experienced by the atoms due to their mass, making such instruments ideal candidates for absolute inertial sensors measuring accelerations or rotations [Clauser 1985].

In 1991, Mark Kasevich and Steven Chu demonstrated the first practical realization of an atomic interferometer using stimulated Raman transitions [Kasevich and Chu 1991], which was subsequently used to measure the gravitational acceleration applied on laser-cooled sodium atoms [Kasevich and Chu 1992]. Nowadays, matter-wave interferometry has demonstrated its importance in a wide range of applications and in particular inertial sensing [Geiger et al. 2020]. If quantum gravimeters based on cold atoms generate an increasing interest and even successfully led to transportable, commercial devices able to operate outside laboratories [Ménoret et al. 2018; Antoni-Micollier et al. 2022], several applications including inertial navigation require onboard and mobile operation of inertial sensors measuring the full acceleration vector instead of its projection on a given axis. In that regard, the utilization of matter-wave interferometry could bring a substantial enhancement of classical sensors — and specifically with respect to the bias drift of classical accelerometers and gyroscopes — but remains challenging in many ways. Indeed, if quantum sensors demonstrate outstanding accuracy, stability and sensitivity to inertial effects which make them so attractive, the same applies to their sensitivity to environmental effects, which is the reason why their utilization is still mainly restricted to laboratories offering quiet and stable environments regarding vibration noise and rotations of the instrument.

Several groups have put significant efforts in tackling some of these field difficulties by performing single-axis measurements of the acceleration projection along a given axis through an active isolation of the parasitic high-frequency vibrations [Oon and Dumke 2022] and a gyro-stabilization of the measurement axis [Bidel et al. 2018]. However, acceleration is a vector and is therefore described by both its norm and pointing direction, which make a single-axis quantum accelerometer insufficient for its full measurement. Additionally, for navigation purposes in particular, it is desirable to maintain a maximum correlation between the motion of the vehicle and that of the inertial measurement unit by having the latter operating in strapdown configuration

rather than with an isolation system which necessarily implies a loss of information. For this reason, the apparatus conceived in the iXAtom joint laboratory consists of a three-axis hybrid accelerometer comprised of three atomic accelerometers, offering remarkable sensitivity, stability and accuracy at the cost of a limited dynamic and dead times, hybridized with three classical accelerometers, providing large dynamic range and bandwidth but suffering from a long-term bias drift. The double hybridization scheme between these two complementary technologies is based on the real-time compensation of the vibration-induced phase shift on the atomic interference pattern coupled to the correction of the classical biases at each measurement of the quantum sensors, enabling a bias-free high bandwidth measurement of the three acceleration components. If a similar technique had already been proposed in the past [Lautier et al. 2014] for a single-axis hybrid sensor, this experiment represents the first realization of a classical-quantum triad of accelerometers which has been successfully demonstrated in quasi-static operation, revealing a fifty-fold improvement on the long-term stability with respect to conventional sensors [Templier et al. 2022]. Nevertheless, dynamic rotations of arbitrary amplitude occurring during an atom interferometer's measurement remain a major hindrance in the quest of a fully mobile hybrid inertial measurement unit.

Rotations in matter-wave interferometry have already been widely investigated. Similarly to quantum gravimeters measuring the gravitational acceleration undergone by free-falling atoms in an interferometer, several experiments have realized atomic gyroscopes exploiting the Sagnac interference effect to measure rotational motion of a launched atomic cloud [Gustavson et al. 1997; Lenef et al. 1997; Barrett et al. 2014], and notably in the SYRTE laboratory where a continuous cold-atom gyroscope reached a remarkable stability at the nanoradian per second level [Dutta et al. 2016]. Furthermore, the development of rotating atomic accelerometers allowed for multi-axis cold-atom inertial sensing by simultaneously measuring the acceleration in the direction of the Raman laser beam as well as the projection of the rotation vector onto the plane transverse to that direction through the Coriolis acceleration [Canuel et al. 2006; Chen et al. 2019]. However, such instruments are very sensitive to the orientation of their axes and to parasitic vibrations which imposes that they remain in a very stable environment. Furthermore, the amplitude of rotations these can measure is strongly limited by the decoherence of the two arms of the interferometer, typically a few Earth rotation rates amounting to tens to hundreds of microradians per second, thus restricting the prospective application of atomic gyroscopes with no moving parts. In order to overcome this effects, it is possible to install a tip-tilt mirror retroreflecting the interrogation laser beam to oppose the rotation of the device, extending the dynamic range of the measurement up to the radian per second level [Zhao et al. 2021]. This

technique was also used in some experiments of atomic gravimeters to cancel the effect of the Earth rotation, which reduces the overlap of the atomic wave packets at the output of the interferometer as well as introducing a parasitic phase shift related to the Coriolis acceleration [Lan et al. 2012; Sugarbaker et al. 2013]. Ultimately, this method was recently proposed for a cold-atom accelerometer onboard a Nadir pointing satellite with a full calculation of the output phase shift of the interferometer without mechanical compensation of the rotation as well as a calculation of the same phase shift with an independent rotation of the reference mirror based on geometrical considerations [Beaufils et al. 2023]. Nonetheless, all the studies presented in this paragraph were conducted in the absence of strong vibrations, for constant and well-defined angular velocities remaining — in the case of acceleration sensors at least — in the range of one to a few Earth rotation rates, limited to hundreds of microradians per second.

In order to realize mobile and onboard quantum accelerometry, it appears necessary to tackle the simultaneous effects of strong vibrations and time-varying, arbitrary, strong rotations of the instrument. Specifically, the latter can be measured with high-end fiber-optic gyroscopes to determine precisely their amplitudes and axes in order to realize a real-time stabilization of the reference mirror's orientation in the laboratory frame, thus avoiding the restriction of the dynamic range of the atom interferometer, as well as a correction of the laser phase enabling to retrieve the acceleration information when the atomic phase is scrambled. This study will be at the heart of this thesis.

The work presented in this manuscript was carried out in the iXAtom joint laboratory located in the Laboratoire de Photonique Numérique et Nanosciences (LP2N), involved in cutting-edge research activities on atom interferometry, with the collaboration of the French technology company Exail, expert in inertial navigation systems and industrial quantum sensors. This unique context allows for conducting exciting research with the ultimate aim of transferring the technology developed to fully-operational, industrial products in order to address various, practical challenges. After the successful demonstration of the quasi-static operation of the three-axis bias-free hybrid accelerometer, my contribution has been essentially devoted to the study and correction of rotations at unrivaled levels of amplitude for an atomic accelerometer, including the implementation of a real-time rotation compensation system enabling maintaining a constant visibility of the atomic interference pattern over a wide range of time-varying, arbitrary angular velocities. Furthermore, a comprehensive theoretical model was established for the rotating atom interferometer's output phase shift and enabled the reconstruction of the atomic fringes under random, strong vibrations and angular velocities up to five thousand Earth's rotation rates, which is beyond the scope of all the research conducted on the compensation of the rotations in cold-atom accelerometry,

in addition to large variations of the tilt angle. This study paves the way for truly mobile applications of multi-axis quantum inertial sensors operating in a strapdown configuration.

Organization of the thesis

In Chapter 1, I provide theoretical tools of atom-light interaction with a particular consideration for the realization of atom interferometers. The concept of atom optics enabling the manipulation of matter waves using laser beams is reviewed, before introducing the sensitivity function allowing to investigate the case of an atom interferometer undergoing non-constant accelerations. The study is further extended to the motion of an atomic cloud in an arbitrary moving frame, leading to the modifications of the measurement of an atomic accelerometer experiencing arbitrary angular velocities both with and without a compensation of the rotation on the reference mirror.

In Chapter 2, I give a succinct description of the apparatus developed in the iXAtom joint laboratory including the architecture of the laser system, with a specific definition of the technological choices which enable this laser source to be as compact as it is agile. Subsequently, the sensor head where atoms are manipulated to realize multi-axis interferometry for the reconstruction of the acceleration vector is depicted. It is followed by a more detailed characterization of the inertial measurement unit, comprised of three mechanical accelerometers and two fiber-optic gyroscopes, in addition to the piezo-actuated tip-tilt stage where the reference mirror of a measurement axis is mounted. Ultimately, the real-time compensation electronics used for the hybridization of the classical and quantum inertial sensors as well as the experimental sequence implemented on the apparatus, are reviewed.

In Chapter 3, I analyze the practical implementation and performances of the quantum accelerometer in quasi-static configuration. It is first characterized along the vertical axis for the measurement of the gravitational acceleration, followed by the three-axis atomic accelerometer able to operate in arbitrary orientations over a wide range of tilt angles to measure the three orthogonal components of the acceleration vector. Eventually, I present the closed-loop hybridization scheme enabling for large bandwidth and dynamic range measurements of the acceleration components through the correction of the classical accelerometers' biases with the signals of the atom interferometers.

In Chapter 4, I carry out a comprehensive review of the effects of arbitrary rotations applied on the multi-axis hybrid accelerometer. First, a completion of the theoretical model provided in chapter 1 is provided in order to account for the measurement of

the rotating classical accelerometer in the output phase shift of the hybridized atom interferometer. In the second part, atomic fringes recorded in the regime of weak rotations are analyzed, including the impact of the angular velocity on the visibility of the interference pattern as well as the scrambling of the atomic phase due to the complex trajectory of the atoms in the rotating frame of the instrument, before presenting the method used to retrieve the acceleration signal. Ultimately, after introducing the algorithm implemented to compensate the rotations of the reference mirror in real time, the performances and current limitations of the rotating hybrid accelerometer are estimated so as to provide an outlook on the implementation of such inertial sensors for mobile and strapdown accelerometry.

Throughout this manuscript, the vectors will be represented in **bold**. Furthermore, parameters related to accelerations will be mostly expressed in units of g where $1\ \mathrm{g} = 9.80665\ \mathrm{m/s^2}$ denotes the standard acceleration of free fall, defined as the nominal gravitational acceleration of an object in a vacuum near the surface of the Earth.

Chapter 1

Theoretical tools for onboard cold-atom interferometry

In this chapter, some theoretical tools for studying atom-light interaction are provided. It includes in particular the concept of atom optics, allowing to diffract matter waves with laser beams featuring well-defined frequencies and phases. This technique has enabled matter-wave interferometers, in particular using light pulses and free-falling cold atoms, first demonstrated by Mark Kasevich and Steven Chu in 1991 [Kasevich and Chu 1991]. The ability to calculate accurately the phase shift resulting from such interactions as well as from the propagation of atomic wave packets in a given potential has led to high sensitivity and accuracy acceleration sensing [Geiger et al. 2020]. The study of such schemes is presented and further extended to onboard applications, namely in the presence of strong mechanical vibrations, accelerations and rotations of the carrier.

Contents

1.1 Key principles of a cold-atom accelerometer

An interferometric measurement consists in the coherent splitting of a wave, which propagates along several distinct paths before they are recombined. On each of these arms, the waves accumulate a phase which depends on the physical properties of the path related to the experimental setup, such as the length of the arm. The phase difference at the output of the experiment can therefore be used to measure these physical properties, by comparing one arm to another.

Furthermore, contrary to their optical counterpart using massless photons to measure this phase difference, atomic interferometers as proposed in [Clauser 1985] make use of the propagation of matter waves which are able to probe various inertial effects, including accelerations and rotations. However, in order to realize such matter-wave interferometers, it is important to have tools which enable to coherently split, deflect and recombine the matter waves. To that end, we will use two-photon stimulated Raman transitions.

1.1.1 Two-photon stimulated Raman transitions

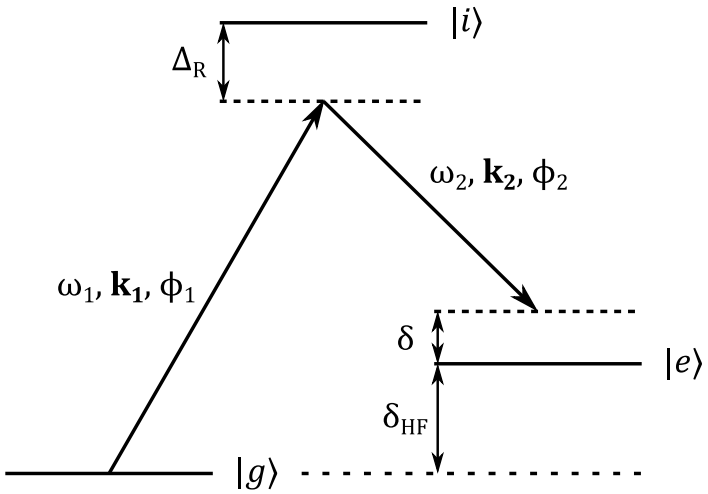

Figure 1.1: Representation of a Raman transition between two energy levels $|g\rangle$ and $|e\rangle$ with two lasers set at frequencies $\omega_{1,2}$ and phases $\phi_{1,2}$ carried by wave vectors $\boldsymbol{k_{1,2}}$. δ_{HF}: hyperfine splitting; δ: detuning from resonance; Δ_R: Raman detuning.

Raman transitions are two-photon processes coupling an atomic ground state $|g\rangle$ to an excited state $|e\rangle$ *via* an intermediate state $|i\rangle$, allowing to drive coherent transitions in order to connect two states which do not feature an energy splitting compatible with optical frequencies. When using ^{87}Rb atoms, as is the case in this work, these two states correspond to the two hyperfine levels $|F = 1\rangle$ and $|F = 2\rangle$ of the ground state $5^2S_{1/2}$ and the intermediate state is the excited state $5^2P_{3/2}$ (all the hyperfine levels of

this state contributing to the transition). In order to drive this two-photon transition, two laser beams detuned by a frequency close to the hyperfine splitting are shone onto an atom initially in the ground state $|g\rangle$ such that this atom absorbs a photon from the first laser $(\omega_1, \boldsymbol{k_1}, \phi_1)$ and reaches the excited state $|e\rangle$ by stimulated emission of a photon in the mode of the second laser $(\omega_2, \boldsymbol{k_2}, \phi_2)$. In addition to this change in the internal state of the atom, a momentum kick $\hbar\boldsymbol{k_{\text{eff}}}$ is transferred to the atom with $\boldsymbol{k_{\text{eff}}} = \boldsymbol{k_1} - \boldsymbol{k_2}$ the effective wave vector associated to the transition.

In order to avoid to populate the intermediate state $|i\rangle$, which would result in spontaneous emission and thus a loss of coherence between the two coupled states $|g\rangle$ and $|e\rangle$, the two lasers are detuned from the intermediate state by a frequency Δ_R called the Raman detuning and visible on figure 1.1. To verify the energy and momentum conservation rules, we introduce the detuning from resonance or two-photon detuning $\delta = \omega_1 - \omega_2 - \delta_{\text{HF}}$, for which the resonance condition can be written:

$$\delta = \omega_D + \omega_R + \omega_{\text{LS}} \tag{1.1}$$

where $\omega_D = \boldsymbol{p}.\boldsymbol{k_{\text{eff}}}/m$ is the Doppler frequency, $\omega_R = \hbar k_{\text{eff}}^2/(2m)$ the recoil frequency and $\omega_{\text{LS}} = \Omega_{\text{LS}}^e - \Omega_{\text{LS}}^f$ the differential light shift, also called AC Stark shift. In the expressions of the Doppler and recoil frequencies, m denotes the atomic mass. Under this resonance condition, the detuning of the Raman lasers corresponds to the ground state hyperfine splitting $\omega_1 - \omega_2 = \delta_{\text{HF}}$. Additionally, for a Raman detuning large with respect to the Rabi frequencies associated to the optical transitions $\Delta_R \gg \Omega_{1,2}$, we define the effective Rabi frequency of the two-photon transition [Steck 2007]:

$$\Omega_{\text{eff}} = \frac{\Omega_1^* \Omega_2}{2\Delta_R}. \tag{1.2}$$

In the following, we will consider negligible spatial distributions and Gaussian velocity distributions:

$$G(v) = \frac{1}{\sigma_v \sqrt{\pi}} \exp - \frac{(\boldsymbol{v} - \boldsymbol{v_0})^2}{\sigma_v^2} \tag{1.3}$$

where $\boldsymbol{v_0}$ is the wave packet's group velocity and $\sigma_v = \sqrt{2k_B\mathcal{T}/m}$ its velocity spread depending on the atomic cloud's temperature $\mathcal{T}$. For an atom prepared in the state $|g, \boldsymbol{p_0}\rangle$, $\boldsymbol{p_0}$ being its initial momentum, and assuming perfectly square pulses, the probability for it to be transferred to the state $|e, \boldsymbol{p_0} + \hbar\boldsymbol{k_{\text{eff}}}\rangle$ is given by [Moler et al. 1992]:

$$P(\tau, \delta, v) = \frac{\Omega_{\text{eff}}^2}{\Omega_R^2} \sin^2\left(\frac{\Omega_R \tau}{2}\right) \tag{1.4}$$

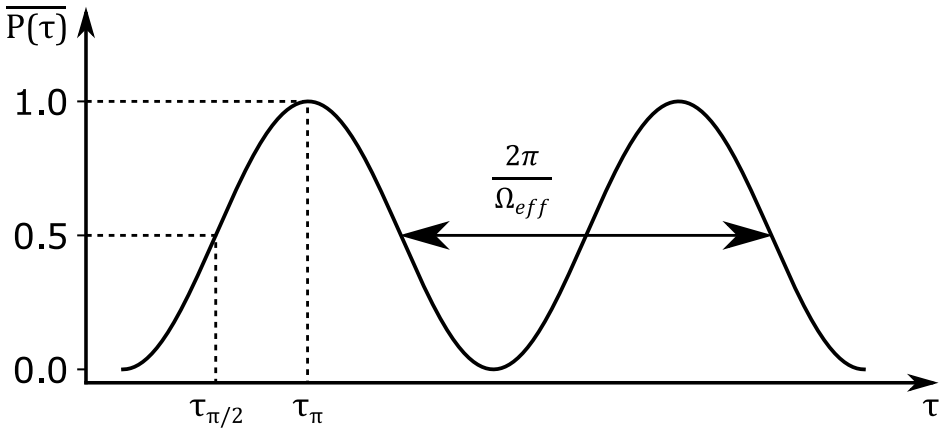

Figure 1.2: Evolution of the effective transition probability with the duration of the laser pulse, emphasizing the particular cases of an atomic beam-plitter (duration $\tau_{\pi/2}$) and of an atomic mirror (duration τ_π). The period of these oscillations is $2\pi/\Omega_{\text{eff}}$ with Ω_{eff} the effective Rabi frequency

with τ the pulse duration and

$$\Omega_R = \sqrt{\Omega_{\text{eff}}^2 + (\delta - \omega_D - \omega_R - \omega_{\text{LS}})^2} \tag{1.5}$$

the exact Rabi frequency. Displaying this transition probability as a function of the pulse duration exhibits a behavior known as Rabi oscillations displayed in figure 1.2. When the resonance condition is verified, $\Omega_R = \Omega_{\text{eff}}$ and the theoretical amplitude of these Rabi oscillations amounts to 1. In that situation, only the Raman laser pulse duration τ needs to be adapted in order to operate a coherent splitting or an inversion of the atomic population, analogous to beam-splitters and mirrors in optical interferometers.

With these parameters in mind, we can introduce the effective transition probability corresponding to the integration of the transition probability (given by the Fourier transform of the pulse's shape) over the velocity distribution of the cloud, written $G(v)$. This yields:

$$\overline{P(\tau,\delta)} = \int P(\tau,\delta,v)G(v)dv. \tag{1.6}$$

1.1.2 Velocity sensitivity of Raman transitions

Two distinct types of two-photon transitions can be considered depending on the orientation of the two laser pulses and their respective polarization states. First, with the two lasers propagating in opposite directions in a lin⊥lin polarization configuration notably, one can perform velocity-sensitive counter-propagating Raman transitions. Using equations 1.3 and 1.4, we observe that a Raman pulse with a duration τ will address a velocity class with a spread proportional to $1/\tau$. A π pulse has a

maximum efficiency of transition while addressing the widest possible velocity class, hence with a minimum pulse duration. Conversely, longer pulses address a narrower velocity class thus they transfer fewer atoms from a state to the other. In any case, the recoil momentum will be defined by the direction of the effective wave vector $\pm\boldsymbol{k_{\text{eff}}} = \pm(\boldsymbol{k_1} - \boldsymbol{k_2}) \approx \pm 2\boldsymbol{k_1} \approx \mp 2\boldsymbol{k_2}$. Since the absorption and stimulated emission of the photons occur in the same direction, such transitions are sensitive to the velocity of the atoms relative to the laser beams, and a recoil momentum will be inferred to the atoms in the direction of the effective wave vector, namely $\boldsymbol{k}_\uparrow \equiv +\boldsymbol{k_{\text{eff}}}$ and $\boldsymbol{k}_\downarrow \equiv -\boldsymbol{k_{\text{eff}}}$. In order to select which pair of counter-propagating beams will drive Raman diffraction, the resonance detuning is adapted according to the Doppler frequency $\omega_D(v) = \pm k_{\text{eff}} v$ and it can be reversed from one measurement to the other to eliminate some systematic shifts in the interferometric measurement [Louchet-Chauvet et al. 2011]. As a consequence of this Doppler frequency shift, the transition probability of the atoms is highly dependent on their respective velocities.

However, in the case of Raman beams not exactly counter-propagating or if the polarization of the light is not rigorously linear, another type of transition is possible. Indeed, if a single laser beam carries the two frequencies, co-propagating transitions can be achieved with circular polarizations $\sigma_\pm/\sigma_\pm$. In this configuration, the absorption and stimulated emission of the photons are made in opposite directions, yielding $k_{\text{eff}} \simeq 0$ and thus making the transition insensitive to Doppler frequency shift. Additionally, the exact Rabi frequency is changed to $\Omega_{\text{co}} = \sqrt{\Omega_{\text{eff}}^2 + (\delta - \omega_{\text{LS}})^2}$. As this technique allows us to address all the atoms regardless of their velocities, making their manipulation similar to what can be achieved with micro-waves, it can be used to prepare the atoms in a non-magnetic state by scanning the resonance detuning as a scan of the Zeeman frequency shift. Alternatively, co-propagating transitions can be used to scan the hyperfine splitting δ_{HF} in order to perform Ramsey spectroscopy and frequency measurements [Döring et al. 2009]. In the case of an atom interferometer, we need to induce a spatial displacement between the two arms and co-propagating transitions are mostly a parasitic transfer reducing the efficiency of the velocity-sensitive pulses, which is why the polarization of the laser beams is a critical parameter.

1.1.3 Phase shift of an atom interferometer

In an interferometric measurement using atoms, it is possible to calculate a phase difference associated to the propagation of the matter-wave along the different arms of the interferometer ϕ_{prop}, as well as the phase acquired from its interaction with the diffracting laser fields ϕ_{las}. Additionally, atom interferometers feature a third contribution which can arise if the classical positions of the two interfering trajectories

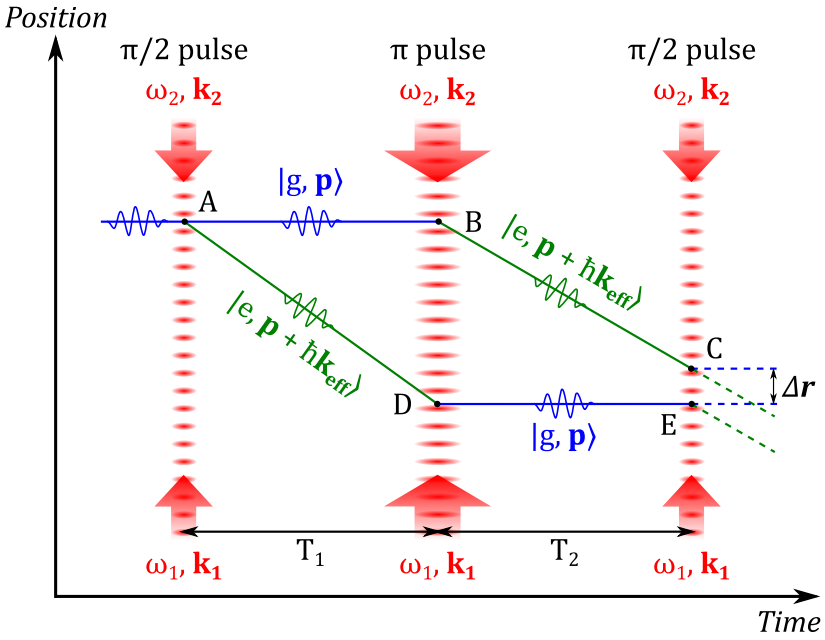

Figure 1.3: General representation of an open atom interferometer, here in a Mach-Zehnder configuration for non-necessarily equal interrogation times T_1 and T_2. The two atomic trajectories are not necessarily properly recombined, hence a spatial separation $\Delta \boldsymbol{r}$ of the wave packets can be observed at the output.

are not overlapped at the exit of the interferometer, called the separation phase ϕ_{sep}.

The total phase of the interferometer, calculated by summing these different contributions, determines the probability to measure an atom in a given state at the end of the sequence, namely $|g, \boldsymbol{p}\rangle$ or $|e, \boldsymbol{p} + \hbar \boldsymbol{k_{\text{eff}}}\rangle$. It is written:

$$\Phi = \phi_{\text{las}} + \phi_{\text{prop}} + \phi_{\text{sep}}. \tag{1.7}$$

The modeling of this physical quantity associated to the measurement of the state of the atom at the output of the interferometer allow to retrieve the desired inertial effect.

1.1.4 Evolution matrix for atom-light interaction

In order to realize a light-pulse atom interferometer, we need to determine how Raman laser beams can diffract the atomic wave packets and coherently split or swap the populations between two given energy levels $|g\rangle$ and $|e\rangle$. Let us define the Hamiltonian associated with the considered system:

$$\widehat{H} = \sum_j \hbar \omega_j \, |j\rangle \langle j| - \boldsymbol{D}.(\boldsymbol{E_1} + \boldsymbol{E_2}) \tag{1.8}$$

where $|j\rangle$ denote the system's eigenstates and $\boldsymbol{D}$ represents the electric dipole coupling between the atoms and Raman lasers of electric field $\boldsymbol{E_{1,2}}$. For a freely-propagating

atom in a given initial state $|g\rangle$ or $|e\rangle$ and provided with a well-defined initial momentum $\boldsymbol{p_0}$, its interaction with a laser field can result in a change (or not) in its internal state and transverse momentum [Storey and Cohen-Tannoudji 1994]. The evolution of the atomic wave function $|\psi(t)\rangle$, describing the probability for this system to be in a given internal state, is obtained by solving the Schrödinger equation:

$$i\hbar\frac{\partial\,|\psi(t)\rangle}{\partial t} = \widehat{H}\,|\psi(t)\rangle\,. \tag{1.9}$$

Assuming that the condition on the Raman detuning mentioned above is verified, such that equation 1.2 is true, the wave function at a time t_0 can be written:

$$|\psi(t_0)\rangle = C_g(t_0)\,|g\rangle + C_e(t_0)\,|e\rangle \tag{1.10}$$

with $C_g(t)$ and $C_e(t)$ the time-varying probability amplitudes to find the atom in the state $|g\rangle$ or $|e\rangle$ respectively. The time evolution of the atomic wave function between times t_0 and $t_0+\tau$ is governed by the following equation:

$$|\psi(t_0+\tau)\rangle = \mathcal{S}(t_0,\tau,\phi)\,|\psi(t_0)\rangle\,. \tag{1.11}$$

where $\phi=\phi_1-\phi_2$ denotes the relative phase of the Raman lasers and $\mathcal{S}(t_0,\tau,\phi)$ the system's evolution matrix given by [Cheinet 2006]:

$$\begin{pmatrix} \left[\cos\left(\frac{\Omega_R\tau}{2}\right) - i\cos\theta\sin\left(\frac{\Omega_R\tau}{2}\right)\right]e^{-i\omega_g^-\frac{\tau}{2}} & -i\sin\theta\sin\left(\frac{\Omega_R\tau}{2}\right)e^{i[(\omega_1-\omega_2)t_0+\phi]}e^{-i\omega_g^-\frac{\tau}{2}} \\ -i\sin\theta\sin\left(\frac{\Omega_R\tau}{2}\right)e^{-i[(\omega_1-\omega_2)t_0+\phi]}e^{-i\omega_e^+\frac{\tau}{2}} & \left[\cos\left(\frac{\Omega_R\tau}{2}\right) + i\cos\theta\sin\left(\frac{\Omega_R\tau}{2}\right)\right]e^{-i\omega_e^+\frac{\tau}{2}} \end{pmatrix} \tag{1.12}$$

where the notations $\cos\theta=(\delta-\omega_{\mathrm{LS}})/\Omega_R$ and $\sin\theta=|\Omega_{\mathrm{eff}}|/\Omega_R$ have been introduced, as well as $\omega_{\mathrm{g,e}}^{\pm}=\overline{\omega_{\mathrm{LS}}}\pm\delta+2\omega_{\mathrm{g,e}}$ with $\overline{\omega_{\mathrm{LS}}}=\Omega_{\mathrm{LS}}^e+\Omega_{\mathrm{LS}}^f$ the mean light shift.

Atomic beam-splitter and mirror

Now that the evolution of the atomic wave function interacting with the Raman laser beams is established, experimental parameters can be chosen to design the targeted atom optics. First, to realize an atomic mirror, the laser pulse duration must be set to a value τ_π verifying $\Omega_{\mathrm{eff}}\tau_\pi=\pi$. This will correspond to the peak of the Rabi oscillation depicted in figure 1.2 and ensure a maximum probability of transferring an atom in the state $|g,\boldsymbol{p_0}\rangle$ to the state $|e,\boldsymbol{p_0}+\hbar\boldsymbol{k_{\mathrm{eff}}}\rangle$ and reciprocally. For a perfect mirror presenting a 100% transition probability, the evolution matrix can be written:

$$\mathcal{S}_\pi = \begin{pmatrix} 0 & -ie^{-i\phi_{\mathrm{las}}} \\ -ie^{i\phi_{\mathrm{las}}} & 0 \end{pmatrix}. \tag{1.13}$$

where

$$\phi_{\text{las}}(t) = \boldsymbol{k}_{\text{eff}}.\boldsymbol{r}(t) - \omega_{\text{eff}}t + \phi(t) \tag{1.14}$$

represents the phase imprinted by the laser onto the atoms, with $\omega_{\text{eff}} = \omega_1 - \omega_2$ standing for the effective frequency associated to the two-photon Raman transition. It can be observed that the first term appearing in ϕ_{las} denotes a change of $\pm\hbar\boldsymbol{k}_{\text{eff}}$ in the transverse momentum of the atom after the absorption or stimulated emission of a photon. Additionally, the third term indicates that the relative phase of the two Raman lasers is present in the output signal, meaning that laser phase noise can hinder or limit the accuracy of the measurement. This can be dealt with by using a single laser beam retroreflected by a reference mirror.

Following the same reasoning, an atomic beam-splitter can be achieved by choosing a pulse duration $\tau_{\pi/2}$ such that $\Omega_{\text{eff}}\tau_{\pi/2} = \pi/2$, corresponding to a 50% transition probability on the Rabi oscillations plot showed in 1.2. Such a transition applied to an atom prepared in either the ground or excited state will result in a coherent superposition of these two states, and can be used for both splitting or recombining the two arms of an interferometer. In the ideal case, the matrix associated to this operation is given by:

$$\mathcal{S}_{\pi/2} = \frac{1}{\sqrt{2}} \begin{pmatrix} 1 & -ie^{-i\phi_{\text{las}}} \\ -ie^{i\phi_{\text{las}}} & 1 \end{pmatrix}. \tag{1.15}$$

It must be noted that the change operated in the system's internal state, whether having the whole atomic cloud or just part of it transferring from $|g, e\rangle$ to $|e, g\rangle$, comes with a spatial deviation of the involved atoms related to a momentum transfer from the laser field to each atom by $\pm\hbar\boldsymbol{k}_{\text{eff}}$. This feature is illustrated on the vertical axis in figure 1.3, which represents the spatial trajectories of the atomic wave packets propagating along each arm after the atomic beam-splitter, mirror and recombiner.

1.1.5 Atoms' free evolution in a gravitational potential

Now that the evolution of the atomic wave function after interacting with the laser beams has been investigated, we need to evaluate the phase shift associated to the free propagation of the wave packet in the absence of the light field. To that end, we use the Feynman path integral approach which describes the dynamic of a classical particle using Lagrangian mechanics, as detailed in [Storey and Cohen-Tannoudji 1994].

The Lagrangian $\mathcal{L}$ is a function of a system's dynamic variables, namely its position and velocity, defined as the difference between the kinetic energy T and the potential

energy V:

$$\mathcal{L}(z, \dot{z}) = T - V \tag{1.16}$$

$$= \frac{1}{2} m \dot{z}^2 - V(z). \tag{1.17}$$

According to the principle of least action, among all the space-time trajectories joining the points $z_a = z(t_a)$ and $z_b = z(t_b)$, the one followed by a particle is such that the classical action S_{cl} is extremal and is called the classical path Γ_{cl}. The classical action is given by the temporal integral of the Lagrangian over this space-time area, namely:

$$S_{\text{cl}} = \int_{t_a}^{t_b} \mathcal{L}(z(t), \dot{z}(t)) dt. \tag{1.18}$$

Furthermore, using the differential form of the principle of least action, one can write the Euler-Lagrange equation stating:

$$\frac{\partial \mathcal{L}}{\partial z} - \frac{d}{dt} \frac{\partial \mathcal{L}}{\partial \dot{z}} = 0 \tag{1.19}$$

which leads to the equation of motion describing the behavior of the studied particle.

In order to determine the final state of the studied quantum system, we define the evolution operator $U_{\text{prop}}(t_b, t_a)$ describing the evolution of the wave function of a system propagating in a given environment from the time t_a to t_b, such that:

$$|\psi(t_b)\rangle = U_{\text{prop}}(t_b, t_a) \, |\psi(t_a)\rangle \, . \tag{1.20}$$

Subsequently, this final state can be projected in the position space, which leads to defining the possibility for the particle starting from point $z_a t_a$ to reach the point $z_b t_b$. This probability is represented by the quantum propagator:

$$K(z_b t_b, z_a t_a) \equiv \langle z_b | \, U_{\text{prop}}(t_b, t_a) \, | z_a \rangle \tag{1.21}$$

$$= \mathcal{N} \sum_{\Gamma} \exp\left(i \frac{S_\Gamma}{\hbar} \right) \tag{1.22}$$

where Γ runs over the different paths connecting $z_a t_a$ to $z_b t_b$, $\mathcal{N}$ is a normalization constant and $S_\Gamma / \hbar$ is the phase accumulated along a given path Γ. Hence, for the studied particle, we can write the propagation phase associated to the classical path:

$$\phi_{\text{prop}} = \frac{S_{\text{cl}}}{\hbar}. \tag{1.23}$$

Let us now consider a particle in a gravitational field $\boldsymbol{g} = g \boldsymbol{u_z}$, described by the

Lagrangian:

$$\mathcal{L}(z, \dot{z}) = \frac{1}{2} m \dot{z}^2 - mgz; \tag{1.24}$$

The dynamic variables of the system can be calculated from equation 1.19, yielding for the two endpoints of the space-time trajectory $(z_a t_a, z_b t_b)$:

$$v_b = v_a - g(t_b - t_a) \tag{1.25}$$

$$z_b = z_a + v_a(t_b - t_a) - \frac{1}{2} g(t_b - t_a)^2 \tag{1.26}$$

$$v_a = \frac{z_b - z_a}{t_b - t_a} - \frac{1}{2} g(t_b - t_a). \tag{1.27}$$

Using the previous results, the system's Lagrangian can be integrated over the classical path to calculate the classical action:

$$S_{\mathrm{cl}}(z_b t_b, z_a t_a) = \frac{m}{2} \left[\frac{(z_b - z_a)^2}{t_b - t_a} - g(z_b + z_a)(t_b - t_a) - \frac{g^2}{12}(t_b - t_a)^3 \right] \tag{1.28}$$

where all the variables are determined, given that we know the initial position of the particle z_a. We note that for a free particle which is not evolving in any potential, the Lagrangian only consists in the kinetic energy and the previous calculations are straightforward. Combining equations 1.23 and 1.28, the phase associated to the propagation of the atomic wave packet from $z_a t_a$ to $z_b t_b$ is given by:

$$\phi_{\mathrm{prop}} = \frac{m}{2\hbar} \left[\frac{(z_b - z_a)^2}{t_b - t_a} - g(z_b + z_a)(t_b - t_a) - \frac{g^2}{12}(t_b - t_a)^3 \right]. \tag{1.29}$$

Calculating this phase for all the free-falling sections of a given arm of an interferometer, and comparing the total phases of the different arms at the output of the interferometer, finally leads to the phase difference associated to the propagation along the different arms. If not null, this result will directly appear in the interferometric measurement.

1.1.6 Mach-Zehnder atom interferometer for acceleration sensing

Exploiting the atom optics defined in 1.1.4, we can control the trajectory of an atomic wave packet in order to realize a symmetrical Mach-Zehnder atom interferometer. If different types of atomic transitions are compatible with such devices, velocity-selective Raman transitions allow for internal state labeling [Ch. J. Bordé 1989] meaning that the detection of a given output port can be performed based on its energy level, contrarily to Bragg transitions for example where the different arms of the interferometer are in the same internal state. Figure 1.4 shows the principle operation of such an atomic

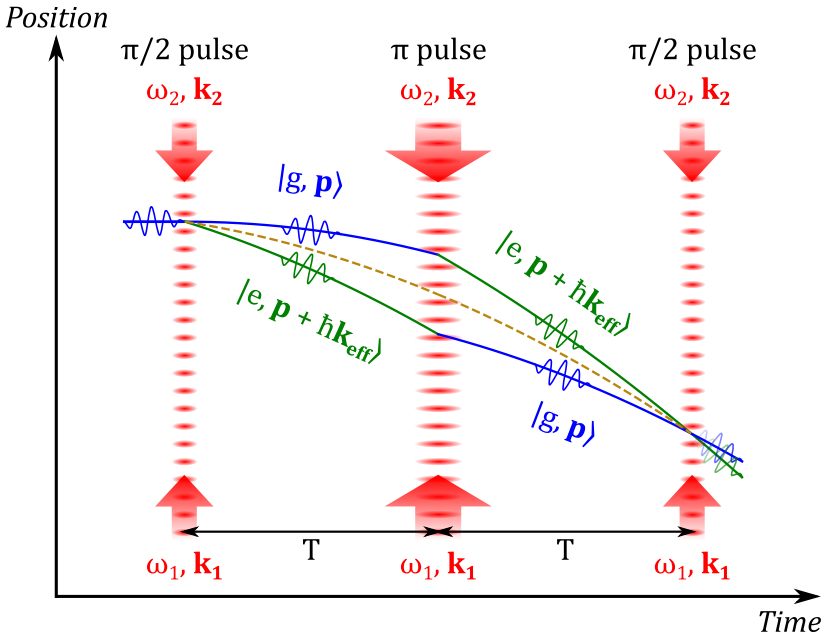

Figure 1.4: Illustration of the space-time propagation of two matter waves in a gravitational potential along the two arms of a Mach-Zehnder atomic interferometer. The Raman lasers couple the states $|g, \boldsymbol{p}\rangle$ (blue) and $|e, \boldsymbol{p} + \hbar \boldsymbol{k_{\text{eff}}}\rangle$ (green). The mid-point trajectory is also displayed (brown dotted line).

interferometer using Raman transitions in a Mach-Zehnder configuration. Hence, shining a laser resonant with the $|F = 2\rangle \rightarrow |F' = 3\rangle$ allows to detect the population in the upper ground state $|e\rangle \equiv |F = 2\rangle$ by fluorescence using photodetectors instead of high spatial resolution cameras for imaging the interference pattern. The relevant parameter one wants to observe is then the fraction of atoms in the state $|e\rangle$ at the output of the interferometer, defined by:

$$P_e = \frac{N_e}{N_g + N_e} \tag{1.30}$$

where N_g and N_e represent the number of atoms in the states $|g\rangle \equiv |F = 1\rangle$ and $|e\rangle \equiv |F = 2\rangle$ respectively. This fraction is connected to the total interferometric phase shift through the equation:

$$P_e = P_0 - \frac{C}{2} \cos \Phi \tag{1.31}$$

where P_0 and C stand for the offset and the contrast of the interferometric fringes respectively. Displaying the evolution of the population in the state $|e\rangle$ as a function of the total interferometric phase shift then allows to retrieve the relevant information contained in the latter. In the case of atom interferometers, manipulating massive matter waves sensitive to various inertial effects, the interferometric phase shift related to the path difference between the two arms will contain information on the acceleration of the atomic cloud relative to the reference mirror.

As mentioned above, the phase shift accumulated between the arms of the atomic interferometer is the sum of three terms, namely the laser phase imprinted by the Raman lasers onto the atoms ϕ_{las} defined in 1.1.4, the free evolution of the atomic wave packets ϕ_{prop} defined in 1.1.5 and a possible spatial separation between the wave packets coming from the different arms at the moment of the last Raman pulse meant to perform the recombination ϕ_{sep}. This separation phase is given by [Bongs et al. 2006]:

$$\phi_{\text{sep}} = \frac{\overline{\boldsymbol{p}}.\Delta\boldsymbol{r}}{\hbar} \tag{1.32}$$

where $\overline{\boldsymbol{p}} = (\boldsymbol{p}(C) + \boldsymbol{p}(E))/2$ is the mean momentum of the wave packets in a given output port and $\Delta\boldsymbol{r}$ is the spatial separation between the centers of each wave packet at the instant of the recombination pulse, as illustrated in figure 1.3 where a Mach-Zehnder geometry was depicted.

In a balanced Mach-Zehnder geometry, the perfect overlap of the two wave packets at the moment of the recombination ensures no separation phase $\phi_{\text{sep}} = 0$. Additionally, the propagation phases associated to each arm are identical due to the symmetrical geometry (same interrogation time in the two free-evolution areas separating the Raman beams) and no contribution is added to the measurement $\phi_{\text{prop}} = 0$. It must be noted that this last result is, in general, not true and only depends on the interferometer's geometry.

Additionally, if the interferometer is not perfectly closed and the wave packets not overlapped at the time of the recombination (which is the case when undergoing rotations or gravity gradients for example), the propagation and separation phases ϕ_{prop} and ϕ_{sep} taken independently are, in general, not null anymore. Nevertheless, for a Lagrangian at most quadratic in position and momentum, these two terms perfectly cancel out as it is demonstrated in [Antoine and Bordé 2003], so much so that the interferometric phase shift still arises from the interaction with the Raman lasers only:

$$\Phi = \phi_{\text{las}}. \tag{1.33}$$

In this case, making use of equation 1.14, the phase shift accumulated between the two arms of the atomic interferometer can be described by the mid-point theorem [Antoine and Bordé 2003; Overstreet et al. 2021]:

$$\Phi_{\text{MP}} \equiv \sum_{i=1}^{N} \boldsymbol{k}_{\mathbf{eff,i}}.\overline{\boldsymbol{r}}_i - \omega_{\text{eff,i}} t_i + \phi_i \tag{1.34}$$

with i the index running over the N atom-light interaction and

$$\overline{\boldsymbol{r}}_i = \frac{\boldsymbol{r}_{\mathrm{A,i}} + \boldsymbol{r}_{\mathrm{B,i}}}{2} \tag{1.35}$$

the average displacement of the two arms A and B with respect to the laser at the i^{th} interaction. This equation assumes that the atomic wave packets follow the mid-point trajectory represented by the brown, dotted line in figure 1.4. In a symmetric Mach-Zehnder geometry, the frequency-dependent terms cancel out and the interferometric phase shift simplifies to the expression:

$$\Phi_{\mathrm{MZ}} = \boldsymbol{k}_{\mathbf{eff}}(0).\overline{\boldsymbol{r}}(0) - 2\boldsymbol{k}_{\mathbf{eff}}(T).\overline{\boldsymbol{r}}(T) + \boldsymbol{k}_{\mathbf{eff}}(2T).\overline{\boldsymbol{r}}(2T) + \phi_1 - 2\phi_2 + \phi_3. \tag{1.36}$$

For example, considering the case of an atom in a gravitational potential with a constant effective wave vector and a constant laser phase, this equation yields the simplified phase shift:

$$\Phi = k_{\mathrm{eff}} g T^2 \tag{1.37}$$

where we observe that the gravity acceleration the atoms are subject to is contained in the phase imprinted by the lasers onto the wave packets even though the laser phase ϕ is maintained constant during the interferometer. Provided that the Lagrangian describing the motion of the particles is known, the technique described in this section can be applied to all sorts of systems and in particular to the case of a rotating frame.

1.2 Atom interferometry under non-constant accelerations

In the previous section, the theoretical realization of a symmetrical Mach-Zehnder using free-falling cold atoms was reported. The value of the phase shift determined at the end of this study, however, only holds as long as the atoms are falling under the action of the gravitational acceleration and the laser used to prepare and interrogate them is perfectly immobile. As soon as time-varying accelerations are introduced in the system, and in particular in the case of vibrations applied on a mirror retroreflecting the Raman laser beam, the position of the atoms at the space-time points intervening in the mid-point theorem are no longer straightforwardly calculated. In practice, it results in the quantum accelerometer quickly becoming inoperative and the phase shift at its output being significantly modified such that the interferometric fringes are completely blurred. Indeed, in that situation, the retroreflecting mirror serves as a phase reference and its movements, as small as they can be, can have a strong impact

on the measurement.

1.2.1 The sensitivity function formalism

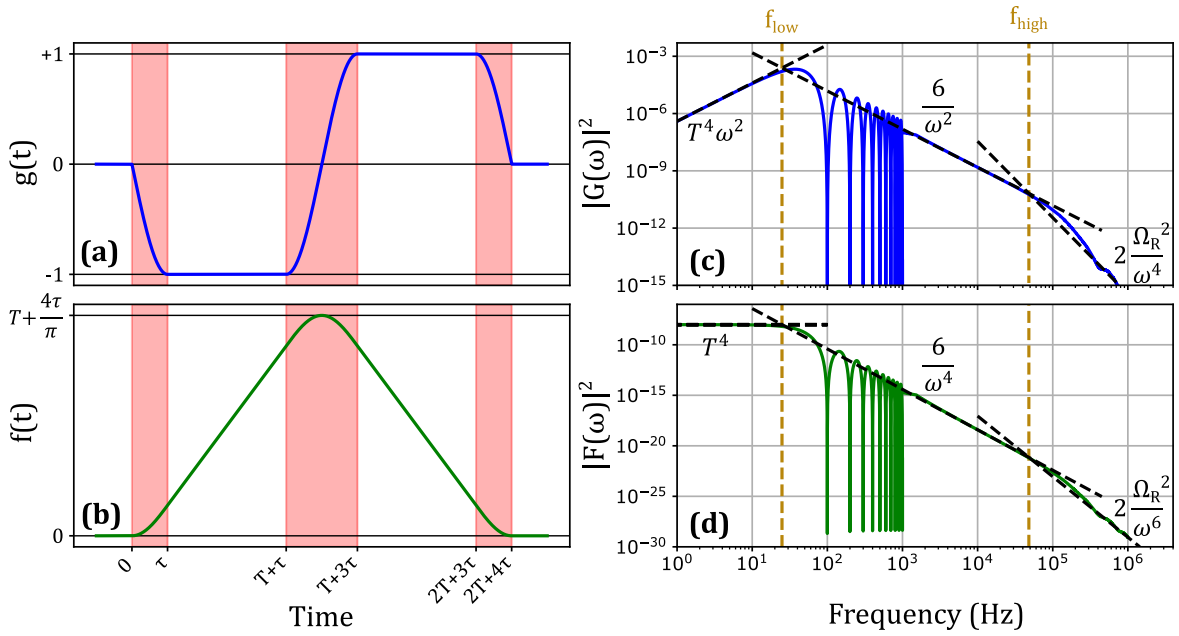

Figure 1.5: (a) Sensitivity function $g(t)$ and (b) response function $f(t)$ characterizing the response of the interferometer to temporal fluctuations in the velocity and acceleration of the atomic cloud relative to the reference mirror respectively. The pulses' durations are expanded ten times to better see what happens during these. The squared modulus of the transfer functions (c) $G(\omega)$ and (d) $F(\omega)$ exhibit the response to sinusoidal excitation of the same parameters. The cutoff frequencies and asymptotic behaviors are computed for typical experimental parameters values, namely an interrogation time $T = 10$ ms, a $\pi/2$ pulse duration $\tau = 3$ μs and considering perfect beam-splitters and mirror with $\Omega_R = \pi/(2\tau)$.

The sensitivity function of an atomic interferometer $g(t)$ is a tool characterizing the influence of a phase jump $\delta\phi$, occurring on the Raman phase ϕ at a time t, on the transition probability $P(t)$ [Cheinet et al. 2008]. It is defined by:

$$g(t) = 2 \lim_{\delta\phi \to 0} \frac{\delta P(\delta\phi, t)}{\delta\phi} \tag{1.38}$$

with $\delta P(\delta\phi, t)$ the change in the transition probability induced by the phase jump. For square pulses of duration $\tau = \tau_\pi/2$, an interrogation time T and an effective Rabi

frequency Ω_R, it can be rewritten:

$$g(t) = \begin{cases} 0 & \text{for } t \leq 0 \text{ and } t > 2T + 4\tau \\ -\frac{\sin(\Omega_R t)}{\sin(\Omega_R \tau)} & \text{for } 0 < t \leq \tau \\ -1 & \text{for } \tau < t \leq T + \tau \\ -\frac{\sin(\Omega_R (t-T-2\tau))}{\sin(\Omega_R \tau)} & \text{for } T + \tau < t \leq T + 3\tau \\ +1 & \text{for } T + 3\tau < t \leq 2T + 3\tau \\ -\frac{\sin(\Omega_R (t-2T-4\tau))}{\sin(\Omega_R \tau)} & \text{for } 2T + 3\tau < t \leq 2T + 4\tau \end{cases} . \tag{1.39}$$

This sensitivity function, displayed in figure 1.5 (a), is particularly useful to assess the variations of the interferometric phase Φ arising from an arbitrary Raman laser phase noise $\phi(t)$, given by:

$$\delta\Phi = \int_{-\infty}^{+\infty} g(t) d\phi(t) = \int_{-\infty}^{+\infty} g(t) \frac{d\phi(t)}{dt} dt = \int_{-\infty}^{+\infty} g(t)\omega(t) dt. \tag{1.40}$$

This leads to the transfer function of the interferometer, defined by the evolution of the interferometric phase under a sinusoidal modulation of the Raman phase and calculated using the Fourier transform of the sensitivity function:

$$\begin{aligned} G(\omega) &= \int_{-\infty}^{+\infty} e^{-i\omega t} g(t) dt \\ &= \frac{4i\Omega_R}{\omega^2 - \Omega_R^2} \sin\left(\frac{\omega(T+2\tau)}{2}\right) \left[\sin\left(\frac{\omega(T+2\tau)}{2}\right) + \frac{\Omega_R}{\omega} \sin\left(\frac{\omega T}{2}\right)\right]. \end{aligned} \tag{1.41}$$

This transfer function to a sinusoidal variation of the frequency $\omega(t)$, associated with the sensitivity function $g(t)$ and represented in figure 1.5 (c), is particularly useful to study the influence of changes in the laser frequency or in the atomic resonances. Subsequently, as the motion of the atomic cloud is related to the laser frequency through the Doppler shift which can modify the resonance condition, the transfer function $G(\omega)$ can provide information about the velocity of the atoms relative to the optical standing wave formed by the counter-propagating laser beams. In the case of a retroreflected configuration, this corresponds to the velocity of the atoms with respect to the reference mirror. Alternatively, the transfer function defined by $H(\omega) = \omega G(\omega)$ is used to characterize the influence of the Raman lasers' relative phase noise on the interferometric phase thanks to the equation:

$$\sigma_\Phi^2 = \int_0^{+\infty} \frac{1}{2\pi} |H(\omega)|^2 S_\phi(\omega) d\omega \tag{1.42}$$

with $S_\phi(\omega)$ the power spectral density of the lasers' relative phase noise.

Now if one wants to investigate the sensitivity of the atomic interferometer to accelerations of the atomic wave packet relative to the reference mirror, it is more convenient to use the response function described in [Ménoret 2012] by the equation:

$$\begin{aligned} f(t) &= -\int_0^t g(t')dt' \\ &= \begin{cases} 0 & \text{for } t \leq 0 \text{ and } t > 2T + 4\tau \\ \frac{1-\cos(\Omega_R t)}{\Omega_R} & \text{for } 0 < t \leq \tau \\ t - \tau + \frac{1}{\Omega_R} & \text{for } \tau < t \leq T + \tau \\ T + \frac{1-\cos(\Omega_R(T+2\tau-t))}{\Omega_R} & \text{for } T + \tau < t \leq T + 3\tau \\ 2T + 3\tau - t + \frac{1}{\Omega_R} & \text{for } T + 3\tau < t \leq 2T + 3\tau \\ \frac{1-\cos(\Omega_R(2T+4\tau-t))}{\Omega_R} & \text{for } 2T + 3\tau < t \leq 2T + 4\tau \end{cases} \end{aligned} \tag{1.43}$$

and depicted in figure 1.5 (b), such that the kinetic phase related to the atomic cloud's motion is calculated:

$$\phi_{\text{kin}} = \int_{-\infty}^{+\infty} f(t)\boldsymbol{k_{\text{eff}}}.\boldsymbol{a}(t)dt \tag{1.44}$$

where $\boldsymbol{a}(t)$ is the acceleration of the atomic wave packet relative to the reference mirror. In the case of a constant Rabi frequency over the duration of the interferometer, the response function of the interferometer is null outside this time interval and this integral can be restricted to these bounds. Additionally, as this function characterizes the response of the atom interferometer to accelerations, it can be used to define the scale factor of the resulting atomic accelerometer by calculating the phase shift arising from the measurement of a constant acceleration a_0:

$$\mathcal{S}_{\text{kin}} = \frac{\phi_{\text{kin}}}{a_0} = k_{\text{eff}} \int_0^{2T+4\tau} f(t)dt = k_{\text{eff}} \left(T + 2\tau\right) \left[T + \frac{2}{\Omega_R} \tan\left(\frac{\Omega_R \tau}{2}\right)\right] \tag{1.45}$$

with $k_{\text{eff}} = \|\boldsymbol{k_{\text{eff}}}\|$ the norm of the effective wave vector (or wave number) of the laser. Assuming perfect Raman pulses associated with an effective Rabi frequency $\Omega_R = \pi/2\tau$, this simplifies as:

$$\mathcal{S}_{\text{kin}} = k_{\text{eff}} \left(T + 2\tau\right) \left(T + \frac{4\tau}{\pi}\right) \tag{1.46}$$

Similarly to the development made on the sensitivity function, the acceleration transfer function is given by its Fourier transform: $F(\omega) = -G(\omega)/\omega$ and is exhibited in figure 1.5 (d).

The two transfer functions $G(\omega)$ and $F(\omega)$ display oscillations at frequencies given

by $1/(T+2\tau)$, as well as two cutoff frequencies:

$$\begin{aligned} f_{\text{low}} &= \frac{1}{2\pi}\frac{\sqrt[4]{6}}{T} \\ f_{\text{high}} &= \frac{1}{2\pi}\frac{\Omega}{\sqrt{3}} \end{aligned} \tag{1.47}$$

defining the sensitivity range of the interferometer. In particular, the transfer function $G(\omega)$ features a peak at $f_{\text{low}} \simeq 25$ Hz for $T = 10$ ms, revealing a critical sensitivity in this area of the spectrum to frequency shifts arising from the Autler-Townes effect (laser power fluctuations) or Zeeman effect (magnetic field fluctuations) for example. As for the transfer function $F(\omega)$, its squared modulus has the shape of a low-pass filter meaning that the interferometric phase shift will be mostly sensitive to mirror vibrations below $\simeq 100$ Hz where the first resonance occurs at $T = 10$ ms.

1.2.2 Case of an imbalanced Mach-Zehnder atom interferometer

The results presented in the previous subsection hold for a perfectly symmetric Mach-Zehnder geometry, with identical interrogation times during the two free-falling areas of the interferometer $T_1 = T_2 \equiv T$ and the same Raman pulses' durations for the splitting and recombination (half of the atomic mirror's duration), namely $\tau_1 = \tau_3 \equiv \tau$ and $\tau_2 \equiv 2\tau$. Additionally, they assume a consistent Rabi frequency all along the interferometer as well, that is $\Omega_1 = \Omega_3 \equiv \Omega_R$ and $\Omega_2 \equiv 2\Omega_R$.

In practice, the timings of the sequence are very well-defined and the assumptions on the pulses lengths and interrogation time can be considered correct. Nevertheless, supposing imperfections in the shape of the laser beams, power fluctuations or the atoms scanning the intensity profile of a Gaussian beam when they are not falling rigorously along its propagation axis, the effective Rabi frequency will indeed vary throughout the interferometer leading to a modification of the interferometer's sensitivity function as follows:

$$g(t) = \begin{cases} 0 & \text{for } t \leq 0 \text{ and } t > 2T + 4\tau \\ -\frac{\sin(\Omega_1 t)}{\sin(\Omega_1 \tau)} & \text{for } 0 < t \leq \tau \\ -1 & \text{for } \tau < t \leq T + \tau \\ -\frac{\sin(\Omega_2 (t-T-2\tau)/2)}{\sin(\Omega_2 \tau/2)} & \text{for } T + \tau < t \leq T + 3\tau \\ +1 & \text{for } T + 3\tau < t \leq 2T + 3\tau \\ -\frac{\sin(\Omega_3 (t-2T-4\tau))}{\sin(\Omega_3 \tau)} & \text{for } 2T + 3\tau < t \leq 2T + 4\tau \end{cases} . \tag{1.48}$$

In addition to modifying the contrast of the interference fringes pattern, by changing the efficiency of the Raman laser pulses throughout the interferometer, this altered sensitivity function with inhomogeneous Rabi frequencies leads to a redefinition of the atom interferometer's scale factor. The new expression of the output phase shift, involving the initial velocity of the atomic cloud at the instant of the first pulse v_0, is given by:

$$\begin{aligned}\phi_{\text{kin}} = &- k_{\text{eff}} v_0 \left[\frac{1}{\Omega_3}\tan\left(\frac{\Omega_3\tau}{2}\right) - \frac{1}{\Omega_1}\tan\left(\frac{\Omega_1\tau}{2}\right)\right] \\ &- k_{\text{eff}} g(T+2\tau)\left[T + \frac{1}{\Omega_1}\tan\left(\frac{\Omega_1\tau}{2}\right) + \frac{1}{\Omega_3}\tan\left(\frac{\Omega_3\tau}{2}\right)\right. \\ &\left.+\tau\left(\frac{\cot(\Omega_1\tau)}{\Omega_1} - 2\frac{\cot(\Omega_2\tau)}{\Omega_2} + \frac{\cot(\Omega_3\tau)}{\Omega_3}\right) - \left(\frac{1}{\Omega_1^2} - \frac{2}{\Omega_2^2} + \frac{1}{\Omega_3^2}\right)\right]\end{aligned} \tag{1.49}$$

where Ω_i is the effective Rabi frequency associated with the i^{th} Raman pulse of the interferometer.

1.3 Matter-wave interferometry with a rotating device

If vibrations can add a parasitic signal in the quantum accelerometer's output, which is not what is meant to be measured depending on the frequency range, they are not the only problem one can face when trying to build an atom interferometer meant for onboard applications. Indeed, an atom interferometer undergoing arbitrary rotations will see its fringes degraded, blurred and even extinguished almost immediately. Two main effects are at the origin of this degradation: first, a decrease in the spatial overlap of the two atomic wave packets' envelopes will lead to a reduction of the fringes' visibility but also to a spatial interference pattern when recombining the two arms, which further reduces the contrast when using an averaging detection system [Roura et al. 2014]. Second, supplementary phase shifts between the atomic paths due to a combination of complex inertial trajectories modify the output of the interferometer in a hardly predictable way, making it complicated to retrieve the desired acceleration value.

1.3.1 Behavior of the atoms in an arbitrary moving frame

We know that in the laboratory's frame $\mathcal{R}_0$, assimilated to the terrestrial frame if we neglect Earth's rotation or if it is accounted for in the total rotation rate considered, the atoms only fall under the action of gravity as illustrated in figure 1.6 (a) and we

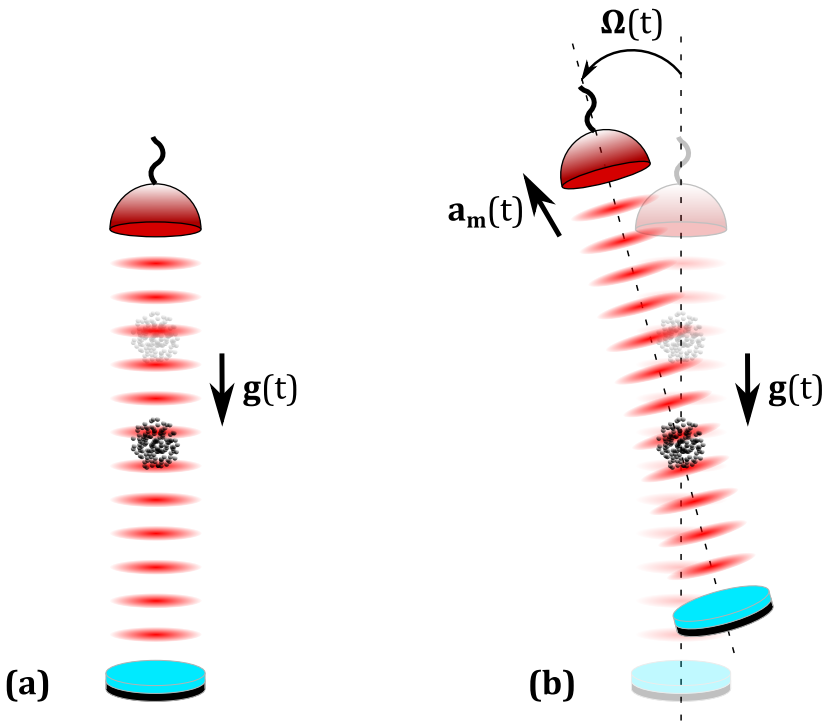

Figure 1.6: Comparison of (a) a static retroreflected laser beam which interrogates atoms falling under the action of gravity and (b) a mobile setup undergoing arbitrary, time-varying accelerations and rotations. In this case as well, the atoms only free-fall under gravity and are isolated from external inertial effects.

can express the Lagrangian of a free falling atom as:

$$\mathcal{L}_0 = \frac{1}{2} m \boldsymbol{v_0}^2(t) + m \boldsymbol{g}.\boldsymbol{r_0}(t) \tag{1.50}$$

with $\boldsymbol{v_0}(t)$ and $\boldsymbol{r_0}(t)$ the velocity and position of the atom in the frame $\mathcal{R}_0$. Under arbitrary motions of the interferometer as depicted in figure 1.6 (b), and especially rotations of the laser beam, we need to operate the following velocity transformation:

$$\boldsymbol{v_0}(t) = \boldsymbol{v_m}(t) + \boldsymbol{\Omega}(t) \times \boldsymbol{r_m}(t) \tag{1.51}$$

with $\boldsymbol{\Omega}(t)$ the rotation rate of the mobile frame $\mathcal{R}_m$ (or rotating frame, attached to the laser collimator) in the external frame $\mathcal{R}_0$, $\boldsymbol{r_m}(t)$ and $\boldsymbol{v_m}(t)$ the position and velocity of the atoms in the mobile frame $\mathcal{R}_m$. By placing the origin of this frame at the center of mass of the mobile, also defined as its center of rotation, the position of the atoms will be established with respect to this point, so much so that we can standardize the notations $\boldsymbol{r}(t) \equiv \boldsymbol{r_0}(t) = \boldsymbol{r_m}(t)$. Additionally, for convenience, we define $\dot{\boldsymbol{r}}(t) \equiv \boldsymbol{v_m}(t)$. Substituting 1.51 in 1.50 enables us to write this Lagrangian in the mobile frame:

$$\mathcal{L} = \frac{1}{2} m (\dot{\boldsymbol{r}}(t) + \boldsymbol{\Omega}(t) \times \boldsymbol{r}(t))^2 + m \boldsymbol{a}(t).\boldsymbol{r}(t) \tag{1.52}$$

with $\boldsymbol{a}(t)$ the linear acceleration of the atoms relative to the mobile which can be decomposed as $\boldsymbol{a}(t) = \boldsymbol{g} - \boldsymbol{a_m}(t)$. The term $\boldsymbol{a_m}(t)$ includes both the DC component of the mobile frame's acceleration and its vibrations. Developing equation 1.52 yields:

$$\mathcal{L} = \frac{1}{2}m(\dot{\boldsymbol{r}}(t) + \boldsymbol{\Omega}(t) \times \boldsymbol{r}(t))^2 + m\boldsymbol{a}(t).\boldsymbol{r}(t) \tag{1.53}$$

$$= \frac{1}{2}m\left[(\dot{\boldsymbol{r}}^2(t) + 2\dot{\boldsymbol{r}}(t).\left(\boldsymbol{\Omega}(t) \times \boldsymbol{r}(t)\right) + \left(\boldsymbol{\Omega}(t) \times \boldsymbol{r}(t)\right)^2\right] + m\boldsymbol{a}(t).\boldsymbol{r}(t). \tag{1.54}$$

Using the Euler-Lagrange equation finally leads to the equation of motion:

$$\ddot{\boldsymbol{r}}(t) + 2\left(\boldsymbol{\Omega}(t) \times \dot{\boldsymbol{r}}(t)\right) + \boldsymbol{\Omega}(t) \times \left(\boldsymbol{\Omega}(t) \times \boldsymbol{r}(t)\right) + \dot{\boldsymbol{\Omega}}(t) \times \boldsymbol{r}(t) = \boldsymbol{a}(t). \tag{1.55}$$

Hence, the total acceleration $\boldsymbol{a}(t)$ which will be measured when realizing a matter-wave interferometer in a rotating frame is the result of four contributions:

- The first term $\boldsymbol{a_{rel}}(t) = \ddot{\boldsymbol{r}}(t) = \frac{\partial^2 \boldsymbol{r}}{\partial t^2}$ denotes the relative acceleration, formulated with respect to the mobile frame.
- The second term $\boldsymbol{a_{Cor}}(t) = 2\left(\boldsymbol{\Omega}(t) \times \dot{\boldsymbol{r}}(t)\right)$ represents the Coriolis acceleration, which appears when studying the movement of an object moving in a frame rotating with respect to an inertial frame of reference.
- The double cross-product $\boldsymbol{a_{cen}}(t) = \boldsymbol{\Omega}(t) \times \left(\boldsymbol{\Omega}(t) \times \boldsymbol{r}(t)\right)$ stands for the centrifugal acceleration, which illustrates the inertial effect resulting from the lever arm of the rotation and is oriented in the direction opposite to the center of rotation.
- The last term $\boldsymbol{a_{tan}}(t) = \dot{\boldsymbol{\Omega}}(t) \times \boldsymbol{r}(t)$ is the tangential acceleration, related to the angular acceleration of the mobile frame relative to the external one.

1.3.2 Rotation-induced exponential decay of the atomic fringes' contrast

Imperfections in the geometry of a Mach-Zehnder atom interferometer can lead to a reduction in the fringes' visibility. Specifically for rotations, when studying the atom-light interaction in a non-rotating frame, the orientation of the momentum transfer $\hbar\boldsymbol{k_i}$ associated with each laser pulse $i = 1, 2, 3$ will be different, and in particular differently applied on the two arms of the interferometer. Indeed, the Raman beams diffract each atom to bring it into a quantum superposition of the two states participating in the interferometer (namely $|g, \boldsymbol{p}\rangle$ and $|e, \boldsymbol{p} + \hbar\boldsymbol{k_{eff}}\rangle$), the associated probabilities of which being described by the atom's wave function $|psi(t)\rangle$. Because of this, the fringes pattern is produced by the interference of each atom with itself, with a coherence

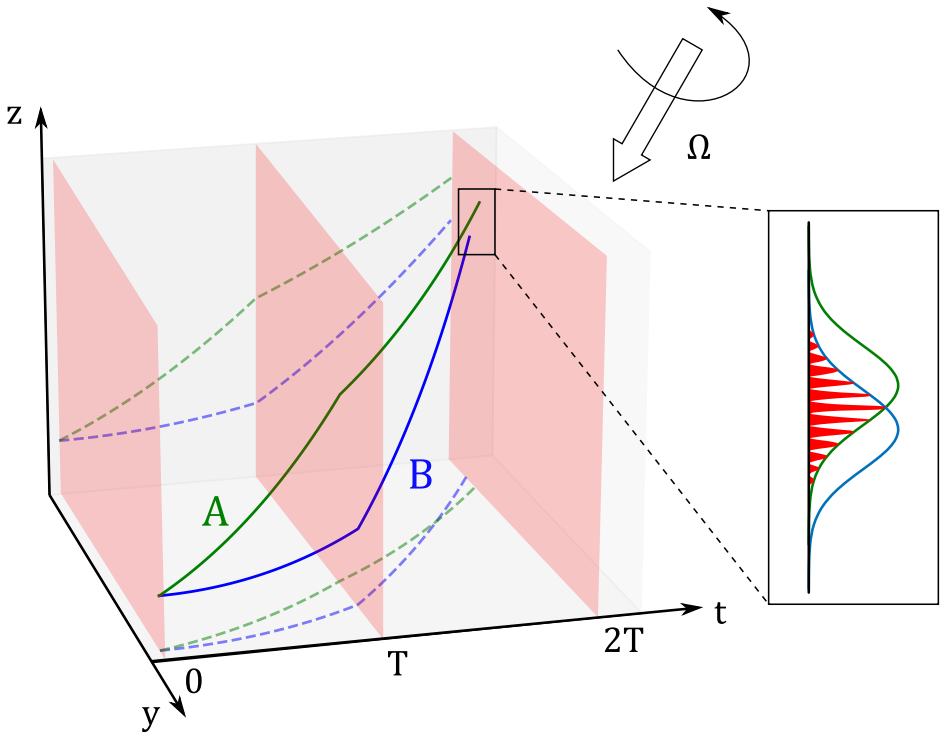

Figure 1.7: Representation of the two atomic wave packets' propagation under arbitrary rotations. Solid lines show the trajectories of the wave packets while dotted lines are their projections orthogonal to the y-z plane. Red sections illustrate the 3 Raman laser pulses. Pulses' duration is omitted on the temporal axis. Inset: spatial oscillations due to the reduced overlap between the atomic wave packets.

length assimilated to the thermal de Broglie wavelength:

$$\lambda_{\text{th}} = \sqrt{\frac{2\pi\hbar^2}{mk_B\mathcal{T}}} \tag{1.56}$$

where m and $\mathcal{T}$ respectively stand for the atom's mass and temperature. Hence, any rotation of the momentum kick inferred to the atoms will lead to a decoherence of this superposition and a reduction of the quantum overlap between the wave packets associated with the two arms of the interferometer. This will translate into spatial oscillations at each output port, as shown in figure 1.7, and even prevent any interference to occur in the case of an output separation larger than the coherence length. Using an averaging detection system such as photodiodes makes it impossible to resolve these spatial oscillations and only displays a general reduction of the interference fringes' contrast [Roura et al. 2014].

In order to quantify this contrast loss, we use an approach to take into account the fact that the rotation rate $\boldsymbol{\Omega}(t)$ is not constant during the atom interferometer. Our approach is based on the study [Roura et al. 2014] which introduces the phase-space displacement vector $\boldsymbol{\chi}(t) = (\boldsymbol{\mathcal{R}}(t), \boldsymbol{\mathcal{P}}(t))^T$ for the classical trajectories associated with

each branch of the interferometer. Additionally, writing $\widehat{\boldsymbol{\xi}} = (\widehat{\boldsymbol{x}}, \widehat{\boldsymbol{p}})^T$ the phase-space coordinates vector and introducing the matrix

$$J = \begin{pmatrix} 0 & \mathbb{1} \\ -\mathbb{1} & 0 \end{pmatrix} \tag{1.57}$$

one can define the displacement operator:

$$\widehat{\mathcal{D}}(\boldsymbol{\chi}) = \exp\left(-\frac{i}{\hbar}\boldsymbol{\chi}^T J \widehat{\boldsymbol{\xi}}\right) \tag{1.58}$$

so that the contrast of the interferometric fringes is given by:

$$C = \left|\langle\psi_c(t)|\, \widehat{\mathcal{D}}(\delta\boldsymbol{\chi})\, |\psi_c(t)\rangle\right| \leq 1 \tag{1.59}$$

where $\delta\boldsymbol{\chi}$ represents the relative displacement vector at a given output port, which is defined as:

$$\delta\boldsymbol{\chi} = \delta\boldsymbol{\mathcal{P}} - \frac{m}{\Delta t}\delta\boldsymbol{\mathcal{R}} \tag{1.60}$$

with $\delta\boldsymbol{\mathcal{P}}$ and $\delta\boldsymbol{\mathcal{R}}$ the separation in space and momentum respectively. It can be seen from this expression that the contrast becomes inferior to 1 whenever the relative displacement is not null. This situation will be called an open interferometer in the following.

Neglecting the shift by $\delta\boldsymbol{\mathcal{R}}$ of the wave packet's envelope (acknowledging that the envelope does not vary too rapidly in space, its size is much larger than $\delta\boldsymbol{\mathcal{R}}$) and considering late-time free evolution of the wave packet (where it takes a simpler form in position representation, similarly to Fraunhofer diffraction in optics), one can reach a convenient expression of the contrast in position representation:

$$C \approx \left|\int \exp\left[\frac{i}{\hbar}\left(\delta\boldsymbol{\chi}\cdot\boldsymbol{r}\right)\right] |\psi(\boldsymbol{r},t)|^2 \mathrm{d}^3\mathrm{r}\right|. \tag{1.61}$$

In the inertial frame determined by the Raman laser beam and the initial position and velocity of the atoms at the first pulse, we evaluate the position and momentum vectors' evolution of the center of mass after each interaction with the laser. For simplicity, we take the origin of time $t = 0$ at the first pulse and $\boldsymbol{r}(0^-) = \boldsymbol{v}(0^-) = \boldsymbol{p}(0^-) = \boldsymbol{0}$ since initial position, velocity and momentum of the wave-packet will be common to each arm of the interferometer and simplify when studying their relative displacement at the output. Considering the arms A and B of the interferometer receiving a momentum kick respectively at the first and second Raman pulses and assuming infinitely short pulses, we can calculate the space and momentum separation

at the output of the interferometer after a time $2T$ (with T the interrogation time separating two consecutive laser pulses, see figure 1.7):

$$\text{First pulse:} \begin{cases} \boldsymbol{r_A}(0^+) = \mathbf{0} \\ \boldsymbol{p_A}(0^+) = \hbar \boldsymbol{k_{\text{eff}}^{(1)}} \\ \boldsymbol{v_A}(0^+) = \dfrac{\boldsymbol{p_A}(0^+)}{M} = \dfrac{\hbar}{M} \boldsymbol{k_{\text{eff}}^{(1)}} \end{cases} \tag{1.62}$$

$$\text{Second pulse:} \begin{cases} \boldsymbol{r_A}(T^+) = \boldsymbol{r_A}(0^+) + T \cdot \boldsymbol{v_A}(0^+) = \dfrac{\hbar T}{M} \boldsymbol{k_{\text{eff}}^{(1)}} \\ \boldsymbol{p_A}(T^+) = \boldsymbol{p_A}(0^+) - \hbar \boldsymbol{k_{\text{eff}}^{(2)}} = \hbar \left(\boldsymbol{k_{\text{eff}}^{(1)}} - \boldsymbol{k_{\text{eff}}^{(2)}} \right) \\ \boldsymbol{v_A}(T^+) = \dfrac{\boldsymbol{p_A}(T^+)}{M} = \dfrac{\hbar}{M} \left(\boldsymbol{k_{\text{eff}}^{(1)}} - \boldsymbol{k_{\text{eff}}^{(2)}} \right) \end{cases} \tag{1.63}$$

$$\text{Third pulse:} \begin{cases} \boldsymbol{r_A}(2T^+) = \boldsymbol{r_A}(T^+) + T \cdot \boldsymbol{v_A}(T^+) = \dfrac{\hbar T}{M} \left(2\boldsymbol{k_{\text{eff}}^{(1)}} - \boldsymbol{k_{\text{eff}}^{(2)}} \right) \\ \boldsymbol{p_A^g}(2T^+) = \boldsymbol{p_A}(T^+) = \hbar \left(\boldsymbol{k_{\text{eff}}^{(1)}} - \boldsymbol{k_{\text{eff}}^{(2)}} \right) \\ \boldsymbol{p_A^e}(2T^+) = \boldsymbol{p_A}(T^+) + \hbar \boldsymbol{k_{\text{eff}}^{(3)}} = \hbar \left(\boldsymbol{k_{\text{eff}}^{(1)}} - \boldsymbol{k_{\text{eff}}^{(2)}} + \boldsymbol{k_{\text{eff}}^{(3)}} \right) \end{cases} \tag{1.64}$$

with $\boldsymbol{p_A^k}(2T)$ the momentum associated to the output port $k = g, e$ of the interferometer. After an analogous treatment for the second arm B, we can calculate the space and momentum separation at the output of the interferometer:

$$\begin{aligned} \Delta \boldsymbol{r} &= \boldsymbol{r_A}(2T) - \boldsymbol{r_B}(2T) = \frac{2\hbar T}{m} \left(\boldsymbol{k_{\text{eff}}^{(1)}} - \boldsymbol{k_{\text{eff}}^{(2)}} \right) \\ \Delta \boldsymbol{p} &= \boldsymbol{p_A}(2T) - \boldsymbol{p_B}(2T) = \hbar \left(\boldsymbol{k_{\text{eff}}^{(1)}} - 2\boldsymbol{k_{\text{eff}}^{(2)}} + \boldsymbol{k_{\text{eff}}^{(3)}} \right). \end{aligned} \tag{1.65}$$

We note that the splitting in the momentum space is the same at each output port:

$$\Delta \boldsymbol{p} = \Delta \boldsymbol{p^f} = \Delta \boldsymbol{p^e} \tag{1.66}$$

We now may rewrite the expression of the displacement vector in equation 1.60 as:

$$\delta \boldsymbol{\chi} = \Delta \boldsymbol{p} - \frac{M}{2T} \Delta \boldsymbol{r} = \hbar \left(\boldsymbol{k_{\text{eff}}^{(3)}} - \boldsymbol{k_{\text{eff}}^{(2)}} \right). \tag{1.67}$$

This equation shows that, in the particular case of rotations, the main contribution comes from the orientation of the effective wave vector for the second and the third pulses with respect to the first pulse, which transfers a rotation-dependent momentum kick to the atoms. We define a rotation rate vector $\boldsymbol{\Omega} = \Omega \boldsymbol{u}$ with $\Omega = \sqrt{\Omega_x^2 + \Omega_y^2 + \Omega_z^2}$ the rotation rate and $\boldsymbol{u} = (u_x, u_y, u_z)^T$ the rotation axis. In the most general case, this rotation rate vector may vary during the interferometer and the rotation at a time t

corresponds to an angle $\boldsymbol{\theta}(t)$ given by:

$$\boldsymbol{\theta}(t) = \theta(t)\boldsymbol{u} = \int_0^t \boldsymbol{\Omega}(t')\, dt'. \tag{1.68}$$

Denoting $\mathcal{R}(\theta)$ the matrix associated with a rotation of angle $\boldsymbol{\theta}(t)$, defined by the equation:

$$\mathcal{R}(\theta) = \begin{pmatrix} u_x^2(1-C)+C & u_xu_y(1-C)-u_zS & u_xu_z(1-C)+u_yS \\ u_xu_y(1-C)+u_zS & u_y^2(1-C)+C & u_yu_z(1-C)-u_xS \\ u_xu_z(1-C)-u_yS & u_yu_z(1-C)+u_xS & u_z^2(1-C)+C \end{pmatrix} \tag{1.69}$$

with $C = \cos(\theta(t))$ and $C = \sin(\theta(t))$, the rotation-induced displacement vector can be expressed as:

$$\begin{aligned} \delta\boldsymbol{\chi} &= \hbar\left(\boldsymbol{k}_{\mathbf{eff}}^{(\mathbf{3})} - \boldsymbol{k}_{\mathbf{eff}}^{(\mathbf{2})}\right) \\ &= \hbar\left[\mathcal{R}(\theta(2T)) - \mathcal{R}(\theta(T))\right] \cdot \boldsymbol{k}_{\mathbf{eff}}^{(\mathbf{1})}. \end{aligned} \tag{1.70}$$

Now, setting $k_{\text{eff}}^{(1)} = (0,0,1)^T$, we get in the small-angle approximation:

$$\delta\boldsymbol{\chi} \approx \frac{\hbar k_{\text{eff}}}{2} \begin{pmatrix} u_xu_z[\theta^2(2T) - \theta^2(T)] + 2u_y[\theta(2T) - \theta(T)] \\ u_yu_z[\theta^2(2T) - \theta^2(T)] - 2u_x[\theta(2T) - \theta(T)] \\ (u_z^2 - 1)[\theta^2(2T) - \theta^2(T)] \end{pmatrix}. \tag{1.71}$$

For time-varying rotation rates, it is possible to compute numerically the vectors $\boldsymbol{k}_{\mathbf{eff}}^{(\mathbf{2})}$ and $\boldsymbol{k}_{\mathbf{eff}}^{(\mathbf{3})}$ using the rotation matrices corresponding to $\Omega(t)$ at each instant. In the particular case of a constant rotation rate (in direction and amplitude) where $\theta(t) = \Omega t$, the expression of the displacement simplifies to:

$$\delta\boldsymbol{\chi} \approx \frac{\hbar k_{\text{eff}}}{2} \begin{pmatrix} 3\Omega_x\Omega_zT^2 + 2\Omega_yT \\ 3\Omega_y\Omega_zT^2 - 2\Omega_xT \\ -3(\Omega_x^2 + \Omega_y^2)T^2 \end{pmatrix}. \tag{1.72}$$

Let us now consider a centered Gaussian wave packet. Its spatial probability density function (PDF) is:

$$|\psi(\boldsymbol{r},t)|^2 = \frac{1}{\left(\sqrt{\pi}\sigma_r(t)\right)^3} \exp[-\frac{\|\boldsymbol{r}\|^2}{\sigma_r(t)^2}] \tag{1.73}$$

where

$$\sigma_r(t) = \sqrt{\left(\frac{\hbar}{\sigma_p}\right)^2 + \left(\frac{\sigma_p t}{m}\right)^2} \tag{1.74}$$

is the $1/e$ radius of the wave-packet in spatial representation, m is the mass of

the atom and $\sigma_p = \sqrt{2k_B m\mathcal{T}}$ is the $1/e$ radius of the wave-packet in momentum representation with k_B the Boltzmann constant and $\mathcal{T}$ the temperature of the atom cloud. Substituting equation 1.73 in 1.61 allows us to calculate the normalized contrast for an open interferometer:

$$C \approx \frac{1}{\left(\sqrt{\pi}\sigma_r(t)\right)^3}\left|\int \exp\left[\frac{i}{\hbar}\left(\delta\boldsymbol{\chi}\cdot\boldsymbol{r}\right) - \frac{\|\boldsymbol{r}\|^2}{\sigma_r(t)^2}\right]\mathrm{d}^3\mathrm{r}\right|. \tag{1.75}$$

which after integration in three dimensions yields:

$$C \approx \exp\left[-\frac{\sigma_r(t)^2}{4\hbar^2}\|\delta\boldsymbol{\chi}\|^2\right]. \tag{1.76}$$

Using the expression of the displacement found in equation 1.72, we finally reach a convenient expression of the rotation-induced contrast loss in an open interferometer for a constant angular velocity:

$$C \approx \exp\left[-\left(\frac{\sigma_r(2T)k_{\text{eff}}T}{2}\right)^2\left(\Omega_x^2+\Omega_y^2\right)\left(1+\frac{9}{4}T^2\Omega^2\right)\right]. \tag{1.77}$$

Considering interrogation times of the millisecond order and temperatures on the order of the microkelvin, the assumption $(4Tk_B\mathcal{T})^2 \gg \hbar^2$ is valid. Furthermore, the typical operating conditions that we consider also ensure $9\Omega^2T^2/4 \ll 1$, which allows us to write an approximate equation easier to manipulate:

$$C \approx \exp\left[-\left(\sqrt{\frac{2k_B\mathcal{T}}{m}}k_{\text{eff}}T^2\right)^2\left(\Omega_x^2+\Omega_y^2\right)\right]. \tag{1.78}$$

Note that this expression only contains terms that are accessible experimental parameters such as the temperature of the atom cloud or the interrogation time of the interferometer and the rotation rate which can be measured by gyroscopes. Figure 1.8 exhibits the rapidity of the contrast's decay versus the rotation rate for two different temperatures and interrogation times. On the one hand, we can observe a slower decrease with lower temperatures due to the slower thermal expansion of the atomic cloud, curbing the spatial separation between the two atomic wave packets. On the other hand, one can notice the strong influence of the interrogation time on this contrast reduction which seems pretty intuitive, as leaving a longer time for the cloud to free-fall will increase the spatial separation at the output of the interferometer.

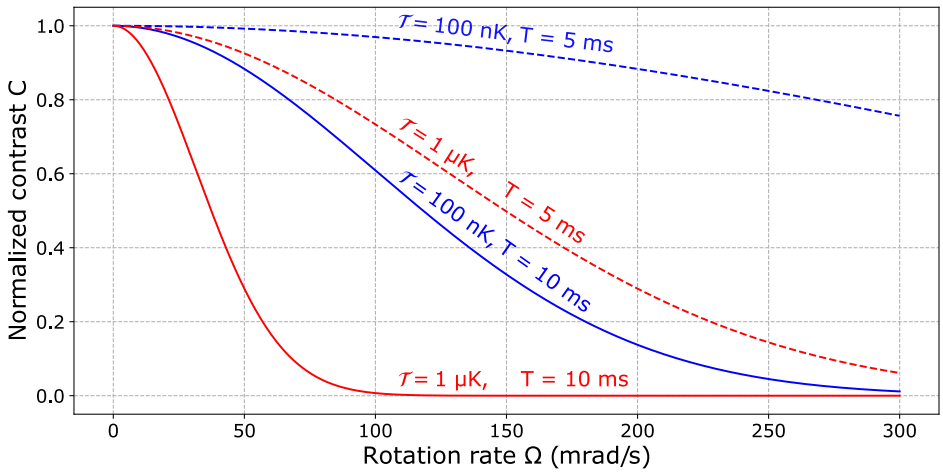

Figure 1.8: Simulation of the normalized contrast drop under arbitrary, constant rotations up to 300 mrad/s according to equation 1.78. The blue (respectively red) curves correspond to a $\mathcal{T} = 100$ nK (respectively $\mathcal{T} = 1$ µK) atomic cloud temperature. The plain and dotted lines display the evolution of the contrast for interrogation times $T = 10$ ms and $T = 5$ ms respectively.

1.3.3 Rotating interferometer's output phase shift

The calculation of the general phase shift of an atom interferometer undergoing random accelerations and rotations is carried out in the mobile frame $\mathcal{R}_m$ of the laser field (namely the collimator delivering the beam) which would also correspond to that of a vehicle if the measurement is made in a strapdown configuration. To that end, and similarly to the protocol previously used by other groups [Beaufils et al. 2023], we use the mid-point theorem given by [Antoine and Bordé 2003]:

$$\begin{aligned}\Phi_{\text{at}} = \boldsymbol{k}_{\mathbf{eff}}(0).\left(\boldsymbol{r}_{\mathbf{at}}(0) - \boldsymbol{r}_{\boldsymbol{m}}(0)\right) - 2\boldsymbol{k}_{\mathbf{eff}}(T).\left(\frac{\boldsymbol{r}^{\boldsymbol{A}}_{\mathbf{at}}(T) + \boldsymbol{r}^{\boldsymbol{B}}_{\mathbf{at}}(T)}{2} - \boldsymbol{r}_{\boldsymbol{m}}(T)\right) \\ + \boldsymbol{k}_{\mathbf{eff}}(2T).\left(\frac{\boldsymbol{r}^{\boldsymbol{A}}_{\mathbf{at}}(2T) + \boldsymbol{r}^{\boldsymbol{B}}_{\mathbf{at}}(2T)}{2} - \boldsymbol{r}_{\boldsymbol{m}}(2T)\right)\end{aligned} \tag{1.79}$$

with $\boldsymbol{k}_{\mathbf{eff}}(t)$, $\boldsymbol{r}_{\mathbf{at}}(t)$ and $\boldsymbol{r}_{\boldsymbol{m}}(t)$ the effective wave vector of the laser, the position of the atoms and the position of the mirror in the rotating frame $\mathcal{R}_m$ at the instant t respectively. The superscripts A, B on the atomic cloud's position vectors denote the interferometer's path they follow, visible in figure 1.7. Hence, the interferometric phase shift depends on the position of the atoms with respect to the reference mirror at the instant of the laser pulses, the time evolution of the effective wave vector's norm and its orientation. As far as the mid-point theorem is concerned, the propagation and separation phase shifts are either null or they cancel out, thus only the laser phase describing the interaction of the atomic wave-packets with the laser field remains. This is well described by this expression, which involves the pair of laser beams represented by the effective wave vector $\boldsymbol{k}_{\mathbf{eff}}(t)$ as well as the position of the atoms in the standing wave

formed by the counter-propagating lasers, which act as a phase ruler, at the instants of the Raman pulses. This means that the atomic trajectories are fully described by these three positions relative to the reference mirror, while what happens between two successive pulses does not take part in the output phase shift of the interferometer.

To solve this equation and calculate the atomic trajectories we use a polynomial decomposition of the atoms' position, considering at first constant accelerations and rotation rates. The case of rapidly varying accelerations is handled independently using the sensitivity function formalism introduced in section 1.2, as no modeling can represent arbitrary variations of the acceleration signal due to mechanical vibrations. With regard to the rotation rate, for short enough interrogation times, we consider that an at most linear variation is a very good approximation as confirmed by the experimental data presented in chapter 4. In order to simplify the notations, the results here are presented for constant rotation rates but the calculation for an affine-like rotation rate is presented in appendix A.

This decomposition is truncated to third order terms.

$$r_i(t) = \sum_{n=0}^{3} c_{\mathrm{in}} t^n \tag{1.80}$$

with $i = 1, 2, 3$ the axes of the chosen frame, which are rewritten $r_1 = x$, $r_2 = y$ and $r_3 = z$. We consider initial conditions as follows:

$$\begin{pmatrix} c_{\mathrm{x0}} \\ c_{\mathrm{y0}} \\ c_{\mathrm{z0}} \end{pmatrix} = \begin{pmatrix} x_0 \\ y_0 \\ z_0 \end{pmatrix} ; \begin{pmatrix} c_{\mathrm{x1}} \\ c_{\mathrm{y1}} \\ c_{\mathrm{z1}} \end{pmatrix} = \begin{pmatrix} v_{\mathrm{x0}} \\ v_{\mathrm{y0}} \\ v_{\mathrm{z0}} \end{pmatrix} \tag{1.81}$$

with $\boldsymbol{r_0}$ and $\boldsymbol{v_0}$ the position and velocity of the atoms in the mobile frame at the instant of the first pulse.

Substituting the polynomial ansatz into the equation of motion given in 1.55, we can decompose it into a system of as many equations as there are powers of t under the condition

$$\alpha + \beta t + \gamma t^2 + \delta t^3 = 0 \ \forall t \Leftrightarrow \alpha = \beta = \gamma = \delta = 0. \tag{1.82}$$

This yields four equations enabling us to determine the remaining coefficients of

the polynomial decomposition of the atomic trajectories.

$$\begin{cases} c_{\mathrm{x2}} = \frac{1}{2}\left[\left(\Omega_y^2+\Omega_z^2\right)c_{\mathrm{x0}} - \Omega_x\left(\Omega_y c_{\mathrm{y0}}+\Omega_z c_{\mathrm{z0}}\right) - 2\left(\Omega_y c_{\mathrm{z1}}-\Omega_z c_{\mathrm{y1}}\right)+a_x\right] \\ c_{\mathrm{y2}} = \frac{1}{2}\left[\left(\Omega_z^2+\Omega_x^2\right)c_{\mathrm{y0}} - \Omega_y\left(\Omega_z c_{\mathrm{z0}}+\Omega_x c_{\mathrm{x0}}\right) - 2\left(\Omega_z c_{\mathrm{x1}}-\Omega_x c_{\mathrm{z1}}\right)+a_y\right] \\ c_{\mathrm{z2}} = \frac{1}{2}\left[\left(\Omega_x^2+\Omega_y^2\right)c_{\mathrm{z0}} - \Omega_z\left(\Omega_x c_{\mathrm{x0}}+\Omega_y c_{\mathrm{y0}}\right) - 2\left(\Omega_x c_{\mathrm{y1}}-\Omega_y c_{\mathrm{x1}}\right)+a_z\right] \end{cases} \tag{1.83}$$

$$\begin{cases} c_{\mathrm{x3}} = \frac{1}{6}\left[\left(\Omega_y^2+\Omega_z^2\right)c_{\mathrm{x1}} - \Omega_x\left(\Omega_y c_{\mathrm{y1}}+\Omega_z c_{\mathrm{z1}}\right) - 4\left(\Omega_y c_{\mathrm{z2}}-\Omega_z c_{\mathrm{y2}}\right)\right] \\ c_{\mathrm{y3}} = \frac{1}{6}\left[\left(\Omega_z^2+\Omega_x^2\right)c_{\mathrm{y1}} - \Omega_y\left(\Omega_z c_{\mathrm{z1}}+\Omega_x c_{\mathrm{x1}}\right) - 4\left(\Omega_z c_{\mathrm{x2}}-\Omega_x c_{\mathrm{z2}}\right)\right] \\ c_{\mathrm{z3}} = \frac{1}{6}\left[\left(\Omega_x^2+\Omega_y^2\right)c_{\mathrm{z1}} - \Omega_z\left(\Omega_x c_{\mathrm{x1}}+\Omega_y c_{\mathrm{y1}}\right) - 4\left(\Omega_x c_{\mathrm{y2}}-\Omega_y c_{\mathrm{x2}}\right)\right] \end{cases} \tag{1.84}$$

Assuming the reference mirror is immobile in the mobile frame, such that the effective wave vector's norm and orientation remain constant and the terms containing the mirror's position vector cancel out, the expression from the mid-point theorem simplifies as:

$$\Phi_{\mathrm{at}} = \boldsymbol{k_{\mathrm{eff}}}.\left[\boldsymbol{r_{\mathrm{at}}}(0) - 2\frac{\boldsymbol{r_{\mathrm{at}}^{A}}(T)+\boldsymbol{r_{\mathrm{at}}^{B}}(T)}{2} + \frac{\boldsymbol{r_{\mathrm{at}}^{A}}(2T)+\boldsymbol{r_{\mathrm{at}}^{B}}(2T)}{2}\right] \tag{1.85}$$

We set $\boldsymbol{k}(t) = k_{\mathrm{eff}}.\boldsymbol{u_z}$ at any time t, and consider only rotations in the plane transverse to the effective wave vector of the laser. This is a fairly good approximation since the interferometer is not impacted by rotations around its effective wave vector, as long as the incident and reflected laser beams are considered perfectly overlapped. Nevertheless, some terms depending on Ω_z still appear in the complete expression and the full calculation can be found in appendix A.

With these considerations in mind, the phase shift at the output of the interferometer developed to the third order in T for constant rotations in the transverse plane is given by the following equation:

$$\begin{aligned} \Phi_{\mathrm{at}} = k_{\mathrm{eff}}T^2\big[&a_z + 2(v_x+a_xT)\Omega_y - 2(v_y+a_yT)\Omega_x \\ &+ (z_0 - 3v_zT + 2x_0\Omega_yT - 2y_0\Omega_xT)\,\Omega^2\big] \end{aligned} \tag{1.86}$$

with $\Omega^2 = \Omega_x^2+\Omega_y^2$, v_i and i_0 the initial velocity and position along the i axis respectively, and under the infinitely short pulses assumption. Here, we recognize on the first line the relative acceleration and two terms of Coriolis effect related to the motion of the atomic cloud in the plane transverse to the effective wave vector of the laser. On the second line, one can recognize the centrifugal acceleration with a lever arm z_0, corresponding to the distance of the atoms from the center of rotation, along with

higher-order terms arising from the integration of the atomic cloud's motion.

For angular velocities below 1 rad/s verifying $|\Omega| \geqslant |\Omega|^2$, the Coriolis phase shift ϕ_{Coriolis} scaling linearly with the rotation rate is predominant. By comparison, the centrifugal acceleration related to the science chamber's rotation induces a phase shift in general negligible before the Coriolis acceleration. However, for rotation rates above 1 rad/s, the centrifugal effect rapidly becomes predominant which is particularly true for large lever arms between the instrument's center of rotation and the atomic cloud's initial position z_0.

1.4 Impact of a reference mirror's rotation on the phase shift

The previous section was concluded on the expression of the atomic phase shift when the apparatus is undergoing arbitrary rotations, meaning that measuring all the spatial components of the rotation rate and acceleration would allow to retrieve the absolute acceleration measurement out of the blurred interferometric signal. Nevertheless, the exponential decrease in the amplitude of these fringes is still present and will strongly limit the measurement range of the device in terms of both rotation rate and interrogation time. To tackle this effect, several solutions can be employed such as a gyro-stabilization of the whole science chamber during the interferometer [Bidel et al. 2018] or using ultra-cold atoms in order to dampen the contrast decay as displayed in figure 4.3. Another interesting solution would be to stabilize the orientation of the wave vector alone in the external frame $\mathcal{R}_m$ (see chapter 4) by applying a rotation to the reference mirror. However, such technique also affects the interferometric phase shift, as discussed below.

Although the mechanical compensation on the reference mirror effectively addresses the loss of visibility of the atomic fringes, it also changes the phase shift at the output of the atom interferometer. We know from equation 1.79 that both the trajectory of the mirror and the evolution of the wave vector in the frame of the sensor head affect the total phase shift at the output. Figure 1.9 summarizes all the relevant distances and positions.

Let us first focus on the motion of the mirror, rotating around a certain point with a lever arm of constant distance d_m. Since there is no translation, and supposing the rotation rate of the mirror with respect to the vacuum chamber is constant, the only acceleration will correspond to the centripetal term. Knowing the initial orientation, we can apply to this vector the rotation matrix defined in equation 1.69 by writing

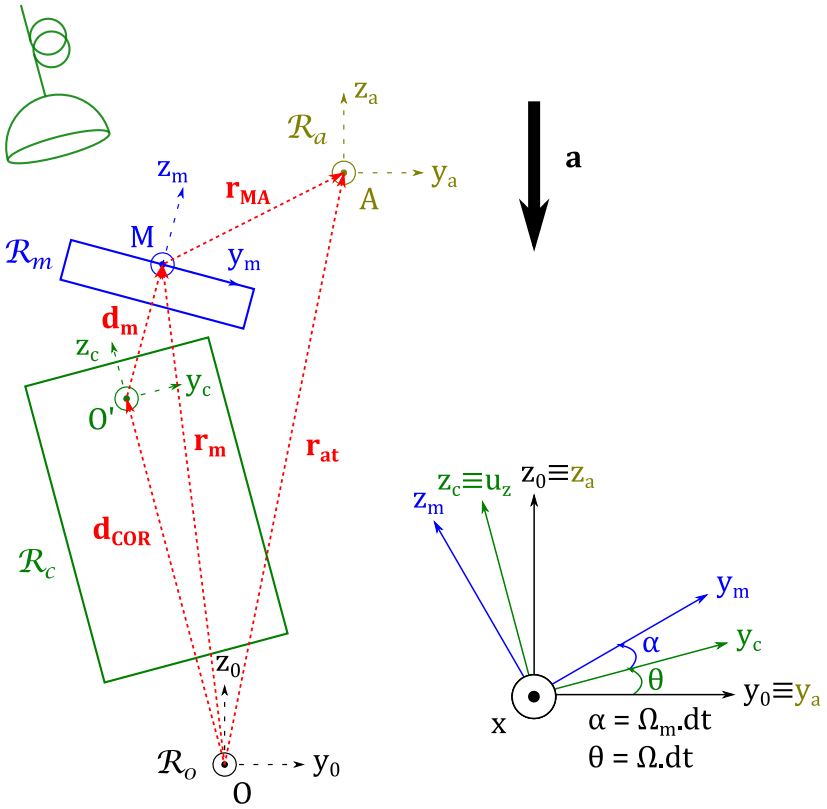

Figure 1.9: 2D representation of the relevant frames' axes and distances for compensated rotations. The terrestrial frame $\mathcal{R}_0$, the science chamber's frame $\mathcal{R}_c$, the mirror's frame $\mathcal{R}_m$ and the atomic cloud's frame $\mathcal{R}_a$ are represented in black, green, blue and gold respectively. O: center of rotation of the apparatus; O': center of rotation of the mirror; M: center of the mirror's surface; A: center of the atomic cloud; $\boldsymbol{d_m}$: lever arm of the mirror; $\boldsymbol{d_{COR}}$: distance between the centers of rotation of the chamber and the mirror; $\boldsymbol{r_{MA}}$: distance between the mirror's surface and the atomic cloud; $\boldsymbol{r_m}$: position of the mirror in the terrestrial frame; $\boldsymbol{r_{at}}$: position of the atomic cloud in the terrestrial frame.

$\boldsymbol{\theta}(t) = \boldsymbol{\Omega_m} t$. In the frame of the sensor head, the orientation of the mirror is written:

$$\boldsymbol{d_m}(t) = \mathcal{R}(\Omega_m t).\boldsymbol{d_m}(0) \tag{1.87}$$

$$\approx \frac{d_m}{2}\begin{pmatrix} \Omega_{mx}\Omega_{mz}t^2 + 2\Omega_{my}t \\ \Omega_{my}\Omega_{mz}t^2 - 2\Omega_{mx}t \\ 2 - (\Omega_{mx}^2 + \Omega_{my}^2)t^2 \end{pmatrix} \tag{1.88}$$

in the small angles approximation and for $\boldsymbol{d_m}(0) = \boldsymbol{d_m}.\boldsymbol{u_z}$.

With this vector known at each instant, we only need to add the vector $\boldsymbol{d_{COR}}$ going from the center of mass of the sensor head, taken as the reference for all the positions of interest, to the center of rotation of the mirror. This distance is constant in the

vacuum chamber's frame and set along the z axis as well, leading to:

$$\boldsymbol{r_m}(t) = \boldsymbol{d_{COR}} + \mathcal{R}(\Omega_m t).\boldsymbol{d_m}(0) \tag{1.89}$$

$$\approx \begin{pmatrix} \frac{d_m}{2}\left[\Omega_{\mathrm{mx}}\Omega_{\mathrm{mz}}t^2 + 2\Omega_{\mathrm{my}}t\right] \\ \frac{d_m}{2}\left[\Omega_{\mathrm{my}}\Omega_{\mathrm{mz}}t^2 - 2\Omega_{\mathrm{mx}}t\right] \\ d_{COR} + \frac{d_m}{2}\left[2 - (\Omega_{\mathrm{mx}}^2 + \Omega_{\mathrm{my}}^2)t^2\right] \end{pmatrix}. \tag{1.90}$$

Regarding the effective wave vector seen by the atoms, it experiences not only a change in orientation but also a reduction of its norm. Indeed, without applying any rotation on the input collimator to maintain their alignment, there will be a decrease in the incident and reflected laser beams' overlap. Those two effects are accounted for in the following expression:

$$\boldsymbol{k}(t) = \mathcal{R}(\Omega_m t).\boldsymbol{k}(0).\cos\Omega_m t \tag{1.91}$$

$$\approx \frac{k_{\mathrm{eff}}}{2}\left(1 - \frac{\Omega_m^2 t^2}{2}\right)\begin{pmatrix} \Omega_{\mathrm{mx}}\Omega_{\mathrm{mz}}t^2 + 2\Omega_{\mathrm{my}}t \\ \Omega_{\mathrm{my}}\Omega_{\mathrm{mz}}t^2 - 2\Omega_{\mathrm{mx}}t \\ 2 - (\Omega_{\mathrm{mx}}^2 + \Omega_{\mathrm{my}}^2)t^2 \end{pmatrix} \tag{1.92}$$

in the small angles approximation.

Acceleration term	**Notation**	**Associated phase shift expression**
Relative (translational)	ϕ_{relative}	$k_{\mathrm{eff}}T^2 a_z$
Mirror's rotation	$\phi^{\mathrm{mirror}}_{\mathrm{rotation}}$	$k_{\mathrm{eff}}T^3\left[a_x\Omega_{\mathrm{my}} - a_y\Omega_{\mathrm{mx}}\right]$
Residual Coriolis	ϕ_{Coriolis}	$2k_{\mathrm{eff}}T^2\left[\left(v_x + a_x T\right)\delta\Omega_y - \left(v_y + a_y T\right)\delta\Omega_x\right]$
Centrifugal (chamber)	$\phi^{\mathrm{chamber}}_{\mathrm{centrifugal}}$	$k_{\mathrm{eff}}T^2\Omega^2\left[z_0 + 2x_0\Omega_y T - 2y_0\Omega_x T\right]$
Centrifugal (mirror)	$\phi^{\mathrm{mirror}}_{\mathrm{centrifugal}}$	$k_{\mathrm{eff}}T^2\Omega_m^2[-2z_0^{\mathrm{MA}} - d_m - 3T\left(v_z + v_{\mathrm{rec}} + x_0\Omega_{\mathrm{my}} - y_0\Omega_{\mathrm{mx}}\right)]$
Other terms arising from composition of motion	ϕ_{compo}	$3k_{\mathrm{eff}}T^3\Big[-v_z\left(\delta\Omega_x^2 + \delta\Omega_y^2\right) + \left(x_0\Omega_y - y_0\Omega_x\right)\left(\Omega_x\Omega_{\mathrm{mx}} + \Omega_y\Omega_{\mathrm{my}}\right)\Big]$

Table 1.1: Summary of the contributions to the phase shift of an atom interferometer undergoing opposed rotations of the laser input and retroreflection mirror. These contributions are given up to the third order in T, for constant transverse rotation rates. The effective wave vector is considered oriented along $+\boldsymbol{u_z}$ at the instant of the first pulse (see figure 1.9).

Ultimately, following the same procedure as for a static mirror, we calculate the atomic phase shift associated with the interferometric measurement to the third order in T, for constant rotation rates of the chamber and the mirror in the transverse plane, and under the infinitely short pulses assumption. It results from a sum of all the contributions to the total acceleration $\boldsymbol{a_{tot}}$ detailed in table 1.1 with $\Omega^2 = \Omega_x^2 + \Omega_y^2$ the norm of the chamber's rotation rate and $\Omega_m^2 = \Omega_{\text{mx}}^2 + \Omega_{\text{my}}^2$ the norm of the mirror's rotation rate. The following notations have also been introduced for clarity:

- $z_0^{\text{MA}} = z_0 - d_{\text{COR}} - d_m = \boldsymbol{r_{MA}}(t_0).\boldsymbol{u_z}$ the distance between the reference mirror's surface and the atomic cloud at the instant of the first Raman pulse, projected on the z axis (see figure 1.9);
- $\delta\Omega_i = \Omega_i + \Omega_{\text{mi}}$ $(i = x, y)$ the residual rotation rate on a given axis, considering $\Omega_{\text{mi}} \simeq -\Omega_i$;
- $\delta\Omega_x^2 + \delta\Omega_y^2 = \Omega_x^2 + 2\Omega_x\Omega_{\text{mx}} + \Omega_{\text{mx}}^2 + \Omega_y^2 + 2\Omega_y\Omega_{\text{my}} + \Omega_{\text{my}}^2$ the squares of the transverse residual rotation rates

We identify the same relative acceleration as before, the mirror's rotation now compensates for most of the Coriolis effect and adds some specific terms to the centrifugal acceleration. In addition, some Coriolis-like terms appear due to the fact that the atomic measurement axis is varying in orientation as well as in norm because of the overlap mismatch between the incident and reflected beams. Ultimately, some terms more complicated to physically understand and related to the complex combination of movements appear in the expression of the final phase shift. Hence, summing all the contributions above, we can write:

$$\Phi_{\text{at}}^{\text{comp}} = \phi_{\text{relative}} + \phi_{\text{rotation}}^{\text{mirror}} + \phi_{\text{Coriolis}} + \phi_{\text{centrifugal}}^{\text{chamber}} + \phi_{\text{centrifugal}}^{\text{mirror}} + \phi_{\text{compo}}. \tag{1.93}$$

For angular velocities below 1 rad/s verifying $|\Omega| \geqslant |\Omega|^2$, the phase shift induced by the mirror's rotation $\phi_{\text{rotation}}^{\text{mirror}}$ becomes predominant over the Coriolis phase shift ϕ_{Coriolis}, mostly residual in the case of an imperfect compensation and null for a mirror's rotation perfectly opposing the instrument's one. Then, for comparable rotation rates $|\Omega| \simeq |\Omega_m|$, the centrifugal acceleration related to the science chamber's rotation induces a phase shift in general much larger than the one arising from the mirror's motion, due to the difference in the lever arms appearing in the first-order contributions to these two terms $z_0 \geqslant 2z_0^{\text{MA}} + d_m$. However, for rotation rates above 1 rad/s, the centrifugal effect rapidly becomes predominant over the terms scaling linearly with the rotation rate. Ultimately, the complex phase shift resulting from the composition of motion between the different frames remains mostly negligible as it is either related to

a residual rotation or it scales in $(\Omega T)^3$.

Conclusion

The key principles for wave packets manipulation with lasers and propagation in a given potential, with a practical example of a gravitational potential, have been reviewed. These building blocks are essential for the achievement of matter-wave interferometers, which are presented with a particular attention paid to the Mach-Zehnder geometry utilizing two-photon Raman transitions and free-falling cold atoms, enabling for inertial sensing.

Nevertheless, these techniques are very sensitive to the environment they are performed in and even modest variations in the longitudinal position of the retroreflecting mirror, serving as the phase reference for the atomic interferometer, can lead to enormous errors on the measurement making the sensor inefficient. For this reason, the formalism of sensitivity function allowing to track the motion of the reference mirror was introduced.

Alternatively, a rotation of the effective wave vector within the duration of the interferometer can modify the orientation of the momentum kick inferred from the laser beams to the matter waves, reducing the control over the atomic trajectories as well as the efficiency of the atomic beam splitter, mirror and recombiner. To tackle this effect, a solution aiming at stabilizing the effective wave vector in the external frame was developed and the modification of the quantum sensor's measurement in each case was examined.

Chapter 2

Description of the apparatus

Cold atom inertial sensors are often complex, bulky experiments hardly suitable for mobile operation. If some groups successfully developed compact and robust systems able to perform measurements out of the lab, such as the recent volcanic activity monitoring with an absolute quantum gravimeter from Exail Quantum Systems (formerly μQuans) [Antoni-Micollier et al. 2022], they remain transportable devices and are not truly mobile. For mobile operation, these apparatuses need to be placed on vibrations damping and rotations compensation platforms [Bidel et al. 2018] which are heavy, cumbersome and incompatible with on-board requirements. Moreover, the strapdown and multi-axis features present advantages for many applications as they enable a full reconstruction of the acceleration vector rather than its projection onto a given axis, in addition to increasing the correlations between the movements of the vehicle and those of the inertial sensor.

This chapter gives an overview of the apparatus used to perform the hybrid quantum acceleration measurements presented in this thesis. This instrument was designed with an emphasis on the compactness of the device and robustness to environmental factors like vibrations, rotations or temperature variations. Among its most important specificities, a single laser source is split into 3 beams retroreflected by reference mirrors, and the same laser is used for the cooling stage and Raman interferometry. In addition to the sensor head including the vacuum chamber where the atoms are prepared and interrogated, the whole experiment fits in two racks 19" wide and 900 mm deep, with a height capacity of 18U. Most of the technological choices regarding electronics or optical components were exhaustively described in [Templier 2021], hence after a reminder on the important parts of the sensor head, this chapter will focus on the new hardware and software added during my PhD course. It includes the modifications on the optical path from the laser source to the science chamber, the evolution of the classical inertial measurement unit comprising two triads of orthogonal mechanical accelerometers and fiber-optic gyroscopes, and the electronic control system.

Contents

2.1 Laser system

2.1.1 Architecture

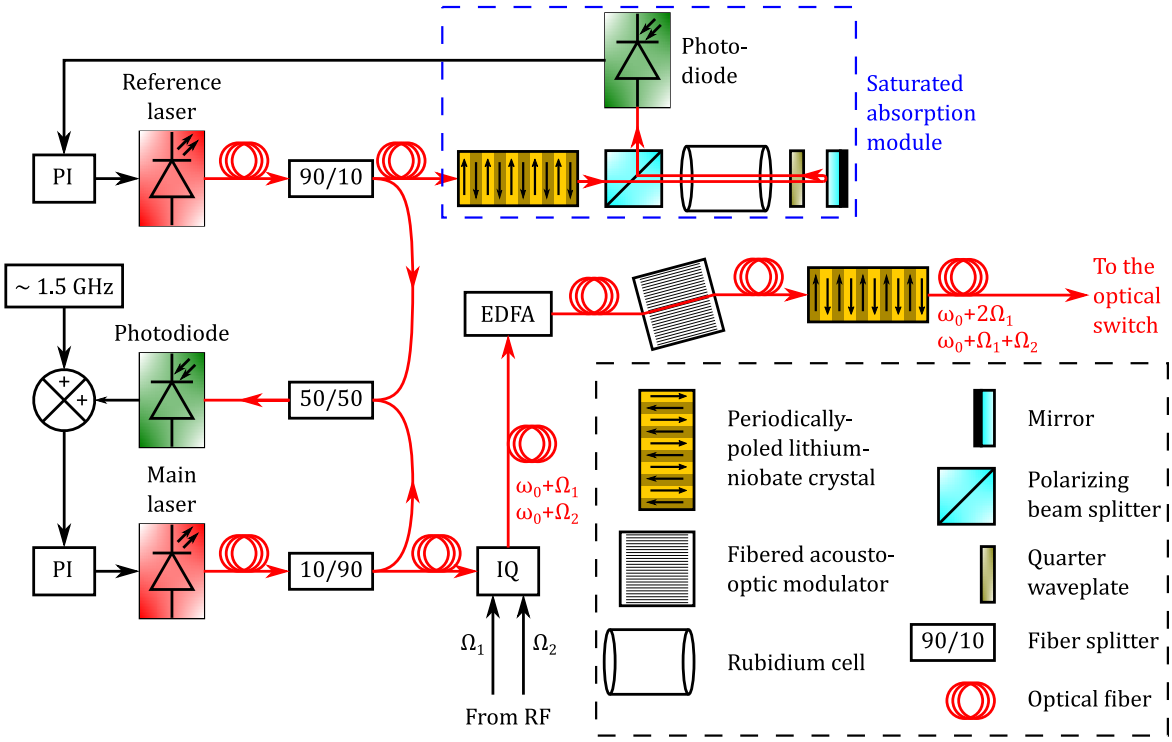

Figure 2.1: Schematic of the laser architecture. PI: Proportional-Integral controller; IQ: In-phase & Quadrature modulator; EDFA: Erbium-Doped Fiber Amplifier.

The laser system is composed of standard 19" racks for a 9U total height, two of which are dedicated to the reference laser ensuring frequency stability (2U for the laser diode and temperature control, 1U for the frequency doubling and saturated absorption module) and the third and largest one, occupying the remaining 6U in height (referred to as Modbox later on), serving for the phase modulation, fast frequency switching and amplification. The simplified architecture is depicted in figure 2.1.

The reference external-cavity laser diode (ECDL), operating at 1560 nm in the telecom band, is frequency doubled through a periodically-poled lithium-niobate (PPLN) crystal waveguide in order to interrogate a rubidium gas cell and frequency lock to the $|F = 2\rangle \rightarrow |F' = (2, 3)\rangle$ crossover transition of ^{87}Rb using saturated absorption spectroscopy. Both the diode laser and PPLN crystal are stabilized in temperature through an internal controller, and placed in boxes also stabilized through external Peltier devices. The main laser is frequency locked with a detuning of 1.5 GHz to the red of the reference using an optical beat note. Then, the main laser is sent through an in-phase and quadrature (IQ) modulator to generate two independent sidebands using electro-optic modulation (EOM). Depending on the RF frequencies fed to the IQ

modulator, these sidebands will be used for either cooling and repumping the atoms in the appropriate energy level, or for generating the two frequencies required to perform Raman interferometry. The optical power output by the IQ modulator is then amplified in an erbium-doped fiber-amplifier (EDFA) and passes through a fibered acousto-optic modulator (FAOM) for power regulation and generation of the Raman pulses, before passing through a PPLN crystal waveguide where the light undergoes sum frequency generation (SFG) to 780 nm.

Unfortunately, the diode laser power has been slowly declining and does not saturate the EDFA anymore, which has forced us to increase the MOT loading and Raman pulses durations in order to have a decent detection level and match the $\pi/2$ and π conditions. Optimization and added features have been considered to replace the whole architecture present inside the Modbox and a general upgrade is planned. It will be designed such that features — as a possible two-dimension magneto-optical trap (2D-MOT) for instance — can be added. As for now, the optical power at the output of the Modbox takes a typical value of 250 mW.

2.1.2 IQ modulation

The main specificity of this laser setup lies in the use of an IQ modulator for phase and intensity modulation. In order to understand how the scheme we use works, let us explain how sidebands can be generated through an optical Mach-Zehnder interferometer (MZI): light is propagated in the MZI where both sidebands are shifted by π between the two arms, allowing to suppress the carrier through destructive interference. Then only remain the two sidebands, of which the phase separation is determined by the input RF phase. This operation, called CS-DSB for carrier-suppressed dual sideband modulation, can be extended by interlocking two interferometers in a bigger one and thus suppressing an additional harmonic, leading to carrier-suppressed single sideband (CS-SSB) modulation. Finally, taking advantage of these two designs, the carrier-suppressed dual-single-sideband (CS-DSSB) operation scheme used at iXAtom relies on an IQ modulator receiving two distinct radio frequencies from a custom RF source in order to generate two independent sidebands controlled in frequency, phase and power [Templier 2021].

This setup presents several advantages. Indeed, controlling the two sidebands independently allows us to produce the cold-atom source and perform the interferometric inertial measurement using a single laser diode making it a compact system particularly suitable to onboard and mobile applications, in addition to being even more agile than phase modulators. Additionally, efforts were put in the rejection of parasitic

sidebands which can produce resonant atomic transitions leading to spontaneous emission, inhomogeneous atomic populations and even large systematic shifts in the acceleration measurement. This shift was estimated to be around 6 mrad or 95 ng, corresponding to two orders of magnitude below phase modulators [Templier et al. 2021].

2.1.3 Optical power distribution

At the output of the Modbox described in figure 2.1, The laser light travels in a single optical fiber and needs to be split and recombined (for the cooling and trapping stages) or switched reasonably quickly (typically a few milliseconds) between different channels during the interferometric sequence, depending on the axis we want to measure the acceleration on (x, y, z).

Originally, this task was performed by a 1×4 780 nm micro-mechanical all-fibered switch which has already been described in [Templier 2021], sending all the power on a given axis for Raman interferometry or balancing the three channels for the MOT stage.

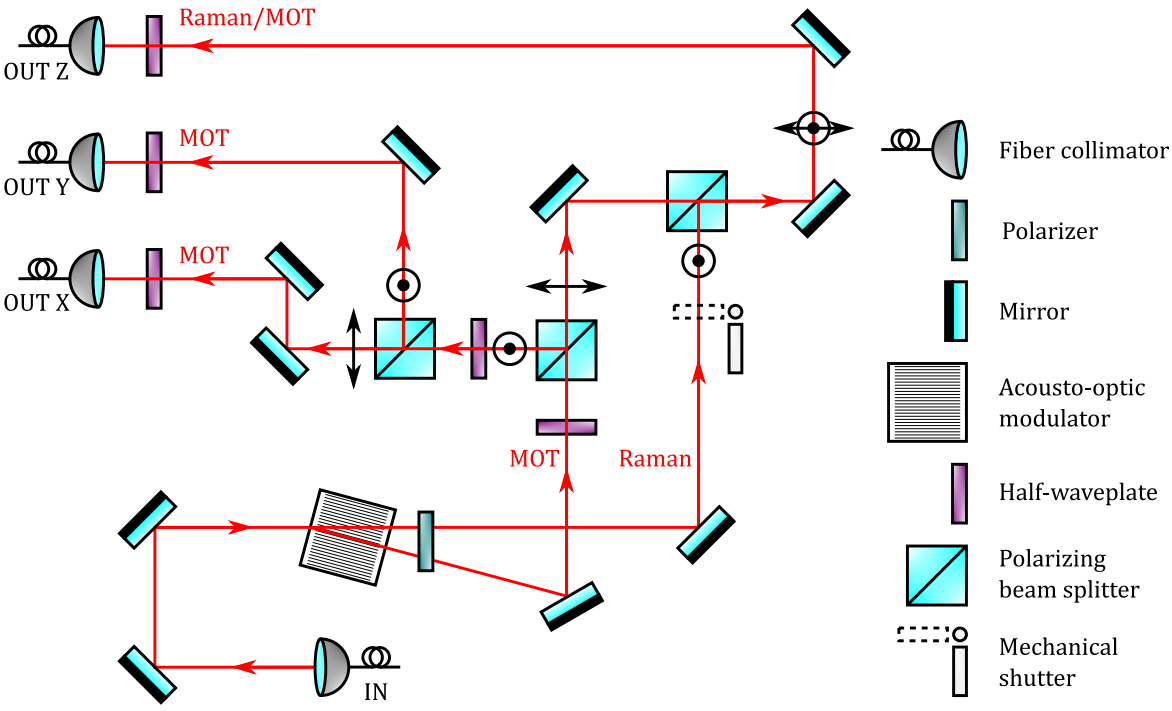

Figure 2.2: Schematic of the switching free-space optical bench. Depending on the logical signal sent to the acousto-optic modulator, two modes are available: power balanced on the three channels for the MOT, or full power sent to the z axis for Raman interrogation.

After this all-fibered optical switch broke down, a free-space optical bench was designed. Since it would be complicated to reproduce the functions of the 1×4 fiber

switch in free-space and in a compact way, this optical bench was designed as a 1×2 optical switch either transmitting all the laser power to the z axis for single-axis interferometry or equally splitting the optical power into three channels for the MOT and molasses steps. The schematics of this setup is given in figure 2.2.

	x	y	z
MOT (mW)	36	35	39
Raman (mW)	NA	NA	125
PER (dB)	> 23	> 23	> 23

Table 2.1: Optical power budget and maximum polarization extinction ratio (PER) on each axis. Due to the replacement of the fiber switch, no Raman interferometry is possible on the x and y axes at the moment.

The fiber output of the Modbox is sent through an AOM, driven by the TTL command indicating the MOT or Raman configuration. In Raman mode, the 0^{th} order of the AOM is selected and sent directly to the z axis collimator in order to minimize optical losses. In MOT configuration, the beam is deflected to the $+1$ order of the AOM and experiences a $+80\,\text{MHz}$ frequency shift. After the AOM, a first splitting stage occurs between the z axis and the other two thanks to a polarizing beam splitter (PBS) preceded by a half-waveplate to balance the power in both paths. A similar splitting is performed between the x and y axes before injecting the fiber collimators (FC-APC). Additionally, a mechanical shutter is placed on the Raman z path to prevent any residual zeroth order of the AOM to imbalance the optical power during the MOT, and half-waveplates are placed before every collimator in order to align the light polarization on the polarization-maintaining axes of the optical fibers. As for our typical operating conditions, the average optical power budget is given in table 2.1.

In a near future and in order to be able to perform multi-axis atom interferometry, this home-made free-space optical bench will be replaced with an integrated micro-optics bench (MOB) for beam splitting and combining from Exail Integrated Systems (formerly Kylia), represented on figure 2.3. The micro-optics benches provided by this company are compact systems mounted on glass, making them insensitive to temperature fluctuations and mechanical vibrations.

The choice was made to adopt a simpler architecture than what was used before, in order to have a small, compact design that can fit inside the magnetic shield. Indeed, with a splitting bench closer to the sensor head, most of the travel between the laser rack and the vacuum chamber is covered by a single optical fiber and the fluctuations of polarization or intensity are common to all the axes. Additionally, as the input of the bench is polarization filtered before a 1% pickup of the light, all the fluctuations are converted into power fluctuations and can be monitored for correlation

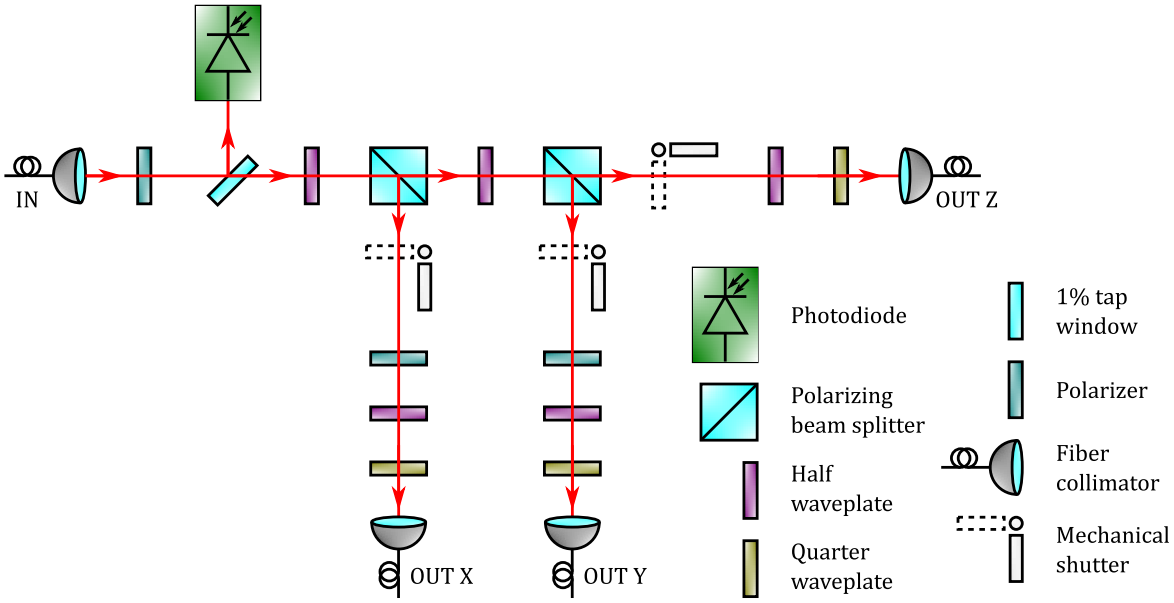

Figure 2.3: Schematic of the fixed-ratio, 1×3 splitting micro-optics bench. The power is always split between the three paths, and some can be individually closed with mechanical shutters for one-axis operation.

with the experimental results, or even fed back to the AOM driver to reach more stable operation. Further on, the three optical paths are almost identical with two stages of beam-splitting comprised of a half-waveplate ahead of a PBS (similarly to the previous setup) followed by mechanical shutters (for switching between MOT and Raman configuration) and polarization extinction ratio (PER) optimization modules including a polarizer, a half-waveplate and a quarter-waveplate. Finally, the light is coupled into fiber collimators and sent directly to the experimental chamber.

2.2 Sensor head

The central part of an atomic physics' sensor head is the vacuum chamber. Our experiment, depicted in figure 2.4, is based on a 100x150x160 mm^3 titanium parallelepiped fitted with six custom-designed viewports to provide optical access to laser inputs (fiber collimators) as well as detectors. A non-evaporable getter (NEG) combined with an ion pump provided by SAES (NexTorr D100) maintains an ultra-high vacuum inside the chamber, and two alkali metal dispensers are continuously fed with electrical current in order to heat them and release rubidium vapor into the chamber. As an addition to this design, 1 cm-high neoprene pads were added between the vacuum chamber and the rotary platform in order to damp high-frequency vibrations which enables us to focus more on the study of rotations.

On the optical side, the laser beams delivered by the three orthogonal fiber colli-

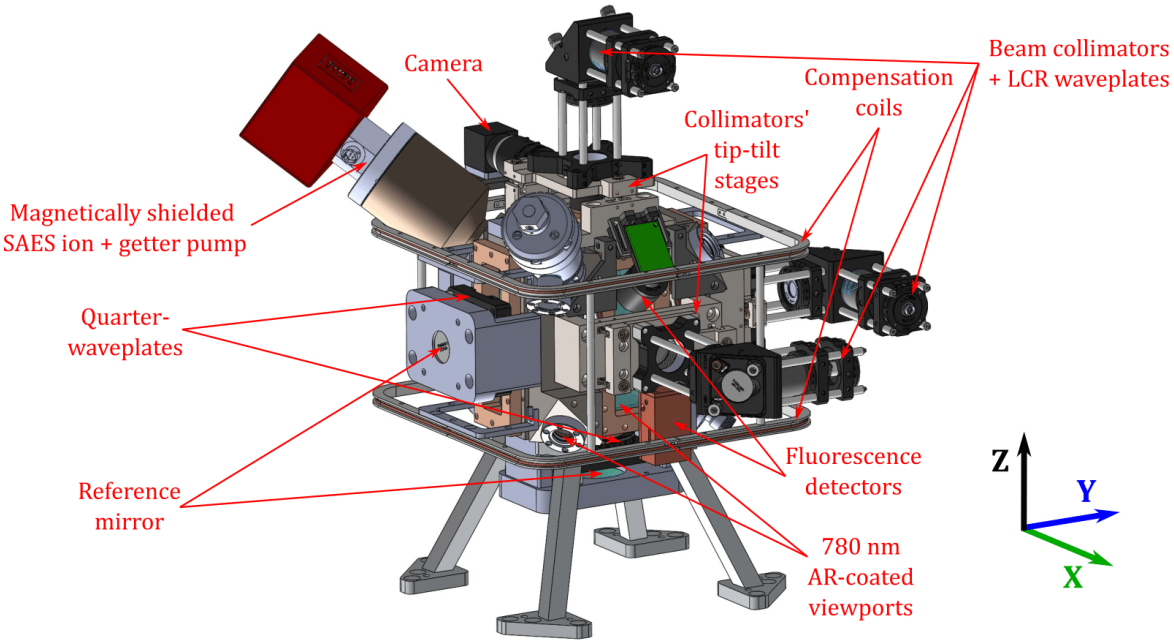

Figure 2.4: Schematic view of the vacuum chamber along with the electronic and optical components mounted on it. Only z-axis compensation coils are displayed, MOT coils are not visible since they are wound in the titanium chamber itself. The measurement axes perpendicular to the reference mirrors. LCR: Liquid Crystal Retarders

mators go through liquid crystal retardance (LCR) waveplates for fast polarization switching. Indeed, while the MOT requires circular polarization, Raman interferometry is performed with linear polarization. These waveplates are placed in a temperature-controlled oven in order to minimize polarization fluctuations that may degrade the interrogation sequence. At the output of the LCRs, the beam is expanded and collimated to a beam waist of ≈ 25 mm thanks to a Galilean telescope before entering the science chamber through a custom viewport. Three retroreflecting mirrors are placed outside the vacuum chamber, opposite to each collimator and preceded by quarter-waveplates to rotate the polarization by 90°. This setup allows for $\sigma\pm/\sigma\pm$ configurations for the MOT and co-propagating Raman transitions, and lin$\perp$lin configuration for counter-propagating transitions.

At the end of the interferometric sequence, we use fluorescence detection to measure the atomic populations in both internal states and the background light due to the laser scattering on optics or fluorescence from the atomic vapor. Near-resonant light is radiated along the measurement axis and three photodiodes placed at the top, bottom and middle of the experiment chamber observe the light re-emitted by the atoms at 780 nm due to spontaneous emission.

As for magnetic fields, a pair of anti-Helmholtz coils is installed on the x axis to trap the atoms in the MOT by generating a magnetic field gradient. Additionally,

three pairs of mutually-orthogonal coils in Helmholtz configuration driven by a DC current allow us to cancel the background magnetic field coming from the Earth and surrounding electronics amongst others. These coils are also used to generate a DC bias magnetic field along the measurement axis in order to define the quantization axis and lift the degeneracy between the Zeeman sub-levels. Insensitivity to ambient magnetic field is further increased by placing the whole setup inside a µ-metal shield of $660 \times 660 \times 515$ mm^3, facilitating the dynamic operation of the interferometer.

2.3 Classical inertial measurement unit

2.3.1 Navigation-grade mechanical accelerometers

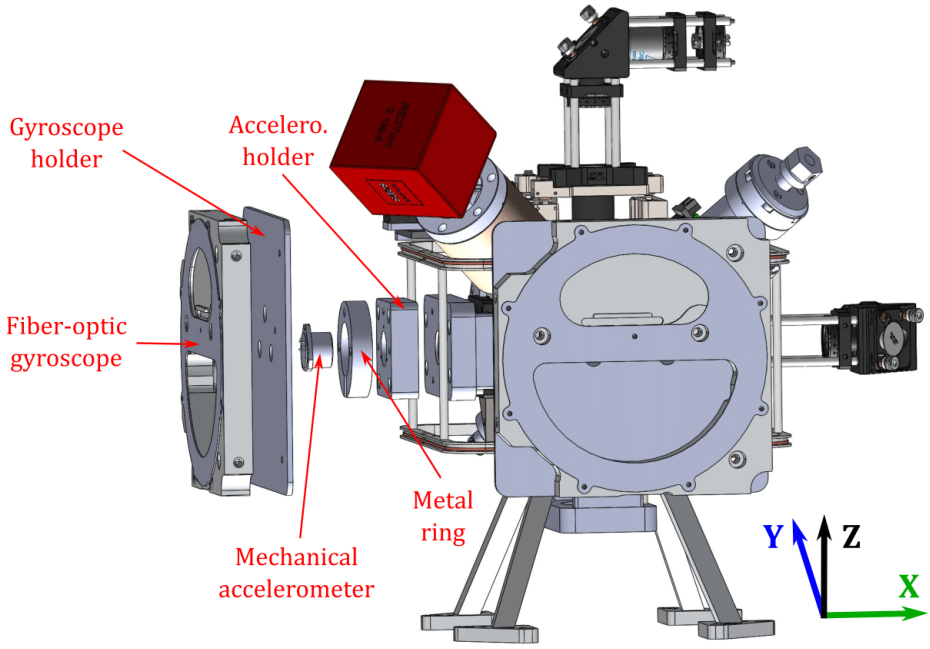

Figure 2.5: Exploded view of the x-axis classical inertial measurement unit's (IMU) components mounted onto the science chamber. The mechanical accelerometer (MA), fixed at the back of the reference mirror with a rigid mount, is encircled by a metal ring in order to mount the fiber-optic gyroscope (FOG) on top of it. The FOG and the MA then share the same measurement axis. The y-axis classical IMU is assembled in the front plan as well.

A triad of navigation-grade mechanical accelerometers, with typical long-term stability below 100 µg, is installed in the science chamber (one placed at the back of each reference mirror which retroreflects the Raman interrogation laser beam back), as depicted in figure 2.5. These devices are navigation-grade, MICAL pendulous rebalanced accelerometers [Radix 2000] manufactured by Thales (J192AAM on the x and y axes and EMA 1000-B1 on the z axis) which benefit from high sensitivity (characterized below) and high dynamic range (above ±10 g). They output an analog

current signal, which presents low sensitivity to electrical noise compared to voltage signals, and this output is sent directly to the real-time system rack via shielded coaxial cables and transimpedance amplifiers.

These devices were characterized on a massive marble table in the past to assess the ultimate performances they can reach under a good isolation from ambient vibrations [Templier 2021]. This study led to an utmost sensitivity of 2 µg/$\sqrt{\text{Hz}}$ on the z axis, and a minimum noise level of 1 µg at 4 s, before the bias drift causes the signal to increase again. A temperature calibration was also performed in order to adapt the accelerometers' scale factor according to the temperature measured at the center of the science chamber. The real-time calibration of the bias dependence on temperature is not implemented as the bias is eventually tracked and corrected thanks to the atomic measurement.

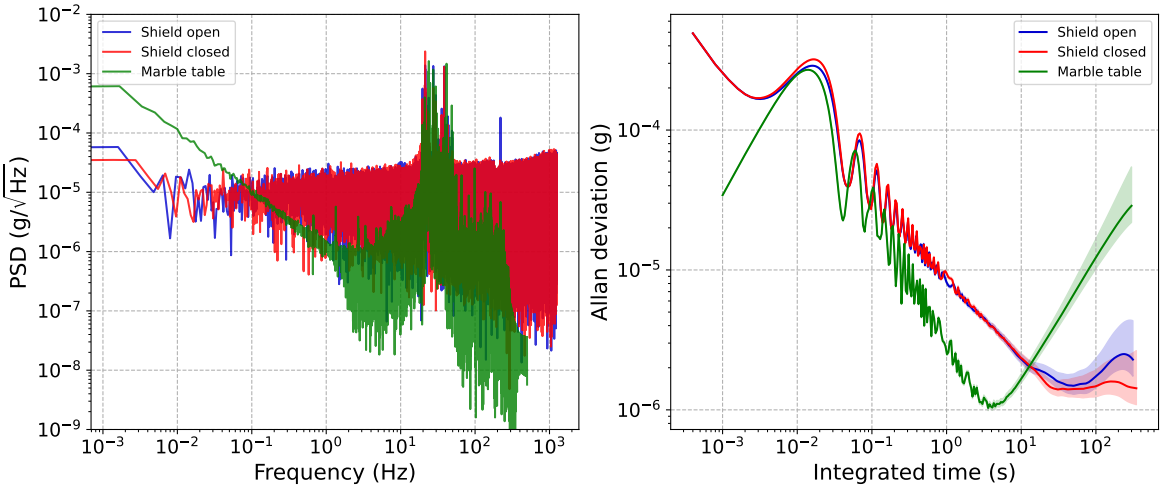

Figure 2.6: Characterization of the classical accelerometer, namely its power spectral density (left) and Allan deviation (right), under different environmental conditions. Data were recorded during 10 minutes for a 2.5 kHz sampling rate. The faded area around the Allan deviation curve corresponds to the two-sided confidence interval on the measurement.

For the data and results presented in this manuscript, experiments were exclusively carried out with the science chamber placed on a 3-axis rotary platform allowing us to reach ± 90° on the horizontal axes, and ± 45° around the base of the sensor head (corresponding to a rotation around the z axis in the chamber's frame, but not necessarily in the laboratory's frame). Figure 2.6 displays the power spectral density (PSD) and Allan deviation of the mechanical accelerometer used on the z axis. This accelerometer is oriented along the vertical with its measurement axis upwards on the marble table (green curve) and downwards on the rotary platform (blue and red curves) during the ten minutes acquisition. In the low frequencies (high integrated times), the frequency response is mostly flat on the platform compared to the spectrum

acquired on the marble table two years earlier. The slow drift which appears on the Allan deviation can be related to temperature fluctuations, since the thermal contact on the marble table is worse than when the accelerometer is recessed in the sensor head. Additionally, we can observe an increase in the sensor's self-noise above 200 Hz where the signal was heavily suppressed on the previous data. The main reason for this difference is that previously, data were averaged by a cascaded integrated comb (CIC) filter downsampling the signal from 5 kHz to 1 kHz. Since this operation is equivalent to a low-pass filtering stage, it seems normal that high frequencies were cut then. Eventually, in the $10^{-1} - 10^{2}$ Hz frequency interval, we observe a similar spectrum with higher amplitude, characteristic of the mechanical vibrations exacerbated on the rotational table with respect to the marble table, with a peak at the mg level between 20 and 40 Hz. Finally, on the green Allan deviation curves, we observe a main integration in $1/\tau$ corresponding to quantization noise while the vibrations of the rotary platform make the integration slower and the noise higher on average.

2.3.2 Fiber-optic gyroscopes

In order to compensate for adverse rotational effects on atomic interference, we need to know accurately the rotation axis and rate of the apparatus. For this purpose, we use a triad of high sensitivity and accuracy fiber-optic gyroscopes (FOGs) originally meant for three-component rotational seismometry. Since the work presented in this thesis focuses on the correction of rotations in the plane transverse to the interrogation axis of the atomic interferometer, only two of them are visible in figure 2.5. They measure the projections of the rotation rate on the x and y axes. Indeed, as far as the rotations compensation's proof of principle is concerned, all the experiments were limited to one-axis interferometry.

Figure 2.7 exhibits the typical behavior of the x-axis gyroscope lying on the heavy marble table, ensuring a good isolation from surrounding mechanical noise (green curves) and on the rotary platform (blue and red curves) which corresponds to the standard operating conditions. Both gyroscopes have a very similar spectrum, so only the characterization of the sensor placed on the x-axis is shown for clarity. Indeed, most data were acquired with a tilt $\theta_z = 0$ so the x axis of the sensor head coincides with a rotation axis of the platform, in which case only this sensor is used and the second one mostly measures noise. These graphs show an important drift at low frequencies on the marble table (mostly due to temperature sensitivity), less visible on the platform where the good thermal contact with the sensor head can act as a heatsink. In the absence of vibrations, the sensor displays a sensitivity around 40 nrad/s/$\sqrt{\text{Hz}}$ and the noise floor is reached in the $1 - 10$ Hz region where it gets as low as 2 nrad/s, before

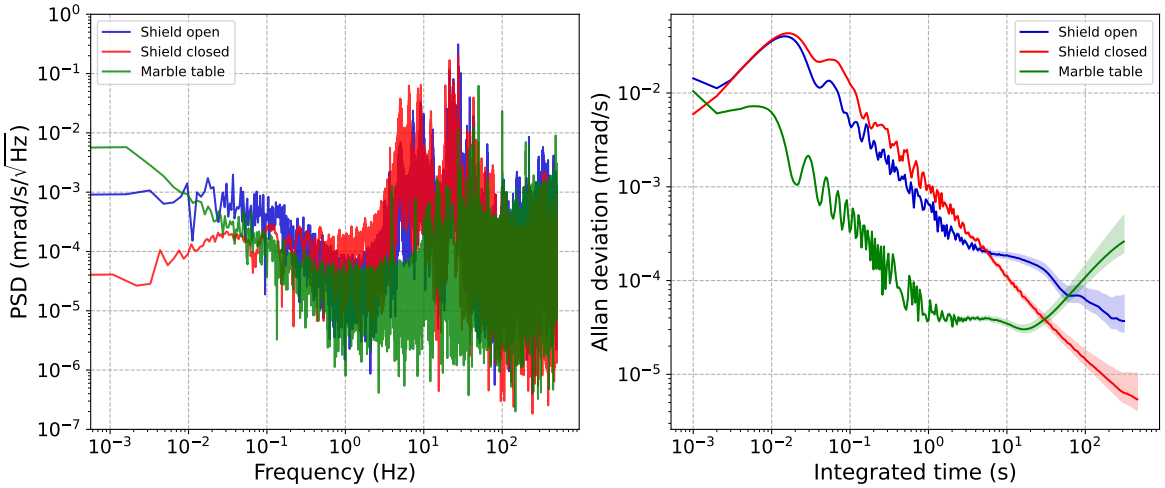

Figure 2.7: Characterization of the x-axis fiber-optic gyroscope, showing their power spectral density (left) and Allan deviation (right) of the sensor on the marble table (green curves) and rotary platform with (red curves) and without (blue curves) the magnetic shield. Data were recorded during 10 minutes for a 1 kHz sampling rate. The faded area around the Allan deviation curves corresponds to the two-sided confidence interval on the measurement.

worsening again with a 80 µrad/s peak around 50 Hz. Usually, these devices are meant for seismometry and thus optimized for measuring slowly-varying phenomena, hence they are typically operated at 200 or 400 Hz. However, due to our timing requirements, a custom electronics board was designed for the operation of these gyroscopes which can explain the increase in the noise level above 200 Hz. Nevertheless, these gyroscopes still show a very interesting trade-off between their sensitivity and size (they are 20×20 cm squares) which make them good candidates for the targeted applications.

2.4 Piezo-actuated tip-tilt platform and controller

With the correction of the environmental factors defined in chapter 1 in mind, and especially regarding parasitic rotations of the apparatus during an atomic interferometry sequence, it is crucial to address the exponential decay of the fringes' amplitude. As mentioned previously, several schemes can be implemented but we will focus on the stabilization of the effective wave-vector's orientation with respect to the terrestrial frame. To that end, we will operate a rotation of the reference mirror opposed to the rotation of the science chamber through the use of a piezo-actuated tip-tilt stage. The whole setup, provided by Physik Instrumente (PI) is composed of an electronic controller (E-727.3SD) receiving digital commands and transmitting analog signals to the platform itself (S-335.2SHM2), subsequently converted into piezo-actuators motion. There is a total of four actuators arranged in pairs along two relatively orthogonal axes. The assembly of the platform on the sensor head is depicted in figure 2.8.

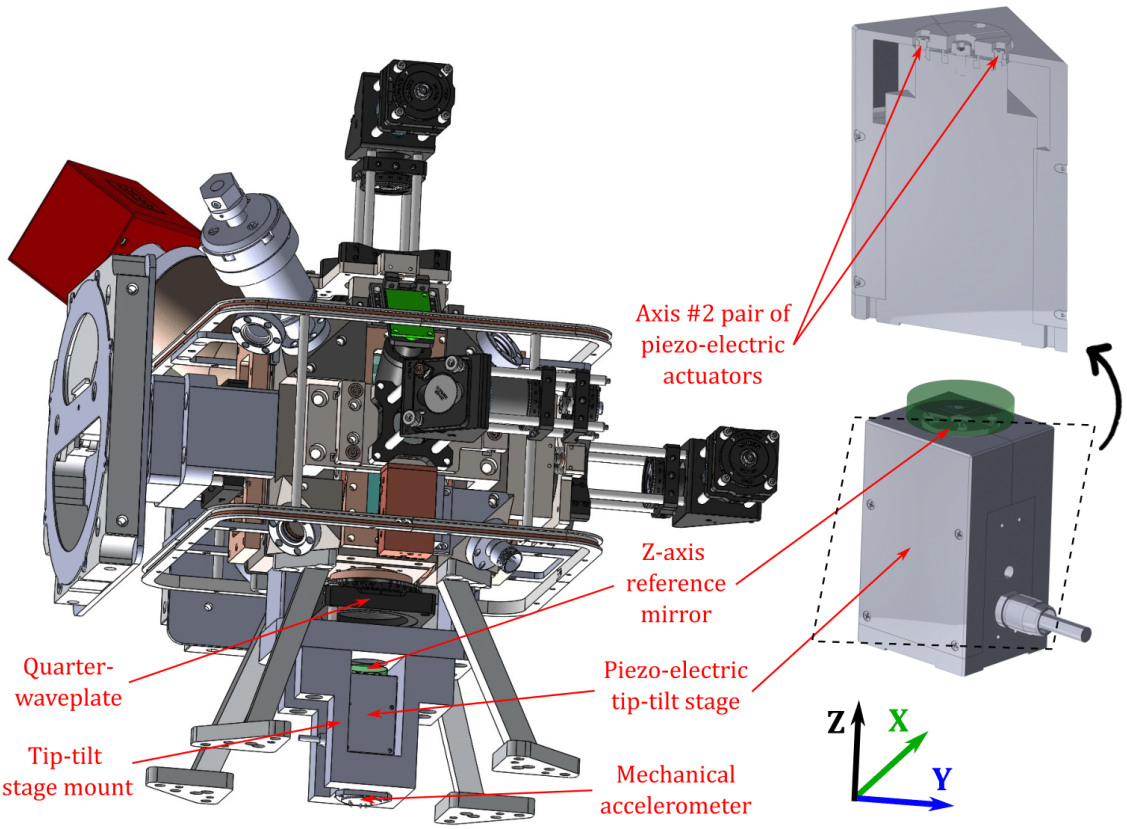

Figure 2.8: Assembly of the piezo-electric tip-tilt stage on the z-axis, along with the corresponding 1" reference mirror and mechanical accelerometer.

2.4.1 Description of the components

The E-727.3SD controller receives digital commands corresponding to the angular setpoints for each axis of the platform, transforms these data into a voltage ranging from -30 V to 130 V and transmits them to the actuators. It also features strain gauges for each motion axis so that the stage can be operated in closed-loop, in addition to the open-loop configuration.

The S-335.2SHM2 tip-tilt stage is built around two analogous motion axes enabling a 35 mrad ($\simeq 2°$) total deflection angle along each axis, the two actuators of a same pair moving in opposite directions with the same amplitude. These axes are placed at approximately 45° with the body's lateral surfaces and *a priori* orthogonal to each other. An angular setpoint for a given axis corresponds to a rotation around this axis, thus meaning a displacement of the other axis' actuators.

While one actuator has its negative electrode connected to the ground, the other one's positive electrode is connected to a fixed +100 V reference voltage; the remaining two electrodes (one for each actuator) are tied together and connected to the piezo voltage sent by the controller as displayed in figure 2.9. This electrical scheme ensures

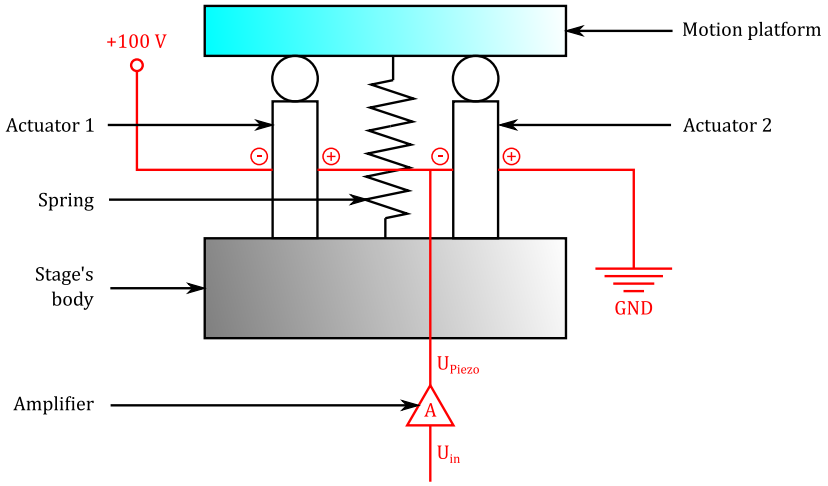

Figure 2.9: Electrical schematic showing the operating principle of one of the two axes of the tip-tilt stage. The electrodes of both axes are electrically switched ensuring a symmetrical motion around the center of rotation and preventing any translation.

that a negative displacement of an actuator will give an equal positive displacement on the other side, ensuring a pure rotation around the platform's center with no translational motion leading to an undesired piston effect which could affect the absolute phase reference of the interferometer. According to the datasheet, the platform's center of rotation is located at the vertical of the mount's body, 3.3 mm below, corresponding to a 7.3 mm distance to the 1" mounted mirror's surface. As the body is sealed, this distance cannot be measured and will be taken as the value given in the datasheet.

There are different ways to transfer data to the controller: for example, the manufacturer software delivered with the hardware elements, PIMikroMove, is meant to be used with the USB interface. However, when the tip-tilt platform's motion is driven by the FPGA board, the communication is enabled through the Serial Peripheral Interface (SPI) protocol. This method, in addition to enabling synchronous and simultaneous transmission and reception of data, is much faster than the TCP/IP or the USB protocol, which is required for real-time operation. Indeed, the delay in the other communication protocols can easily reach tens of milliseconds, making us enable to transmit one command to the piezo-electric actuators before the end of the interferometer. Furthermore, the protocol is built as follows: a data packet sent by the host (here the FPGA program) is evaluated by the PI-Controller and received with a delay of one communication cycle, while the corresponding answer from the controller needs to be evaluated as well before being received by the host. Thus the motion axes' position provided by the strain gauges corresponding to a given couple of angular setpoints will be delayed by two transmission/reception cycles.

To understand the dynamics of the piezo-electric actuators used for rotating the

mirror, the manufacturer software PIMikroMove can be used. Using a USB link, the CPU where the software is installed detects the controller and associated tip-tilt stage when turned on, along with the number of motion axes. On program start-up, an AutoZero procedure sets both axes in motion so that a displacement limit is found for both of them and the corresponding voltage is set as an extremum. From this point on, returned values are reset to 0 mrad and can be changed up to 35 mrad giving a median value of 17.5 mrad, corresponding to the nominal position of the mirror in principle.

2.4.2 Orthogonality of the motion axes

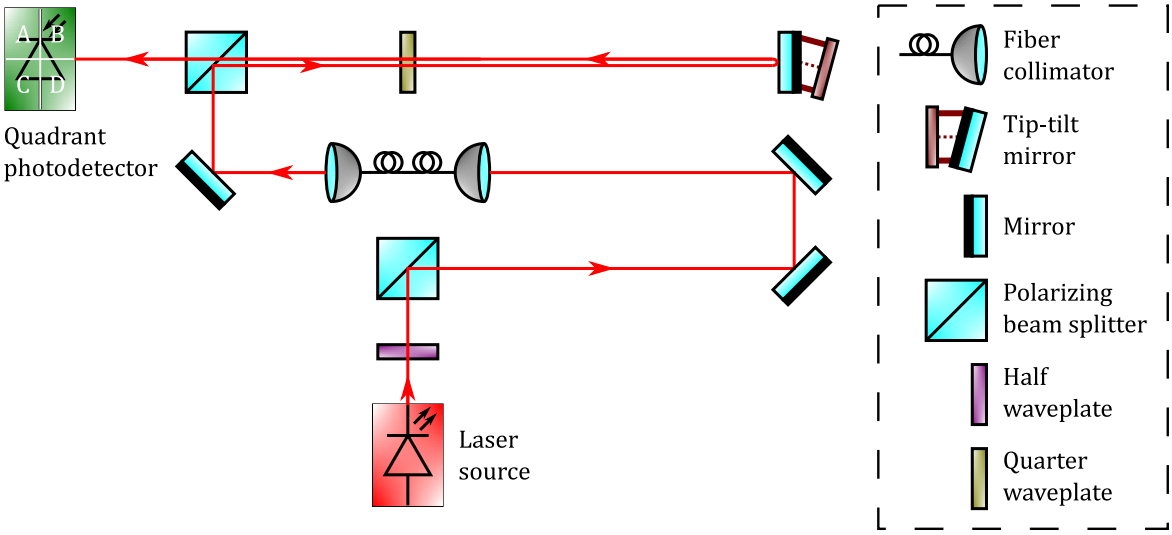

Figure 2.10: Schematic of the setup realized for the optical characterization of the tip-tilt platform.

In order to characterize the behavior of the tip-tilt stage, we realized an optical setup to measure the displacement of a laser beam depending on the commands it receives. This setup is represented in figure 2.10. A laser source shines light on a half-waveplate followed by a PBS for total power adjustment, before being coupled in a fiber collimator to ensure we have a circular and Gaussian mode. A second fiber collimator transmits this light so it hits the mirror mounted on the platform at normal incidence, before it finally reaches a quadrant photodetector (Thorlabs PDP90A). The mirror of interest is separated from the quadrant photodetector by 97(1) cm, enabling for a resolution of 0.97(1) mm/rad. The photodetector is then oriented with its axes, supposed orthogonal, at 45° with respect to the marble table's surface so that they are presumably aligned with the ones of the tip-tilt platform. That way, a displacement along one axis of the stage should lead to a voltage difference on a single channel of the photodetector.

Once the operating conditions are satisfying, the displacement of the laser on the

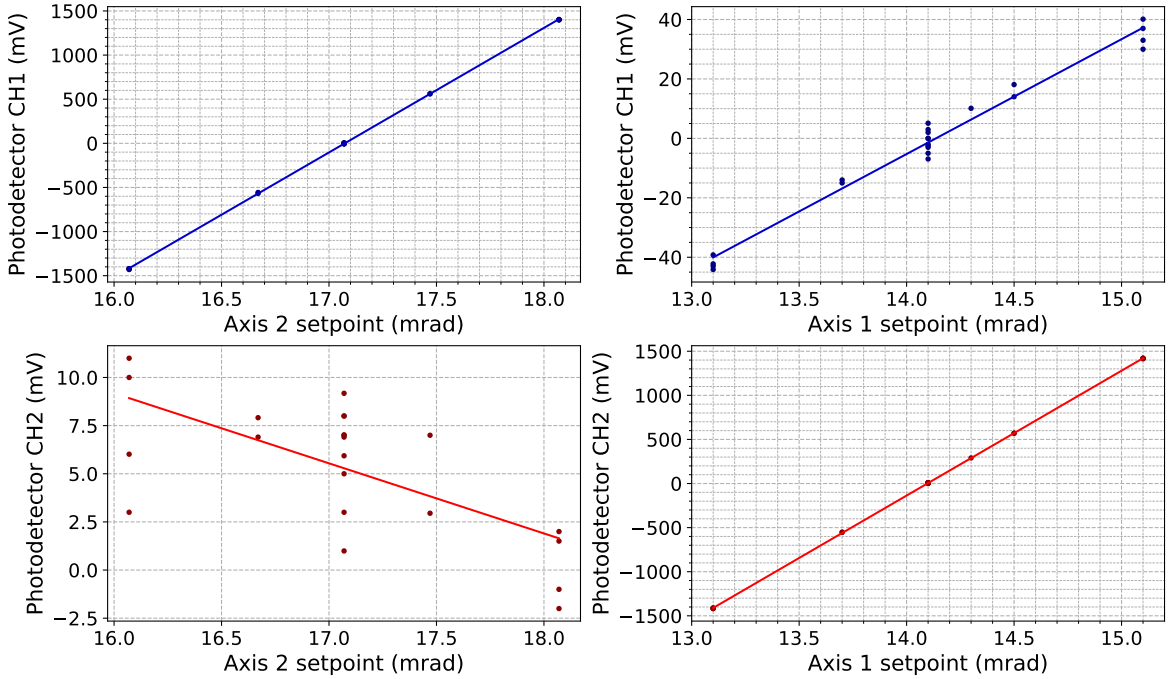

Figure 2.11: Characterization of the orthogonality of the two motion axes of the tip-tilt stage, displaying the displacement on each axis of the quadrant photodetector versus the setpoint angles of the piezo-actuators.

photodetector was recorded and compared to the setpoints sent to the tip-tilt stage, one axis being moved at a time, as displayed in figure 2.11. For the first motion axis, the fit yielded slopes equal to 39 mV/mrad and 1416 mV/mrad for the first and second measurement axes of the photodetector respectively. The angle between the considered rotation axis of the mirror and one of the photodiode's axes, given by the tangent of the ratio of these slopes, leads to a 1.58° misalignment. The same characterization for the second motion axis produced slopes of 1412 mV/mrad and -4 mV/mrad, hence a -0.16° mismatch. The conclusion reached from this study is that the deviation from orthogonality of the piezo-actuated mirror's motion axes is equal to 1.74°, with the second axis fairly well oriented at 45° with respect to the faces of the platform's body, as we can see in figure 2.12.

2.4.3 Response of the two actuators

The manufacturer software PIMikroMove offers the opportunity to adjust the PID controller coefficients, namely the digital proportional gain, integrator time constant and derivative coefficient while observing the response to a step angular setpoint. This enables us to optimize the steady-state error (difference between the setpoint and final position), response time and damping factor. Apart from the steady state error, showing little sensitivity to the PID coefficients, the most critical feature of the actuators' behavior is the settling time, corresponding to the delay between the

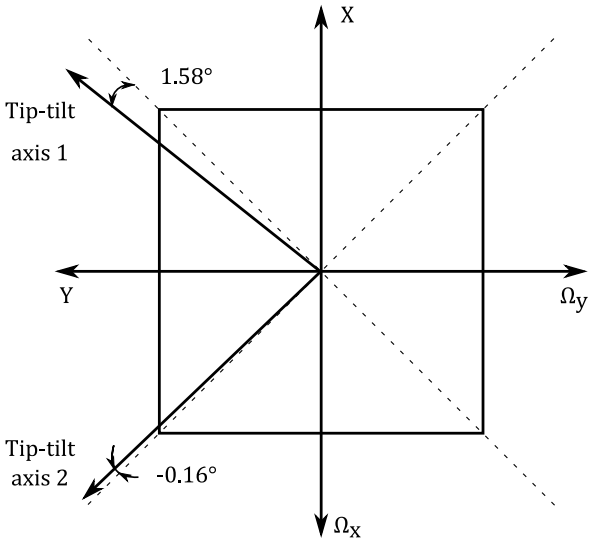

Figure 2.12: Schematic top view of the tip-tilt stage showing the misalignment of the motion axes with their assumed orientations. The x and y axes of the experiment, normal to their respective reference mirrors, are shown. The measurement axes of the FOGs opposed to these axes, written Ω_x and Ω_y, are also provided.

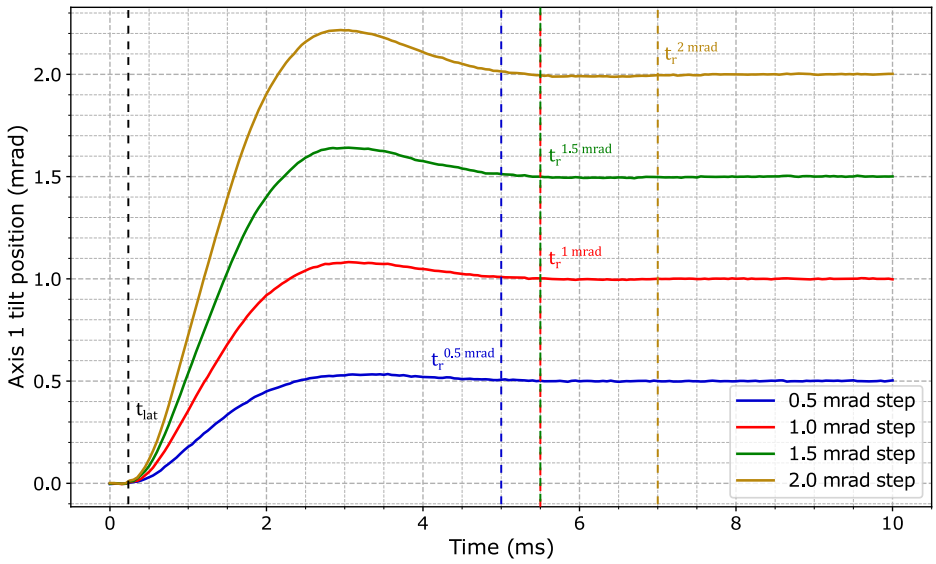

Figure 2.13: Analysis of the axis 1 settling time for optimal PID settings and different setpoint amplitudes, showing the delay time between the setpoint reception and the motion of the axis t_{lat} as well as the settling time for a x mrad amplitude $t_r^{\text{x mrad}}$.

reception of the new command and the reach of this angular position. This parameter depends not only on the PID tuning but also on the amplitude of the setpoint: a PID optimized to reach the critical regime for low amplitudes will have a large overshoot for higher amplitudes and, reciprocally, a PID optimized for large displacements will be severely overdamped in lower regimes. Considering a typical interrogation time $T = 10\,\text{ms}$ and rotation rates below 300 mrad/s, the stroke of one axis should remain under 3 mrad. In order to realize the best trade-off giving the most satisfying results

in this range, the response is adjusted for 1.5 mrad amplitudes and we find optimal values of $P = 8.10^{-3}$, $I = 5.5.10^{-6}$ and $D = 2.10^{-5}$ (given in arbitrary units as these are digital parameters). This ensures a settling time of 5.5 ms for setpoints between 1 and 1.5 mrad which is our typical operation range, as displayed in figure 2.13.

However, these empirical settings are determined by an optimization of the response based on the strain gauges' measurements, thus provided that these are accurate. Using the optical setup described in the previous subsection, we performed dynamic measurements where the mirror is rotated according to the information received by the FPGA board. The setpoints correspond to digital values overriding the FOG's signals, simulating perfectly constant rotation rates over an interferometer's duration. This configuration will produce two equal successive tilt jumps on the second axis of the platform, which proved to be accurately oriented at 45° with respect to the surface of the marble table. The single-axis high-precision linear translation stage allowed to establish a 0.87 V/mm gain on the quadrant photodetector's horizontal axis. The calibration parameters, for the angle to linear displacement and for the displacement to voltage conversions, allowed us to convert the photodetector's output values into an equivalent angle directly compared to the angular setpoint and strain gauge feedback.

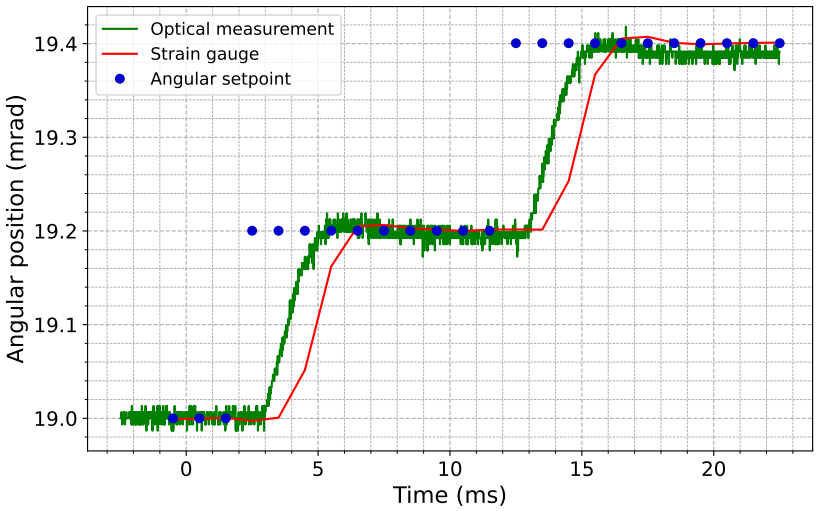

Figure 2.14: Response of the axis 2 of the tip-tilt for a simulated rotation of $\Omega = 20$ mrad/s at an interrogation time $T = 10$ ms, corresponding to two successive 200 µrad jumps.

This optical measurement is recorded on an oscilloscope synchronized with the experimental sequence, and the data communicated through the SPI link (angular setpoints and strain gauges measurements) are streamed at 1 kHz directly from the FPGA board. Figure 2.14 shows the overlay of these three signals for comparison. The time $t = 0$ ms corresponds to the first laser pulse, thus the other two pulses are placed respectively 10 and 20 ms later. We know that the angular setpoint value is

updated 2.5 ms after the first and second pulse, noticeable by the first jump in the blue dots. From the optical response, we observe a displacement starting 500 µs after the setpoint was updated (this delay will be studied in detail in appendix C). What can be seen as well is the 2 ms delay between the reception of the new setpoint and the mirror's motion provided by the strain gauge, corresponding to the two cycles delay mentioned in the description of the components. In terms of amplitude, a fairly good agreement is observed between the strain gauge measurement and the photodetector's signal. If the overlap is not perfect, the amplitude is highly sensitive to the calibration parameters depending on the distance between the tip-tilt mirror's surface and the photodetector. We assume a 1 cm uncertainty on the distance separating the mirror and the photodetector, leading to a fractional uncertainty on the angular displacement equal to:

$$\frac{\sigma_\alpha}{\alpha} = \frac{1}{\alpha}\frac{|\delta y|\sigma_L}{\delta y^2 + L^2} = 1.02 \tag{2.1}$$

where α and L are respectively the angular displacement of the mirror and the distance between the mirror and the photodetector, σ_α and σ_L are their associated uncertainties, and δy is the displacement of the laser beam on the quadrant photodetector (its uncertainty is considered small with respect to σ_L). This measurement was repeated in different regimes of rotation rates and interrogation times, giving very similar fractional uncertainties. A negative steady state error was noticed in most of the cases, presenting an angular displacement slightly smaller than the expected one. Though, this error is highly fluctuating from a run to another (from -3 to -28%) which can be due to various factors including the influence of temperature on the piezo-electric actuators' positions. It must be noted that an error of the order of 10% on the displacement would have a strong influence on the performances of an atom interferometer and would be immediately noticed, so it appears unlikely. For these reasons, no conclusion can be made from these results and data should be retaken in better controlled conditions.

2.5 Real-time compensation electronics

Apart from the vacuum chamber, the whole experiment fits in two racks 19" wide and 900 mm deep, with a height capacity of 18U. On one side are placed electrical power supplies for the rubidium dispenser, MOT coils and ion pump, the RF chain distributing the signals handling the experimental sequence and the laser system. On the other side, we can find the power supply for bias coils (aiming at compensating the ambient DC magnetic field and generating a bias magnetic field along the measurement axis), the experiment's computer along with the National Instruments card including various analog and digital inputs/outputs, and finally the real-time system. All these

hardware elements and their specifications are described in [Templier 2021].

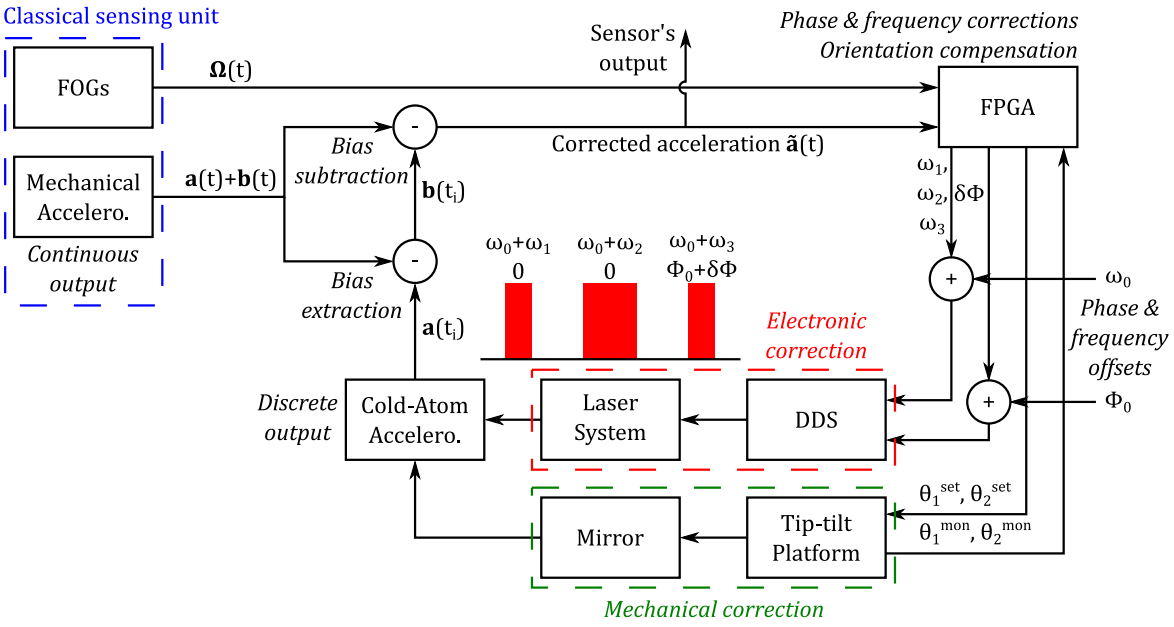

Figure 2.15: Block diagram of the closed-loop operation of the hybrid accelerometer showing the rotations compensation scheme. FOG: Fiber-Optic Gyroscope; FPGA: Field-Programmable Gate Array; DDS: Direct Digital Synthesizer

In order to control parameters or correct for effects requiring fast changes, a real-time circuit composed of two identical Artix 7 FPGA mounted on custom printed circuit boards (PCB) is installed on the electronics rack. Relevant timing parameters are transferred from the central processing unit (CPU) to these two components before each sequence, namely the time-of-flight, interrogation time and Rabi pulse duration for, *inter alia*, synchronization purposes. Similarly, triggers placed at the end of the cooling stage or at the end of the interferometric sequence are communicated directly from the sequencer, operated by Cicero Word Generator. The closed-loop operation of this real-time chain, primarily used for hybridizing the classical inertial measurement unit (IMU) with the atomic interferometer, is depicted on figure 2.15. Here, closed-loop means that the atomic acceleration measurement is compared to the mechanical accelerometer's signal in order to isolate the bias of the latter. This bias is then subtracted from the classical measurement which, once corrected, is used for the final hybrid inertial sensor's output. In comparison, an open-loop mode is achievable by high-pass filtering the information from the classical accelerometer in order to correct only for high frequency vibrations of the mirror and use the atomic measurement as the hybrid sensor's output signal. In both cases, the mechanical accelerometer's signal is used to retrieve the central atomic fringe with a coarse measurement of the acceleration, and for laser frequency and phase hybridization purposes.

The first board handles the acquisition of the high-bandwidth analog signals output

by the three classical accelerometers, treated by analog-to-digital converters (ADC). These are further processed by a fully digital temperature modeling of these sensor's scale factor, relying on an internal temperature sensor present in each accelerometer, and a switchable high-pass filter depending on the operating mode of the hybrid accelerometer. Subsequently, the FPGA uses these measurements to calculate two important parameters: the first one is the Doppler frequency shift, determined with respect to the first pulse using the time integral of the acceleration:

$$\omega_2 = \omega_1 + k_{\text{eff}} \int_0^{T+2\tau} a_{\text{cl}}(t)\, dt \tag{2.2a}$$

$$\omega_3 = \omega_2 + k_{\text{eff}} \int_{T+2\tau}^{2T+4\tau} a_{\text{cl}}(t)\, dt \tag{2.2b}$$

and the second is the inertial phase corresponding to the movements of the mirror, notably its vibrations, which calculation is based on the convolution of the acceleration with the interferometer's acceleration sensitivity function:

$$\phi = k_{\text{eff}} \int_0^{2T+4\tau} f(t).a_{\text{cl}}(t)\, dt \tag{2.3}$$

with $f(t)$ the response function described in 1. The Doppler frequency shift information is used for updating the frequency direct digital synthesizer (DDS) controlling the Raman laser's frequency and phase a few microseconds before each Raman pulse, making the interferometric measurement robust to changes in the sensor head's orientation. As for the computed inertial phase, it is used to retrieve the number of atomic fringes scanned by the vibrations of the mirror and the remainder of its division by 2π is transmitted to the same DDS in order to readjust the measured phase, which prevents the signal from being blurred by parasitic accelerations.

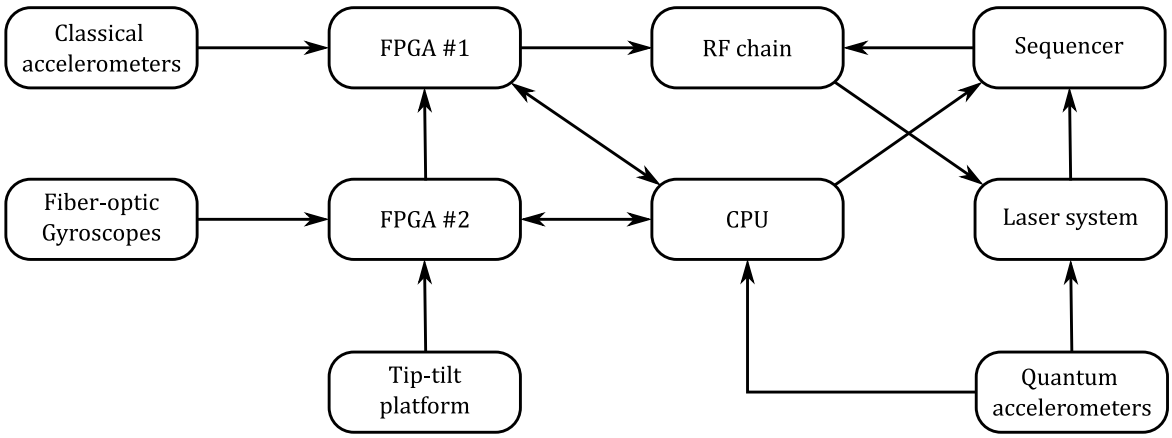

Figure 2.16: Block diagram of the design architecture of the setup. The blocks designate the hardware elements, lines exhibit the electrical connections between them and arrows show the flow of information.

In addition to these hybridization features, this FPGA also interacts with the CPU to override the sequencer and change some parameters' values in real time between two sequences (or even within an ongoing sequence), namely timing parameters, setpoint values for magnetic coils and liquid crystal retardance waveplates, or fast-switching of the measurement axis through the TTL signal sent to the switching optical bench. Finally, a higher-rate link is established between the FPGA and the CPU in parallel of the main one and is used for continuously streaming and recording high-bandwidth measurements from the classical accelerometers at $2.5\,\mathrm{kHz} = f_{\mathrm{ADC}}/2$. In comparison, the primary connection and the graphical user interface (GUI) conceived on LabVIEW are configured to record one data point at every sequence, during the time of the detection. All these interactions are summarized in figure 2.16.

Regarding the second board, it was specifically implemented for the compensation of rotations that may occur during the interferometer. The digital output signals from the fiber-optic gyroscopes are acquired using the universal asynchronous receiver transmitter (UART) protocol and stored in FPGA's registers. As the electronics board used for the gyroscopes' signal treatment is customized for this application, it requires a triggering signal at the desired frequency which is provided by this FPGA. Then, these measurements undergo the processing serving to correct for the wave vector's orientation evolution in the presence of rotations of the science chamber, as it will be described in chapter 4. The result of this treatment takes the form of angular setpoints for the two-axis tip-tilt platform, communicated to its controller using a dedicated serial peripheral interface (SPI) protocol. This is a two-way synchronous process, allowing to simultaneously transmit updated setpoints while receiving the monitoring data from the strain gauge sensors in closed-loop operation. In addition to this main purpose, this second board also receive information like the timing parameters from the CPU in order to precisely synchronize its operation with the experimental sequence. Equivalently to the first board of the real-time chain, a parallel linkage between this FPGA and the CPU enables for high-rate streaming of relevant experimental data, notably the rotation rate measured by the two FOGs, angular setpoints communicated to the two axes of the tip-tilt stage and the corresponding axes' strain gauges measurements returned from the controller. This connection is established at 1 kHz, corresponding to the throughput of the fiber-optic gyroscopes' data.

2.6 Experimental sequence

The whole experimental sequence, timing and analog/digital signals handling is managed with the free software collection Cicero Word Generator (CWG) conceived

by the MIT Center of Ultracold Atoms research group and described in details in [Templier 2021]. This software reloads the designed experimental sequence in an integrated field-programmable gate-array (FPGA) after every cycle, thus adding a $\simeq 1\,\mathrm{s}$ dead time to the total cycling time. If this is not optimal, as the performances of an atomic accelerometer are intrinsically related to the repetition rate, it still benefits from high flexibility in the sequence shaping. Since the control parameters are now well known and optimized, the design of a dedicated sequencer is currently ongoing and this new solution should highly improve this particular timing feature.

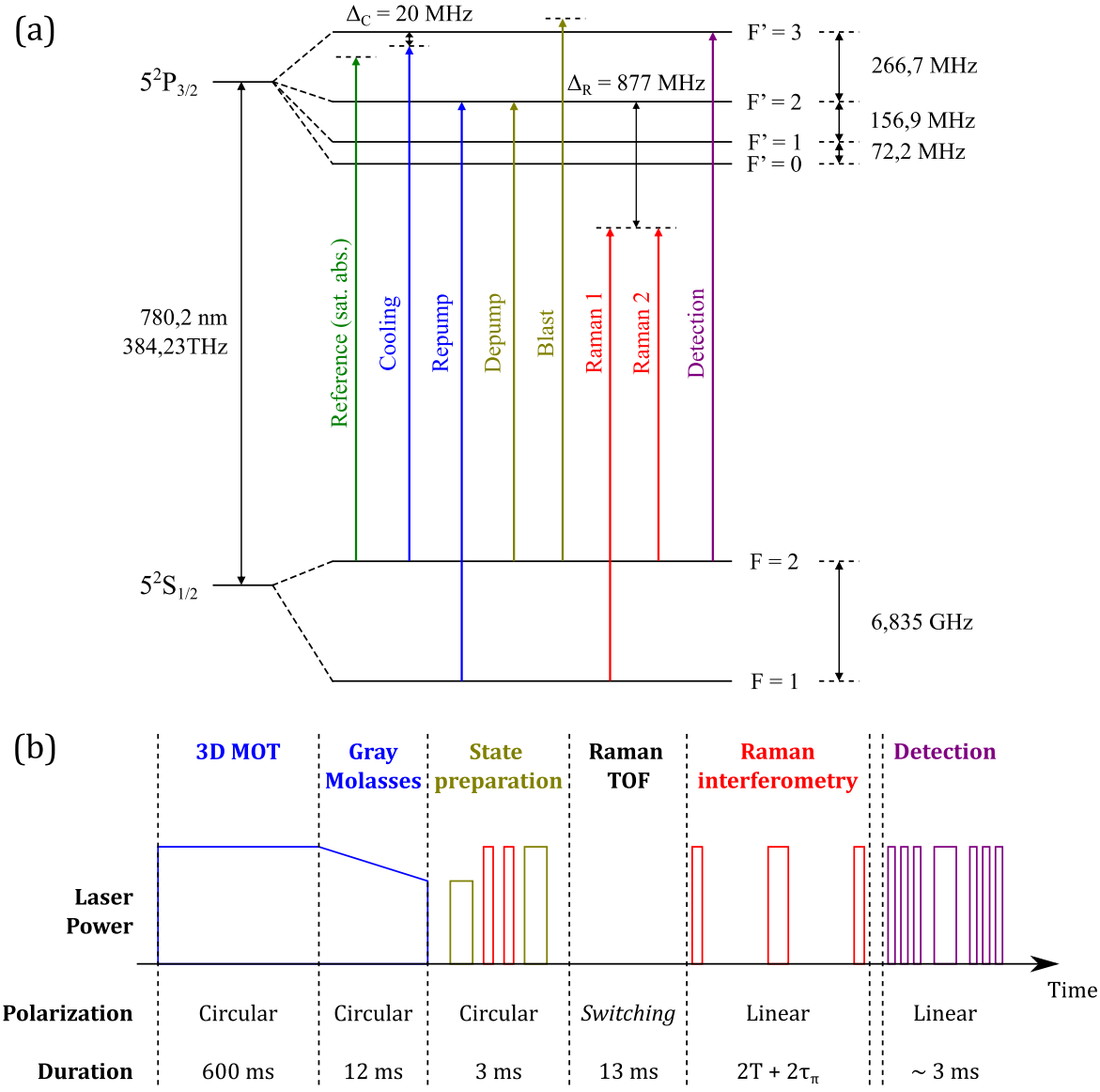

Figure 2.17: Representation of the operating scheme for a typical cooling and interrogation sequence with (a) the relevant atomic transitions addressed by the laser, depending on the step, and (b) the sequence timeline letting appear the evolution of the laser power and polarization.

The rubidium vapor is released in the vacuum chamber by the heated dispenser, driven by a typical electrical current of 4.5 A. This vapor is cooled down in a 3D MOT

using a pair of magnetic coils operated at 8 A and three retroreflected 1" laser beams balanced around 35 mW. In addition to the progressive depletion of the rubidium in the dispenser, a notable decrease occurred in the laser power, identified as a deterioration of the diode laser, which forced us to increase both the driving current in the dispenser and the MOT duration from 250 to 600 ms in order to have a decent detection signal at the end of the sequence.

The experimental sequence is summarized in figure 2.17 (b). After the loading of the atoms in the MOT, the cloud is further cooled down to $\simeq 4\,\mu$K via a 12 ms step of gray molasses, consisting in ramping down the repumper optical power while the cooling frequency is slightly blue-detuned from the $|F = 2\rangle \rightarrow |F' = 2\rangle$ transition. Up to this stage, the optical power is still balanced between the three orthogonal directions. All the relevant atomic transitions are identified in figure 2.17 (a).

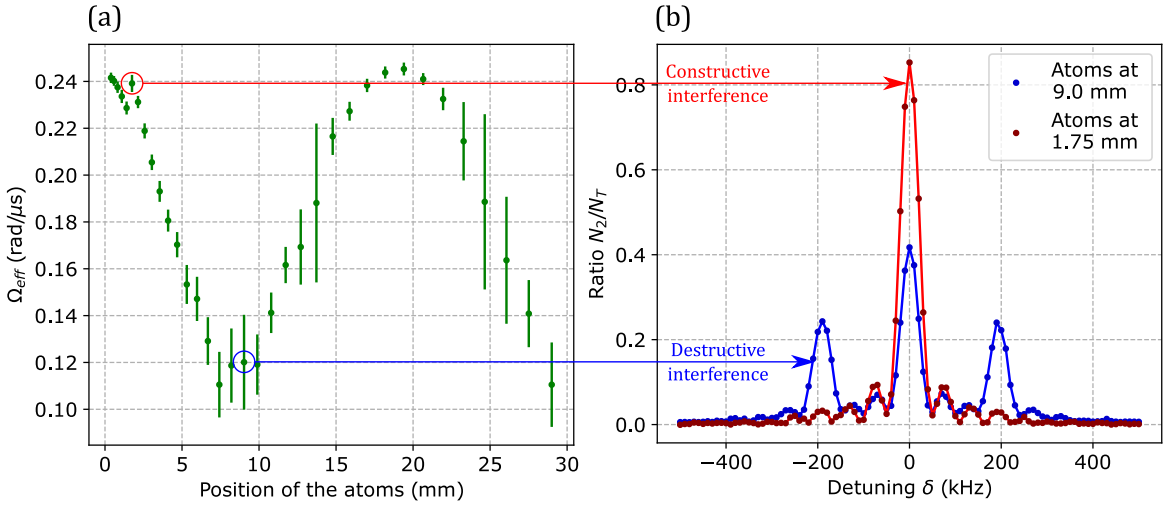

Figure 2.18: Competition of the incident and reflected co-propagating transitions. (a) Evolution of the effective Rabi frequency depending on the position of the atoms relative to the reference mirror, 0 mm denoting their initial position when released from the Gray molasses. (b) Co-propagating Raman spectra for a state preparation performed in two extreme cases (constructive and destructive interference).

Next, a vertical magnetic bias is generated in order to lift the degeneracy of the sub-Zeeman hyperfine energetic levels, and all the optical power is sent to the fiber collimator corresponding to the vertical (z) axis. With the most recent setup, specifically with the free-space optical bench, this power corresponds to 120 mW. The atoms are then prepared into the non-magnetic sensitive state $|F = 1,\ m_F = 0\rangle$. To that end, all the atoms are transferred into the state $|F = 1\rangle$ via a depump pulse, followed by two non velocity-sensitive co-propagating Raman transitions pumping the atoms in $|F = 1,\ m_F = \pm 1\rangle$ to $|F = 2,\ m_F = \pm 1\rangle$. Once all the atoms in magnetic-sensitive states are placed in the upper ground state, a blast pulse removes them, leaving only

the atoms in $|F = 1,\ m_F = 0\rangle$. The whole process lasts less than 1 ms. Since the laser beam is retroreflected, the co-propagating transitions in one way or the other are in competition and the efficiency of the state preparation step depends on the atoms' position relative to the mirror [Templier 2021]. In particular, when the tip-tilt stage was added below the z-axis retroreflecting mirror, the phase reference defined by its surface was shifted by about one centimeter upwards which considerably degraded the state preparation as shown in figure 2.18. This forced us to add a 1 cm wedge between the platform and the rest of the apparatus in order to return to normal operating conditions. In the meantime, working with this 1 cm difference was possible by adding a 45 ms time-of-flight before performing the state preparation, hence strongly limiting the maximum possible interrogation time.

At this stage, the atomic sample which will serve for the acceleration measurement is fully prepared. The atoms are then released in order to fall under gravity for a typical 20 ms time-of-flight (TOF), increasing their velocity and thus the Doppler frequency shift. It is necessary to resolve the counter-propagating transition frequencies from the residual co-propagating one (due to imperfect linear polarization), which is particularly critical while operating with a tilted laser beam. This free-evolution time additionally provides some time to switch components like the magnetic field bias or the LCR operating voltage from MOT mode (circular polarization) to Raman configuration (linear polarization).

After the atoms have fallen for the desired time and the polarization has been switched to lin$\perp$lin, thanks to the LCR waveplate combined with the quarter-waveplate placed before the retroreflecting mirror, velocity-sensitive counter-propagating Raman transitions can be performed to realize the interferometer. The Mach-Zehnder geometry consists in a sequence of three laser pulses coherently splitting, reflecting and recombining the atomic wavepackets using this type of transitions. The first and third steps are realized using $\pi/2$ pulses placing the atoms in a coherent superposition between two energy levels, while the reflection corresponds to a population inversion achieved with a π pulse. The implementation of such atom optics depends on the laser power and pulse duration, which in this case is reached using typical durations of $\tau = 3\,\mu s$ ($\pi/2$ pulse) and $2\tau = 6\,\mu s$ (π pulse) at a 120 mW optical power. These pulses are separated by a free-evolution time called interrogation time (T), defining the area of the interferometer and thus its sensitivity. During this step, the classical accelerometers' signals are processed by the real-time system in order to adjust the Doppler frequency shift before each pulse and the laser phase before the last one (for vibrations compensation and central fringe retrieval).

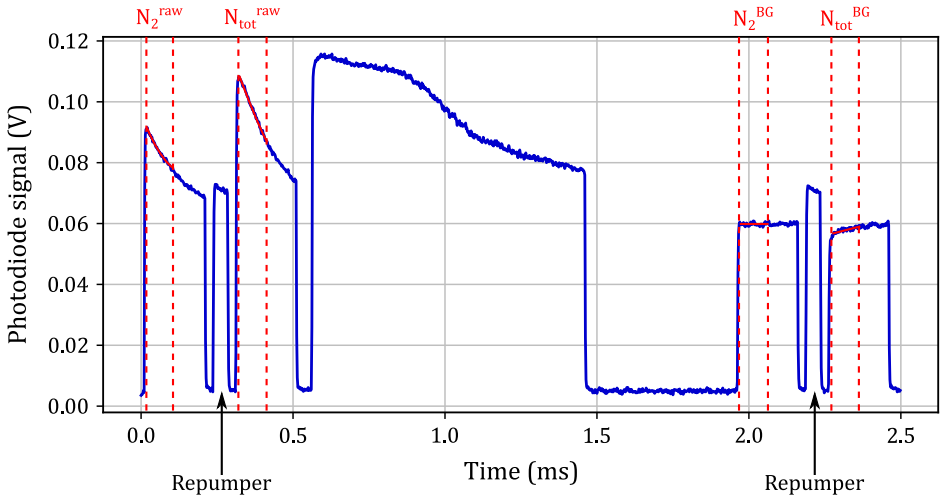

Figure 2.19: Typical detection signal showing the raw population in $|F = 2\rangle$, the raw total population after repumping the atoms in $|F = 1\rangle$ and the background detection levels after the atoms participating to the interferometer are blasted away.

After the end of the interferometric measurement, a laser pulse near-resonant with the transition $|F = 2\rangle \rightarrow |F' = 3\rangle$ is shone onto the atomic cloud to generate fluorescence by spontaneous emission, which allows us to detect the number of atoms in $|F = 2\rangle$ using the photodiodes installed on the science chamber. The same process is repeated after repumping atoms in $|F = 1\rangle$ to $|F = 2\rangle$ in order to detect the total number of atoms. The whole process lasts approximately half a millisecond. These are subsequently blasted using a 1 ms pulse resonant with the cycling transition $|F = 2\rangle \rightarrow |F' = 3\rangle$ heating the atoms and removing them from the detection region. All the steps described above are repeated one more time to access the background detection levels corresponding to residual light, parasitic reflections on the viewports or background atoms which did not participate in the interferometer. The entire scheme is represented in figure 2.19 showing the temporal evolution of the photodiode's signal during a typical detection sequence. The effective population in $|F = 2\rangle$ is then divided by the effective total population, leading to the ratio of interest for the acceleration measurement:

$$R = \frac{N_2 - N_2^{\mathrm{BG}}}{N_T - N_T^{\mathrm{BG}}} \tag{2.4}$$

Dividing the population in the upper ground state by the total population notably makes the measurement robust to fluctuations of power or polarization.

Conclusion

The realization of a three-axis hybrid accelerometer, with the implementation of a one-axis real-time arbitrary rotation compensation scheme, has been described. The static operation of the three-axis hybrid accelerometer has already been demonstrated with the same vacuum chamber and most of the optical and electronic components mounted on it were the same used for this study, hence a synthetic summary was provided but further details can be found in [Templier 2021]. The changes in the laser setup were presented, with particular consideration for the free-space bench which has replaced the all-fiber optical switch in addition to the glass-mounted micro-optic bench which will be installed in the science chamber in a near future.

A more exhaustive description was provided regarding the classical inertial measurement unit, based on triads of navigation-grade mechanical accelerometers and high-end fiber-optic gyroscopes, used for real-time hybridization purposes through FPGA control. The signals of these sensors are fed back to the laser phase as well as to a piezo-electric tip-tilt platform controlling the orientation reference mirror, in order to perform interferometry under high rotation rates. The rotating stage itself was characterized in static and dynamic operation schemes, from the orthogonality of its motion axes to its static gain and response time as a second order system.

This report on the behavior of our experimental setup will help analyze and understand the measurements of the atomic interferometer and more generally of the hybrid accelerometer in different configurations and environments, depending on the noise which can come from mechanical vibrations, rotations of the sensor head and tilt angles with respect to gravity.

Chapter 3

Static operation of the three-axis hybrid accelerometer

This chapter introduces the different steps leading to the conception of a three-axis hybrid accelerometer able to continuously and accurately reconstruct the acceleration vector in quasi-static configuration and at any arbitrary orientation. The preparation of the atomic source used in our matter-wave interferometer is first investigated and optimized for a vertical Raman beam. This includes in particular the atomic cooling and state preparation, as the atomic cloud needs to be as cold as possible with a maximum number of atoms in the same non-magnetic state so as to enhance the quantum state purity and the signal-to-noise ratio of the final measurement. The correlation between the quantum system and a classical accelerometer, as well as the tracking algorithm developed to optimize the acceleration measurement, are also introduced. The performances of the resulting quantum gravimeter operated with a single vertical laser beam are subsequently investigated, specifically its sensitivity, long-term stability and accuracy.

The same study is carried out for a three-axis quantum accelerometer operated at an arbitrary orientation, for which novel techniques need to be developed as new limitations arise from performing matter-wave interferometry with an inclined Raman laser beam. Furthermore, in addition to the capabilities of each independent quantum accelerometer, the calibration of the triad necessary to ensure an accurate reconstruction of the acceleration vector's norm is briefly introduced.

Ultimately, the real-time hybridization scheme with classical accelerometers is demonstrated, notably the compensation in real time of the parasitic phase noise induced by mechanical vibrations and of the Doppler effect which otherwise tunes the laser field out of resonance for a time-varying orientation of the apparatus. The performances of the instrument along with the errors introduced by the classical-quantum correlation are finally investigated, leading to the first conception of a continuous, bias-free accelerometer hybrid triad.

In this whole chapter, *quantum accelerometer* (or *gravimeter*) will refer to the presented instrument using the interferometric measurement as the sensor's output with a partial hybridization with classical accelerometers for vibrations compensation only (called *open-loop* hybridization scheme). On the contrary, *hybrid accelerometer* designates the same instrument using a full hybridization scheme with the classical accelerometers' signals as the device's output, the biases of which being corrected in real time by their corresponding atom interferometers. This operating principle is based on the *closed-loop* hybridization scheme.

Contents

3.1 Gravity measurement with a vertical atom interferometer

In order to realize an atomic gravimeter, a very good knowledge of the apparatus and operating conditions is required. In particular, the preparation of the atomic ensemble including the temperature and state purity are critical as they condition the sensitivity of the interferometer to environmental factors such as the magnetic field through the Zeeman effect, laser beams introducing optical aberrations and light shifts or even Earth's rotation, related to the initial velocity of the atoms. These effects will eventually play a part in the sensor's sensitivity and accuracy by adding phase noise and systematic shifts to the acceleration measurement, which must be rigorously quantified.

3.1.1 Atomic source preparation

A portion of the rubidium atomic vapor continuously distributed in the vacuum chamber is trapped and cooled down by a 600 ms 3D magneto-optical trapping (MOT) enabling the formed cloud to reach the Doppler cooling limit, defined by the competition between cooling and heating processes related to the absorption of a photon, inducing a momentum recoil opposing the atom's motion, and the spontaneous emission of a photon in a random direction. Many cycles of such interactions will nullify the averaged spontaneous emissions while the absorption of photons will impulse a kick to the atoms towards the center of the trap, reducing their velocity and thus their temperature. For ^{87}Rb cooled on the $5^2S_{1/2} \rightarrow 5^2P_{3/2}$ of the D_2 line, this Doppler cooling limit is equal to:

$$\mathcal{T}_D = \frac{\hbar\Gamma}{2k_B} \approx 145.5 \ \mu\text{K} \tag{3.1}$$

with $\Gamma = 38.11 \ \mu s^{-1}$ the natural linewidth of the atomic transition. However, this limit temperature remains too high for the targeted applications, which is why the 3D MOT is followed by a 12 ms stage of optical gray molasses [Rosi et al. 2018], enabling the generated atomic cloud to reach sub-Doppler temperatures. The efficiency of the overall cooling process can then be evaluated by measuring the temperature via counter-propagating Raman spectroscopy.

In chapter 1, we assumed a Gaussian velocity distribution with a dispersion equal to:

$$\sigma_v = \sqrt{\frac{2k_B\mathcal{T}}{m}} \tag{3.2}$$

with k_B the Boltzmann constant, m the atomic mass and $\mathcal{T}$ the atomic cloud's

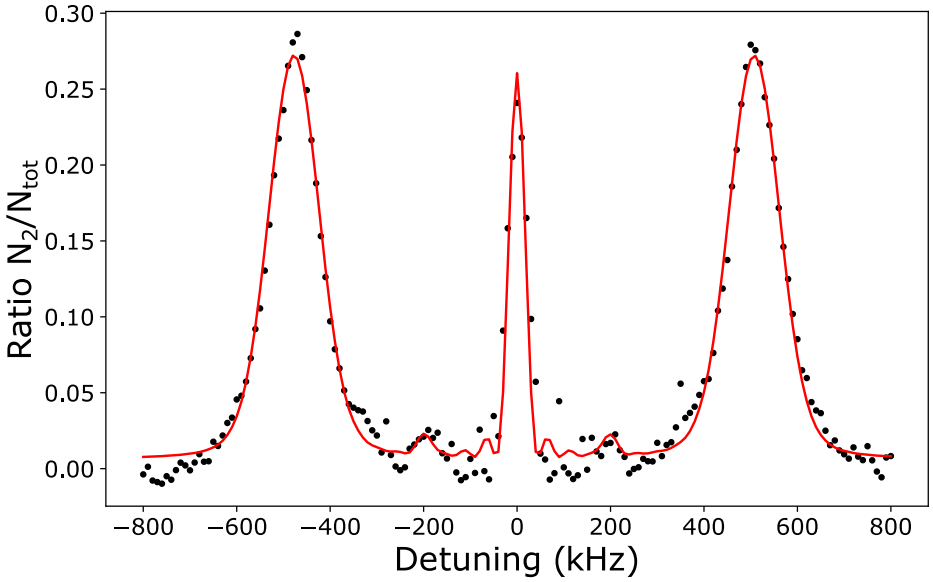

Figure 3.1: Raman spectroscopy after a state preparation stage with lin⊥lin polarized beams (see chapter 1), a 20 ms TOF and $\tau_\pi = 16$ µs pulses. Black dots represent the experimental points while the red curve displays a fit accounting for the two Doppler-sensitive transitions (wide Gaussian peaks on the extremities) as well as a residual co-propagating transition for atoms in the non-magnetic state $|m_F = 0\rangle$ (high, narrow peak at zero-detuning). Small rebounds in between correspond to the residual transitions for atoms in the Zeeman sub-levels $|m_F = \pm 1\rangle$.

temperature. We use equation 1.6 to fit the velocity-sensitive peaks corresponding to the counter-propagating transitions on a Raman spectrum as displayed in figure 3.1. As a reminder, the frequency splitting between the peaks is connected to the velocity of the atoms through the Doppler frequency shift ω_D (see section 1.1). For the determination of the atomic cloud's temperature, the laser power is decreased in order to have a longer Raman pulse (here $\tau_\pi = 16$ µs) and thus thinner and better-resolved velocity-selective peaks during the Raman spectroscopy. The fit to these data, collected after a 20 ms time-of-flight (TOF), yields an approximate cloud temperature $\mathcal{T} \approx 3.8$ µK. Instead of just fitting a Gaussian distribution to the counter-propagating peaks of the spectrum, the function used is the Fourier transform of the square pulse convoluted by the velocity distribution of the atomic cloud, hence the pulse duration which remains quite short should not limit the estimation of the cloud's temperature.

After the cooling stages, the atomic cloud needs to be prepared into a common energy state to maximize the quantum purity of the ensemble before the interferometric measurement. We target the magnetic-insensitive Zeeman sub-level $|F = 1, m_F = 0\rangle$ which ensures insensitivity to ambient magnetic field at the first order. To that end, all the atoms are optically pumped into the state $|F = 1\rangle$ (which will be called the depump stage later on, as the atoms are actually pumped into the lower ground

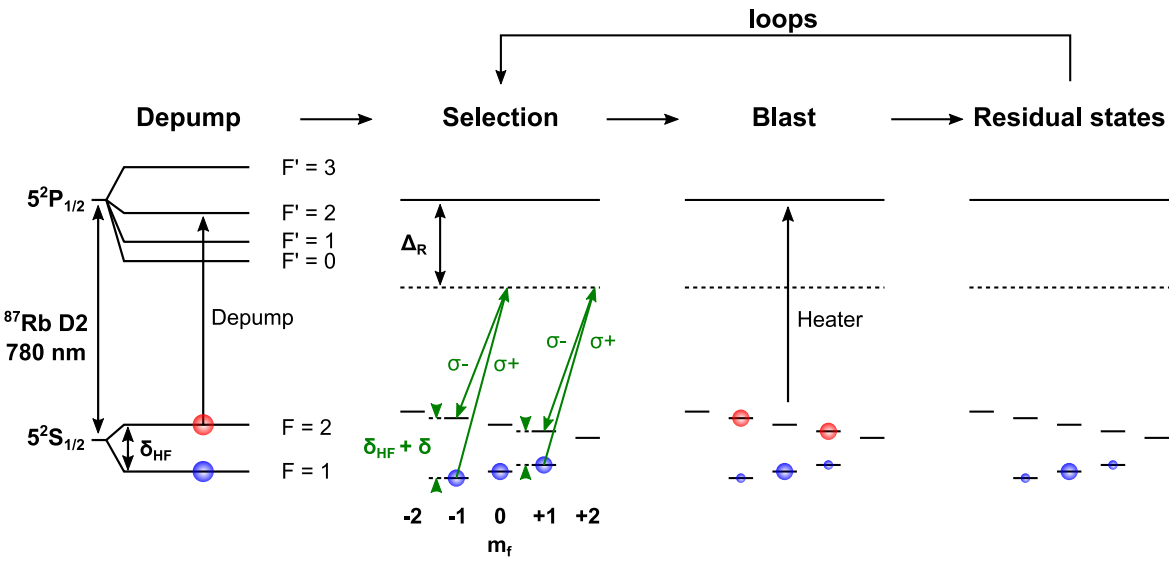

Figure 3.2: Scheme of the state preparation using co-propagating transitions along with a blast pulse to increase the quantum purity of the system, taken from [Templier 2021]. During the selection step, the frequency is continuously chirped through the atomic transitions with the laser power turned on except for the transition from $|m_F = 0\rangle$.

state) and a bias magnetic field is applied along the measurement axis both to lift the degeneracy between the magnetic sub-levels of the hyperfine structure, and to define the quantization axis along the laser beams. Subsequently, co-propagating Raman transitions are performed with $\sigma_\pm/\sigma_\pm$ polarized laser fields to transfer atoms from $|F = 1, m_F = \pm 1\rangle$ to $|F = 2, m_F = \pm 1\rangle$, still along the quantized axis. In our case, this is achieved by scanning the resonance detuning δ with the laser on, the latter being turned off only at the frequency resonant with the transition involving atoms in the sub-state $|m_F = 0\rangle$. Then, atoms present in the state $|F = 2\rangle$ are heated in three dimensions with a blast pulse on the $|F = 2\rangle \rightarrow |F' = 3\rangle$ cycling transition, while chirping the optical frequency to the blue to address all the Doppler velocity classes. This sequence, looped three times to further increase the state purity – but at the cost of approximately two thirds of the atoms –, ensures the heated atoms no longer participate in the measurement and only the atoms in the non-magnetic state remain.

Figure 3.3 displays typical Raman spectra using co-propagating Raman transitions with (red) and without (blue) the three loops of the state preparation scheme described above. The frequency splitting between the Zeeman sub-levels is equal to $2\mu_B B/h$ with μ_B the Bohr magneton and $B = 68.5$ mG the bias magnetic field generated by the pair of coils in Helmholtz configuration. Here, we see that 3 loops are enough to efficiently remove atoms in the magnetic-sensitive energy states. However, the 0.7 amplitude of the peak corresponding to the transition between the $|m_F = 0\rangle$ sub-levels is a bit low, which could arise from a normalization issue or from the Rabi frequency's dependence

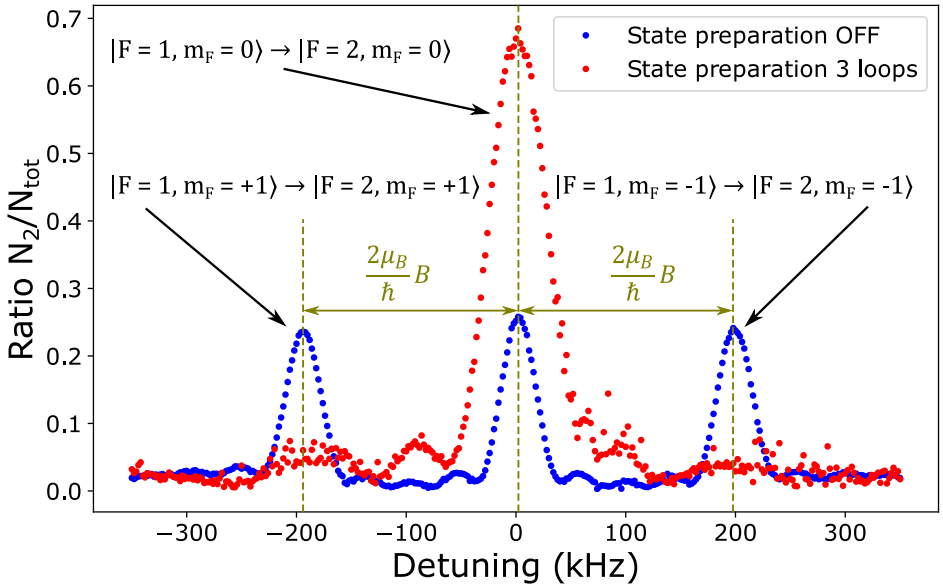

Figure 3.3: Raman spectroscopy with $\sigma_{\pm}/\sigma_{\pm}$ polarized beams scanning the Zeeman magnetic sub-levels of the hyperfine transition with (red dots) and without (blue dots) state preparation.

on the atomic cloud's position relative to the mirror, related to the competition between the incident and reflected co-propagating transitions (see section 2.6).

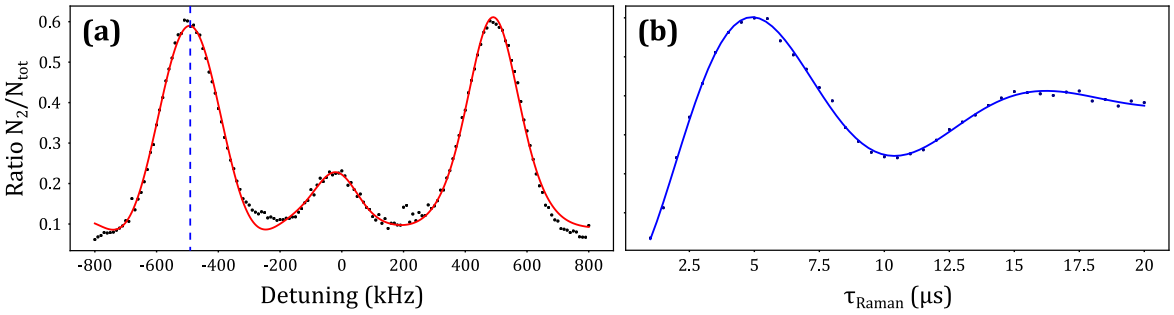

Figure 3.4: (a) Raman spectroscopy with lin⊥lin polarized beams, a 20 ms TOF and $\tau_\pi = 5$ µs pulses. (b) Corresponding Rabi oscillations with the frequency set resonant with the counter-propagating $k_\downarrow$ Raman transition, indicating a pulse duration $\tau_\pi = 5$ µs.

Ultimately, in order to perform atom interferometry, the laser power is turned back on at its maximum value $P_{\text{opt}} \approx 120$ mW leading to much shorter Raman pulses which will result, for instance, in an increased contrast of the interferometric fringes. Indeed, shorter Raman pulses imply a wider Fourier transform and thus addressing a larger number of velocity classes, as mentioned in section 1.1. A typical Raman spectrum with lin⊥lin polarized beams to achieve counter-propagating transitions is given in figure 3.4 (a), and the corresponding Rabi oscillations are displayed in figure 3.4 (b) indicating a pulse duration equal to $\tau_\pi = 5$ µs. Since the laser power has decreased during my thesis, the pulse duration used for the interferometric measurements showed in this work may vary from $\tau_\pi = 5$ µs to $\tau_\pi = 6.5$ µs depending on the time data were

acquired.

3.1.2 Operating schemes for gravity measurement

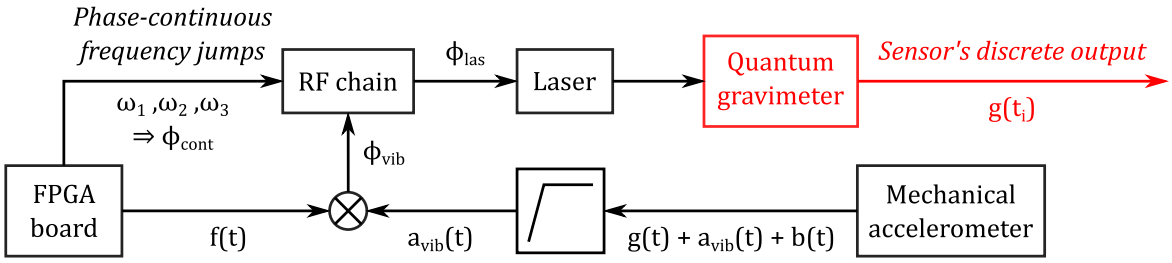

Figure 3.5: Open-loop operation of the quantum gravimeter where the discrete measurement of the atom interferometer is used as the sensor's output signal. The atomic fringes are scanned through the phase shift ϕ_{cont} resulting from the phase-continuous frequency jumps. The slow-varying gravitational acceleration $g(t)$ and mechanical accelerometer's bias $b(t)$ are suppressed by the high-pass filter, only leaving the vibrations $a_{\text{vib}}(t)$ at higher frequencies to be correlated with the interferometer's response function for hybridization purposes.

Our atomic gravimeter is based on a three-pulse Mach-Zehnder matter-wave interferometer with the laser field aligned with the gravity vector. According to the description made in chapter 2, the Raman beam is retroreflected by a mirror acting as a phase reference for the interferometer, since the output phase shift will be sensitive to the motion of the atomic cloud with respect to this reference mirror. Using this operating scheme, the goal is to measure the gravitational acceleration $g(t)$ slowly varying in time (on typical timescales of 100 s) with the quantum gravimeter. This instrument being very sensitive to high-frequency vibrations (typically between 1 and 100 Hz or between $1/T_c$ and $1/T$ with $T_c \approx 1.6$ s the cycling time of our experiment, see section 1.2) which can deteriorate the measurement of the atomic sensor, a mechanical accelerometer is attached at the back of the mirror and measures its motion in real time. As it is shown in figure 3.5, the output signal of this classical sensor is high-pass filtered to conserve only the higher-frequency components, and then correlated with the response function of the interferometer $f(t)$ defined in section 1.2, leading to a vibrations-induced equivalent phase ϕ_{vib} which is directly fed back to the laser system before the last Raman pulse:

$$\phi_{\text{vib}} = \int_0^{2\text{T}+4\tau} f(t) a_{\text{vib}}(t) dt. \tag{3.3}$$

This hybridization between the quantum and classical inertial sensors is further discussed in section 3.3. The main purpose of the high-pass filtering is to remove the gravitational acceleration from the classical signal so that it does not interfere with the quantum measurement. Besides, it is interesting to note that this operation scheme also allows

us to get rid of the mechanical accelerometer's bias, slowly varying in time and thus cut-off by the high-pass filter.

Doppler frequency shift compensation

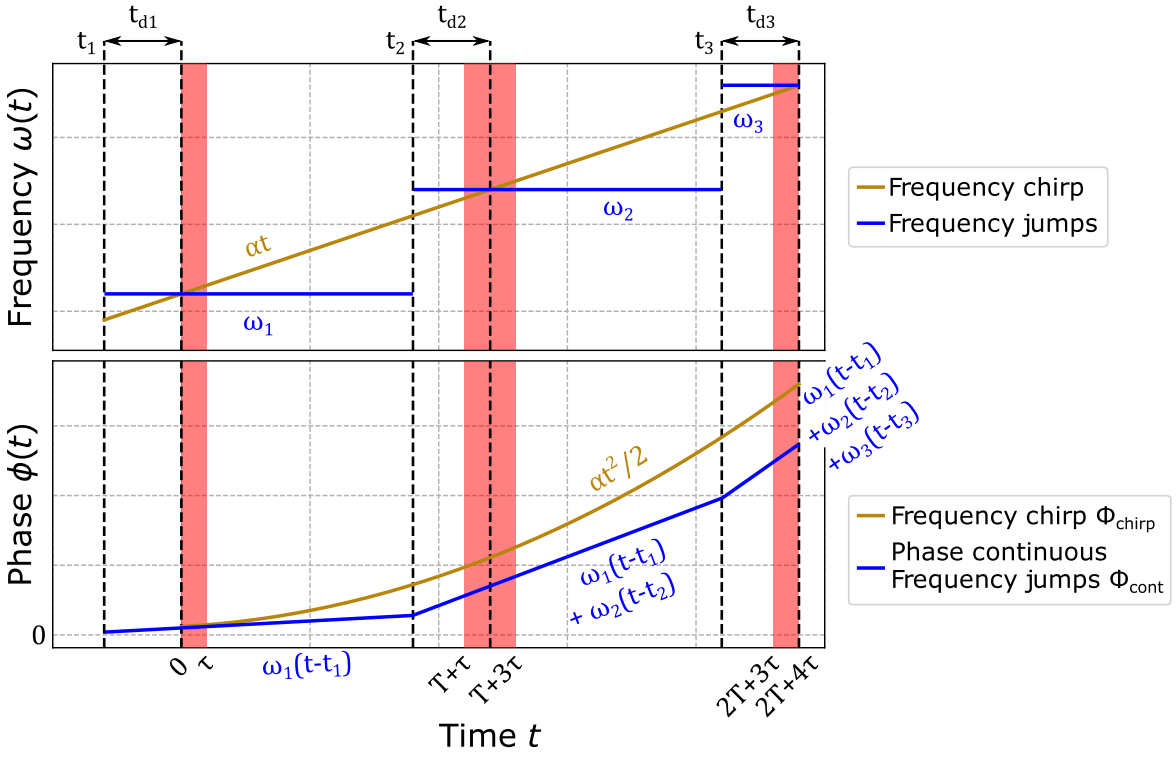

Figure 3.6: Evolution of the laser frequency $\omega(t)$ and phase $\phi(t)$ throughout the atom interferometer for Doppler frequency shift compensation schemes using a frequency chirp (brown) and phase-continuous frequency jumps (blue). The laser phase $\phi(t)$ is imprinted onto the atomic wave packets during the Mach-Zehnder atom interferometer.

Throughout the interferometric sequence, the atomic cloud gains velocity from the gravitational acceleration and the laser beams can become tuned out of resonance due to the Doppler effect. To maintain the laser tuned on resonance, the most intuitive solution consists in applying a chirp (or ramp) α to the laser frequency so that $\omega(t) = \alpha t$, as is the case in most atomic gravimeters. Along with the phase related to the atomic cloud's movement described in 1.2, this effect will also lead to a phase term imprinted onto the atoms which can be calculated with the sensitivity function formalism:

$$\begin{aligned} \phi_{\text{chirp}} &= \int_{-\infty}^{+\infty} f(t)\alpha dt \\ &= \alpha(T+\tau)\left[T + \frac{2}{\Omega_R}\tan\left(\frac{\Omega_R \tau}{2}\right)\right]. \end{aligned} \tag{3.4}$$

Consequently, the interferometric phase shift will be given by the sum of this phase shift and the kinetic phase shift resulting from the motion of the atomic cloud ϕ_{kin}

defined in chapter 1:

$$\Phi = \phi_{\text{chirp}} + \phi_{\text{kin}} = (\alpha - k_{\text{eff}} g) T_{\text{eff}}^2 \tag{3.5}$$

and the atomic fringes are scanned through the laser chirp α.

Nevertheless, the orientation of the Raman beam with respect to the gravity vector is critical as an incorrect compensation of the Doppler effect leads to a decrease in the fringes' visibility and unpredictable measurement shifts. This is not a major issue for an atomic gravimeter set at a fixed orientation but can become critical in the context of a multi-axis atom interferometer operating at a non-constant, random tilt angle as discussed in the next sections. For that reason, and in order to anticipate dynamic rotations of the sensor head, we choose to generate three phase-continuous frequency jumps ω_1, ω_2 and ω_3 corresponding to the Doppler frequency shift at the instants of each Raman pulse. These frequency jumps are set with a delay t_{di} relative to respectively the beginning, middle and end of their associated pulse i as displayed in figure 3.6. Setting $t_{\text{d1}} = t_{\text{d2}} = t_{\text{d3}} = t_d$, this operating scheme introduces the phase shift ϕ_{cont} in the laser phase as follows:

$$\begin{aligned} \phi_{\text{cont}} &= \int_{-\infty}^{+\infty} g(t)\omega(t)dt \\ &= T(\omega_2 - \omega_1) + (t_d - \tau)(\omega_1 - 2\omega_2 + \omega_3) + \frac{\omega_3 - \omega_1}{\Omega_R} \tan\left(\frac{\Omega_R \tau}{2}\right). \end{aligned} \tag{3.6}$$

Setting the frequency jumps with respect to the first one in this way:

$$\omega_2 = \omega_1 + k_{\text{eff}} a_0 (T + 2\tau) \tag{3.7}$$

$$\omega_3 = \omega_2 + k_{\text{eff}} a_0 (T + 2\tau) \tag{3.8}$$

with a_0 an arbitrary setpoint acceleration value related to the sweep of the laser frequency used to scan the atomic fringes. In this configuration, we find the same scale factor as for the inertial phase:

$$\mathcal{S}_{\text{cont}} = \frac{\phi_{\text{cont}}}{a_0} = k_{\text{eff}} (T + 2\tau) \left[T + \frac{2}{\Omega_R} \tan\left(\frac{\Omega_R \tau}{2}\right) \right]. \tag{3.9}$$

In order to scan the interferometric fringes and be able to retrieve the targeted acceleration, we scan the value of the setpoint acceleration a_0 which modifies accordingly the frequency jumps $\omega_{2,3}$ relative to the initial value ω_1 and, eventually, the continuous phase ϕ_{cont}. This yields the following expression of the laser phase:

$$\phi_{\text{las}} = \phi_{\text{vib}} + \phi_{\text{cont}}. \tag{3.10}$$

The operation of the atomic gravimeter is summarized in figure 3.5.

Let us remind the expression of the interferometric phase shift:

$$\Phi = \phi_{\text{kin}} + \phi_{\text{las}} = \mathcal{S}_{\text{kin}} a + \phi_{\text{las}} \tag{3.11}$$

with $a = -(g + a_{\text{vib}})$ the projection of the acceleration of the atoms relative to the reference mirror along the laser beam's axis and $\mathcal{S}_{\text{kin}}$ the interferometer's scale factor defined in section 1.2 by

$$\mathcal{S}_{\text{kin}} = k_{\text{eff}} \left(T + 2\tau\right) \left(T + \frac{4\tau}{\pi}\right) = k_{\text{eff}} T_{\text{eff}}^2. \tag{3.12}$$

The phase shift at the output of the atom interferometer then simplifies as:

$$\Phi = -k_{\text{eff}} g T_{\text{eff}}^2 + \phi_{\text{cont}} = k_{\text{eff}} (a_0 - g) T_{\text{eff}}^2. \tag{3.13}$$

Consequently, the central fringe containing the desired acceleration information will be found for a continuous phase $\phi_{\text{cont}} = k_{\text{eff}} g T_{\text{eff}}^2$ associated to a total phase at the output of the interferometer $\Phi = 0$.

Mid-fringe lock algorithm

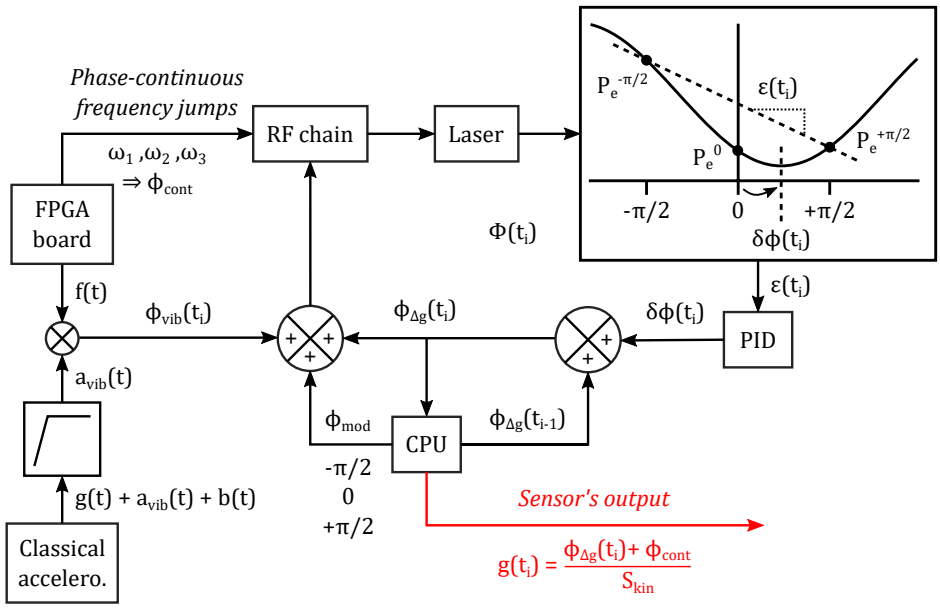

Figure 3.7: Mid-fringe lock algorithm for an atomic gravimeter in open-loop configuration.

Alternatively, instead of having a full scan of the interferometric fringes through the value of a_0 and measure for each point the population ratio in the upper ground state $|F = 2\rangle$:

$$P_2 = P_0 - \frac{C}{2} \cos \Phi \tag{3.14}$$

which allows us to display the complete sinusoidal signal but takes a considerable time, it is possible to fix the value of the setpoint acceleration a_0 appearing in the expression of the frequency jumps $\omega_{2,3}$ and then add a modulation to the laser phase ϕ_{mod} in order to converge faster towards an accurate value of the acceleration. While utilizing the modulation phase, the setpoint acceleration a_0 equals an independent measurement of the local gravitational acceleration. The phase corresponding to the central fringe will change over time due to the tides, fluctuations of the apparatus' inclination or time-dependent systematic phase shifts, which is what the tracking algorithm was designed for. Furthermore, remaining on the side of the fringe allows to maximize the sensitivity of the population to the atomic phase, in addition to reducing the sensitivity to contrast fluctuations.

Two different schemes were implemented: first, the two-point fringe tracking where $\phi_{\text{mod}} = \pm\pi/2$ switches between two points located on the sinusoid's linear part, where the sensitivity of the population ratio to phase changes is maximum contrary to the fringe's maxima and minima which display a quadratic behavior. By measuring the difference in the population ratio between these two points, it is possible to generate an error signal providing information about the position of the central fringe with respect to our initial guess:

$$\varepsilon(t_i) = \frac{1}{C}\left[P_{-\pi/2}(t_i) - P_{+\pi/2}(t_i)\right] \tag{3.15}$$

where $P_{+\pi/2}(t_i)$ and $P_{-\pi/2}(t_i)$ respectively designate the probability transitions measured at the i^{th} shot with a modulation phase $\phi_{\text{mod}} = +\pi/2$ and with a modulation phase $\phi_{\text{mod}} = -\pi/2$. The subscript i denotes two experimental points with opposed values of the modulation phase at a given momentum recoil direction.

Feeding this error signal into a PID controller, we reach an approximation of the phase shift of the i^{th} atom interferometer $\delta\phi(t_i)$ which is compared to the accumulated phase shift of the previous iterations $\phi_{\Delta g}(t_{i-1})$ according to:

$$\phi_{\Delta g}(t_i) = \phi_{\Delta g}(t_{i-1}) + \delta\phi(t_i) \tag{3.16}$$

so that we can adjust the estimation of the phase until we are able to accurately track the changes in the gravitational acceleration. This will finally allow us to have a good evaluation of the phase at the output of the atom interferometer. The other implementation of this algorithm is the three-point fringe tracking scheme, adding a third measurement for $\phi_{\text{mod}} = 0$ at the bottom of the fringe permitting to determine the contrast of the fringes as well, though this scheme is not used much in practice.

Applying this algorithm with averaged measurements along the two interferometric

trajectories $\boldsymbol{k}_\uparrow$ and $\boldsymbol{k}_\downarrow$ enhances the rejection of systematic bias shifts independent of the direction of the wave vector, including first-order light shifts and quadratic Zeeman shift [Louchet-Chauvet et al. 2011]:

$$\phi_{\Delta g}(t_i) = \frac{\phi^{\uparrow}_{\Delta g}(t_i) - \phi^{\downarrow}_{\Delta g}(t_{i-1})}{2} \tag{3.17}$$

and finally yields an increasingly accurate measurement of the gravitational acceleration:

$$g(t) = \frac{\phi_{\text{cont}} + \phi_{\Delta g}(t)}{\mathcal{S}_{\text{kin}}} \tag{3.18}$$

with $\mathcal{S}_{\text{kin}}$ the scale factor of the atom interferometer.

3.1.3 Performances of the atomic gravimeter

The performances of the quantum gravimeter were extensively quantified on the marble table introduced in chapter 2 in order to determine its ultimate sensitivity, long-term stability and accuracy. While the detailed measurements can be found in [Templier 2021], this subsection provides a synthesis of the device's main performances.

Sensitivity to the gravitational acceleration

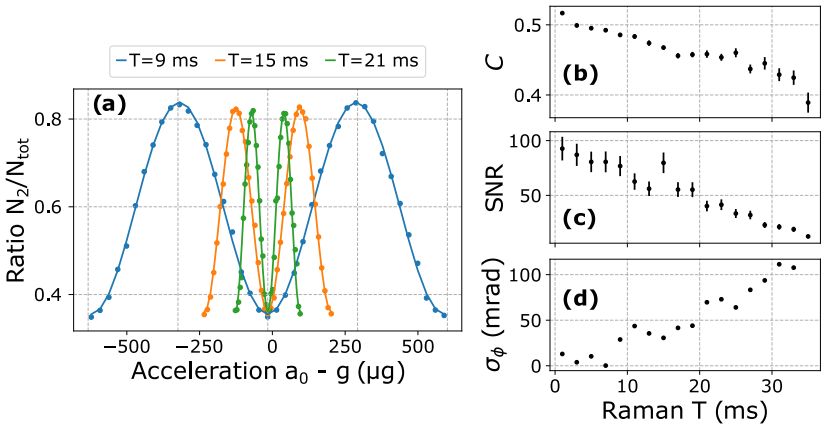

Figure 3.8: Evaluation of the device's sensitivity to acceleration taken from [Templier 2021]. (a) Interferometric fringes scanned through the series of phase-continuous frequency jumps with Raman beams resonant with the velocity classes of direction $-k_{\text{eff}}$. The right-hand side of the figure displays the evolution of the contrast (b), the signal-to-noise ratio (SNR) (c) and the phase noise (d) with the interrogation time, for a time-of-flight $TOF = 16$ ms.

As stated in 3.1.2, the laser phase imprinted onto the atoms by the phase-continuous frequency jumps meant to compensate for the Doppler frequency shift is equal to $\phi_{\text{cont}} = k_{\text{eff}} a_0 T_{\text{eff}}^2$ with a_0 the setpoint acceleration. By scanning this parameter and thus the corresponding frequency and phase setpoints sent to the direct-digital-synthesizer

(DDS) controlling the Raman laser, it is possible to scan the interferometric fringes and display the sinusoidal evolution of the population ratio $P_2 = N_2/N_{\text{tot}}$. Here, we choose to display the full data set corresponding to the atomic fringes and not to use the mid-fringe lock algorithm in order to retrieve the fitted contrast and signal-to-noise ratio which serve to estimate the sensitivity of the instrument (see figure 3.5). The physical quantity g appearing on the abscissa of figure 3.8 (a) comes from an independent measurement of the local gravity $g \approx 9.805642$ m/s^2 [Ménoret et al. 2018]. For these measurements, since the vibrations are compensated for by the high-pass filtered output of the mechanical accelerometer as described by equation 3.3, the interferometric phase shift is equal to $\Phi = k_{\text{eff}}(a_0 - g)T_{\text{eff}}^2$.

The contrast, signal-to-noise ratio (SNR) and phase noise resulting from the fringes' fit estimations are given in figure 3.8 (b), (c) and (d) respectively. The SNR is calculated as $SNR = C/\sigma_\phi$ with C the contrast of the interference pattern and σ_ϕ the standard deviation of the fit estimation's residuals $r_i = P_i - \widetilde{P_i}$. At a typical interrogation time of $T = 20$ ms, we find mean values of $C = 0.47$ and $SNR = 47$ and a phase noise equal to $\sigma_\phi = 59$ mrad/shot.

Gravity tracking for long-term stability evaluation

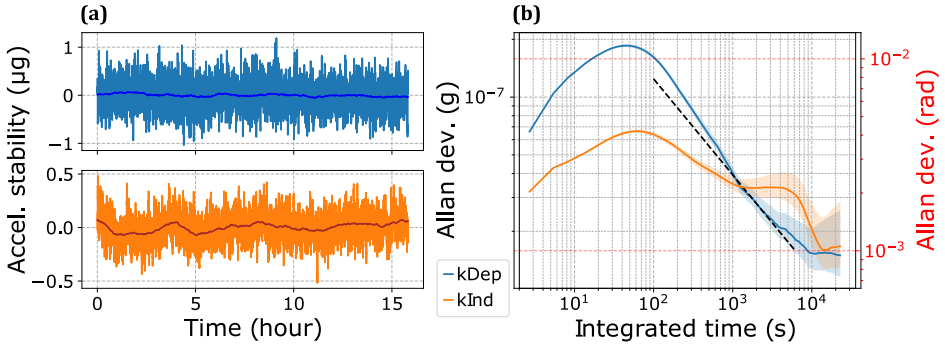

Figure 3.9: (a) Time series and (b) Allan deviation of (blue) the true acceleration experienced by the atoms and (orange) the systematic shifts rejected through the momentum recoil reversing technique, taken from [Templier 2021]. The blue curves denote the true acceleration experienced by the atoms while the orange one is not a proper acceleration measurement, it rather provides information on the stability of the rejected systematic phase shifts. These measurements correspond to a 15 hours-long tracking run and were performed at an interrogation time $T = 20$ ms with the tides removed from the dependent acceleration. Solid lines on the time series display a one hour moving average, while the dashed line on the Allan deviation exhibit a $1/\sqrt{t}$ time integration of uncorrelated measurements.

The long-term stability of the acceleration measurement along the vertical axis can be obtained by tracking the central interferometric fringe with the mid-fringe lock algorithm. The sign of the effective wave vector is reversed so that two interferometric

paths are alternatively followed, namely $a_\uparrow$ and $a_\downarrow$. This operation gives access to two quantities: the "dependent" acceleration $a_{\text{dep}} = (a_\uparrow + a_\downarrow)/2$ corresponds to the true acceleration experienced by the atoms where some systematic phase shifts dependent on the momentum recoil direction are rejected, including the one-photon light shift or part of the quadratic Zeeman shift. The second parameter is the k-independent measurement $a_{\text{ind}} = (a_\uparrow - a_\downarrow)/2$ which provides information about the stability of the systematic effects rejected by the reversing of the effective wave vector's direction, but is not a proper acceleration measurement.

The time evolution and integration of these two quantities are presented in figure 3.9 for a 15 hours-long recording of interferometers performed at $T = 20$ ms. The bump located at 50 ms on the Allan deviation plot corresponds to oscillations of the mid-fringe lock due to the integrator time constant, averaged at longer integration times. Looking at the blue curve representing the k_{dep} measurement (which contains the acceleration information), it integrates as $1/t$ between 10^2 and 10^3 s, which reflects an integration of the classical sensor's noise integration and yields an acceleration sensitivity of $\sigma_a \approx 1.5\mu\text{g}/\sqrt{\text{Hz}}$. The $1/\sqrt{\text{t}}$ fit of the measurements above 10^3 s and represented by the black dashed line yields a sensitivity of $\sigma_a = 1.24\mu\text{g}/\sqrt{\text{Hz}}$, equivalent to a phase sensitivity of $\sigma_\phi = 68$ mrad/shot for a cycling time $T_c \approx 1.6$ s. The acceleration stabilizes at the level of 10 ng after 5h30 of integration.

Absolute accuracy of the sensor

After the shot sensitivity and long-term stability of the measurement have been evaluated, we still need to determine the accuracy of the sensor. Indeed, the quantum gravimeter could provide a measurement of the vertical acceleration both very sensitive and stable but at the same time far from the actual physical quantity. To estimate this feature, the various systematic phase shifts related to the laser, magnetic field or environment must be rigorously quantified.

First, the frequency of the hyperfine transition is sensitive to the magnetic field through the second order Zeeman frequency shift $\omega_B(z) = 2\pi K|B(z)|^2$ with $K = 575.15$ Hz/G^2 the clock transition Zeeman shift and $B(z)$ the magnetic field at position z. Nevertheless, reversing the recoil direction allows rejecting most of this effect and the resulting phase shift for $T = 20$ ms and $TOF = 15$ ms, computed using the sensitivity function of the interferometer correlated with measurements of the magnetic field, amounts to $\phi_B = (5.3 \pm 0.7)$ ng.

Fluctuations in the light polarization also affect the stability of the measurement as it can lead to variations in the efficiency of the residual co-propagating transition,

variations in the Rabi frequency of the velocity-sensitive transitions as well as one- or two-photon light shifts for instance. The polarization control of this experiment is ensured by liquid-crystal retardance waveplates (LCR) which are externally temperature-controlled to increase their outputs' stability. In order to evaluate the phase shift associated with the polarization stability, a monitoring photodiode sensitive to the polarization was calibrated to measure the difference of the polarization between the first and last pulse of the interferometer. Correlating the stability of the co-propagating Raman transitions over time and its impact on the phase shift yielded a phase shift peaking at 0.5 mrad. While this can have a strong impact at low interrogation times, it amounts to 8 ng at $T = 20$ ms. Additionally, a temperature control of the LCR was implemented after this characterization, reducing the polarization fluctuations observed then. Similarly, reversing the momentum kick in addition to adapting the Raman detuning enables us to neglect the AC stark shift. As for the two-photon light shift, modulating the laser power and comparing the phase shift associated with two distinct intensities efficiently reduces its significance on the interferometer. The residual systematic effect was estimated at $\phi_{\mathrm{TPLS}} = 80$ ng at $TOF = 15$ ms.

Additionally, an error can arise from a difference of scale factors associated with the phase terms involving an acceleration measurement. As it was seen in chapter 1, the most general expression of the atom interferometer's scale factor $\mathcal{S}_{\mathrm{kin}}$ considering non-homogeneous Rabi frequencies is given by:

$$\frac{\mathcal{S}_{\mathrm{kin}}}{k_{\mathrm{eff}}} = (T + 2\tau)\left[T + \frac{1}{\Omega_{\mathrm{eff}}^{(1)}}\tan\left(\frac{\Omega_{\mathrm{eff}}^{(1)}\tau}{2}\right) + \frac{1}{\Omega_{\mathrm{eff}}^{(3)}}\tan\left(\frac{\Omega_{\mathrm{eff}}^{(3)}\tau}{2}\right)\right] \tag{3.19}$$

with $\Omega_{\mathrm{eff}}^{(i)}$ the effective Rabi frequency at the i^{th} pulse and $\tau = \tau_\pi/2$ the $\pi/2$-pulse duration. Coming back to the Doppler compensation schemes, a linearly chirped laser with inhomogeneous Rabi frequencies leads to [Templier 2021]:

$$\begin{aligned}\phi_{\mathrm{chirp}} =& \omega_1\left[\frac{1}{\Omega_3}\tan\left(\frac{\Omega_3\tau}{2}\right) - \frac{1}{\Omega_1}\tan\left(\frac{\Omega_1\tau}{2}\right)\right] \\ &+ \alpha(T + 2\tau)\left[T + \frac{1}{\Omega_1}\tan\left(\frac{\Omega_1\tau}{2}\right) + \frac{1}{\Omega_3}\tan\left(\frac{\Omega_3\tau}{2}\right)\right. \\ &\left.+\tau\left(\frac{\cot(\Omega_1\tau)}{\Omega_1} - 2\frac{\cot(\Omega_2\tau)}{\Omega_2} + \frac{\cot(\Omega_3\tau)}{\Omega_3}\right) - \left(\frac{1}{\Omega_1^2} - \frac{2}{\Omega_2^2} + \frac{1}{\Omega_3^2}\right)\right]\end{aligned} \tag{3.20}$$

using equation 1.48 with ω_1 the frequency of the Raman laser at the instant of the first pulse. One can notice that in the case of a perfectly compensated Doppler frequency shift, the kinetic (or inertial) phase and the laser phase cancel out $\phi_{\mathrm{kin}} + \phi_{\mathrm{chirp}} = 0$. Now in the case of phase-continuous frequency jumps, inhomogeneous Rabi frequencies

throughout the interferometer yield a more complex expression of the phase imprinted onto the atoms:

$$\begin{aligned}\phi_{\text{cont}} =&\omega_1 \left[\frac{1}{\Omega_3}\tan\left(\frac{\Omega_3\tau}{2}\right) - \frac{1}{\Omega_1}\tan\left(\frac{\Omega_1\tau}{2}\right)\right] \\ &+ k_{\text{eff}} a_0 (T+2\tau)\left[T + \frac{2}{\Omega_3}\tan\left(\frac{\Omega_3\tau}{2}\right)\right]\end{aligned} \tag{3.21}$$

which, as can be noticed, differs from the terms obtained for the inertial phase ϕ_{kin} and the phase ϕ_{chirp} arising from a linear chirp α. Now, even for a compensated Doppler frequency shift, the two phase terms ϕ_{kin} and ϕ_{cont} will not cancel out anymore - which is not the case for a linear chirp with homogeneous Rabi frequencies - and the difference in their associated scale factors gives rise to a systematic error. This phase shift is associated with the following scale factor:

$$\frac{\mathcal{S}_{\text{cont}}}{k_{\text{eff}}} = (T+2\tau)\left[T + \frac{2}{\Omega_{\text{eff}}^{(3)}}\tan\left(\frac{\Omega_{\text{eff}}^{(3)}\tau}{2}\right)\right] \tag{3.22}$$

which will lead to a scale factor error $\delta\mathcal{S} = \mathcal{S}_{\text{cont}} - \mathcal{S}_{\text{kin}}$ and a phase output equal to:

$$\Phi = a(\mathcal{S}_{\text{cont}} - \mathcal{S}_{\text{kin}}) = a\delta\mathcal{S} \tag{3.23}$$

where a stands for the acceleration of the atomic cloud, also chosen for the frequency jumps application. The resulting systematic phase shift then amounts to:

$$\phi_{\text{SF}} = k_{\text{eff}} a(T+2\tau)\left[\frac{1}{\Omega_{\text{eff}}^{(3)}}\tan\left(\frac{\Omega_{\text{eff}}^{(3)}\tau}{2}\right) - \frac{1}{\Omega_{\text{eff}}^{(1)}}\tan\left(\frac{\Omega_{\text{eff}}^{(1)}\tau}{2}\right)\right] \tag{3.24}$$

$$\approx k_{\text{eff}} a(T+2\tau)\left(\Omega_{\text{eff}}^{(3)} - \Omega_{\text{eff}}^{(1)}\right)\left(\frac{\pi}{2} - 1\right)\left(\frac{2\tau}{\pi}\right)^2 \tag{3.25}$$

at the first order. This term depending on the effective Rabi frequencies, it can be rejected using the same power correction method as for the two-photon light shift.

Other effects also take part in the output phase shift but can be considered negligible to a certain extent. Regarding the experimental apparatus, the misalignment between the incident and reflected beams was estimated to produce a -500 ng shift uncertainty for a 1 mrad relative angle. This effect will be discussed in detail in section 3.2, but can be neglected as long as the back coupling of the laser power in the optical fiber is ensured.

As for the Mach-Zehnder interferometer's geometry, an asymmetry in terms of frequency detuning or Raman pulse efficiency can lead to an additional phase shift

[Gillot et al. 2016]:

$$\phi_{\mathrm{MZA}} = \frac{1}{C}\int G(v)C(v)\Delta\Phi_{\mathrm{MZA}}(v)dv \tag{3.26}$$

with $G(v)$ the Gaussian velocity distribution of the atomic cloud, $C(v)$ and $\Delta\Phi_{\mathrm{MZA}}(v)$ the velocity-dependent contrast and output phase shift of the interferometer. The expressions of the two latter for upwards or downwards momentum recoil are given in [Gillot et al. 2016]. The full calculation, available in [Templier 2021], yielded a phase shift of $\phi_{\mathrm{MZA}} = (22 \pm 2)$ ng at $T = 20$ ms.

Eventually, for a Gaussian beam of curvature R, the phase shift related to wavefront distortions is given by [Schkolnik et al. 2015]:

$$\phi_{\mathrm{WD}} = k_{\mathrm{eff}}\frac{(\sigma_v T)^2}{R} \approx (6 \pm 1) \text{ ng} \tag{3.27}$$

for $T = 20$ ms. The contributions of the window, quarter-waveplate and mirror crossed by the Raman beam should in principle be considered as well, but their individual characterizations being delicate (especially for the window which is sealed), they remain to be done and we cannot provide an estimation of the produced systematic phase shift nor its uncertainty at the moment.

On another note, environmental factors independent from the apparatus are also involved in the measurement's overall accuracy. For instance, the gravity gradient being a non-constant acceleration, it can also affect the atomic path and its expression is given by [Dubetsky 2019]:

$$\phi_\Gamma = \pm k_{\mathrm{eff}}\Gamma_{zz}\left(vT + \frac{7}{12}gT^2\right)T^2 \tag{3.28}$$

with v the initial velocity of the atoms and Γ_{zz} the vertical component of the gravity gradient tensor. In our conditions, this shift equals $\phi_\Gamma \approx 100$ µrad ≈ 1.6 ng at $T = 20$ ms, which is negligible. Alternatively, the Earth rotation will induce a Coriolis acceleration measured by the quantum gravimeter and also dependent on the momentum kick direction according to [Lan et al. 2012]:

$$\phi^{\oplus}_{\mathrm{Cor}} = \mp 2\left[\boldsymbol{k_{\mathrm{eff}}} \times (\boldsymbol{v_0} + \boldsymbol{a}T)\right].\boldsymbol{\Omega}_{\oplus}T^2 \tag{3.29}$$

with $\boldsymbol{\Omega}_{\oplus}$ the Earth's rotation rate. For a vertical-only acceleration due to gravity, there are no components transverse to the laser's effective wave vector, thus the resulting phase shift was estimated to $\phi^{\oplus}_{\mathrm{Cor}} = 0 \pm 315$ ng with an uncertainty mostly related to the uncertainty on the Raman laser's tilt angle.

Ultimately, the table from [Templier 2021] summarizing the investigated systematic

Systematic effect	**Bias shift (ng)**	**Uncertainty (ng)**
Two-photon light shift	+81	10.2
Quadratic Zeeman shift	+5.3	0.7
Scale factor error	-130	50
Parasitic laser lines	+195	5
RF non-linearity	+170.9	0.2
Mach-Zehnder asymmetry	+22	2
Gravity gradient	+1.6	4×10^{-3}
Coriolis acceleration	0	315
Beams misalignments	-	500
Wavefront distortion	+6	-
Total	**+351.8**	**$\geqslant$883.1**

Table 3.1: Summary of the systematic phase shifts measured at the output of the vertical atom interferometer with an interrogation time of $T = 20$ ms.

phase shifts and associated uncertainties for an atomic gravimeter operating at $T = 20$ ms and $TOF = 15$ ms is reported in 3.1. These acceleration biases estimations are made considering the momentum recoil alternation and the power modulation rejecting most of the two-photon light shift and scale factor error. The total bias shift of the acceleration measurement with this atom interferometer-based quantum gravimeter finally amounts to approximately 351.8 ± 883.1 ng, though the partial characterization of the wavefront distortion prevents us to reach the total uncertainty on the systematic phase shifts.

If the uncertainty on the systematic shift remains fairly high, as 1 µg is above the tides amplitude, the short- and long-term performances are still in agreement with our expectations. Indeed, some groups such as the SYRTE laboratory reached impressive sensitivity and stability, respectively 6 ng/$\sqrt{\text{Hz}}$ and 2 ng [Le Gouët et al. 2008; Louchet-Chauvet et al. 2011], on an apparatus dedicated to measuring gravity in a quiet environment with interrogation times above 100 ms. Our instrument is aimed for robust measurements of acceleration components in an arbitrary orientation and in strapdown configuration, i.e. without any gyro-stabilized or active vibrations cancellation platform. Thus, limiting the interrogation time to 20 ms restrains the utmost performances we can reach but also our sensitivity to vibration-induced phase noise, the latter increasing dramatically with the interrogation time. With these considerations in mind, we reached the targeted performances of a sensitivity below 2 µg/$\sqrt{\text{Hz}}$ and a long-term stability at the 10 ng level, only the accuracy remains to be reduced by an order of magnitude to remain below a satisfying 100 ng level.

3.2 Acceleration vector reconstruction through multi-axis atom interferometry with partial hybridization

In the previous section, the Mach-Zehnder atom interferometer implemented on our apparatus has been demonstrated to measure the gravitational acceleration with a $1.24\mu g/\sqrt{Hz}$ sensitivity and a bias stability reaching the 10 ng level after 5h30 of integration for a $T = 20$ ms interrogation time with a Raman laser beam aligned with the gravity vector. Although this technology has been demonstrated multiple times including on-field measurements, it is highly sensitive to the orientation of the laser beam with respect to the gravity vector. Additionally, such apparatus only provides information on the projection of the acceleration along a given direction and is thus not suitable to onboard or mobile operation where the full acceleration vector must be recovered.

3.2.1 Operation of a tilted sequential multi-axis atom interferometer

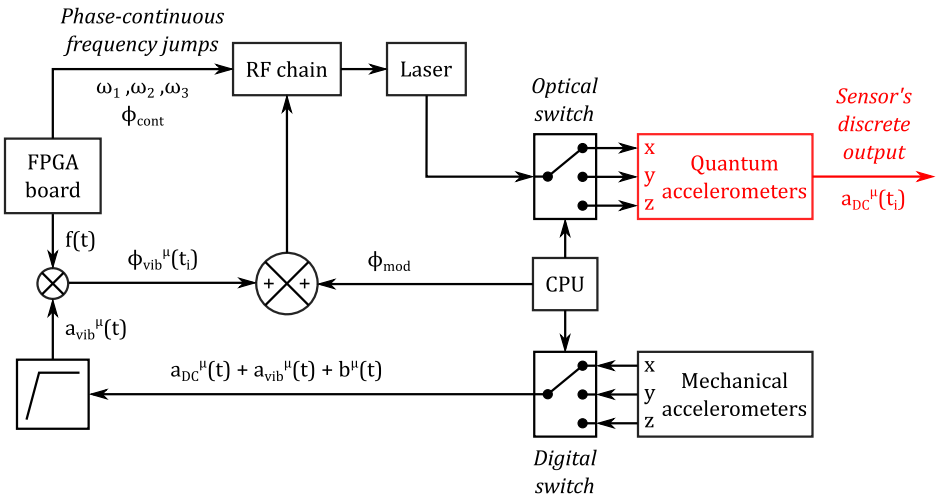

Figure 3.10: Open-loop operation of the sequential three-axis quantum accelerometer, where the discrete measurement of the atom interferometer along a given axis is used as the sensor's output signal. The superscript μ visible on the acceleration components and the vibrations phase designates the selected measurement axis x, y or z.

The design presented in the previous subsection and demonstrated in the case of a gravimeter operating in vertical was duplicated along two additional measurement axes, including the Raman laser beams retroreflected by a reference mirror and the mechanical accelerometers attached at the back of each mirror. Identically, the output

of these classical sensors are high-pass filtered to conserve only the high-frequency vibrations, before being correlated with the response function of the atom interferometer (referred to as open-loop hybridization scheme). Figure 3.10 summarizes the open-loop operating scheme of the three-axis atomic accelerometer. Regarding the technical implementation alone, the only difference lies in the axis selection. The CPU sends a command signal to the real-time system in order to select the mechanical accelerometer used for the compensation of vibrations, one classical sensor being attached to each axis' reference mirror. Likewise, the optical switch used to select the Raman axis on which the interferometer will be performed is controlled by the CPU. Thus, the acceleration can be measured sequentially on each of the three orthogonal axes of the quantum triad.

Nevertheless, the development of a multi-axis atom interferometer enabling the tracking of the acceleration vector in any arbitrary orientation comprises physical considerations beyond the sole technical implementation. For instance, the atomic source preparation and measurement sequence are not necessarily optimized using the same parameters as before - including the steps durations, laser frequency or power -, in particular regarding the co-propagating transitions used for the state preparation and which are dependent on the position of the cloud relative to the reference mirror of the considered measurement axis. After reviewing the performances of each axis, with particular effects induced by the beams' inclination, the whole quantum accelerometers triad is characterized so as to qualify the total acceleration norm's measurement.

The quantum gravimeter described in the previous section made use of the velocity gained by the atoms during the time-of-flight to separate the achievable velocity-sensitive Raman transitions $\boldsymbol{k}_{\uparrow}$ and $\boldsymbol{k}_{\downarrow}$ in frequency and select one of them. However, this technique cannot be used in the case of a horizontal Raman laser, where the atoms would not gain any velocity on the measurement axis. In this situation, other methods have proven efficient like the double-diffraction regime [Lévèque et al. 2009], particularly adapted to interferometry in the horizontal plane or in micro-gravity for instance. Nevertheless, in order to have a comparable operating scheme for the gravimeter and the accelerometer, the sensor head is tilted so that no axis is either vertical or horizontal, and each of them benefits from the Doppler effect induced by the projection of the gravity. Since the free-falling atoms still follow the gravity vector, the limited transverse size of the Raman beams only allows for a total drop time of ≈ 50 ms. Considering the time-of-flight preceding the interferometer, the interrogation time is thus reduced to $T = 10$ ms.

In order to tilt the interrogation axes, the sensor head is placed on the rotary

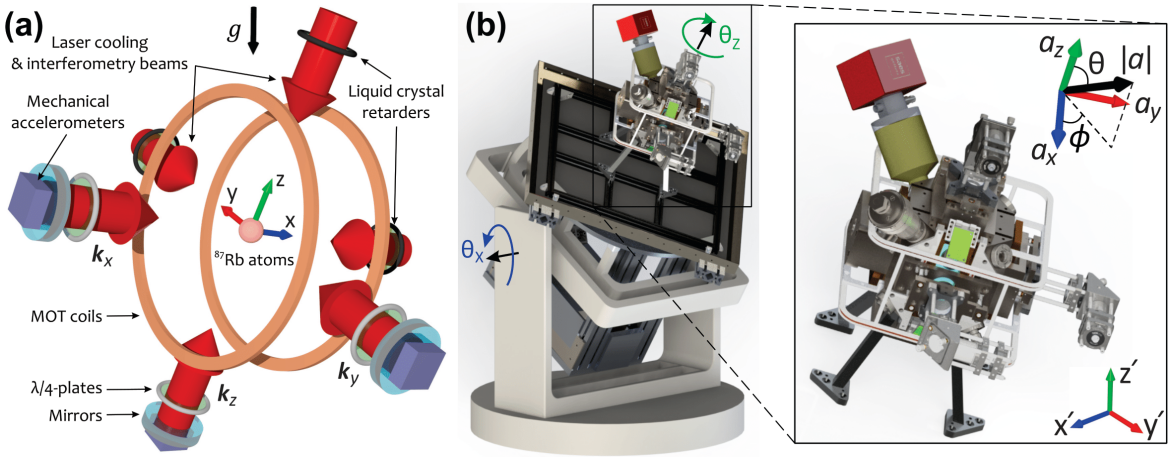

Figure 3.11: (a) Design concept of the quantum accelerometers' triad, measuring the acceleration components along the three orthogonal axes x, y and z. (b) 3D model of the sensor head mounted on the rotary platform, exhibiting the two rotation angles θ_z and θ_x which, applied in this order, transform the coordinates from the laboratory frame (x', y', z') to the body frame (x, y, z).

platform introduced in chapter 2. This platform can be rotated along two axes z and x' by angles θ_z and θ_x respectively as displayed in figure 3.11. The angle θ_z varies from $-180°$ to $+180°$ in steps of $15°$ while θ_x can take any value between $-90°$ and $+90°$. The rotation of the platform along these axes corresponds to the successive applications of two rotation matrices $\mathcal{R}_z(\theta_z)$ and $\mathcal{R}_x(\theta_x)$leading to the following transformation of the gravitational acceleration vector:

$$\boldsymbol{a} = \begin{pmatrix} a_x \\ a_y \\ a_z \end{pmatrix} = \mathcal{R}_z(\theta_z).\mathcal{R}_x(\theta_x).\begin{pmatrix} 0 \\ 0 \\ -g \end{pmatrix} = g\begin{pmatrix} \sin(\theta_x)\sin(\theta_z) \\ \sin(\theta_x)\cos(\theta_z) \\ -\cos(\theta_x) \end{pmatrix}. \tag{3.30}$$

In order to reach balanced acceleration projections $a_x \simeq a_y \simeq a_z \simeq g/\sqrt{3}$, we must set the tilts $\theta_x = 54.7°$ and $\theta_z = 45°$.

Except for the sequential switch of the interrogation axis and the tilt of the Raman beams relative to the gravity vector, the measurement sequence remains mostly unchanged. Magnetic coils in Helmholtz configuration are installed along the three measurement axes and are now driven with a $\simeq 145$ mG magnetic field in order to both lift the degeneracy between the Zeeman sub-levels and define the quantization axis along which the Raman transitions will be performed. Besides the magnetic field intensity, the state preparation is performed with the same settings used on the single-axis quantum gravimeter. Ultimately, Raman spectroscopy with velocity-sensitive counter-propagating transitions after the cooling stage is employed here as well to estimate the temperature of the atomic cloud along each direction. The latest

temperatures measured in this configuration, prior to the replacement of the fibered optical switch, amounted to ≈ 2 µK on each axis at $\theta_x = 42°$ and $\theta_z = 45°$. These data are relatively outdated, which explains the temperatures marginally lower than the one presented in the previous section for the quantum gravimeter, but are given here as they will be useful for the results showed further on.

3.2.2 Performance of the multi-axis quantum accelerometer

Sensitivity to the acceleration components

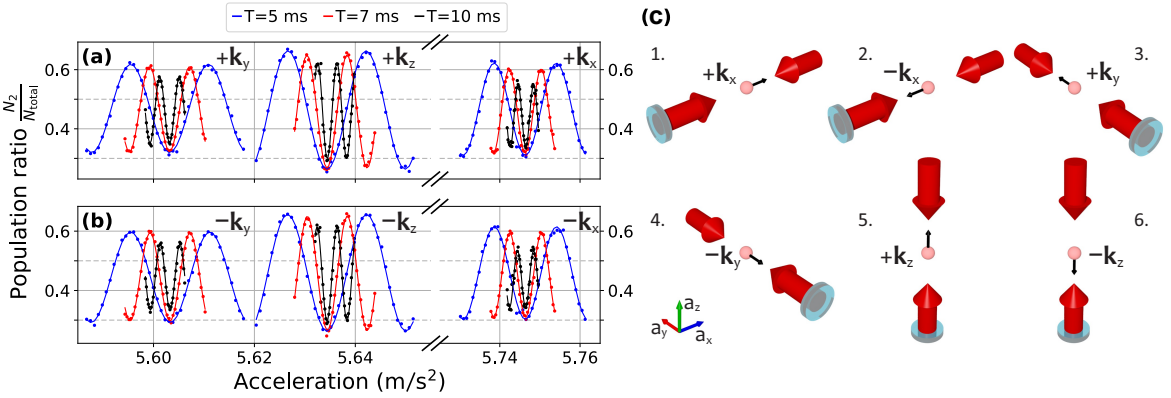

Figure 3.12: Atomic interference fringes obtained on axes y (left), z (middle) and x (right) as a function of the laser-induced acceleration a^μ through the phase-continuous frequency jumps, for a momentum transfer along (a) $+k^\mu_{\text{eff}}$ and (b) $-k^\mu_{\text{eff}}$, $\mu = x, y, z$ designating the measurement axis. Fringes are displayed for interrogation times $T = 5$ ms (blue), $T = 7$ ms (red) and $T = 10$ ms (black) at tilt angles of $\theta_x = 54.7°$ and $\theta_z = -45°$. (c) Description of the measurement sequence alternating between each axis with momentum recoil reversing.

In the same manner as the acceleration sensitivity of the quantum gravimeter was investigated in the previous section, interferometric fringes are scanned through the phase-continuous frequency jumps serving to compensate for the Doppler frequency shift on each of the three measurement axes. The interferometric fringes obtained for interrogation times of 5, 7 and 10 ms along the three measurement axes $\mu = x, y, z$ are exhibited in figure 3.12 (a) for a momentum transfer along $k_\uparrow = +k^\mu_{\text{eff}}$ and in figure 3.12 (b) for a momentum transfer along $k_\downarrow = -k^\mu_{\text{eff}}$. The operating scheme, in which the mechanical accelerometers attached to the reference mirrors are correlated with the atom interferometer's response function to compensate for the vibrations, is depicted in figure 3.10. The sequence describing the measurement along each direction μ with momentum kick reversing is illustrated in figure 3.12 (c). The output phase of the interferometer in this configuration μ is given by the expression:

$$\Phi = \phi_{\text{kin}} + \phi_{\text{las}} \tag{3.31}$$

with $\phi_{\text{kin}} = \pm k_{\text{eff}}(a^{\mu}_{\text{DC}} + a^{\mu}_{\text{vib}})T^2_{\text{eff}}$ the inertial phase shift, related to the motion of the atomic cloud with respect to the reference mirror of the considered axis, and $\phi_{\text{las}} = \phi^{\text{cor}}_{\text{vib}} + \phi_{\text{cont}}$ is the laser phase imprinted onto the atoms. The sign of each term depends on the momentum recoil direction $\pm k^{\mu}_{\text{eff}}$. The superscript *cor* on the vibration term of the laser phase denotes a correction arising from the open-loop hybridization, distinguished from the inertial effect due to the mirror's vibrations in the kinetic phase ϕ_{kin}. The term ϕ_{cont} stands for the phase introduced by the phase-continuous frequency jumps used for Doppler effect correction as described in section 3.1.

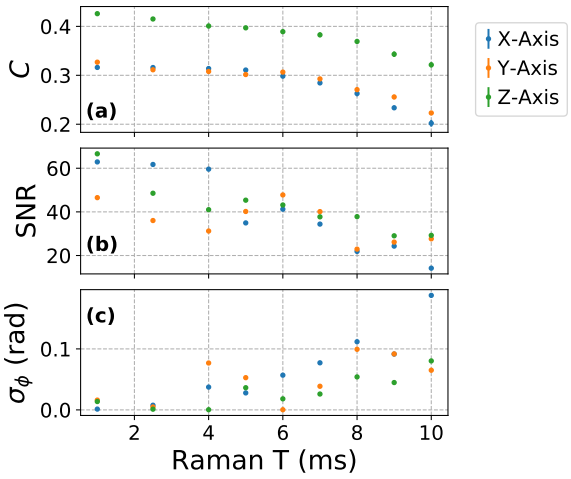

Figure 3.13: Evolution of (a) the contrast, (b) the SNR and (c) the phase noise of the interferometric fringes as a function of the interrogation time. These plots, taken from [Templier 2021], were obtained from the sine-fitting of the fringes and display the mean value of the estimations for $k_{\uparrow}$ and $k_{\downarrow}$ momentum transfers.

The analysis of the atomic fringes is reported in figure 3.13. Regarding the contrast, it is consistently higher on the z axis which can be explained by the fact that this axis was used for the demonstration of the quantum gravimeter, and some experimental parameters were just carried forward on the two other axes without particular optimization. Additionally, the competition between the pairs of co-propagating Raman transitions used for the state preparation depends on the position of the atomic cloud relative to the mirror. Therefore, every change in the sensor head's orientation may lead to a different relative position at the instant of the state preparation and induce a deterioration of the latter's efficiency.

As for the sensitivity on the measurement of the acceleration, it is evaluated at $\sigma^x_a = 11.9$ µg/shot, $\sigma^y_a = 4.1$ µg/shot and $\sigma^z_a = 5.1$ µg/shot for an interrogation time of $T = 10$ ms. The inferior performance on the x axis is likely to be related to the mechanical accelerometer or its electric line, delivering a noisier signal which can result in a degraded correlation for compensating the vibrations of the mirror.

Long-term stability of the acceleration's norm measurement

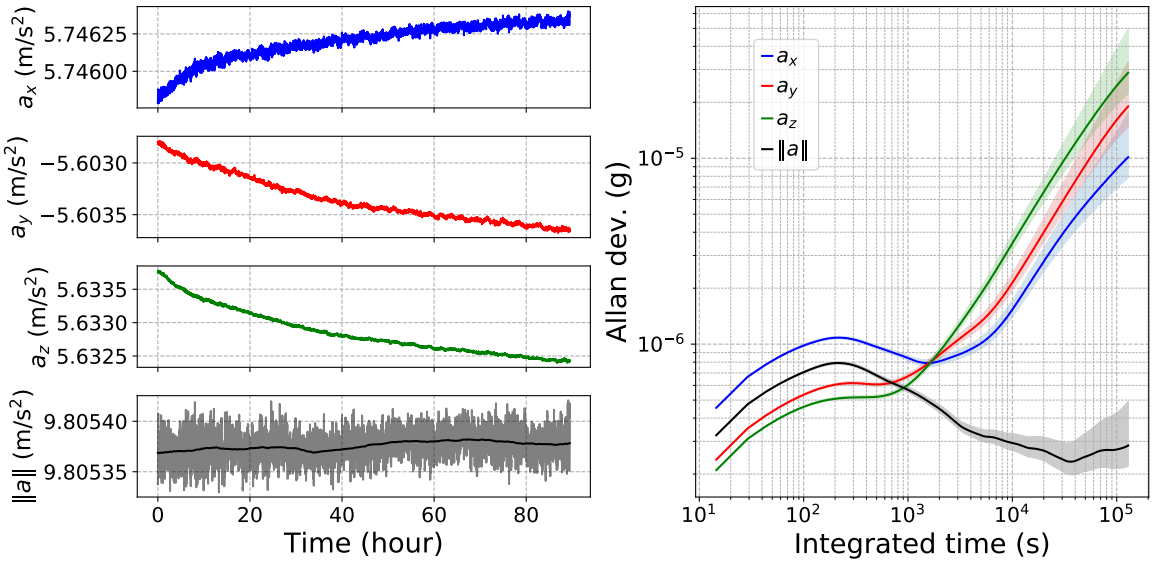

Figure 3.14: Time-series of the acceleration components on the x (blue), y (red) and z (green) axes as well as their norm (black) over 90 hours are displayed on the left. The right-hand plot displays the Allan deviation of these measurements, demonstrating the device's long-term stability.

Using the mid-fringe lock algorithm to track the acceleration components on each axis, the long-term stability of the three-axis quantum accelerometer triad was characterized during a 90 hours-long run at an interrogation time $T = 10$ ms with tilt angles $\theta_x = 54.7°$ and $\theta_z = -45°$. The norm of the acceleration vector $\|\boldsymbol{a}\| = \sqrt{a_x^2 + a_y^2 + a_z^2}$ is computed as well, and its time-series and Allan deviation are presented along those of the acceleration components in figure 3.14. The evolution of the individual components is due to a slow drift of the platform's tilt angle θ_x evaluated around 10 µrad over 30 hours. Nevertheless, this shift being equally applied on all the acceleration projections, it does not influence the acceleration vector's norm reaching a 200 ng stability level after 9 hours of integration.

Accuracy of the acceleration components' measurements

The systematic phase shifts degrading the accuracy of the acceleration components' measurements, and thus its norm, are mostly coming from the same sources as the ones presented for the quantum gravimeter. However, some of them will be even worsened in the particular case of a tilted Raman beam and need to be further elaborated.

The major change in the operation of an atom interferometer with an inclined Raman laser is the increased Rabi frequency inhomogeneity. Indeed, the atoms free-falling under the gravitational force will have a transverse motion in the Gaussian-shaped light field, and will thus scan its intensity profile as exhibited in figure 3.15. The position of

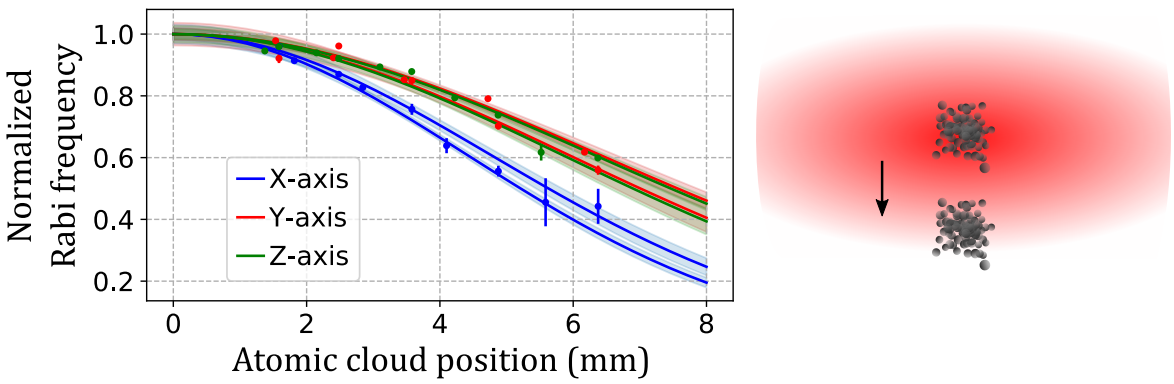

Figure 3.15: Evolution of the Rabi frequency along each axis x, y and z with the atomic cloud position, scanned through the value of the time-of-flight. This figure, taken from [Templier 2021], is based on the assumption of a Gaussian-shaped atomic ensemble centered inside the optical molasses. Two sets of data were recorded with tilt angles of $\theta_x = 54.7°$ and $\theta_z = -45°$ for the first one, and $\theta_x = 45°$ and $\theta_z = -30°$ for the second one.

the atomic cloud relative to the Raman laser in the laboratory frame is transformed to the mobile frame by applying the rotation matrix $\mathcal{R}_z(\theta_z).\mathcal{R}_x(\theta_x)$ to reach a radial position from the center of the beam. The differences observed in the two sets of data may come from a non-centered atomic cloud inside the optical molasses. These inhomogeneities, described in equation 3.19, will give rise to a systematic shift in the interferometric phase, in addition to altering the Raman pulses' efficiency throughout the interferometer which may yield a decreased fringes' visibility.

Systematic effect (µg)	x**-axis bias**	y**-axis bias**	z**-axis bias**	**Norm bias**
Scale factor error	58.9 (6.4)	-31.3 (1.6)	30.3 (0.9)	73.3 (6.6)
TPLS	3.762 (0.006)	-3.091 (0.005)	3.26 (0.030)	5.861 (0.009)
MZ Asymmetry	1.064 (0.027)	-0.124 (0.010)	0.345 (0.009)	1.125 (0.031)
Coriolis effect	0.65 (0.44)	-2.42 (0.37)	-1.77 (0.26)	3.07 (0.63)
RF non-linearity	0.060 (0.023)	0.057 (0.023)	0.058 (0.023)	0.101 (0.040)
Parasitic lines	-0.048 (0.040)	0.030 (0.072)	0.046 (0.005)	0.098 (0.050)
Quadratic Zeeman	0.003 (0.021)	-0.007 (0.019)	0.010 (0.022)	0.007 (0.077)
Beams misalignments	0.00 (0.500)	0.00 (0.500)	0.00 (0.500)	0.00 (0.870)
Total	64.4 (7.4)	-36.8 (2.6)	32.3 (1.7)	83.6 (8.3)

Table 3.2: Summary of the three-axis atom interferometer's systematic effects with an interrogation time of $T = 10$ ms and tilt angles of $\theta_x = 54.7°$ and $\theta_z = -45°$ applied to the sensor head. These measurements were conducted with momentum recoil direction flip to reject some systematics and are expressed in µg with the uncertainties in parentheses. The norm bias indicates the bias on the norm of the total acceleration vector.

Table 3.2 summarizes the systematic shifts on the acceleration components of each

axis as well as on the acceleration norm. These systematic effects are estimated at a $T = 10$ ms interrogation time with alternated momentum kick directions for rejection of the trajectory-independent systematic effects [Louchet-Chauvet et al. 2011]. However, the optical power modulation performed on the atomic gravimeter allowing to reject most of the two-photon light-shift and scale factor error was not executed here. The most important observation in this table is that the scale factor error due to Rabi frequency inhomogeneities is, by far, the most critical effect as it yields the highest uncertainty on the norm bias.

Ultimately, a major issue of an inertial sensing triad like an inertial measurement unit (IMU) lies in the relative misalignments of the sensing devices, here the quantum accelerometers. Indeed, the measurement axes defined by the wave-vectors $\pm\boldsymbol{k}_{\mathbf{eff}}^{\boldsymbol{x}}$, $\pm\boldsymbol{k}_{\mathbf{eff}}^{\boldsymbol{y}}$ and $\pm\boldsymbol{k}_{\mathbf{eff}}^{\boldsymbol{z}}$ normal to their respective reference mirrors can be aligned at best by construction of the sensor head but slight positioning errors can subsist. This effect yields considerable errors on the norm estimation, amounting to $\sin(\varepsilon) \approx 100$ µg for a $\varepsilon = 100$ µrad misalignment between two axes, even with accurate individual measurements.

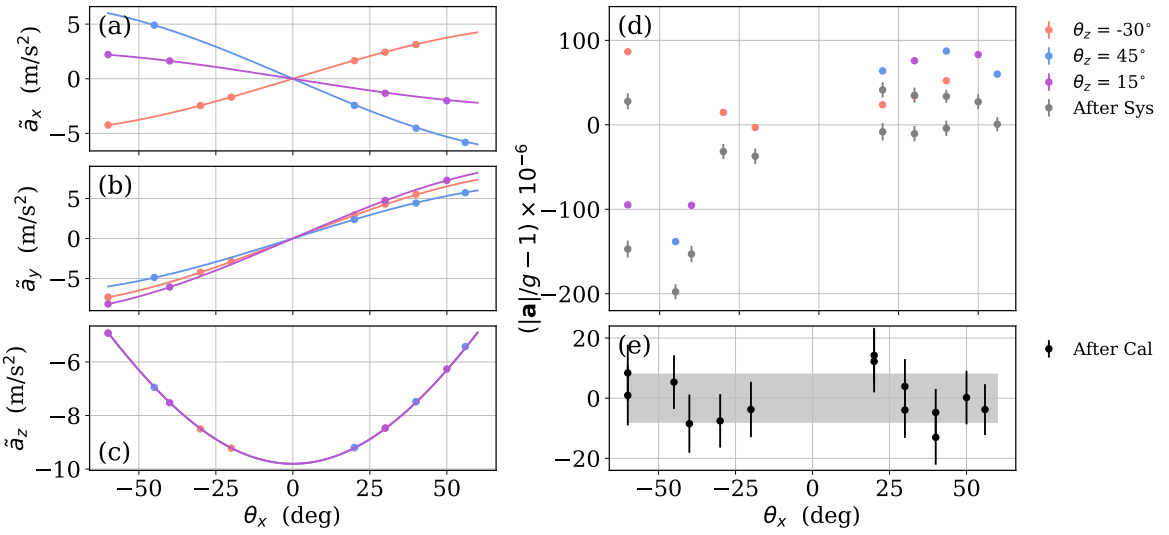

Figure 3.16: Calibration of the quantum accelerometers triad. (a to c) Acceleration components measured for each orientation defined by the couple $(\theta_x, \theta_z$, solid lines corresponding to the expected variations. (d) Error in the acceleration norm (colored) before and (gray) after the subtraction of systematic biases. (e) Zoom on the acceleration norm error after the calibration procedure, the shaded gray area indicating the remaining RMS spread of ±7.7 µg.

In order to curb the effect of the quantum accelerometers triad's misalignment, a calibration protocol developed for classical IMU [Yang et al. 2012] was implemented, the results of which are displayed in figure 3.16. It consists in the measurement of the norm of the acceleration vector in various orientations of the sensor head, each time

compared to an independent value of the local gravitational acceleration $g = 9.805642$ m/s^2. The detail of the calibration protocol can be found in [Templier et al. 2022]. As can be seen in figure 3.16 (d), the uncalibrated triad produced errors up to 140 µg in some orientations. Due to the high sensitivity of each atomic accelerometer's accuracy to the inclination of the sensor head, this calibration was conducted after the investigation of the different axes' individual systematic errors. Before the calibration procedure, the root mean squared (RMS) error in the vector norm amounted to 74 µg but, after optimization, was decreased by almost an order of magnitude down to 7.7 µg. Since the acceleration bias associated with the relative misalignments between the triad's axes is assumed to be independent from the systematic phase shifts related to each individual atomic accelerometer, the total uncertainty on the norm bias is calculated as the quadratic sum of the two latter effects. The total bias on the norm of the acceleration vector finally amounts to (83.6 ± 11.3) µg.

3.3 Fully-hybridized classical-quantum accelerometers triads

Whether for a single-axis quantum gravimeter or a multi-axis quantum accelerometer, in the absence of isolation from environmental parasitic motion, we have mentioned the need for classical sensors correlated with the atom interferometers. In particular, parasitic vibrations at an even modest level can rapidly prevent any information to be retrieved from the interferometric signal. After justifying the implemented compensation scheme, the multi-axis hybrid accelerometer benefiting from a continuous and bias-free measurement will be demonstrated in this section.

3.3.1 Measurement and compensation of the vibration-induced phase shift

As detailed in section 1.2, in the case of atom interferometers using a mirror to retroreflect the laser beam, vibrations of this mirror have a strong impact on the phase at the output of the interferometer. Indeed, this mirror serves as a phase reference for the matter-wave interferometer, such that its movements will completely blur the resulted fringes. Figure 3.17 (a) shows the typical level of vibrations measured on the z-axis reference mirror when the sensor head is installed on the rotation platform described in chapter 2, vertical and with the brake applied. Figure 3.17 (b) displays a section of this signal during the simultaneous realization of an atom interferometer with an interrogation time $T = 10$ ms and for $\tau = 3$ µs Raman pulses. The sensitivity

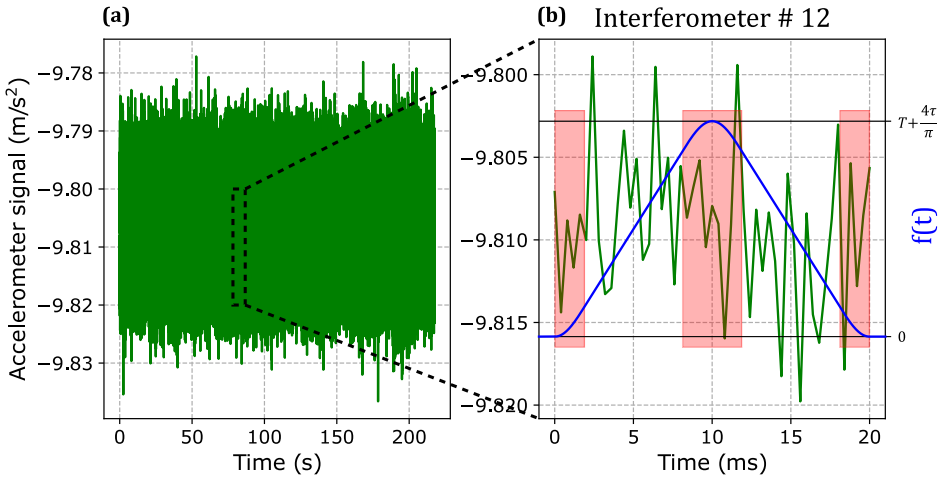

Figure 3.17: (a) Signal from the classical accelerometer mounted on the back of the reference mirror during $\simeq 3$ minutes while the sensor head is installed on the rotary platform. The accelerometer's signal is streamed at $f_{\mathrm{acq}} = f_{\mathrm{ADC}}/2 = 2.5$ kHz. (b) Zoom on a particular section corresponding to an atomic interferometry sequence realized in parallel with an interrogation time $T = 10$ ms and pulses during $\tau = 3$ μs. The green signals represent the measurement of the classical accelerometer, the blue curve stands for the response function to acceleration, and the red squares display the three Raman pulses zoomed in ten times on the horizontal axis for clarity. The difference in the amplitudes observed on the two graphs only results from the very dense signal presented on (a), which does not display the sections with lower noise but only the overall extrema.

function was superimposed on this graph to illustrate the instants where vibrations are the most critical. For this particular interferometer, writing $\boldsymbol{a_{\mathrm{vib}}}(t) = \boldsymbol{a_{\mathrm{tot}}}(t) - \boldsymbol{g}$ the vibrations of the mirror on the static apparatus with $\boldsymbol{a_{\mathrm{tot}}}(t)$ the classical accelerometer's measurement and $\boldsymbol{g}$ the local gravitational acceleration, the resulting phase shift is equal to:

$$\Phi_{\mathrm{vib}}^{=} \int_{-\infty}^{+\infty} f(t)\,[\boldsymbol{k_{\mathrm{eff}}}.\boldsymbol{a_{\mathrm{vib}}}(t)]\,dt \approx 7 \text{ rad} \tag{3.32}$$

with $\Phi_{\mathrm{tot}} \approx 15\,815$ rad the measured phase at the output of the interferometer, associated to the total acceleration $\boldsymbol{a_{\mathrm{tot}}}(t)$ and $\Phi_g \approx 15\,808$ rad the phase associated to the local gravity taking $g = 9.805642$ m/s^2 from an independent measurement. The vibration-induced phase shift being larger than $\pm\pi$ rad, the estimation of the atomic fringe corresponding to the actual useful signal is incorrect and the atomic sensor no longer enables us to accurately measure accelerations.

Different solutions exist to tackle this large scan of the atomic fringes and retrieve the inertial signal measured by a quantum accelerometer. First, these vibrations can be dampened as much as possible by placing the science chamber on neoprene pads, passive vibrations isolation platforms or even active vibrations isolation platforms [Oon and Dumke 2022] for instance. Though, this option is not ideal since most of the time, the better the isolation, the heavier and bulkier the system is. Additionally, depending

on the targeted application, suppressing vibrations in this manner can represent a loss of signal; for navigation purposes for example, the separation between vibrational noise and the useful signal is unclear, a trade-off has to be made on the cutoff frequency and this loss of correlation between the atomic accelerometer and the vehicle can transform into errors in the position or attitude of the latter.

A more favorable solution to maximize the correlations between the motion of the quantum accelerometer and its output is to measure the acceleration of the reference mirror with a high temporal resolution in order to track and correct the random phase shift added by vibrations to every point of the interferometric fringes. Indeed, the same way the scale factor of the atomic accelerometer was calculated in equation 1.45 or the typical vibration-induced phase shift was assessed in equation 3.32, it is possible to subtract the resulting phase from the measurement by correlating the measurement of the classical sensor with the matter-wave interferometer's response function. If this correction scheme can be applied after the measurement by processing the blurred atomic fringes, we chose to develop a real-time hybridization scheme based on a field-programmable gate array (FPGA) acquiring the signal from the mechanical accelerometer and integrating its measurements weighted with the response function all along the inteferometer, feeding back the total phase to the direct digital synthesizer (DDS) controlling the laser phase a few microseconds before the last pulse.

3.3.2 Real-time closed-loop hybridization principle

In the previous sections of this chapter, the open-loop operation of the quantum gravimeter and accelerometer using the high-pass filtered output of classical accelerometers to compensate for vibrations has been presented (see figures 3.5 and 3.10 respectively). In this configuration, the acceleration measurement performed by the atom interferometer is used as the device's output signal. This signal is discrete with an acquisition frequency set by the cycling rate of the experiment $T_{\mathrm{cyc}} \approx 1.6$ s, but it is also absolute and exact since the free-falling atoms represent a perfect inertial frame of reference. The only limit in this measurement's accuracy thus lies in the systematic phase shifts evaluated at the end of the two previous sections.

In order not to be limited by the cycling rate of the device, another functioning scheme referred to as "closed-loop" was conceived. Its operation is summarized in figure 3.18. Instead of high-pass filtering the mechanical accelerometers' output signals, their whole measurement spectrum is correlated with the atom interferometer's response function. Indeed, for a given axis, the true acceleration's low-frequency components as well as higher-frequency vibrations should be equally sensed by both the classical

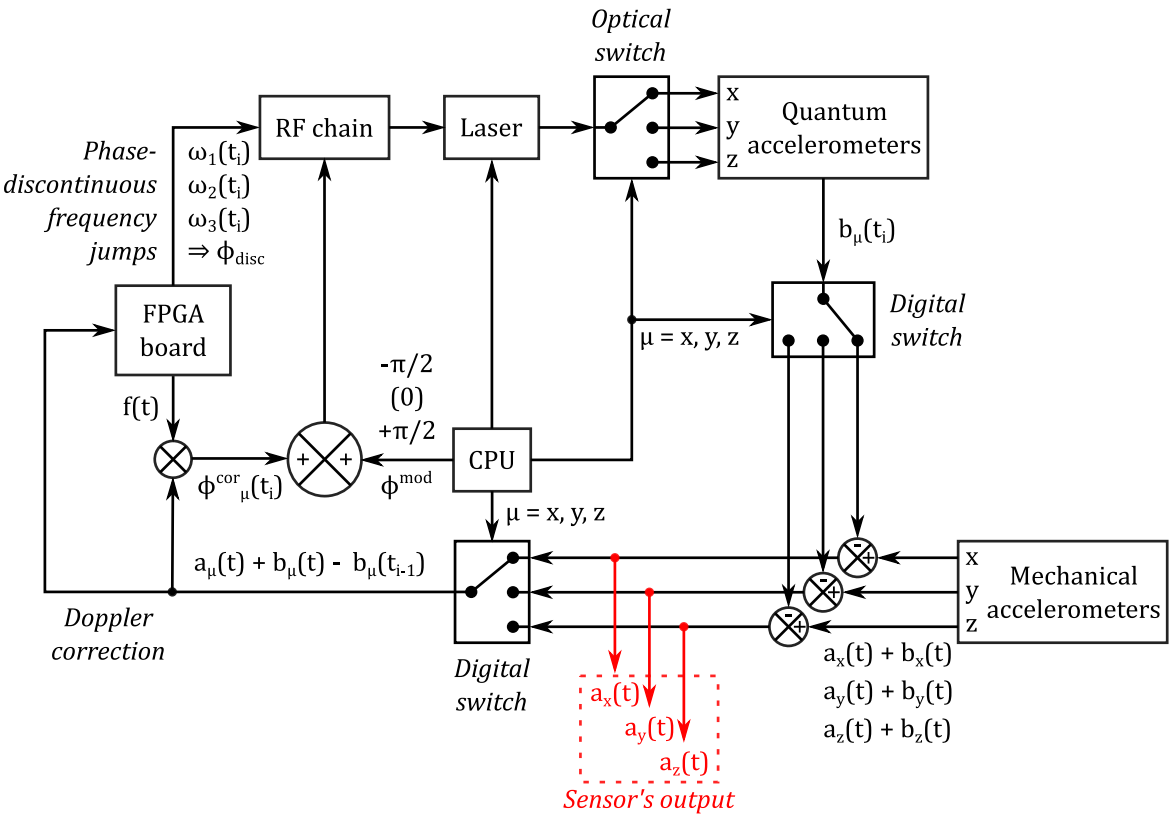

Figure 3.18: Closed-loop operation of the sequential hybrid accelerometer. The discrete measurement of the atom interferometer along a given axis is used to estimate the bias of the associated mechanical accelerometer by comparison of their respective measurements. The resulting continuous, bias-free signals of the three mechanical accelerometers are used as the hybrid sensor's output.

and quantum devices and thus they should cancel out, so much so that the only information remaining after the hybridization will be the slowly-varying bias of the classical accelerometer. This bias is then subtracted from the classical sensor's output at each measurement of the corresponding atom interferometer and, assuming this bias does not vary faster than our cycling rate, we can use the high-bandwidth, bias-corrected signals of the mechanical accelerometers' triad as our hybrid multi-axis sensor's output. Furthermore, filtering the classical measurement requires to determine the cut-off frequency based on a trade-off between what is considered useful signal and what is considered parasitic noise; in practice, this always induces a loss of information, which is undesirable in the context of an onboard inertial sensor.

Real-time Doppler compensation

As it can be noticed in figure 3.18, the signal from the classical accelerometers is now used for a real-time compensation of the Doppler frequency shift as well, so as to maintain the Raman lasers resonant with the velocity-sensitive Raman transition while the atomic cloud is gaining velocity. Indeed, this correction can be accurately

calculated for a given projection of the atoms' velocity on the laser's axis but it is no longer possible for a sensor head subject to inclination changes. For that reason, the Doppler frequency shift ω_i is computed in real time before each Raman pulse i using the measurements of the mechanical accelerometers which provide information on the tilt angle through the projections of the gravitational force.

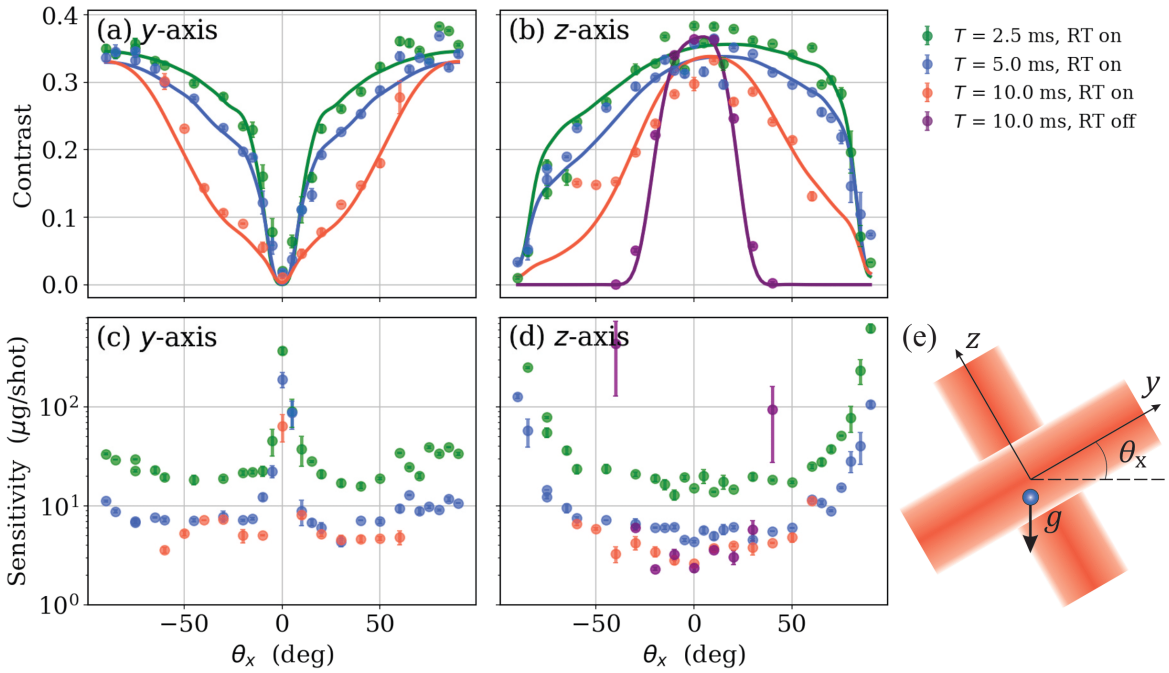

Figure 3.19: (a, b) Contrast of the interference fringes pattern and (c, d) acceleration sensitivity along the y and z axes as a function of the tilt angle θ_x for $\theta_z = 0°$. (e) Geometry of the Raman beams with respect to the atomic trajectory. Colored dots display the result of the interferometric fringes' sinusoidal fit while solid lines represent the model of the fringes contrast (see [Templier et al. 2022]).

Figure 3.19 exhibits the evolution of the contrast and acceleration sensitivity resulting from a sinusoidal fit of the atomic interference fringes. As it can be seen for large inclinations, the Doppler frequency shift limits the performances due to a lower velocity projection on the z axis and the visibility of the fringes sharply drops (purple curve). However, with the real-time compensation enabled, the Doppler effect becomes less critical to the measurement and the smoother decrease in the contrast is mostly due to the atoms falling out of the beam in addition to the Raman transitions' frequencies becoming indistinguishable, namely the residual co-propagating transition and the two counter-propagating transitions $\boldsymbol{k}_\uparrow$ and $\boldsymbol{k}_\downarrow$. Additionally, the Rabi frequencies inhomogeneities studied in the previous section also take part in this contrast limitation.

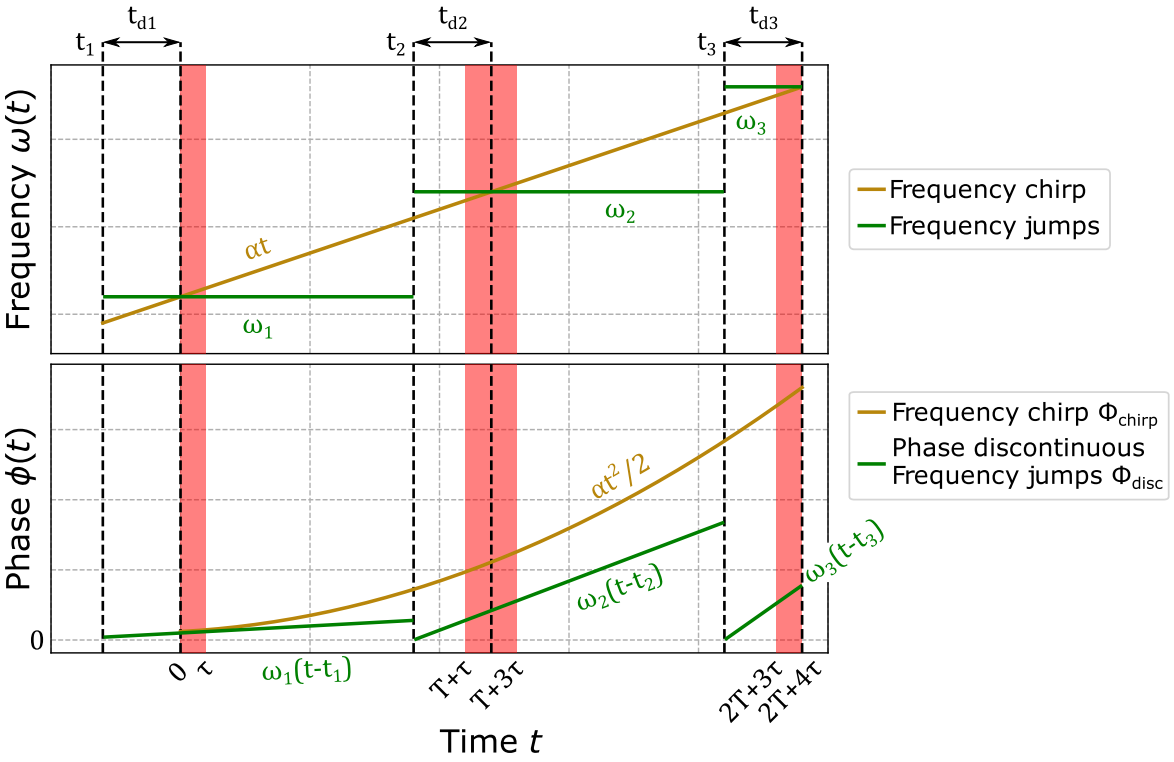

Figure 3.20: Evolution of the laser frequency $\omega(t)$ and phase $\phi(t)$ throughout the atom interferometer for Doppler frequency shift compensation schemes using a frequency chirp (brown) and phase-discontinuous frequency jumps (green). The laser phase $\phi(t)$ is imprinted onto the atomic wave packets during the Mach-Zehnder atom interferometer.

Phase-discontinuous frequency jumps

A Doppler compensation computed in real time will give different frequency jumps both throughout an interferometric sequence and from an interferometer to another, leading to varying Raman laser phases $\phi_{\text{las}}(t)$. For that reason, in order to isolate the Doppler frequency correction from the Raman laser phase, the phase-continuous frequency jumps presented in the beginning of this chapter are replaced with phase-discontinuous frequency jumps. Practically, this means that the laser phase is reset some delay time before each laser pulse so that the effect of the Doppler compensation is not imprinted onto the atomic wave function, as exhibited by the green curve in figure 3.20. The pre-trigger delay between the frequency jump and the laser phase does not necessarily have the same value for each pulse so we define t_{d1} with respect to the beginning of the first pulse, t_{d2} with respect to the middle of the second pulse and t_{d3} with respect to the end of the last pulse.

Hence, the laser phase can be discriminated in three areas:

$$\phi(t) = \begin{cases} \omega_1(t + t_{\mathrm{d1}}) & \text{for } -t_{\mathrm{d1}} < t \leq T + \tau - t_{\mathrm{d2}} \\ \omega_2(t - T - 2\tau + t_{\mathrm{d2}}) & \text{for } T + 2\tau - t_{\mathrm{d2}} < t \leq 2T + 4\tau - t_{\mathrm{d3}} \\ \omega_3(t - 2T - 4\tau + t_{\mathrm{d3}}) & \text{for } 2T + 4\tau - t_{\mathrm{d3}} < t \leq 2T + 4\tau \\ 0 & \text{otherwise} \end{cases} . \tag{3.33}$$

A convenient way to compute the effect from phase discontinuity of the laser is to define the phase sensitivity function $h(t)$ derived from the interferometer's sensitivity function:

$$h(t) = -\frac{dg(t)}{dt} = \begin{cases} \Omega_R \frac{\cos(\Omega_R t)}{\sin(\Omega_R \tau)} & \text{for } 0 < t \leq \tau \\ -\Omega_R \frac{\cos(\Omega_R (t-T-2\tau))}{\sin(\Omega_R \tau)} & \text{for } T + \tau < t \leq T + 3\tau \\ \Omega_R \frac{\cos(\Omega_R (t-2T-4\tau))}{\sin(\Omega_R \tau)} & \text{for } 2T + 3\tau < t \leq 2T + 4\tau \\ 0 & \text{otherwise} \end{cases} . \tag{3.34}$$

The phase associated with the Doppler correction can be straightforwardly calculated:

$$\phi_{\mathrm{disc}} = \int_{-\infty}^{+\infty} h(t)\phi(t)dt = (\omega_3 - \omega_1)\left[\frac{1}{\Omega_R}\tan\left(\frac{\Omega_R \tau}{2}\right) - \tau\right] + \omega_1 t_{\mathrm{d1}} - 2\omega_2 t_{\mathrm{d2}} + \omega_3 t_{\mathrm{d3}}. \tag{3.35}$$

Setting the frequency jumps as stated in equation 3.8, the phase becomes:

$$\phi_{\mathrm{disc}} = 2k_{\mathrm{eff}} a(T+2\tau)\left[\frac{1}{\Omega_R}\tan\left(\frac{\Omega_R \tau}{2}\right) - \tau + t_{\mathrm{d3}} - t_{\mathrm{d2}}\right] + \omega_1 t_{\mathrm{d1}} - 2\omega_2 t_{\mathrm{d2}} + \omega_3 t_{\mathrm{d3}}. \tag{3.36}$$

Moreover, binding the extreme pre-trigger delays with the middle one as follows:

$$\begin{aligned} t_{\mathrm{d1}} &= t_{\mathrm{d2}} - \left(1 - \frac{2}{\pi}\right)\tau \\ t_{\mathrm{d3}} &= t_{\mathrm{d2}} + \left(1 - \frac{2}{\pi}\right)\tau \end{aligned} \tag{3.37}$$

the residual discontinuous phase term can be further simplified:

$$\phi_{\mathrm{disc}} = 2k_{\mathrm{eff}} a(T + 2\tau)\left[\frac{1}{\Omega_R}\tan\left(\frac{\Omega_R \tau}{2}\right) - \frac{2}{\pi}\tau\right] \tag{3.38}$$

which cancels out assuming perfect Raman pulses verifying $\Omega_R \tau = \pi/2$.

However, similarly to the frequency correction schemes introduced previously, an imbalanced atom interferometer with inhomogeneous Rabi frequencies will see this

phase term modified for a more complex expression:

$$\begin{aligned}\phi_{\text{disc}} =& 2k_{\text{eff}}a(T+2\tau)\left[\frac{1}{\Omega_3}\tan\left(\frac{\Omega_3\tau}{2}\right)-\frac{2}{\pi}\tau\right]\\ &+\omega_1\left[\frac{1}{\Omega_3}\tan\left(\frac{\Omega_3\tau}{2}\right)-\frac{1}{\Omega_1}\tan\left(\frac{\Omega_1\tau}{2}\right)\right]\end{aligned} \tag{3.39}$$

with Ω_i the Rabi frequency associated with the i^{th} pulse and ω_1 the laser frequency at the instant of the first pulse.

Closed-loop mid-fringe lock algorithm

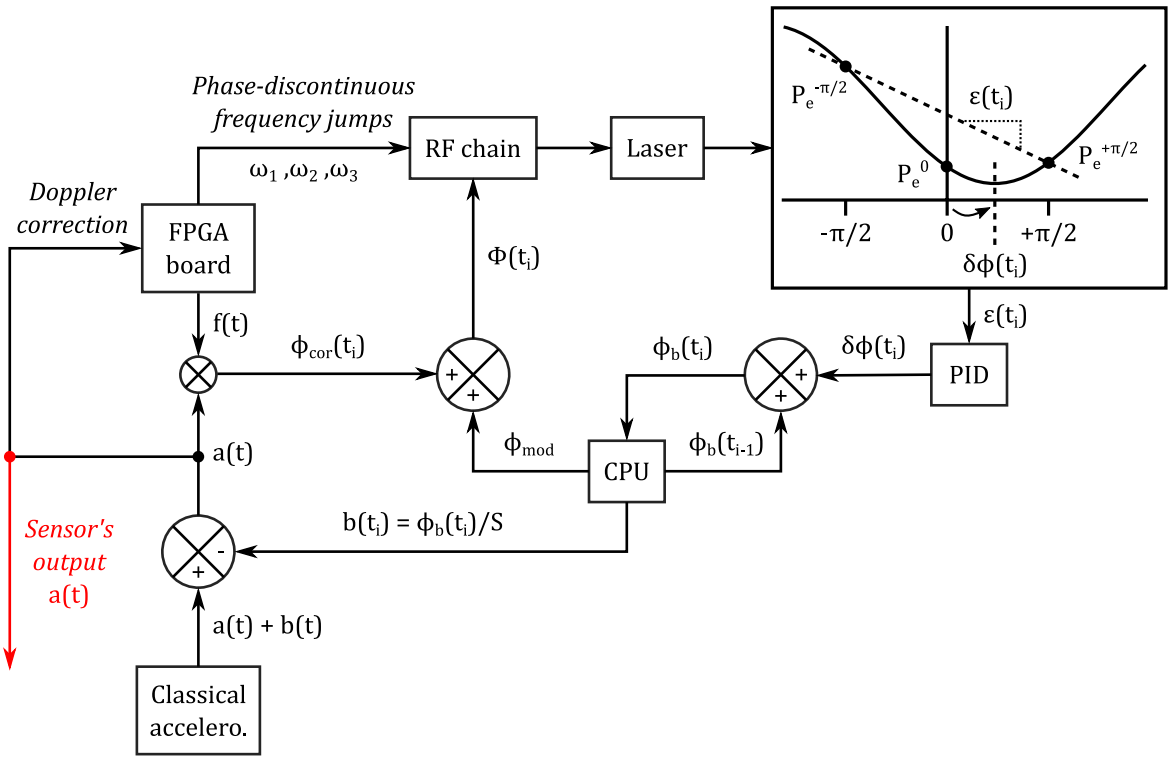

Figure 3.21: Mid-fringe lock algorithm for a hybrid accelerometer in closed-loop configuration.

As well as for the open-loop case, a fringe tracking algorithm was developed in the closed-loop configuration for operating the hybrid accelerometer as depicted in figure 3.21. Here, following the principle of the closed-loop scheme introduced in figure 3.18, the tracked parameter is the one output by the atom interferometer's measurement, namely the classical accelerometer's bias.

Figure 3.22 exhibits the fringe locking sequence switching between the three axes, two modulation phases and two momentum recoil directions. On each axis, the error signal generated from the phase modulation is processed in a PID controller leading to a correction phase shift $\delta\phi(t_i)$, for the algorithm to iteratively compute a bias

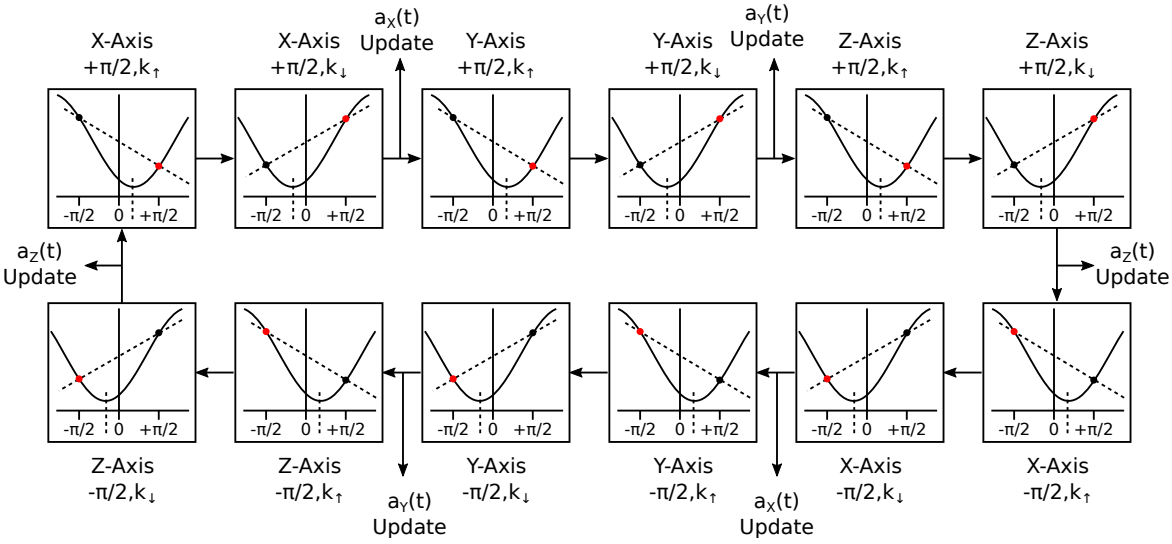

Figure 3.22: Central fringe locking sequence disclosing the order in which parameters are changed from one interferometer to another. For a given axis and modulation phase, two consecutive interferometers are performed with reversed momenta $\pm k_{eff}$ and the acceleration value on this axis is updated. Then, we switch to the next axis and after these six interferometers (two momentum recoil directions times three axes), the process is repeated with a modulation phase flipped from $\pm\pi/2$ to $\mp\pi/2$.

phase $\phi_b(t_i) = \phi_b(t_{i-1}) + \delta\phi(t_i)$. Divided by the atom interferometer's scale factor $\mathcal{S}_{\text{kin}}$, this phase shift is converted into an estimated bias, subtracted from the mechanical accelerometer's signal yielding a continuous and bias-free measurement:

$$a_{hyb}(t) = a(t) + b(t) - b(t_i) \tag{3.40}$$

with $b(t_i) \to b(t)$.

The performance of the mid-fringe lock algorithm implemented on the hybrid accelerometer in closed-loop configuration is demonstrated in figure 3.23. To evaluate the robustness of this fringe tracking, the tilt angle of the sensor head is varied in steps of 5° every 2 to 3 minutes, over a range of 50°. These data were recorded for an interrogation time $T = 5$ ms at $\theta_z = 0°$, corresponding to a rotation along the x axis. Thus, only the measurements on the x and y axes appear on these graphs. The biases output from the atom interferometers' signals, visible in figure 3.23 (b), show variations of ≈ 700 µg arising from a small contribution from the scale factors of the classical accelerometers to their orientation, but also to the inclination-dependent error on the atom interferometer's scale factor. These biases are then subtracted from the classical accelerometers' signals in order to extract the bias-free magnitude of each acceleration component, shown in figure 3.23 (c). Ultimately, figure 3.23 (d) exhibits the norm of the total acceleration vector, effectively stabilizing at the same level some

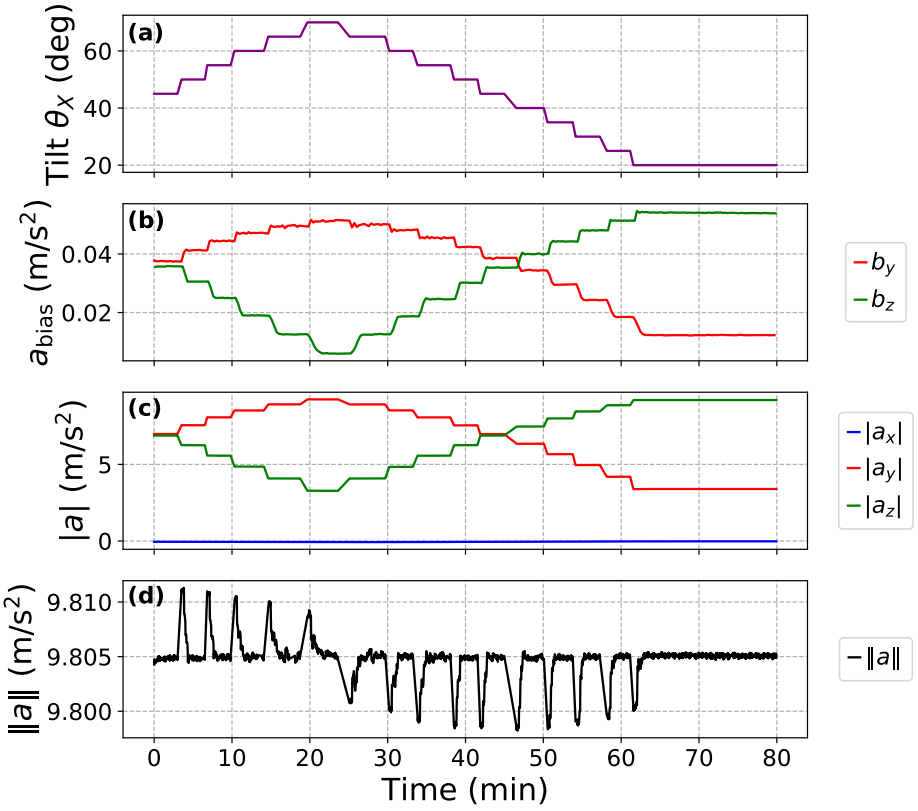

Figure 3.23: Performance of the mid-fringe lock algorithm for an interrogation time $T = 5$ ms at $\theta_z = 0°$ while (a) the tilt angle θ_x is varied in 5° steps over 50°. The evolution of the corresponding (b) classical accelerometers' biases measured by the atom interferometers, (c) magnitude of the acceleration components and (d) acceleration vector norm output by the hybrid triad are displayed as well.

time after each tilt modification.

3.3.3 Quasi-static performance of the three-axis hybrid accelerometer

Long-term stability and sensitivity to the norm of the acceleration vector

The long-term stability of the hybrid accelerometers triad is depicted in figure 3.24. For the acquisition of these data, the fringe tracking algorithm in closed-loop configuration was implemented and the sensor head was tilted at $\theta_x = 45°$ and $\theta_z = 30°$. The matter-wave interferometers were performed at an interrogation time $T = 10$ ms following the sequence presented in figure 3.22. The acceleration components in the mobile frame, as well as the polar angular coordinates exhibit a slow drift resulting from the instability of the rotary platform amounting to approximately 10 µrad over 30 hours. However, the norm of the acceleration vector remains constant and reaches a stability of $\sigma_a = 60$ ng after 24 hours of integration, as it is shown on the Allan deviation

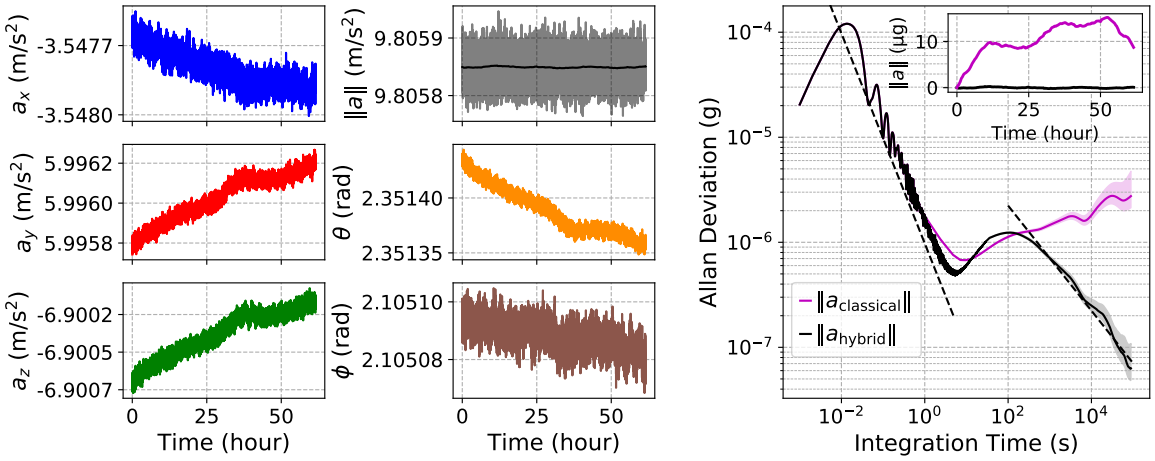

Figure 3.24: Analysis of the hybrid accelerometer triad's stability over 60 hours for an interrogation time $T = 10$ ms at an inclination ($\theta_x = 45°$, $\theta_z = 30°$). Time series at the cycling rate of the experiment are presented in the body frame (left) and polar coordinates (middle) with norm $\|\boldsymbol{a}\| = \sqrt{a_x^2 + a_y^2 + a_z^2}$, inclination $\theta = cos^{-1}(a_z/\|a\|)$ and azimuth $\phi = \text{atan2}(a_x, a_y)$. The solid black curve displays a 10-hour moving average of $\|\boldsymbol{a}\|$. (Right) Allan deviation of the acceleration vector's norm for the hybrid (black) and classical (purple) accelerometer triads. Dashed lines represent integration tendencies as $1/\tau$ and $1/\sqrt{\tau}$ respectively.

on the right of figure 3.24. Simultaneously, the norm of the acceleration measured by the classical triad drifts up to the 3 µg level due to the bias instability of the uncorrected classical sensors, demonstrating a 50-fold improvement in the acceleration vector tracking capability.

Regarding the Allan deviation of the hybrid acceleration norm's measurement, it first integrates as $1/\tau$ indicating the integration of correlated noise produced by the quantization of the classical devices' signals in the analog-to-digital converters (ADC) as well as ambient vibrations. From this point on, while the norm of the classical triad continuously drifts, the norm of the hybrid triad stabilizes at a period $6T_{cyc}$ where $T_{cyc} \approx 1.6$ s is the one-axis measurement cycle time. Due to the integrator time constant of the mid-fringe lock algorithm's feedback loop, the Allan deviation of the hybrid triad increases as well until approximately 100 s before integrating again as $1/\sqrt{\tau}$ indicating white Gaussian noise. The fit of this section yields a sensitivity of 22 µg/$\sqrt{\text{Hz}}$, primarily limited by the cycling rate of the instrument due to the dead times inherent to the sequencer presented in chapter 2.

Accuracy of the acceleration norm's measurement

In a similar manner as for the quantum gravimeter and quantum accelerometer triad, the systematic phase shifts affecting the atom interferometer's measurement

will introduce an error in the calculation of the mechanical accelerometers' biases which, once subtracted from the classical sensors' outputs, represent a new type of bias deteriorating the performances of the apparatus. If most of the systematic effects were examined for the quantum accelerometers triad in section 3.2, new errors arise from the closed-loop hybridization and operating scheme and need to be investigated.

The first important error which comes to mind is the residual laser phase introduced by the phase-discontinuous frequency jumps which is imprinted onto the atoms. Indeed, in the case of perfect Raman pulses with constant Rabi frequencies $\Omega_1 = \Omega_3 = \pi/2\tau$, then this phase term is canceled out at the output of the interferometer. Nevertheless, the study on Rabi frequency inhomogeneities in our tilted instrument conducted in section 3.2 associated to the result of equation 3.39 indicate that the previous assumption is not valid. With the sensor head tilted by $\theta_x = 45°$ and $\theta_z = -30°$, atom interferometers were performed at $T = 10$ ms with the mechanical accelerometers' outputs high-pass filtered so that the phase shift at the output of the interferometer equals $\Phi = \phi_{\text{disc}} + \phi_{\text{kin}}$ where ϕ_{kin} stands for the inertial phase shift due to the atomic motion. Then, subtracting the latter using the scale factor $\mathcal{S}_{\text{kin}}$ given in equation 3.19 at the first order, it was possible to isolate the residual discontinuous phase shift only. The resulting biases on the measurements of the acceleration components amounted to $\sigma_a^x = 22.19(0.35)$ µg, $\sigma_a^y = -18.81(0.45)$ µg and $\sigma_a^z = 18.11(0.27)$ µg yielding a systematic bias of $\sigma_a = 34.27(0.63)$ µg on the norm of the acceleration vector [Templier 2021].

Furthermore, another issue to consider is the application of the matter-wave interferometer's response function correlated with the mechanical accelerometer's signal. In the open-loop scheme, this only involved the AC part of the classical measurement and produced the vibration correction phase $\phi_{\text{vib}}^{\text{cor}}$ but now that the whole unfiltered signal is conserved, this hybridization yields the correlation phase ϕ_{cor}, directly compared to the inertial phase shift arising from the atomic motion ϕ_{kin}. In the case of an imbalanced Mach-Zehnder interferometer, the response function to accelerations is derived from

the sensitivity function $g(t)$ defined in equation 1.48 and can be written:

$$f(t) = \begin{cases} \frac{1}{\Omega_3}\tan\left(\frac{\Omega_3\tau}{2}\right) - \frac{1}{\Omega_1}\tan\left(\frac{\Omega_1\tau}{2}\right) & \text{for } t \leq 0 \\ \frac{1}{\Omega_1}\frac{\cos(\Omega_1\tau)-\cos(\Omega_1 t)}{\sin(\Omega_1\tau)} & \text{for } 0 < t \leq \tau \\ t - \tau + \frac{1}{\Omega_3}\tan\left(\frac{\Omega_3\tau}{2}\right) & \text{for } \tau < t \leq T+\tau \\ T + \frac{1}{\Omega_3}\tan\left(\frac{\Omega_3\tau}{2}\right) - \frac{1}{\Omega_2}\frac{\cos(\Omega_2\tau)-\cos(\Omega_2(t-T-2\tau))}{\sin(\Omega_2\tau)} & \text{for } T+\tau < t \leq T+3\tau \\ -t + 2T + 3\tau + \frac{1}{\Omega_3}\tan\left(\frac{\Omega_3\tau}{2}\right) & \text{for } T+3\tau < t \leq 2T+3\tau \\ \frac{1}{\Omega_3}\frac{\cos(\Omega_3\tau)-\cos(\Omega_3(t-2T-4\tau))}{\sin(\Omega_3\tau)} & \text{for } 2T+3\tau < t \leq 2T+4\tau \\ 0, & t > 2T+4\tau \end{cases} \tag{3.41}$$

with Ω_i the Rabi frequency associated with the i^{th} pulse. However, for computational resources considerations, an approximation of this function was implemented in the FPGA board constituting the core of the real-time chain. This function is defined as below:

$$f_{\mathrm{RT}}(t) = \begin{cases} 0 & \text{for } t \leq 0 \text{ and } t > 2T+4\tau \\ \frac{T+4\tau/\pi}{T+2\tau}t & \text{for } T+\tau < t \leq T+2\tau \\ \frac{T+4\tau/\pi}{T+2\tau}(-t+2T+4\tau) & \text{for } T+2\tau < t \leq 2T+4\tau \end{cases} \tag{3.42}$$

where the value 0 outside the bounds of the interferometer is valid for a symmetrical interferometer.

The scale factor associated to this simplified expression can be straightforwardly calculated assuming a constant acceleration a_0, following:

$$\begin{aligned} \mathcal{S}_{\mathrm{RT}} = \frac{\phi_{\mathrm{cor}}}{a_0} &= k_{\mathrm{eff}} \int_{-\infty}^{+\infty} f_{\mathrm{RT}}(t)dt \\ &= k_{\mathrm{eff}}(T+2\tau)\left(T + \frac{4\tau}{\pi}\right). \end{aligned} \tag{3.43}$$

From this expression, it is possible to deduce the scale factor error $\delta\mathcal{S} = \mathcal{S}_{\mathrm{RT}} - \mathcal{S}_{\mathrm{kin}}$ and associated systematic phase shift for a constant acceleration a_0:

$$\begin{aligned} \phi_{\mathrm{SF}} &= a_0\delta\mathcal{S} \\ &= k_{\mathrm{eff}}a_0(T+2\tau)\left[\frac{4\tau}{\pi} - \frac{1}{\Omega_1}\tan\left(\frac{\Omega_1\tau}{2}\right) - \frac{1}{\Omega_3}\tan\left(\frac{\Omega_3\tau}{2}\right)\right]. \end{aligned} \tag{3.44}$$

The evaluation of this effect, performed in the same conditions as for the residual discontinuous phase shift, produced systematic biases of $\sigma_a^x = -26.2(2.4)$ µg, $\sigma_a^y = 38.4(1.0)$ µg and $\sigma_a^z = -39.9(0.5)$ µg corresponding to a systematic bias of $\sigma_a = 61.3(2.7)$ µg on the norm of the acceleration vector. It should be mentioned that this simplification in the response function of the interferometer does not only add a systematic phase shift degrading the accuracy of the instrument, but may also harm the sensitivity on the

acceleration components. Indeed, using an inexact function induces a loss of correlation between the atom interferometers and the mechanical accelerometers, thus reducing the efficiency of the vibrations rejection. This being added to the finite bandwidth and latency of the classical devices imply a strong sensitivity limitation due to the vibrations which still introduce phase noise and, for high enough regimes, still prevent any measurement to be extracted from the interference fringes.

Systematic effect (µg)	x**-axis bias**	y**-axis bias**	z**-axis bias**	**Norm bias**
Total	16.2 (5.0)	-23.3 (2.4)	17.5 (1.7)	33.3 (5.8)

Table 3.3: Table of the acceleration biases taken from [Templier 2021] including all the contributions from the atom interferometers on the 3-axis hybrid accelerometer as well as the residual discontinuous phase and scale factor error for an imbalanced atom interferometer with a Raman interrogation time of $T = 10$ ms and a sensor head's inclination of $\theta_x = 54.7°$ and $\theta_z = -45°$. The estimations are expressed in μg with the uncertainties in parentheses. The norm bias stands for the bias of the norm of the full acceleration vector.

Ultimately, these systematic errors limiting the accuracy of our measurement of the acceleration vector's norm must be added to the effects previously calculated on the quantum accelerometers triad. The results of this evaluation, summarized in table 3.3, reveal a bias on the norm of $\sigma_a = (33.3 \pm 5.8)$ µg exhibiting an uncertainty two times better than the quantum triad.

3.3.4 Hybridized sensors' misalignments along a given measurement axis

With a hybridization design such as the one presented in this section, the consequences of the misalignments between the respective sensors must be very carefully contemplated. First, the misalignments between the three reference mirrors constituting the measurement axes of the quantum accelerometers triad was assessed in section 3.2. However, the closed-loop operating scheme used for the hybrid device imposes to lay emphasis on the respective misalignments between the quantum and classical accelerometers along each axis. Indeed, each atom interferometer is employed to correct the bias of the corresponding classical sensor, the signal of which is used as the instrument's output. Eventually, if these two sensors are measuring a different projection of the acceleration, a systematic bias dependent on the orientation of the apparatus will be introduced in the real-time correction and diminish the overall accuracy of the instrument. This is not the case with the open-loop hybridization scheme which suppresses the DC component of the classical measurement, thus the projection of the acceleration for the latter is not involved.

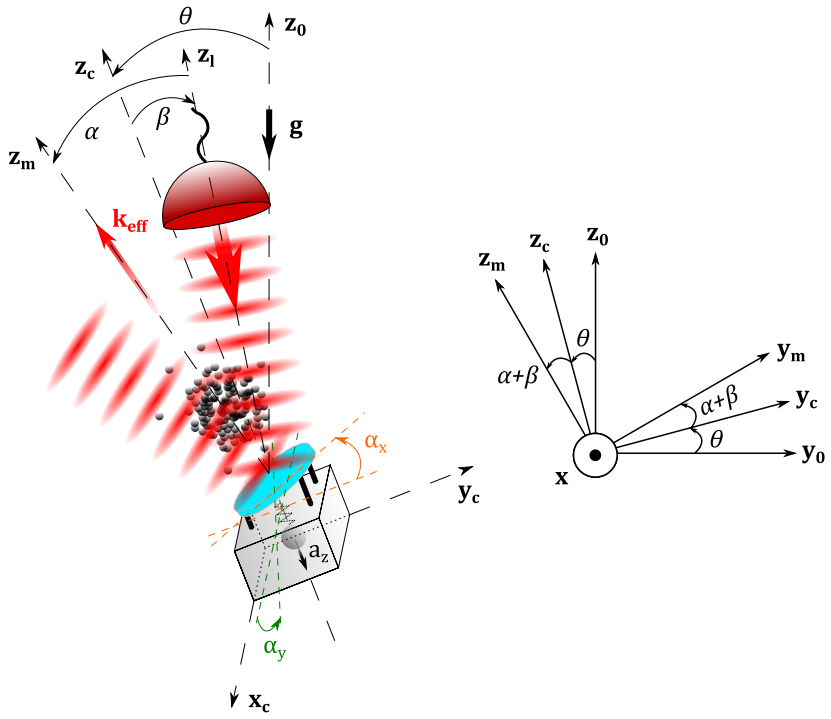

Figure 3.25: Schematic representation of the different elements composing the measurement of the acceleration projection along a single axis, tilted with respect to the gravity vector $\boldsymbol{g}$. The axes $\boldsymbol{z_m}$, $\boldsymbol{z_c}$, $\boldsymbol{z_l}$ and $\boldsymbol{z_0}$ respectively denote the effective wave vector's axis (normal to the reference mirror, defining the atomic accelerometer's measurement axis), the classical accelerometer's measurement axis, the incident laser's axis and the local gravitational acceleration's axis.

As depicted in figure 3.25, the number of elements participating in either the quantum or classical acceleration measurement introduce various potential misalignments. On this schematic representation, we consider a rotation around the axis $\boldsymbol{x} \equiv \boldsymbol{x_0} \equiv \boldsymbol{x_c} \equiv \boldsymbol{x_m}$ for simplicity. Regarding the atom interferometer, its output will be sensitive to the norm and orientation of the wave vector with respect to the incident laser field, assuming an angle α leading to $\boldsymbol{k}_{\mathbf{eff}}^{\mathbf{las}} = k_{\mathrm{eff}} \cos(\alpha) \boldsymbol{z_m}$. The measurement axis being defined by the normal to the reference mirror, it will then sense the acceleration $\boldsymbol{a}_{\mathbf{at}} = -g \cos(\theta + \alpha + \beta) \boldsymbol{z_m}$ with θ the tilt of the sensor head (defined by the mechanical accelerometer's axis) and β the angle between the classical accelerometer and the incident laser beam. On the other hand, the classical accelerometer will measure an acceleration along its own measurement axis, written $\boldsymbol{a}_{\mathbf{cl}} = -g \cos(\theta) \boldsymbol{z_c}$, and is insensitive to the variations of the effective wave vector since its value is computed from the FPGA board and unrelated to the laser's evolution, explicitly $\boldsymbol{k}_{\mathbf{eff}}^{\mathbf{RT}} = k_{\mathrm{eff}} \boldsymbol{z_c}$. From these information, it is possible to calculate a systematic error arising from these misalignments, considering only the approximate response function of the interferometer

as this error was assessed independently:

$$\begin{aligned}\phi_{\text{mis}} &= \int_{-\infty}^{+\infty} f_{\text{RT}}(t)\left[\boldsymbol{k}_{\mathbf{eff}}^{\mathbf{las}}.\boldsymbol{a}_{\mathbf{at}} - \boldsymbol{k}_{\mathbf{eff}}^{\mathbf{RT}}.\boldsymbol{a}_{\mathbf{cl}}\right] dt \\ &= k_{\text{eff}} g(T+2\tau)\left(T+\frac{4\tau}{\pi}\right)\left[\cos\theta\left(1-\cos\alpha\cos(\alpha+\beta)\right)+\sin\theta\cos\alpha\sin(\alpha+\beta)\right] \\ &\approx k_{\text{eff}} g T^2\left[\cos\theta\left(\alpha^2+\alpha\beta+\frac{\beta^2}{2}\right)+\sin\theta(\alpha+\beta)\right]\end{aligned} \tag{3.45}$$

where the last equation is valid in the infinitely short pulses assumption $\tau \ll T$ and for a second-order development of the small angles $\alpha, \beta \ll 1$ rad. Divided by the atom interferometer's simplified scale factor, this phase shift can be expressed in terms of acceleration bias:

$$\sigma_a^{\text{mis}} \approx \frac{\phi_{\text{mis}}}{k_{\text{eff}} T^2} \approx g\left[\cos\theta\left(\alpha^2+\alpha\beta+\frac{\beta^2}{2}\right)+\sin\theta(\alpha+\beta)\right] \tag{3.46}$$

For a 30° inclination of the mechanical accelerometer with respect to the gravity, at an interrogation time $T = 10$ ms and for a reasonable misalignment of $\alpha + \beta = 10$ µrad, the resulting phase shift is as high as $\phi_{mis} \approx 79$ mrad corresponding to a bias $\delta a_{mis} \approx 49$ µg.

Calibration of the misalignment-induced acceleration bias

Here, we observe a first-order dependence on the inclination of the sensor head, proportional to the misalignment between the classical and atomic accelerometers $(\alpha + \beta)$. To illustrate this effect, data shown in figure 3.26 (a) were recorded after changing the reference mirror on the z axis, replaced by a tip-tilt mirror. The alignment was no longer optimized and the fit of these data returned values of $\alpha = 51.7(3)$ mrad and $\beta = -55.7(3)$ mrad, which are extremely important misalignments but fortunately mostly canceled out. Still, a 4 mrad angle between the mechanical accelerometer's and the reference mirror's respective axes induced a 5 mg variation of the bias over 80°. The offset of this bias, estimated at $-18.65(1)$ mg, is due to the absence of any calibration anterior to this experiment. This represents the actual bias of the mechanical accelerometer, independent from the tilt angle of the sensor head but conditioned by the operating conditions and in particular the temperature.

In order to suppress the acceleration bias sensitivity to the sensor head's tilt, obtained by tracking the atomic fringe in closed-loop configuration, the operation described above was repeated by changing the orientation of the mirror using the piezo-actuated tip-tilt platform described in section 2.4. Fitting the evolution of the

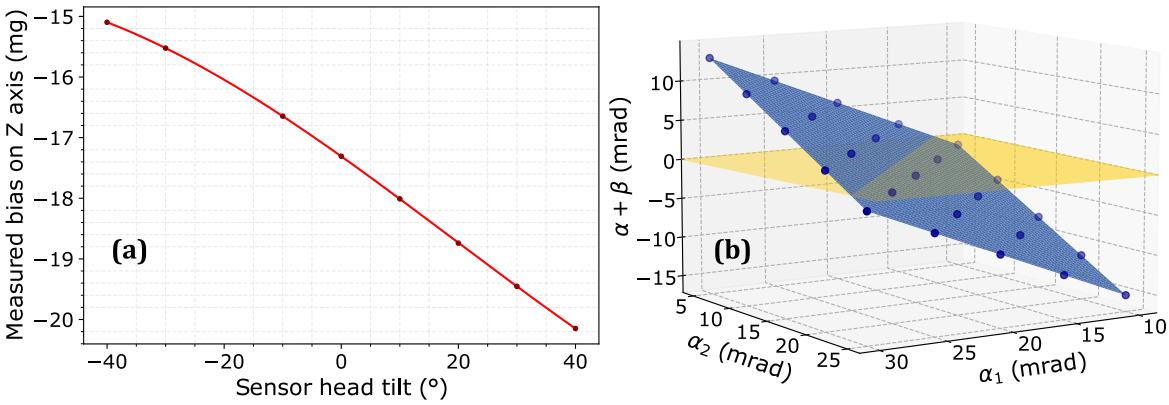

Figure 3.26: (a) Evolution of the bias returned by the fringe tracking algorithm in closed-loop configuration, with the sensor head's and platform's x axes aligned ($\theta_z = 0°$) and θ_x varying between $-40°$ and $+40°$ in steps of $10°$. The dark red dots represent the stabilized value of the bias after a 2 – 3 minutes tracking, while the light red curve illustrates a fit of these data using equation 3.46. (b) The fit of this bias, returning the first order contribution of the misalignment $\alpha + \beta$, is repeated for different inclinations of the mirror driven by the two parameters of the piezo-actuated tip-tilt platform α_1 and α_2 in order to find orientations canceling the tilt-dependent bias at the first order. In the meantime, the angle between the classical accelerometer and laser collimator β remains unchanged. The yellow plane representing the effective cancellation of the misalignment $\alpha+\beta$, its intersection with the experimental points highlights the various couples (α_1, α_2) satisfying our requirements.

bias with equation 3.46, we were able to extract the contributions of the various angles to this bias in different positions focusing on the first-order contribution $\alpha + \beta$. This value was plotted as a function of the two parameters used to drive the tip-tilt platform α_1 and α_2 in figure 3.26 (b) letting appear a linear tendency represented by the light blue plane. We observe on this graph that there is a complete line verifying a cancellation of the bias' sensitivity to the sensor head's inclination, which makes sense since the sensor head is only rotated along the x axis; this result finally shows an alignment of the mechanical accelerometer and the reference mirror in the y, z plane. This fit yielded an arbitrary couple of angular setpoints $(\alpha_1 = 21.53, \alpha_2 = 15)$ mrad ensuring $\alpha = -\beta$ and thus a suppression of the first-order tilt-dependent acceleration bias.

Nevertheless, the calibration performed on the reference mirror does not affect the alignment between the mechanical accelerometer and the laser collimator β. This first means that the incident and reflected laser beams are no longer overlapped, implying a contrast reduction and a scale factor error proper to each quantum accelerometer which can lead to a significant error on the acceleration vector's norm, but also that the second-order contribution of the misalignments to the systematic bias is still present. In order to tackle these two issues, a two-step iterative process was implemented.

It consists in the alignment of the classical sensor and reference mirror through the previously described technique, and laser back-coupling in the optical fiber through the adjustment of the laser collimator's orientation. After several repetitions of these operations going back and forth, the apparatus finally reached a satisfying configuration of $\alpha = \beta = 0$ mrad.

Conclusion

The realization of a quantum gravimeter capable of sensing the acceleration of free-falling atoms with a 1.24 µg/$\sqrt{\text{Hz}}$ sensitivity at a $T = 20$ ms interrogation time has been demonstrated. Additionally, the tracking of the interferometric signal established a stability reaching the 10 ng level after 5 hours 30 minutes of integration and the investigation of the systematic bias induced by the environment and the technological elements of the apparatus yielded an intrinsic accuracy of (351 ± 983.1) ng. If the sensitivity and long-term stability are in good agreement with our expected performances, more efforts should be put in the characterization of the systematic phase shifts (such as the wavefront distortion for instance) in order to gain an order of magnitude in the relative accuracy.

Furthermore, the qualification of the whole quantum accelerometers triad has validated its ability to be operated at an arbitrary orientation, with individual sensitivities of $\sigma_a^x = 13.8\mu\text{g}/\sqrt{\text{Hz}}$, $\sigma_a^y = 4.8\mu\text{g}/\sqrt{\text{Hz}}$ and $\sigma_a^z = 5.9\mu\text{g}/\sqrt{\text{Hz}}$ for an interrogation time of $T = 10$ ms, including the noise of the classical sensors due to the open-loop hybridization (in particular on the x axis). The sequential measurement of the three orthogonal acceleration components allows for the reconstruction of the full vector, with a norm reaching a 200 ng stability level after a 9 hours integration. The effort made on the rejection of the systematic phase shifts and on the calibration of the quantum triad's non-orthogonality has led to a reduction of the three sensors' biases for an accuracy of (83.6 ± 11.3) µg on the acceleration vector's norm.

Ultimately, the real-time system featuring a field-programmable gate-array (FPGA) board has proven efficient in the compensation of both the vibration-induced parasitic phase shift and the Doppler frequency shift tuning the Raman laser out of resonance, even for an orientation of the sensor head slowly varying in time. The closed-loop operating scheme allows the atom interferometers to efficiently measure and remove the biases of the mechanical accelerometers, making possible to use these corrected signals as a continuous and bias-free measurement of the acceleration projections. The qualification of the whole triad yielded a sensitivity of 22 µg/$\sqrt{\text{Hz}}$ on the norm of the acceleration vector at $T = 10$ ms, and the analyze of long-term acquisitions exhibited a stability of 60 ng after 24 hours of integration. This demonstration reveals a 50-fold improvement in our capability to track the acceleration vector, by comparison with the classical accelerometers triad. Here again, the evaluation of the systematic phase shifts and the elimination of the largest ones has produced an accuracy of (33.3 ± 5.8) µg on the norm of the acceleration provided with an uncertainty twice as low as the quantum triad, which proves the efficiency of the implemented sensors fusion scheme.

These compelling results pave the way for field-deployable and mobile applications, but the operation of the hybrid instrument outside the laboratory and even more onboard a vehicle give rise to new challenges. Indeed, the apparatus still needs to be evaluated outside a temperature-stabilized environment which can give rise to instabilities of the mechanical structure. Furthermore, the compensation of the reference mirror's vibrations has proven limited in terms of frequency and amplitude. Eventually, for onboard operation, the sensor head will most likely undergo rotation rates incomparable with the Earth rotation or the slow drift experienced on the rotary platform. This last aspect is acknowledged as a major hindrance in the realization of an atom interferometer, and needs to be tackled as the next primary step as discussed in the next chapter.

Chapter 4

Atom interferometry in the presence of rotations

In this chapter, the major consequences of rotations on the measurement of a matter-wave interferometer are investigated, following the theoretical work described in section 1.3. First, the model of the output phase shift for a rotating atom interferometer both with and without a mechanical compensation on the reference mirror is revised by integrating the closed-loop, full hybridization scheme introduced in section 3.3. On the experimental side, this study includes a demonstration of the exponential decay of the atomic fringes' contrast with a rotating effective wave vector and a validation of the rotation-induced systematic phase shifts model, related to the complex trajectory of the atomic cloud in the rotating frame of the hybrid accelerometer. Following this, a fringes reconstruction scheme is presented in order to retrieve the acceleration information out of the diminished and scrambled interference signal.

Subsequently, after setting the bounds to the applicability of the fringes reconstruction process in terms of interrogation time and angular velocity, an electronic and mechanical design consisting in a compensation of the rotation applied to the reference mirror is presented. In particular, we describe the FPGA design acquiring the signals of the fiber-optic gyroscopes and converting them into angular setpoints for the piezo-actuated tip-tilt platform to stabilize the orientation of the mirror at each light pulse. Some technical details on the practical implementation, data format and timing constraints are provided before demonstrating the performance of the compensated rotating interferometer. Ultimately, the limiting factors in the instrument's sensitivity to accelerations are evaluated in order to determine how this hybrid accelerometer could be employed to perform on-board inertial measurements.

Contents

4.1 Complements to the theoretical model of a rotating, fully-hybridized accelerometer

In chapter 1, the phase shift measured at the output of a rotating Mach-Zehnder atom interferometer was calculated, with a reference mirror mechanically fixed to the vacuum chamber (section 1.3) as well as with its orientation stabilized in the laboratory frame (section 1.4). Moreover, the closed-loop scheme aiming at hybridizing the matter-wave interferometer with the classical accelerometer has been described in section 3.3. In the case of a rotating apparatus, some specific accelerations induced by the rotation of the mechanical accelerometer take part in the hybridized sensor's measurement and either compensate or exacerbate some contributions of the rotating atom interferometer. In particular, the driving acceleration including the centrifugal component will be sensed by both quantum and classical accelerometers with two distinct lever arms as their measurement reference points (respectively the atomic cloud and classical device's proof mass) are not at the same exact position. In order to account for this specificity on the measurement of our hybrid instrument, the phase shift equivalent to the classical measurement of the acceleration must be calculated.

4.1.1 Equivalent phase shift of the classical measurement

Similarly to the rotation-induced inertial phase shifts arising from the modification of the atomic trajectories, the measurement of the classical accelerometer will be impacted by the rotation of the apparatus, and notably the centrifugal force arising from the lever arm between the center of rotation (taken as the mobile's center of mass) and the sensor. Most of the existing classical acceleration sensing technologies rely on a damped proof mass whose displacement is determined to retrieve its acceleration in its own instantaneous rest frame, before an electronic circuit pushes back the proof mass towards its rest position; in practice, there are only very small elements of motion of this proof mass with respect to the sensor's body and it can be overall considered attached to the rest of the apparatus. For this reason, while the quantum accelerometer senses some Coriolis effect due to the motion of the atomic cloud with respect to the reference mirror, we assume that the classical accelerometer will not measure such effect in the absence of any moving parts. It is important to insist that this statement only holds under the assumption of a test-mass immobile in the frame of the mechanical accelerometer's case, which will be discussed more in detail in section 4.3.

Having in mind the equation of motion describing the classical sensor's movements in the laboratory frame, one can define an equivalent phase shift from the classical

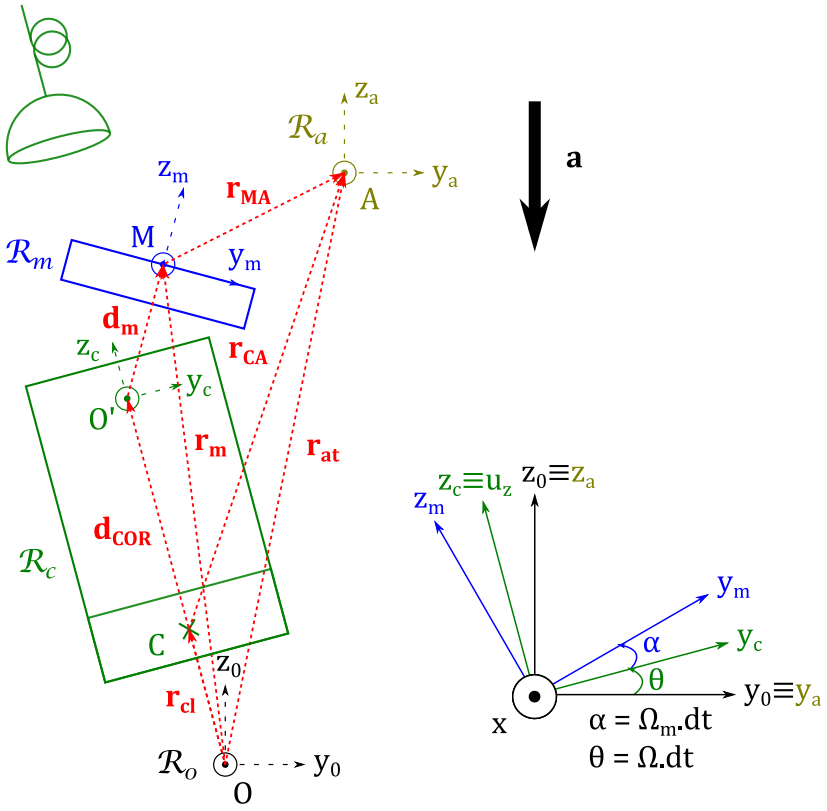

Figure 4.1: 2D representation of the relevant frames' axes and distances for compensated rotations. The terrestrial frame $\mathcal{R}_0$, the science chamber's frame $\mathcal{R}_c$, the mirror's frame $\mathcal{R}_m$ and the atomic cloud's frame $\mathcal{R}_a$ are represented in black, green, blue and gold respectively. O: center of rotation of the apparatus; O': center of rotation of the mirror; M: center of the mirror's surface; A: center of the atomic cloud; C: center of the classical accelerometer's proof mass; $\boldsymbol{d_m} = \overline{O'M}$: lever arm of the tip-tilt mirror in the chamber's frame; $\boldsymbol{d_{COR}} = \overline{OO'}$: distance between the centers of rotation of the chamber and the mirror; $\boldsymbol{r_m} = \overline{OM}$: position of the mirror in the terrestrial frame; $\boldsymbol{r_{at}} = \overline{OA}$: position of the atomic cloud in the terrestrial frame; $\boldsymbol{r_{cl}} = \overline{OC}$: position of the classical accelerometer's test mass in the terrestrial frame; $\boldsymbol{r_{MA}} = \overline{MA}$: distance between the mirror's surface and the atomic cloud; $\boldsymbol{r_{CA}} = \overline{CA}$: distance between the classical accelerometer's test mass and the atomic cloud.

acceleration measurement using the formalism of sensitivity function, the same way the hybridization scheme operates. The term *equivalent* highlights the fact that what is calculated is not an atomic phase shift, as it does not involve any kind of path difference like in interferometric measurements. Here, this expression is the result of a conversion of an acceleration, correlated with the sensitivity function of the atomic interferometer to reveal a quantity homogeneous to a phase and which can be directly compared to the output of the atom interferometer as it raises the same scale factor $k_{\text{eff}}T^2$. Consequently, for an interferometric measurement performed on the z axis, this method provides an equivalent phase shift equal to:

$$\Phi_{\text{cl}} = k_{\text{eff}}T^2\left[a_z + b_z + (z_0^{\text{cl}} + v_z^{\text{cl}}T)\Omega^2\right] \tag{4.1}$$

with b_z the bias of the classical sensor attached to the z axis, Ω the rotation rate applied on the sensor and z_0^{cl} the distance between its center of rotation and its proof mass. This distance corresponds to the quantity $\boldsymbol{r_{\text{cl}}}$ visible in figure 4.1, projected onto the z axis and taken at the first pulse's instant.

Considering that the classical sensor, attached to the experimental chamber, has no relative velocity v_z^{cl} in the rotating frame of the science chamber $\mathcal{R}_c$, equation 4.1 can be simplified as:

$$\Phi_{\text{cl}} = k_{\text{eff}} T^2 \left[a_z + b_z + z_0^{\text{cl}} \Omega^2 \right]. \tag{4.2}$$

It is important to mention that because the mechanical accelerometer is attached to the mobile, its individual output signal will not experience any change whether the mirror rotates or not and will thus yield the same phase shift in both situations (i.e. with and without mechanical compensation).

4.1.2 Output phase shift of the hybrid accelerometer in the case of a static mirror

Let us remind the expression of the phase shift associated to the movement of the atoms with respect to the mirror, immobile in the rotating frame attached to the vacuum chamber, determined in section 1.3:

$$\begin{aligned} \Phi_{\text{at}} = k_{\text{eff}} T^2 \big[& a_z + 2(v_x + a_x T)\Omega_y - 2(v_y + a_y T)\Omega_x \\ & + (z_0 - 3 v_z T + 2 x_0 \Omega_y T - 2 y_0 \Omega_x T)\, \Omega^2 \big] \end{aligned} \tag{4.3}$$

The subtraction of the atomic measurement from the classical equivalent phase shift finally gives us the inertial phase shift remaining to be compensated for, defined by $\Delta\Phi = \Phi_{\text{cl}} - \Phi_{\text{at}}$ and given at the third order in T and Ω for a constant rotation with its axis in the plane transverse to the Raman beam ($\Omega_z = 0$):

$$\begin{aligned} \Delta\Phi = k_{\text{eff}} T^2 \big[& b_z - 2(v_x + a_x T)\Omega_y + 2(v_y + a_y T)\Omega_x \\ & - \left(z_0^{\text{CA}} - 3 v_z T + 2 x_0 \Omega_y T - 2 y_0 \Omega_x T \right) \Omega^2 \big] \end{aligned} \tag{4.4}$$

where $z_0^{\text{CA}} \equiv z_0 - z_0^{\text{cl}} = \boldsymbol{r_{\text{CA}}}(t_0).\boldsymbol{u_z}$ denotes the distance between the atomic wave packet and the classical accelerometer along the z axis at the instant of the first light pulse. It is a projection of the distance $\boldsymbol{r_{\text{CA}}}$ displayed in figure 4.1 taken at the beginning of the interferometer.

On the first line, we recognize the bias of the classical sensor and the Coriolis effect induced by the atomic cloud's transverse motion in the Raman beam. The

second line corresponds to the centrifugal force with a predominant contribution arising from the two sensors' respective lever arms; it is interesting to note that due to the comparison of the classical and quantum measurements, the position of the center of rotation is no longer present at the first order and only the distance separating the two devices remains. Some higher-order terms from the atomic phase shift, related to the composition of motions in the different frames of reference, still appear in the differential phase shift as well.

4.1.3 Phase shift of the hybrid accelerometer with a stabilized reference mirror in the laboratory frame

As for the fixed mirror case, let us first remind the atomic phase shift in the case of a mirror rotating in the mobile frame:

$$\begin{aligned}\Phi_{\text{at}}^{\text{comp}} = k_{\text{eff}}T^2\Big[&a_z + 2(v_x + a_xT)(\Omega_y + \Omega_{\text{my}}) - 2(v_y + a_yT)(\Omega_x + \Omega_{\text{mx}}) \\ &+ (a_x\Omega_{\text{my}} - a_y\Omega_{\text{mx}})T + (z_0 + 2x_0\Omega_yT - 2y_0\Omega_xT)\Omega^2 \\ &- (2z_0 - 2d_{\text{COR}} - d_m + 3v_zT + 3v_{\text{rec}}T + 3x_0\Omega_{\text{my}}T - 3y_0\Omega_{\text{mx}}T)\Omega_m^2 \\ &- 3v_zT(\Omega_x^2 + 2\Omega_x\Omega_{\text{mx}} + \Omega_{\text{mx}}^2 + \Omega_y^2 + 2\Omega_y\Omega_{\text{my}} + \Omega_{\text{my}}^2) \\ &+ 3T(x_0\Omega_y - y_0\Omega_x)(\Omega_x\Omega_{\text{mx}} - \Omega_y\Omega_{\text{my}})\Big]\end{aligned} \tag{4.5}$$

with $\Omega_{\text{mx,my}}$ the angular velocity components of the mirror in the rotating frame of the science chamber as defined in section 1.4 and all the distances detailed in figure 4.1. Equation 4.5 takes up all the contributions to the inertial phase shift described in table 1.1.

Just like in the case of a mirror attached to the rotating frame of the vacuum chamber, we define the output phase shift of the hybrid accelerometer compensated from the rotations of the instrument $\Delta\Phi^{\text{comp}} = \Phi_{\text{cl}} - \Phi_{\text{at}}^{\text{comp}}$. Since the mechanical accelerometer is not sensitive to the rotation of the mirror, the terms subtracted from the above expression are the same as in equation 4.1. To simplify notations, we will write:

- $z_0^{\text{CA}} = z_0 - z_0^{\text{cl}} = \boldsymbol{r_{\text{CA}}}(t_0).\boldsymbol{u_z}$ the distance between the classical sensor and the atomic wave packet along the z axis at the instant of the first pulse, as defined above;
- $z_0^{\text{MA}} = z_0 - d_{\text{COR}} - d_m = \boldsymbol{r_{\text{MA}}}(t_0).\boldsymbol{u_z}$ the distance between the reference mirror's surface and the atomic cloud at the instant of the first pulse;

- $\delta\Omega_i = \Omega_i + \Omega_{\text{mi}}$ $(i = x, y)$ the residual rotation rate on a given axis arising from an imperfect compensation, considering that $\Omega_i \simeq -\Omega_{\text{mi}}$ in practice.

Acceleration term	Notation	**Associated phase shift expression**
Classical bias	ϕ_{bias}	$k_{\text{eff}} T^2 b_z$
Mirror's rotation	$\phi^{\text{mirror}}_{\text{rotation}}$	$k_{\text{eff}} T^3 \left[-a_x \Omega_{\text{my}} + a_y \Omega_{\text{mx}}\right]$
Residual Coriolis	ϕ_{Coriolis}	$2k_{\text{eff}} T^2 \left[-\left(v_x + a_x T\right) \delta\Omega_y + \left(v_y + a_y T\right) \delta\Omega_x\right]$
Centrifugal (chamber)	$\phi^{\text{chamber}}_{\text{centrifugal}}$	$k_{eff} T^2 \Omega^2 \left[-z_0^{\text{CA}} - 2x_0 \Omega_y T + 2y_0 \Omega_x T\right]$
Centrifugal (mirror)	$\phi^{\text{mirror}}_{\text{centrifugal}}$	$k_{eff} T^2 \Omega_m^2 [2z_0^{\text{MA}} + d_m + 3T \left(v_z + v_{\text{rec}} + x_0 \Omega_{\text{my}} - y_0 \Omega_{\text{mx}}\right)]$
Other terms arising from composition of motion	ϕ_{compo}	$3k_{\text{eff}} T^3 \left[v_z \left(\delta\Omega_x^2 + \delta\Omega_y^2\right) - \left(x_0 \Omega_y - y_0 \Omega_x\right) \left(\Omega_x \Omega_{\text{mx}} - \Omega_y \Omega_{\text{my}}\right)\right]$

Table 4.1: Summary of the contributions to the phase shift of a closed-loop hybrid accelerometer undergoing opposed rotations of the laser input and retroreflection mirror. These contributions are given up to the third order in T, for constant transverse rotations. The effective wave vector is considered oriented along $+\boldsymbol{u_z}$ at the instant of the first pulse (see figure 4.1).

Table 4.1 summarizes all the contributions to the output phase shift of the closed-loop hybrid accelerometer while it experiences rotations compensated on the reference mirror $\Delta\Phi^{\text{comp}}$. These rotations are assumed to have a constant amplitude along an axis comprised in the plane transverse to the initial effective wave vector ($\Omega_z = 0$). These results are developed to the third order in T and in Ω for clarity. Additionally, the general expression for three-dimensional rotations considering a non-null first derivative are given in appendix A.

In the same manner as the atomic phase $\Phi^{\text{comp}}_{\text{at}}$ was calculated in section 1.4, this table lets appear the unchanged contributions of the residual Coriolis effect ϕ_{Coriolis} arising from a possibly imperfect stabilization of the mirror's orientation, as well as the higher-order terms resulting from the composition of motions $\phi_{\text{compo.}}$. The phase shifts deriving from the centrifugal accelerations related to the rotation of the chamber $\phi^{\text{chamber}}_{\text{centrifugal}}$ and the mirror $\phi^{\text{mirror}}_{\text{centrifugal}}$ do not involve the position of the sensor head's center of rotation at the first order anymore, due to the hybridization with the classical accelerometer which is also sensitive to this effect. The biggest change is the phase shift associated with the relative acceleration, which is canceled out as a result of the closed-loop operating scheme and only leaves the contribution from the mechanical accelerometer's bias ϕ_{bias} which we want to retrieve in order to compensate

it eventually. Additionally, the term related to the mirror's rotation $\phi^{\text{mirror}}_{\text{rotation}}$ is still present. Ultimately, summing all the contributions above, the output phase shift of the closed-loop hybrid accelerometer with a stabilized reference mirror is given by:

$$\Delta\Phi^{\text{comp}} = \phi_{\text{bias}} + \phi^{\text{mirror}}_{\text{rotation}} + \phi_{\text{Coriolis}} + \phi^{\text{chamber}}_{\text{centrifugal}} + \phi^{\text{mirror}}_{\text{centrifugal}} + \phi_{\text{compo}} \tag{4.6}$$

4.1.4 Systematic phase shift induced by the mirror's rotation

One aspect of the total phase shift $\Delta\Phi^{\text{comp}}$ deserving a particular attention is the contribution arising from the rotation of the mirror, expressed as:

$$\phi^{\text{mirror}}_{\text{rotation}} = k_{\text{eff}} T^3 \left[-a_x \Omega_{\text{my}} + a_y \Omega_{\text{mx}}\right]. \tag{4.7}$$

We consider a mirror's rotation axis restrained to the plane transverse to the Raman laser, regardless of the trajectory of the science chamber. Since this contribution already appeared in the output phase shift of the rotating atom interferometer related to the sole motion of the atoms $\Phi^{\text{comp}}_{\text{at}}$ without any consideration of closed-loop hybridization, this phase shift is likely to be the result of the modification of the wave vector rotating in the frame of the vacuum chamber in addition to have a decreasing norm due to the reducing overlap between the incident and reflected Raman laser beams. This would translate into an atomic scale factor inhomogeneity leading to a systematic phase shift as stated in section 1.4.

However, an independent calculation of the phase shift related to the misalignment between the classical accelerometer, fixed in the mobile frame, and the quantum accelerometer's measurement axis defined by the rotating reference mirror, yields a very similar result. In section 3.3, the phase shift induced by the relative misalignment $\alpha + \beta$ between the two inertial sensors was evaluated. A protocol of alignment of the reference mirror, laser collimator and mechanical accelerometer was then proposed and executed, ensuring a phase shift equal to zero for $\alpha = \beta = 0$. Once implemented on the three axes, a study of the systematic phase shifts should allow for a precise determination of this residual static misalignment.

Now, for a constant rotation of the mirror during the interferometer with an angular velocity Ω_m, the orientation of the wave vector relative to the collimator will evolve as $\alpha(t) = \alpha_0 + \Omega_m t$, $t = 0$ being defined as the beginning of the interferometer. The prior alignment of all the elements at stake allows us to write $\alpha_0 = \beta = 0$, leading to $\alpha(t) = \Omega_m t$. We consider a static Raman laser oriented at an angle θ with respect to the gravity vector, changing slowly enough to be assumed approximately constant

during the interferometer in order to simplify notations. The calculation from section 3.3 with these new considerations yields a phase shift modified as:

$$\phi_{\text{mis}} = -\frac{1}{2} k_{\text{eff}} g \left[T^2 \cos\theta - \frac{\sin^2(\Omega_m T)}{\Omega_m^2} \cos(\theta + 2\Omega_m T) \right]. \tag{4.8}$$

The mirror rotates at typical angular velocities of $\Omega_m \approx 10^{-1}$ rad/s and the interrogation time is limited to $T = 10$ ms. This allows us to use the small angles approximation and, with some trigonometric manipulations, yields the simplified misalignment-induced phase shift:

$$\phi_{\text{mis}} = -k_{\text{eff}} g T^3 \Omega_m \left[\Omega_m T \cos\theta + \sin\theta \right]. \tag{4.9}$$

Considering a static sensor head throughout an interferometer, the transverse acceleration of the atoms is given by $a_y = -g \sin\theta$. Additionally, for a rotation axis along x axis, the contribution of the mirror's rotation to the output phase shift of the hybrid accelerometer simplifies as $\phi^{\text{mirror}}_{\text{rotation}} = k_{\text{eff}} T^3 a_y \Omega_{\text{mx}} = -k_{\text{eff}} g T^3 \Omega_{\text{mx}} \sin\theta$ which leads to $\phi^{\text{mirror}}_{\text{rotation}} = \phi_{\text{mis}}$ at the third order in T for $\Omega_m = \Omega_{\text{mx}}$. Indeed, the phase shift contributions above the order T^4 are neglected in table 4.1 and thus the first term of the misalignment phase, equal to $-k_{\text{eff}} g T^4 \Omega_m^2 \cos\theta$, could not appear in the expression of $\phi^{\text{mirror}}_{\text{rotation}}$.

Hybridization-based compensation of the mirror's rotation in the laser phase

An interesting thing to note is that if we take into account the modification of the wave vector experienced by the atoms during the interferometer (both its rotation and norm decrease) and inject it in the correlation of the classical measurement with the response function of the interferometer, the phase shift related to the rotation of the mirror $\phi^{\text{mirror}}_{\text{rotation}}$ disappears from the output phase shift $\Delta\Phi^{\text{comp}}$. This systematic effect is likely to arise from a rotation of the quantum measurement axis, defined by the reference mirror, with respect to the reference axis of the chamber defined by the classical accelerometer. Given the knowledge of the angle between those two axes at any time, artificially rotating the classical measurement's axis by projecting the output signals of the triad according to the evolution of the wave vector would compensate for the phase shift induced by the mirror's rotation.

It can alternatively be considered in terms of scale factors, with the weighting of the classically measured acceleration components adjusting the scale factor of the classical phase shift to the time-varying scale factor of the matter-wave interferometer related to the effective wave vector's rotation. In practice, it consists in taking into account the angle $\alpha(t) = \Omega_m t$ between the two measurement axes in the correlation product

performed by the real-time software. This calculation is performed in an iterative way with the equivalent phase shift relative to the classical measurement computed throughout the interferometer as:

$$\phi_{\text{cor}}(t+dt) = \phi_{\text{cor}}(t) + f_{\text{RT}}(t+dt)\left[\boldsymbol{k_{\text{eff}}}(t).\boldsymbol{a_{\text{cl}}}(t+dt)\right] \ \forall t \in [0, 2T+4\tau-dt]. \quad (4.10)$$

Since it is difficult for the FPGA-based real-time algorithm to process vector calculus, the actual implementation which does not account for the rotation of the reference mirror can be written:

$$\phi_{\text{cor}}(t+dt) = \phi_{\text{cor}}(t) + f_{\text{RT}}(t+dt)k_{\text{eff}}a_{\text{cl}}(t+dt) \ \forall t \in [0, 2T+4\tau-dt] \quad (4.11)$$

with $k_{\text{eff}} = 4\pi/\lambda$, f_{RT} the simplified response function implemented in the real-time system (defined in equation 3.42) and $a_{\text{cl}}(t+dt) = a_z(t+dt)$ for a Raman beam along the z axis. The proposed solution would simply change this expression by including the reduction of the effective wave vector's norm through the factor $\cos(\Omega_m t)$ as well as its rotation ruled by the rotation matrix $\mathcal{R}(\Omega_m t)$ as follows:

$$\phi_{\text{cor}}(t+dt) = \phi_{\text{cor}}(t)+f_{\text{RT}}(t+dt)\cos(\Omega_m t)\left[\mathcal{R}(\Omega_m t)\boldsymbol{k_{\text{eff}}}\boldsymbol{a_{\text{cl}}}(t+dt)\right] \ \forall t \in [0, 2T+4\tau-dt]. \quad (4.12)$$

An attempt to implement this technique through the real-time vibrations compensation was made, but it proved to be unsuccessful due to practical considerations. Indeed, the rotation of the effective wave vector implies a projection on the other axes and thus to have the different accelerometers intervening in the measurement. The first issue arising from this matter results from the mechanical conception of the sensor head described in chapter 2. By construction, the three mechanical accelerometers are attached to their respective reference mirrors, each separated by approximately ten centimeters from the others. This distance was not taken into account while calculating the lever arm involved in the science chamber's centrifugal acceleration, leading to an incorrect contribution to the phase shift. For the same reason, assuming the structure of the science chamber is not completely rigid, such scheme induces a loss of correlation between the reference mirror's motion and the measurement of the acceleration components by the transverse classical sensors, reducing the efficiency of the vibrations compensation scheme. Ultimately, in the context of the closed-loop hybridization, the computation of the classical accelerometers is indistinguishably performed for the compensation of the vibrations and for the correction of the classical bias. As mixing up the weighted signals of different classical sensors could lead to incorrect biases in the output measurement of the hybrid accelerometer, it appears

preferable not to artificially rotate the classical measurement axis and to process the phase shift $\phi_{\text{rotation}}^{\text{mirror}}$ as an individual systematic phase shift instead, the latter being accounted for in the model of the mid-point theorem anyway.

4.2 Processing the atomic signal in the low-rotation-rate regime

As a first step, it is important to characterize the effect of a rotation of the science chamber with a reference mirror mechanically attached to the rotating frame $\mathcal{R}_c$, i.e. without an independent rotation of the mirror $\boldsymbol{\Omega_m} = \mathbf{0}$. This is necessary to first establish the validity of the theoretical model detailed in sections 1.3 and 4.1, but also to set bounds on the experimental parameters which can be employed before the exponential decay of the atomic fringes' contrast prevents any measurement. Specifically, it consists in evaluating the equivalent acceleration sensitivity σ_a which can be achieved depending on the interrogation time T and the angular velocity $\boldsymbol{\Omega}$ of the instrument in the laboratory frame.

4.2.1 Fringes reconstruction with contrast feedback and phase correction

Let us consider the experimental apparatus described in chapter 2 placed on the rotary table at $\theta_z = -45°$, this angle being reminded in figure 4.2. This orientation leads to two balanced projections of the angular velocity $\Omega_x = \Omega_y$ along the x and y axes of the science chamber (written x_c and y_c in figure 4.2), defined by the measurement axes of the classical accelerometers, when the rotation platform is manually maneuvered along its x axis. The two major consequences of a rotation on an atom interferometer, analyzed in section 1.3, are the exponential decay of the fringes' contrast and the non-gravitational systematic phase shifts induced by the complex trajectory of the atomic cloud in the rotating frame.

The first effect can be described by the simplified equation 1.78, reminded below:

$$C(\Omega) \approx C_0 \exp\left[-\left(\sqrt{\frac{2k_B\mathcal{T}}{m}}k_{\text{eff}}T^2\right)^2\left(\Omega_x^2+\Omega_y^2\right)\right] \tag{4.13}$$

where C_0 denotes the static contrast obtained on a non-rotating instrument and the exponential decay formula is detailed in section 1.3 along with the justifications for the hypotheses and simplifications.

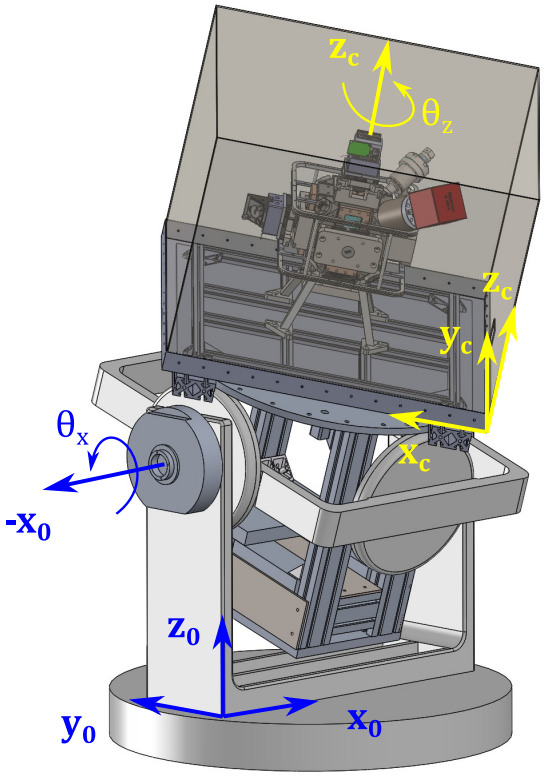

Figure 4.2: Schematic view of the hybrid accelerometer's sensor head placed on the rotary platform introduced in chapter 2. The tilt angle θ_z denotes a rotation of the sensor head along its vertical axis z_c with respect to the rotary table, set before a measurement and constant thereupon, while θ_x is the angle scanned when performing dynamic rotations throughout a set of interferometers.

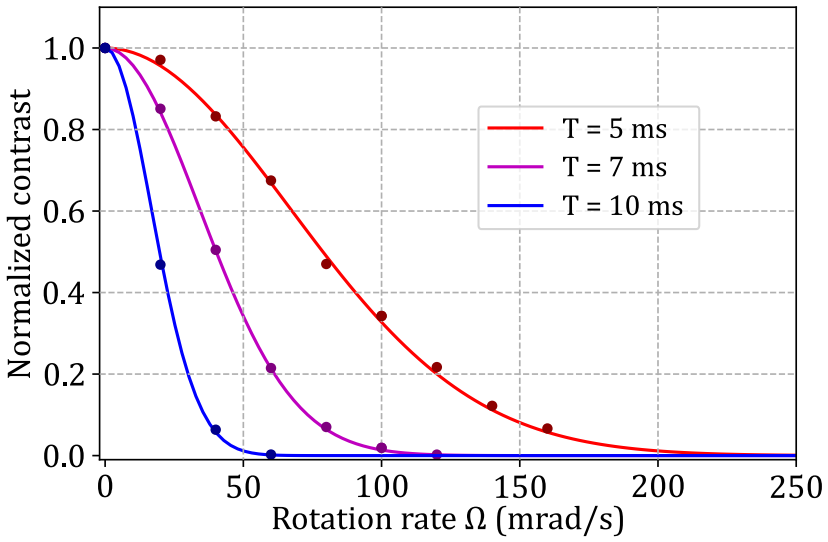

Figure 4.3: Illustration of the exponential decay of the interference pattern's normalized visibility for interrogation times $T = 5$ ms (red), $T = 7$ ms (purple) and $T = 10$ ms (blue). The dots represent experimental data and the straight lines are based on equation 4.13 for a cloud temperature $\mathcal{T} = 3.6$ µK and a normalized static contrast $C_0 = 1$.

This physical outcome is illustrated in figure 4.3 where well controlled angular velocities are applied to the sensor head to verify the agreement between the theory and the exponential decay actually experienced on our apparatus. To do so, the inertial frame attached to the vacuum chamber is maintained immobile while the tip-tilt stage is driven by constant rotation rate signals along the x axis. Hence, performing atom interferometric sequences while scanning the interrogation time and tilt jump amplitude enables us to fit the resulting fringes and retrieve the evolution of the contrast in various situations. It is important to note that the rotation rate being constant during an interferometer but also from one measurement to the other, the phase shift induced by the rotation of the mirror remains the same for a given data set and does not hinder the fitting of the atomic fringes. To coherently compare the different sets of data, the contrast C_0 is evaluated beforehand in static so that a reference value is determined for each interrogation time. Consequently, data are recorded while the apparatus is undergoing rotations and the resulting measured contrast is divided by the static reference value, yielding a normalized value only influenced by the angular motion. The initial tilt angles of the sensor head are $\theta_{\mathrm{x,z}} = 0°$ so that the contrast inhomogeneities related to the atomic cloud falling out of the Raman laser do not play part in this study. The exponential decay of the obtained normalized contrast of the uncompensated atomic fringes is then given by the red, purple and blue dots for interrogation times $T = 5$ ms, $T = 7$ ms and $T = 10$ ms respectively. The straight lines plotted in the same colors depict the theoretical contrast calculated with equation 4.13 for a cloud temperature $\mathcal{T} = 3.6$ µK. This value is consistent with independent measurements of the atoms' temperature via counter-propagating Raman spectroscopy. We observe a very good agreement between the experimental data points and the theoretical curves, indicating the correctness of the theoretical model and the applicability of the hypotheses made to reach the simplified expression.

As for the total phase shift at the output of the interferometer, it is important to mention that all the data presented in this chapter were recorded while our instrument is operated in closed-loop configuration. Hence, the relevant equation describing this parameter is the one given in section 4.1 which accounts for the correlation with the classical accelerometer. At the third order in the interrogation time T and angular velocity Ω, considering the latter is constant and the rotation axis is contained in the transverse plane ($\Omega_z = 0$), this expression is written:

$$\begin{aligned}\Delta\Phi = k_{\mathrm{eff}}T^2\Big[&b_z - 2(v_x + a_xT)\Omega_y + 2(v_y + a_yT)\Omega_x \\ &- \left(z_0^{\mathrm{CA}} - 3v_zT + 2x_0\Omega_yT - 2y_0\Omega_xT\right)\Omega^2\Big].\end{aligned} \tag{4.14}$$

In order to focus on the rotations only, we define a rotation phase $\phi_{\text{rot}} = \phi_{\text{bias}} - \Delta\Phi$ which does not account for the bias of the classical inertial sensor anymore. In practice, a tracking of the classical bias is performed regularly with a static apparatus in order to suppress its effect on the atomic fringes before performing atom interferometers in rotation. All the inertial components, namely acceleration, velocity and position of the atomic wave packet relative to the reference mirror are defined with respect to their values at the instant of the first laser pulse (taken as initial conditions). Acceleration is considered constant in the context of the closed-loop hybridization, where the high-frequency vibrations are equally sensed by the quantum and classical accelerometers and thus compensated for, and velocity can be computed from the moment the atoms are released from the optical molasses, since the atoms are trapped and have no relative velocity in the frame of the experimental chamber prior to this point. Furthermore, we know that the only translational acceleration affecting the atomic cloud comes from the gravity $\boldsymbol{g} = -g.\boldsymbol{u_z}$ which allows us to specify the expressions of the atomic cloud's inertial components:

$$\begin{cases} a_x = g\sin(\theta_z)\sin(\theta_x) = -\dfrac{g}{\sqrt{2}}\sin(\theta_x) \\ a_y = g\cos(\theta_z)\sin(\theta_x) = \dfrac{g}{\sqrt{2}}\sin(\theta_x) \\ a_z = -g\cos(\theta_x) \end{cases} \quad \begin{cases} v_x = -\dfrac{g}{\sqrt{2}}\sin(\theta_x)TOF \\ v_y = \dfrac{g}{\sqrt{2}}\sin(\theta_x)TOF \\ v_z = -g\cos(\theta_x)TOF \end{cases} \tag{4.15}$$

where we observe that $a_x = -a_y$ and $v_x = -v_y$. Furthermore, with the particular tilt angle $\theta_z = -45°$, the two transverse gyroscopes measure the same projection of the angular velocity $\Omega_x = \Omega_y \simeq \Omega/\sqrt{2}$. Ultimately, we neglect the terms scaling as Ω^3 as well as the term scaling as $T^3.TOF$ which are negligible given our experimental parameters and operating conditions. Combining equations 4.14 and 4.15, this yields the simplified expression:

$$\phi_{\text{rot}} = k_{\text{eff}}T^2\Big[-2g\sin(\theta_x)(T+TOF) + z_0^{\text{CA}}\Omega^2\Big]. \tag{4.16}$$

In practice, with a fixed laser phase ϕ_{las}, the atomic fringes will be scanned by both the tilt angle θ_x and angular velocity Ω while maneuvering the rotary platform.

Determination of the sensor head's tilt angle

The signals from the mechanical accelerometers attached to the y and z axes, in addition to the x and y axes fiber-optic gyroscopes, are streamed at $f_{\text{acq}} = 2.5$ kHz. The mechanical accelerometer on the z axis is used to deduct the absolute tilt angle of the sensor head during the interferometer through the projection of the gravity vector

$|\theta_x| = \arccos(-a_z/g)$, while the y axis accelerometer allows us to determine its sign. The first phase shift related to the Coriolis acceleration lets appear the tilt angle of the experiment θ_x, which is naturally varying when an angular velocity is applied to the rotary table. However, in a first approximation, this tilt angle is considered constant during an atom interferometer as the inertial components taking part in this equation are expressed at the beginning of the interferometer[1]. Furthermore, a rotation at a speed $|\Omega| \leqslant 250$ mrad/s during a $2T = 20$ ms-long interferometer will induce a tilt angle difference of $|\delta\theta| < 0.3°$ which is small compared to the average tilt angle $\overline{\theta}$ in most cases. It is important to note that for inclinations not verifying the previous assertion, i.e. for very little angles, the terms proportional to $\sin(\theta)$ are negligible and the terms scaling as $\cos(\theta)$ are not sensitive to the tilt angle at the first order anymore, confirming that the assumption of a constant inclination is reasonable in our operating conditions. Furthermore, taking an isolated measurement of the mechanical accelerometer at the beginning of the interferometer would make our estimation of the angle highly sensitive to the noise of the classical sensor. For this reason, we decide to keep the average value of the tilt angle over the atom interferometer $\theta_x \approx \overline{\theta_x^{\mathrm{AI}}}$.

Distances and lever arms measurement

As for the initial position of the atomic cloud, it can be measured with respect to the reference mirror's surface corresponding to the parameter z_0^{MA} by executing a frequency jump $\Delta\nu$ to the Raman laser at the π pulse of the interferometer. This operation introduces an additional phase shift equal to:

$$\Delta\phi = \frac{8\pi d_\pi}{c}\Delta\nu \tag{4.17}$$

with d_π the distance between the atomic cloud and the reference mirror at the instant of the π pulse and c the speed of light [Xu et al. 2021].

Applying different frequency jumps ranging from -20 MHz to $+20$ MHz allowed us to fit a linear function to the experimental points as displayed in figure 4.4 for two different orientations $\theta_x = 0°$ (blue) and $\theta_x = -20°$ (red). This fit produced very similar results regardless of the orientation, notably a slope $\Delta\phi/\Delta\nu = 0.0105$ rad/MHz on a vertical sensor head with a squared linear correlation coefficient equal to $r^2 = 0.998$ and finally led to a distance equal to $d_\pi = 10.5.10^{-6}c/(8\pi) = 125.3$ mm. Since the displacement of the atomic cloud follows the equation $z(t) = g\cos(\theta_x)t^2/2$ and assuming the position of the cloud when released from the optical molasses is

[1] To account for the variation of this angle, the acceleration components themselves should not be considered constant and it is the whole model of the phase shift, established using the mid-point theorem, which should be revised.

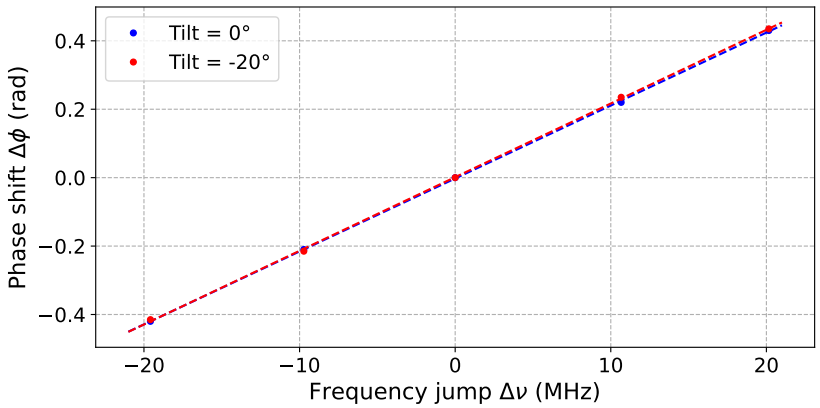

Figure 4.4: Evolution of the phase shift of the atomic fringes $\Delta\phi$ when applying a frequency jump $\Delta\nu$ at the π pulse of the interferometer for a tilt angle $\theta_x = 0°$ (blue) and $\theta_x = -20°$ (red) of the sensor head. The slope of this evolution yields the distance of the atomic cloud relative to the reference mirror's surface according to equation 4.17.

always the same, we calculate its value with respect to the measured position at the π pulse on a vertical sensor head ($\theta_x = 0°$): $z^{\mathrm{MA}}_{\mathrm{GMol}} = d_\pi + g(TOF + T)^2/2 = 129.7$ mm for $TOF = 20$ ms and $T = 10$ ms. The initial position of the atomic wave-packet can be determined along the three axes by adding the tilt-dependent displacement of the cloud during the time-of flight, related to the three components of the gravity vector. Along the axis normal to the mirror, this yields:

$$z_0^{\mathrm{MA}}(\theta) = 129.7 \text{ mm} - \frac{1}{2} g \cos(\theta) TOF^2. \tag{4.18}$$

Consequently, the initial position of the atoms relative to the classical accelerometer's proof mass can be determined using the expression $z_0^{\mathrm{CA}} = z_0^{\mathrm{MA}} + d_m + (d_{\mathrm{CoR}} - z_0^{\mathrm{cl}})$ where the different distances involved are summarized in figure 4.1. The tip-tilt platform's lever arm given in the data sheet amounts to 3.3 mm, which must be added to the 4 mm thickness of the reference mirror. This leads to $d_m = 7.3$ mm. Furthermore, the distance between the mirror's center of rotation and the edge of the mechanical accelerometer was measured on the experimental apparatus and verified on the 3D model, yielding a value equal to 58.7 mm. One subtlety being that the classical sensor is 19.8 mm deep, the position of its test mass cannot be accurately determined. In a first approximation, we assume it is placed in the middle of the device and we can write the required parameter:

$$\begin{aligned} z_0^{\mathrm{CA}}(\theta) &= 75.9 \text{ mm} + z_0^{\mathrm{MA}}(\theta) \\ &= 205.6 \text{ mm} - \frac{1}{2} g \cos(\theta) TOF^2. \end{aligned} \tag{4.19}$$

Analysis of the contrast decay and phase scrambling

Once all the parameters involved in the rotation phase shift ϕ_{rot} are known from the measurements of the classical inertial measurement unit, it is possible to retrieve information from the atomic measurements. Matter-wave interferometry sequences are performed with a fixed laser phase equal to $\phi_{\text{las}} = \pi/2$ rad. This choice of the laser phase value ensures a maximum sensitivity of the population ratio N_2/N_{tot} to the output phase of the interferometer Φ by operating on a linear section of the fringes. The time of flight of the atomic cloud before the interferometer is equal to $TOF = 20$ ms and the interrogation time is set at $T = 6$ ms due to its strong influence on the reduction of the visibility of the interference pattern.

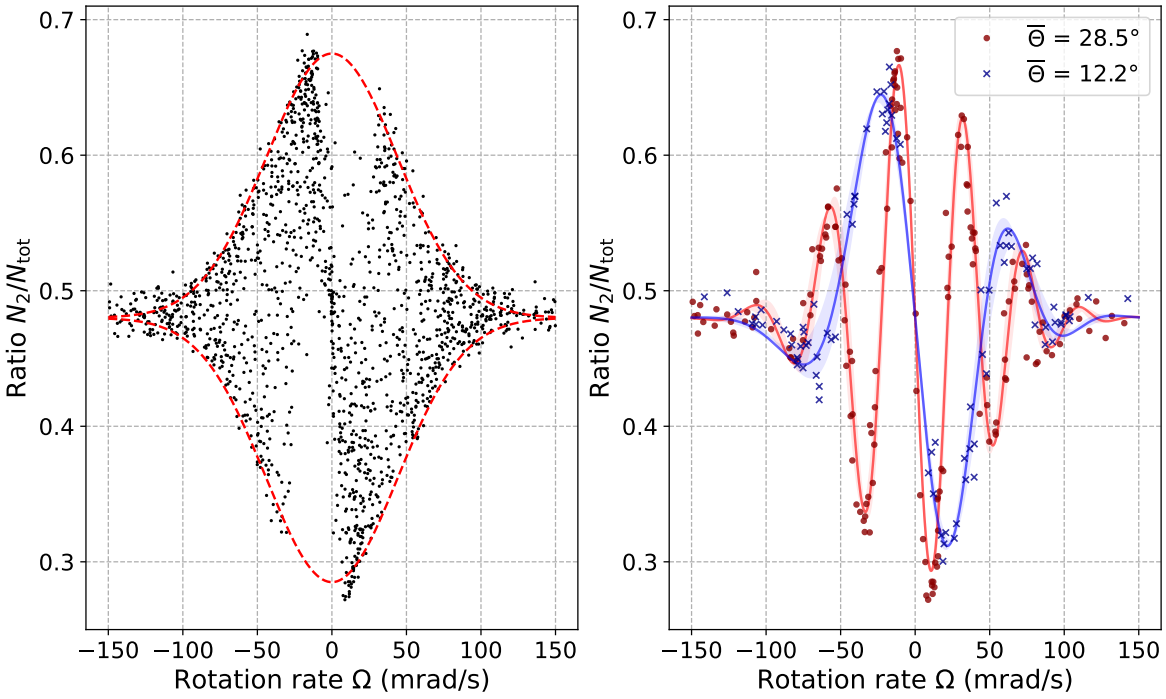

Figure 4.5: Measured population ratio N_2/N_{tot} as a function of the angular velocity of the science chamber. (Left) Concatenated data of the 1600 runs performed for tilt angles $\theta_x \in [0, 30]°$ at $T = 6$ ms. Each black dot corresponds to the measurement of an atom interferometer while the dashed red line is an envelop defined by the rotation-induced contrast drop. (Right) Filtered data for two specific intervals $\theta_x \in [11, 13]°$ (blue) and $\theta_x \in [27, 30]°$ (red). The solid lines are calculated using the models established for the contrast decay and rotation phase shift. The areas filled in lighter colors exhibit the extrema of the chosen angle ranges.

To that end, we measure the ratio of the population in the upper ground state $P = N_2/N_{\text{tot}}$ expressed as:

$$P(C, \phi_{\text{rot}}) = P_0 - \frac{C(\Omega)}{2} \cos(\phi_{\text{rot}}) \tag{4.20}$$

with the angular velocity-dependent contrast $C(\Omega)$ defined by equation 4.13 and the rotation phase ϕ_{rot} defined by equation 4.16. We display these population ratios in figure 4.5 where the left-hand graph shows the output of 1600 interferometers. Data were recorded at $T = 6$ ms for tilt angles $\theta_x \in [0, 30]^\circ$ and angular velocities $|\Omega| \leqslant 150$ mrad/s. The dashed red line exhibits the model of the contrast decrease as a function of the rotation rate based on equation 4.13 with no free parameters and an atomic cloud temperature $\mathcal{T} = 3.6$ µK measured independently through Raman spectroscopy. If this graph demonstrates a good agreement with the experimental data, no more information can be extracted from this plot as the rotation phase depends on several parameters. However, reducing the output of the atomic measurements in narrow intervals of the tilt angle θ_x, it is possible to observe the oscillations characteristic of an interference pattern. This analysis is presented on the right-hand plot, where data were filtered in two distinct intervals $\theta_x \in [11, 13]^\circ$ (blue) and $\theta_x \in [27, 30]^\circ$ (red). The solid lines are calculated using equation 4.20, while the areas filled in lighter colors show the uncertainty related to the span of the tilt angle intervals. Here as well, we observe a very good agreement between the data points and the theoretical curve — graphed with no adjustable parameters — (coefficient of determination $R^2 \approx 0.95$). This shows that our model, both for the loss of contrast and the phase term associated with rotations, describes well the effects of rotations on an atom interferometer, within the parameters of our experiment, and therefore that we are able to reconstruct the interference fringes in the presence of rotations. Beyond this reconstruction, data shown in figure 4.5 demonstrate that for a well-known tilt angle of the sensor head, the hybridization between our atom interferometer and the fiber-optic gyroscopes enable the achievement of an atomic gyroscope fitted with a high dynamic range and able to operate at any arbitrary orientation.

4.2.2 Performance of the uncompensated rotating atom accelerometer

Now that we have demonstrated our good understanding of the measurements performed by a rotating atom interferometer, we are able to apply a normalization of the ratio using the model of the rotation-induced decrease of the fringes' visibility defined in equation 4.13 as well as a correction of the rotation-induced systematic phase shifts using the rotation phase ϕ_{rot} defined in equation 4.16. This way, we should be capable of reconstructing the atomic interference pattern in order to retrieve the desired acceleration information.

Figure 4.6 summarizes the fringes reconstruction process for matter-wave interfero-

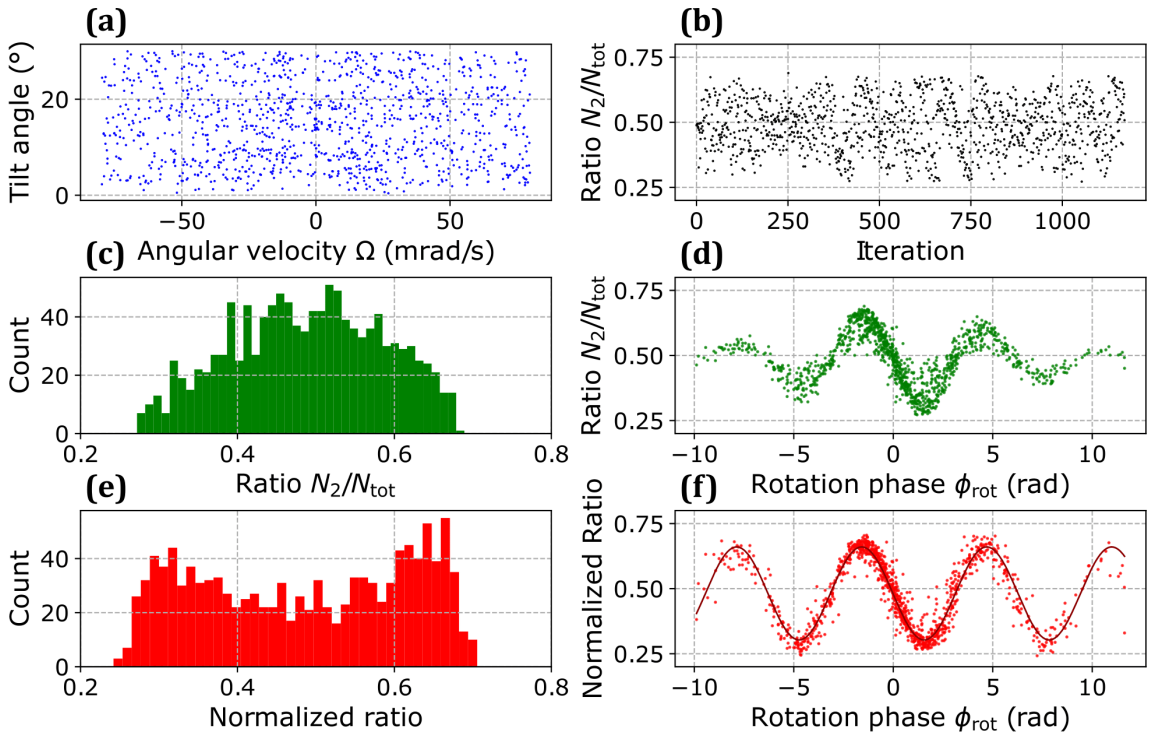

Figure 4.6: Fringes reconstruction process on a Mach-Zehnder atom interferometer undergoing arbitrary rotations with a reference mirror attached to the rotating frame. (a) Distribution of the tilt angles $\theta_x \in [0, 30]°$ and angular velocities $\Omega \in [-80, 80]$ mrad/s for each run. (b) Measured population ratios at the output of each interferometer with a constant phase offset $\phi_{las} = \pi/2$ applied on the laser at the third Raman pulse. (c) Histogram of the measured population ratios exhibiting a Gaussian shape centered on the ratio offset P_0. (d) Same plot as (b) with the population ratios plotted as a function of the rotation phase ϕ_{rot}. This graph features oscillations characteristic of an interference pattern, a decreasing contrast at high phases due to the angular velocity Ω and a thick line due to the different couples (θ_x, Ω) yielding the same rotation phase ϕ_{rot}. (e) Histogram of the population ratios normalized with the model of the rotation-induced contrast decay, revealing a bimodal distribution characteristic of a sinusoidal pattern. (f) Atomic fringes reconstructed by representing the normalized population ratios as a function of the rotation phase ϕ_{rot}. The dark red line shows a cosine fit to the data points using equation 4.20 which produces a contrast $C = 35.7\%$ and a signal-to-noise ratio $SNR = 8.6$.

metric measurements performed as described previously in this section. The angular velocities are restricted to $|\Omega| \leqslant 80$ mrad/s, limit above which the atomic fringes are extinguished. The distribution of the tilt angles $\theta_x \in [0, 30]°$ and rotation rates $\Omega \in [-80, 80]$ mrad/s for each measurement is exhibited in figure 4.6 (a), showing that these two parameters are scanned fairly uniformly over all the recorded runs. The measured population ratio N_2/N_{tot} at the output of each interferometer is displayed in figure 4.6 (b), where they appear as noise due to the rotation-induced phase scrambling. Additionally, the exponential decay of the contrast due to arbitrary rotation rates is highlighted by the distribution of the ratios shown in figure 4.6 (c). Here, the Gaussian

envelope of the histogram is a signature of the contrast loss as it reveals a spread noise around the ratio offset due to the arbitrary distribution of measurements under low rotation rates, where the contrast is preserved, and high rotation rates which extinguish the latter.

As a first step of the post-correction process, the rotation phase ϕ_{rot} is calculated from the knowledge of the interrogation time T, the determination of the initial distance between the mechanical accelerometer's proof mass and the atomic cloud z_0^{CA} described above and the measurements of the classical IMU using equation 4.16. Displaying the population ratios as a function of the resulted rotation phase - and not only the rotation rate Ω as in figure 4.5 -, the oscillations characteristic to an interference pattern become noticeable as presented on the green dots in figure 4.6 (d). While only the rotation rate of the instrument has an impact on the contrast of the fringes, the rotation phase is influenced by both the tilt angle of the sensor head and its angular velocity. For this reason, several couples of these two parameters can lead to the same value of ϕ_{rot} but will produce a different population ratio, justifying the thickening of the line formed by the data points. Furthermore, the amplitude of the population ratio variations is naturally decreasing with the absolute value of the rotation phase since the latter is strongly impacted by the rotation rate, as is the contrast, until the "fringes" are completely extinguished. This is notably why only data points recorded at angular velocities below 80 mrad/s are considered here, as it will be discussed in the next subsection.

Ultimately, this correction of the phase scrambling was coupled to a normalization of the measured ratios based on the model of the contrast's exponential decay described above. If we take up the expression of the population ratio $P(C, \phi_{\text{rot}})$ given in equation 4.20, it is possible to apply a simple correction given the knowledge of the population ratio offset P_0, the static contrast C_0 and the rotation-induced contrast decay $C(\Omega)$ given by equation 4.13, following the expression:

$$\widetilde{P} = \frac{C_0}{C(\Omega)}\Big[P(C, \phi_{\text{rot}}) - P_0\Big] + P_0. \tag{4.21}$$

By doing so, the data points are repositioned on the ordinate axis according to the population ratio which should have been measured in the absence of any contrast decrease. Henceforth, the rotation of the instrument should not influence the amplitude of the interference fringes anymore and the contrast should be constant over the runs performed. It is important to note that this normalization does not artificially improve our performances as it only impacts the amplitude of the reconstructed fringes. Consequently, it does not modify the phase noise σ_ϕ and the signal-to-noise ratio,

defined by $SNR = C/\sigma_\phi$, should eventually be the same as what it usually is in the same conditions, specifically limited by the static contrast C_0 and the regular phase noise arising from vibrations or laser instabilities for instance. The final result of this reconstruction process is depicted on the third row's red graphs of figure 4.6. The histogram of the normalized ratios in figure 4.6 (e) reveals a bimodal distribution which contrasts with the Gaussian shape of the histogram of the raw ratios. As mentioned previously, the bimodal distribution being a distinctive feature of a sinusoidal pattern, it demonstrates the recovery of the contrast of the atomic fringes as supported by the red sine function in figure 4.6 (f). The light red dots represent the result of each atom interferometer just as the plot above, only the ordinate axis no longer displays the raw population ratio but instead the normalized ratio using equation 4.21. Since the parameter displayed in abscissa is the same, we observe the same oscillations as before with the extrema in the same positions, but the amplitude of the fringes now looks fairly constant over the rotation phase ϕ_{rot} scanned over more than twenty radians.

It is now possible to fit a cosine function to the experimental data, using the simpler expression of the normalized ratio:

$$\widetilde{P} = P_0 - \frac{C_0}{2}\cos(\phi_{rot}) \tag{4.22}$$

which is illustrated by the dark red plain curve in figure 4.6 (f). Using the same method as for a static apparatus, this fit allows us to retrieve the key parameters related to the performance of the fringes reconstruction process. In particular, this operation returns a contrast $C_0 = 35.7\%$ and a signal-to-noise ratio equal to $SNR = 8.6$. In terms of sensitivity to acceleration, we can use the following expression to estimate a value from the signal-to-noise ratio:

$$\sigma_a = \frac{1}{k_{\text{eff}} T^2}\frac{2}{SNR} \approx 41.2 \text{ µg/shot} \tag{4.23}$$

the factor 2 coming from the definition of the contrast. This sensitivity is limited by the maximum interrogation time $T_{\text{max}} = 6$ ms achievable in the range $|\Omega| \leqslant 80$ mrad/s. Furthermore, we could consider implementing a real-time control of the rotation phase ϕ_{rot} similar to the control of the laser phase ϕ_{las} in order to maintain the measurement at $\phi_{\text{rot}} = \pm\pi/2$ where the sensitivity of the population ratio to the rotation phase is maximum.

4.2.3 Performances degradation while exploring the full dynamic range of the rotating sensor

If the results presented in the previous subsection are a compelling first step in the process of retrieving acceleration information from a rotating atom interferometer, the technique still presents significant limitations which must be carefully investigated in order to determine the conditions required for applying the fringes reconstruction scheme.

Indeed, the acceleration sensitivity calculated in the previous subsection is estimated on a wide range of angular velocities $|\Omega| \leqslant 80$ mrad/s for which it is still possible to reconstruct the atomic fringes as some amplitude remains in the population ratio oscillations. Furthermore, the signal-to-noise ratio is intrinsically related to the contrast $C(\Omega)$ and thus to the static contrast C_0. Here, the presence of data recorded at very low rotation rates allowed us to get back the interference pattern with a fairly high contrast, yielding a decent signal-to-noise ratio which is not necessarily representative of the performance of the interferometer at high rotation rates. In order to further investigate the performance of the reconstruction process, one interesting thing to do would be to slice the data into narrower angular velocity intervals in order to observe the sensitivity variations on each independent range.

Figure 4.7 exhibits the result of individual analyses of the interferometric fringes on narrow angular velocity ranges. To that end, experimental data are filtered in intervals of 10 mrad/s so that the contrast and rotation phase do not vary too much within a given interval. Subsequently, a cosine function is fitted to the filtered experimental points in order to retrieve the SNR proper to each situation. The resulting measurements are plotted in figure 4.7 (left) represented as black dots and as a function of the average rotation rate of the runs contained inside a given range of angular velocities. We can observe an abrupt decrease in the signal-to-noise ratio which could derive from both the contrast decay and the increasing rotation phase noise. To determine the origin of this degradation, a theoretical prediction based on the data points was made.

We assume an atomic cloud temperature $\mathcal{T} = 3.6$ µK and a static signal-to-noise ratio $SNR_0 = 17.8$ extrapolated from the two first points at $\Omega \leqslant 20$ mrad/s, where the rotation-induced contrast decrease is assumed negligible. The third and most important hypothesis is that the phase noise of the atomic fringes remains constant, regardless of the angular velocity Ω. Under these assumptions, the evolution of the SNR related to the contrast decay only was calculated and displayed as a red curve in figure 4.7 (left). Apart from some experimental measurements slightly remote from the

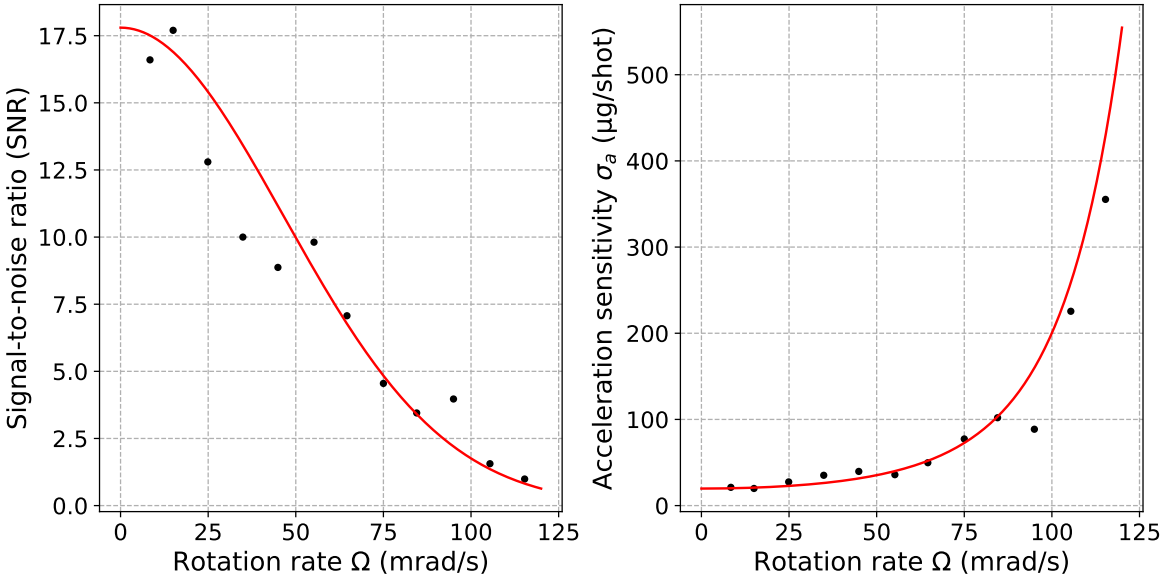

Figure 4.7: Evolution of the performances of the rotating interferometer with the fringes reconstruction process in the absence of mechanical compensation on the reference mirror. (Left) For each rotation rate interval, the signal-to-noise ratio is measured from the fit of raw atomic fringes and plotted as black dots. The red curve is a theoretical prediction of the SNR drop with a cloud temperature $\mathcal{T} = 3.6$ µK, a constant phase noise of the atomic fringes (i.e. independent from the angular velocity) and a static value $SNR_0 = 17.8$ extrapolated from the two first points at $\Omega \leqslant 20$ mrad/s, where the rotation-induced contrast decrease is assumed negligible. (Right) Corresponding acceleration sensitivity converted from the SNR values using equation 4.23, both for experimental measurements (black dots) and theoretical prediction (red curve).

theoretical curve, we observe an overall good agreement with the theory, demonstrating that the performance degradation is primarily limited by the rotation-induced contrast decrease.

Figure 4.7 (right) displays the sensitivity to acceleration of the atomic measurement, calculated from the SNR values using equation 4.23 for both the experimental measurements (black dots) and theoretical prediction (red curve). If the sensitivity remains fairly constant below 40 µg/shot for rotation rates up to 60 mrad/s, it diverges rapidly above this limit until no proper measurement is possible anymore.

Figure 4.8 exposes the results of the fringes reconstruction scheme applied outside its working range, i.e. for couples (Ω, T) of rotation rates and interrogation times completely suppressing the contrast of the fringes. Data were filtered to retain the interferometers performed at rotation rates $|\Omega| \geqslant 100$ mrad/s, still for an interrogation time $T = 6$ ms. On the left-hand plot, these ratio measurements are displayed as a function of the rotation phase ϕ_{rot} but no significant difference can be made with the unsorted ratios as their distribution is overall flat. When applying the ratio normalization to each interferometer, aberrant results are returned as the negligible

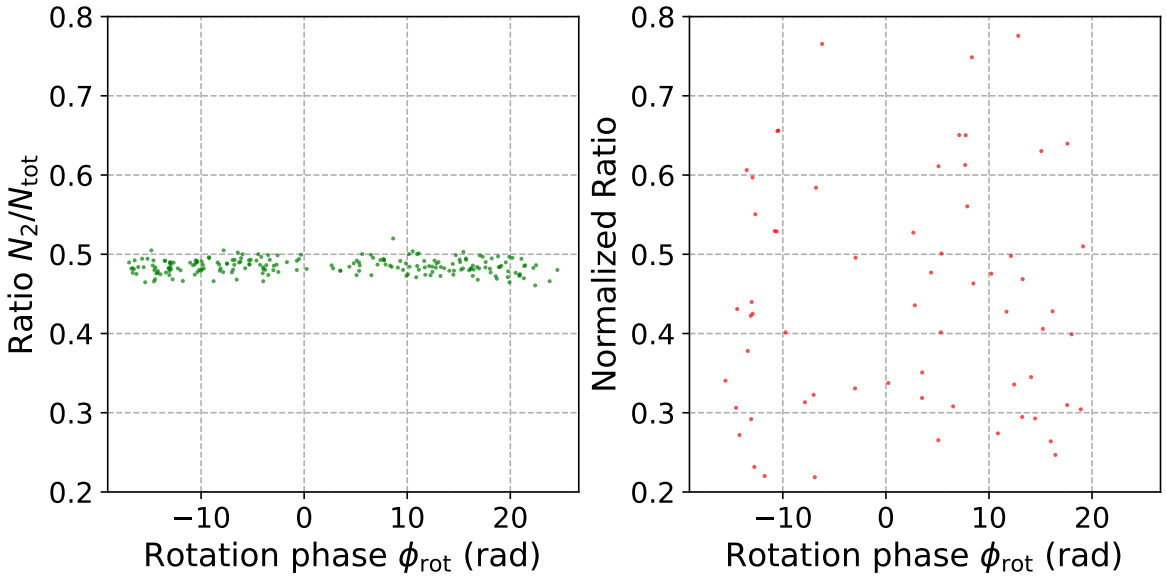

Figure 4.8: Demonstration of the fringes reconstruction process limitation at angular velocities $|\Omega| \geqslant 100$ mrad/s for which the signal is completely extinguished. Points recorded at $|\Omega \in [80, 100]$ mrad/s were omitted as some of them still exhibit a non-zero contrast. (Left) The flat distribution of the population ratios N_2/N_{tot} demonstrates the extinguished contrast and the inability of reconstructing an interference fringes pattern even with the calculation of the rotation phase ϕ_{rot}. (Right) The normalization of the population ratio proves to be meaningless with a random repositioning of the experimental points on the ordinate axis, up to aberrant normalized ratios of several hundreds - though the window is restricted to $[0.2, 0.8]$ for clarity.

contrast dividing the raw ratios leads to normalized values up to several hundreds and the right-hand graph, which should reveal the reconstructed fringes, only outputs a meaningless point cloud, final proof that we cannot reconstruct a signal which is already below the noise limit.

As a conclusion, the loss of contrast restricts the accessible experimental parameters to low angular velocities and short interrogation times. Indeed, while it is always possible to correct for the rotational phase terms provided a sufficiently good knowledge of the sensor head's motion during the interferometer, the loss of contrast constitutes a fundamental limit as no reconstruction of the interference fringes is possible if the contrast becomes lower than the noise threshold. For the purposes of retrieving an acceleration measurement out of a rotating atom interferometer outside this operating range, it thus appears essential to tackle the exponential decay of the contrast first and foremost.

In order to be able to perform atom interferometry at high rotation rates, it is necessary to limit or cancel the loss of contrast. Looking at equation 1.78, the two parameters which can be exploited for this purpose are the atomic cloud's temperature

$\mathcal{T}$ and the interferometer's interrogation time T. Regarding the interrogation time, it is intrinsically related to the atomic accelerometer's sensitivity thus it is not the best option to reach the best performance. Therefore, one approach could be to significantly reduce the temperature of the atoms. For example, with an interrogation time of 10 ms and a maximum rotation rate of 200 mrad s^{-1}; if we wish to limit the contrast drop to fifty percent, the atoms' temperature has to be 35 nK or lower. Although such temperatures can be reached through velocity selection [Kasevich et al. 1991] or evaporative cooling [Anderson et al. 1995] among other techniques, they come with drawbacks such as reduced number of atoms, longer measurement dead times and more complex setups. Furthermore, such methods could present additional challenges in the context of our multi-axis hybrid accelerometer as the condensation of atoms does not ensure such low temperatures in the three dimensions. Instead of reducing the temperature of the atoms to mitigate the loss of contrast of the interferometer, and based on the fact that this loss is the consequence of the rotation of the wave vector of the Raman transition, our approach is to keep the orientation of the reference mirror constant in the laboratory frame $\mathcal{R}_0$ for the duration of the interferometer by applying to this mirror a rotation opposed to that of the science chamber.

4.3 Atom interferometry under arbitrary strong rotations

4.3.1 Mechanical stabilization of the reference mirror's orientation

In order to achieve contrast loss-free atom interferometry under arbitrary rotations, which may vary during a measurement sequence or from an interferometer to the other, it is first necessary to measure the rotation components applied on the science chamber with the highest accuracy and sensitivity possible. The single-axis rotation compensation scheme, including the measurement of the angular velocity components in the plane transverse to the Raman laser axis and a real-time stabilization of the reference mirror's orientation in the laboratory frame, is illustrated in figure 4.9.

The signals from the fiber-optic gyroscopes (FOG) introduced in section 2.3 are exploited to drive a piezoelectric tip-tilt platform (see section 2.4) on which the reference mirror is mounted in order to perform a rotation of the mirror of equal amplitude and opposite direction to the rotation of the sensor head. For this purpose, the components of the rotation vector are integrated over an arbitrary period of time with their signs

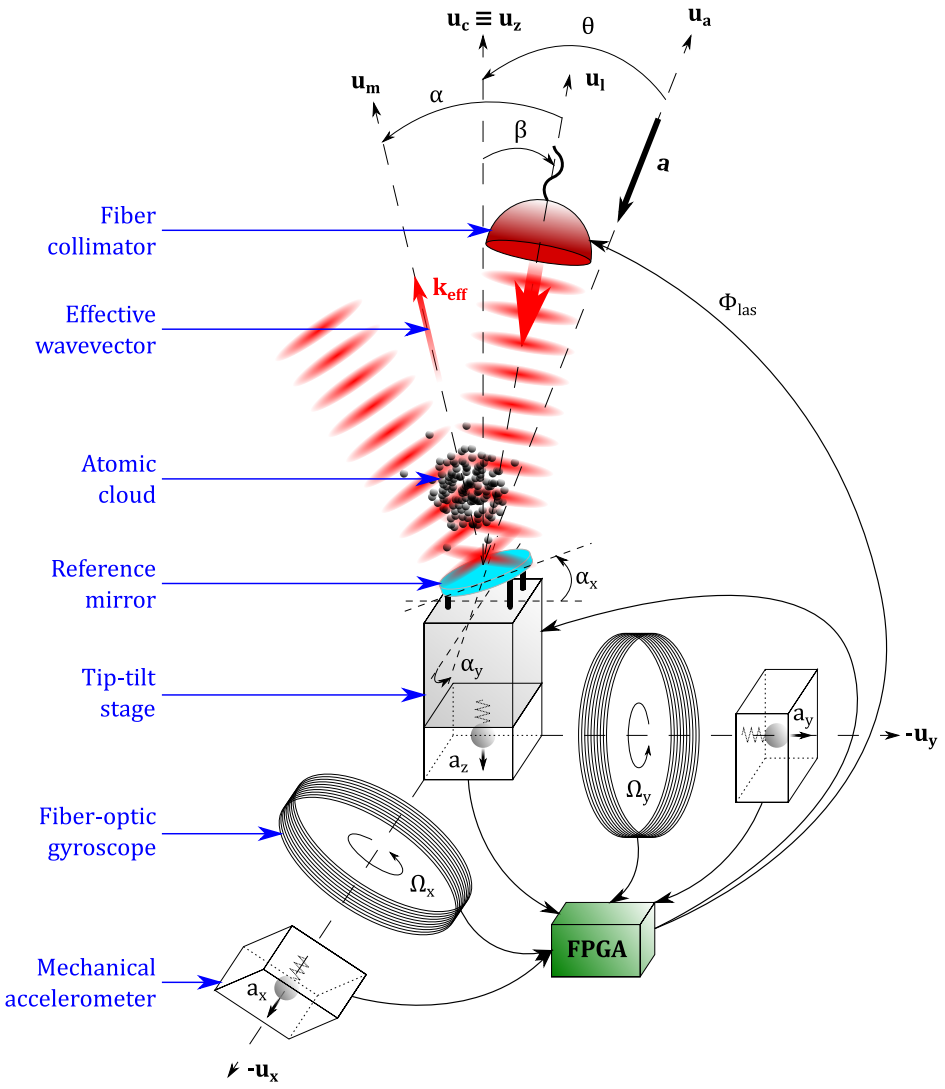

Figure 4.9: Schematic representation of the single-axis rotation compensation scheme. Two fiber-optic gyroscopes (FOG) are placed along the x and y axes of the rotating frame, mechanically attached to the instrument's body. The reference mirror along the z axis, used to perform the matter-wave interferometry sequence, is placed on a piezo-actuated tip-tilt platform. The angular velocity components measured by the FOGs are sent to an FPGA board driving the tip-tilt stage in order to stabilize the orientation of the effective wave vector in the laboratory frame.

reversed to generate a rotation vector describing the opposite evolution of the sensor head's tilt angle in this time interval. The negative sign serves to generate a setpoint angle which will help returning to the initial orientation of the mirror before the rotation of the sensor head. Subsequently, the components of this rotation vector are used to fill a three-dimension rotation matrix applied to the initial wave vector of the laser, yielding a setpoint wave vector rotated at the opposite of the science chamber. Ultimately, a change of basis allows to express this vector in the frame of the tip-tilt platform and in particular along its motion axes, finally generating angular setpoints for the piezo-electric actuators attached to the reference mirror to compensate

for the instrument's rotation. This process is performed in an iterative way, such that the number of corrections applied by the tip-tilt stage can vary from one in an interferometer to one every clock cycle of the FPGA board.

The maximum deflection angle of the tip-tilt is 35 mrad which is amply sufficient for our application since we do not exceed a total interferemoter time of $2T = 20\,\text{ms}$ and angular velocities of 300 mrad/s which correspond to a maximum rotation of 6 mrad. The interferometric measurements are limited to the z axis and, the matter-wave interferometer being invariant by rotation around its measurement axis, the component Ω_z is not considered in the first instance. Consequently, the FOGs described in section 2.3 were mounted on the x and y axes of the sensor head in order to measure the transverse rotation components $\Omega_x(t)$ and $\Omega_y(t)$. Nevertheless, as the reference mirror rotates throughout the interferometer, the Raman laser axis is no longer aligned with the z axis of the mobile frame and the projection of the rotation along this direction will take part in the evolution of the wave vector. The full calculation including the three components of the rotation vector can be found in appendix B.

Description of the real-time algorithm

Figure 4.10 summarizes the operation of the compensation scheme aiming at stabilizing the laser's effective wave vector's orientation in the laboratory frame. The objective being to compensate for the rotation of the science chamber in the laboratory frame, the signs of the FOGs measurements are flipped before they are then integrated over the interrogation time T, yielding the setpoint rotation angles between two successive Raman pulses noted $\theta_{\text{x,y}}(t) = -\Omega_{\text{x,y}}(t)T$. The resulting rotation vector $\boldsymbol{\theta}(t) = (\theta_x(t), \theta_y(t), 0)^T$ can be put under the form $\boldsymbol{\theta}(t) = \theta(t)\,\boldsymbol{N}(t)$ with $\theta(t) = \sqrt{\theta_x^2(t) + \theta_y^2(t)}$ the rotation angle and $\boldsymbol{N}(t) = (N_x(t), N_y(t), 0)^T$ the rotation axis, where $N_{\text{x,y}}(t) = \theta_{\text{x,y}}(t)/\theta(t)$.

This allows us to compute the general expression of a transverse rotation matrix defined by its norm and axis, written:

$$\mathcal{R}(\theta(t)) = \begin{pmatrix} N_x^2(1-\cos\theta)+\cos\theta & N_xN_y(1-\cos\theta) & N_y\sin\theta \\ N_xN_y(1-\cos\theta) & N_y^2(1-\cos\theta)+\cos\theta & -N_x\sin\theta \\ -N_y\sin\theta & N_x\sin\theta & \cos\theta \end{pmatrix} \tag{4.24}$$

which is exact for $\theta_z = 0$, and where the time dependence on the integrated rotation's norm $\theta(t)$ and components $N_{\text{x,y}}(t)$ have been omitted for simplicity. However, this matrix remains complex and heavy to compute in an FPGA board with limited resources. Considering rotation rates in the order of 10^{-1} rad/s and a typical interrogation time

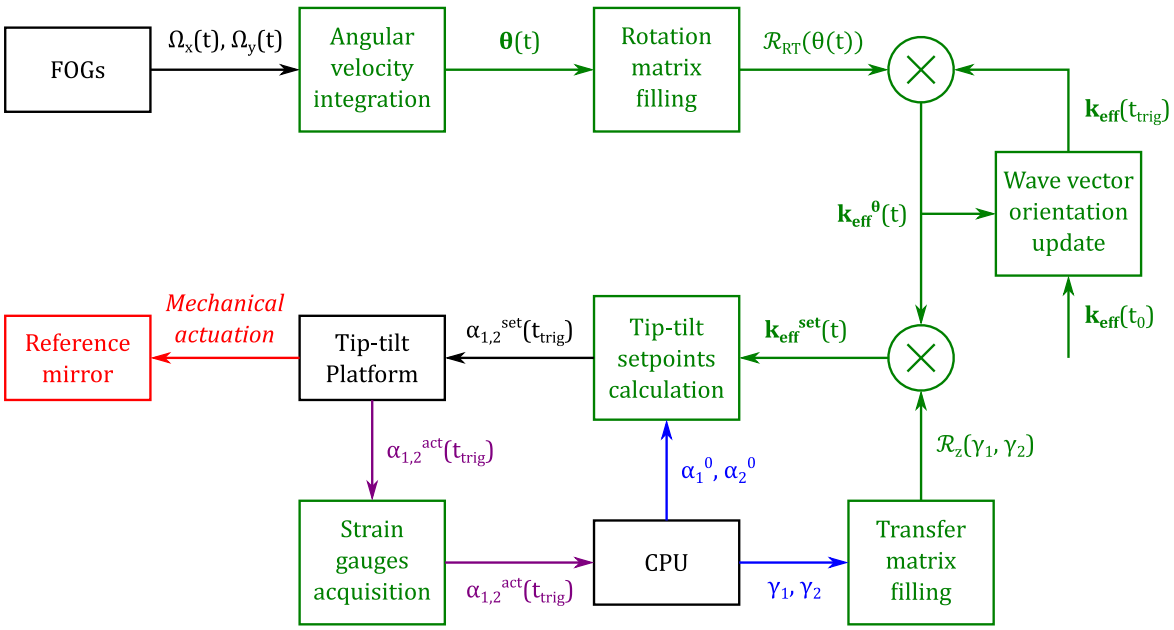

Figure 4.10: Block diagram describing the steps of the real-time incremental rotation compensation scheme, from the acquisition of the transverse rotation rate components $\Omega_{x,y}(t)$ to the mechanical rotation of the matter-wave interferometer's reference mirror. Green blocks denote purely algorithmic calculation stages occurring in the FPGA board and green arrows depict digital signals propagating within the FPGA board. The black arrow represents digital measurements from the FOGs sent to FPGA board and black boxes designate the external electronic devices. Blue arrows describe constant parameters determined beforehand, sent by the CPU to the FPGA before each interferometer and constant for its whole duration. Purple arrows picture the strain gauges signals sent by the tip-tilt platform to the CPU through the FPGA board for monitoring purposes. The red arrow and block, at the end of the diagram, illustrate the mechanical actuation resulting from the upstream real-time calculations. Variables dependent on t are computed at each clock cycle of the FPGA board while the dependence on t_{trig} indicates variables updated on an external trigger signal and unchanged the rest of the time.

$T = 10^{-2}$ s, we obtain rotation angles in the range $\theta \approx 10^{-3} \ll 1$ rad. This allows us to use the small angles approximation and considerably simplify the previous expression in order to build the rotation matrix used in practice:

$$\mathcal{R}_{\mathrm{RT}}(\theta(t)) = \frac{1}{2}\begin{pmatrix} 2-\theta_y^2(t) & \theta_x(t)\theta_y(t) & 2\theta_y(t) \\ \theta_x(t)\theta_y(t) & 2-\theta_x^2(t) & -2\theta_x(t) \\ -2\theta_y(t) & 2\theta_x(t) & 2-\theta^2(t) \end{pmatrix}. \tag{4.25}$$

This matrix must then applied to an well-chosen vector in order to determine the corrected orientation which will subsequently be used as a setpoint for the compensation system. As the primary goal of this scheme is to stabilize the orientation of the reference mirror, we choose to apply the rotation matrix to the effective wave vector of the

Raman laser according to:

$$\boldsymbol{k}^{\boldsymbol{\theta}}_{\mathbf{eff}}(t) = \mathcal{R}_{\mathrm{RT}}(\theta(t)).\boldsymbol{k}_{\mathbf{eff}}(t_{\mathrm{trig}}) \tag{4.26}$$

where $\boldsymbol{k}_{\mathbf{eff}}(t_{\mathrm{trig}}) = (k_x(t_{\mathrm{trig}}), k_y(t_{\mathrm{trig}}), k_z(t_{\mathrm{trig}}))^T$ denotes the current orientation of the effective wave vector, either the default value before the interferometer $\boldsymbol{k}_{\mathbf{eff}}(t_0) = k_{\mathrm{eff}}.\boldsymbol{z_c}$ or after the last rotation of the mirror, triggered by an external signal. This yields:

$$\boldsymbol{k}^{\boldsymbol{\theta}}_{\mathbf{eff}}(t) = \frac{1}{2}\begin{pmatrix} [2-\theta_y^2(t)]k_x(t_{\mathrm{trig}}) + \theta_x(t)\theta_y(t)k_y(t_{\mathrm{trig}}) + 2\theta_y(t)k_z(t_{\mathrm{trig}}) \\ \theta_x(t)\theta_y(t)k_x(t_{\mathrm{trig}}) + [2-\theta_x^2(t)]k_y(t_{\mathrm{trig}}) - 2\theta_x(t)k_z(t_{\mathrm{trig}}) \\ -2\theta_y(t)k_x(t_{\mathrm{trig}}) + 2\theta_x(t)k_y(t_{\mathrm{trig}}) + [2-\theta^2(t)]k_z(t_{\mathrm{trig}}) \end{pmatrix} = \begin{pmatrix} k_x^{\theta}(t) \\ k_y^{\theta}(t) \\ k_z^{\theta}(t) \end{pmatrix}. \tag{4.27}$$

To avoid confusion in the notations, it appears important to insist that the corrected wave vector $\boldsymbol{k}^{\boldsymbol{\theta}}_{\mathbf{eff}}(t)$ is computed continuously (at each clock cycle of the FPGA board) while the "current" effective wave vector is updated at each actual rotation of the mirror, externally triggered. For this reason, we use the distinct time subscript t_{trig} for clarity.

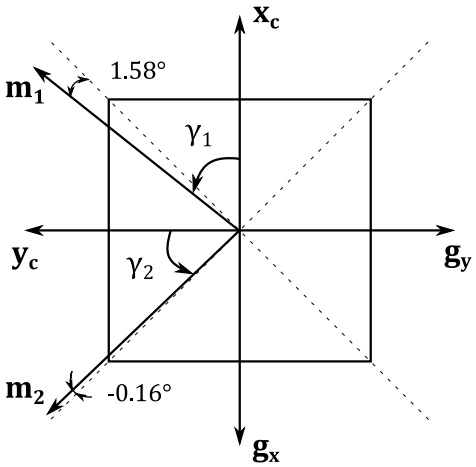

Figure 4.11: Top-view schematic representation of the different axes and angles of the tip-tilt platform. $\boldsymbol{x_c}$ and $\boldsymbol{y_c}$ represent the mobile frame's reference axes, $\boldsymbol{g_x}$ and $\boldsymbol{g_y}$ the measurement axes of the two fiber-optic gyroscopes and $\boldsymbol{m_1}$ and $\boldsymbol{m_2}$ are the motion axes of the tip-tilt stage. The angles $\gamma_{1,2}$ are used to express the change of basis from (g_x, g_y, z) to (m_1, m_2, z), while the 1.58° and -0.16° orthogonality defects were estimated in chapter 2.

By construction of the tip-tilt mount, the rotation axes defined by the pairs of actuators are oriented at approximately 45° relative to the sides of the body and thus to the measurement axes of the gyroscopes as well. For the most general case, these angles will be called $\gamma_{1,2}$ according to figure 4.11. For the components of the previous vector to be expressed in the correct basis with respect to the axes of the platform, we

then need to apply a rotation matrix around the z axis of the experiment:

$$\begin{aligned}\boldsymbol{k}_{\mathbf{eff}}^{\mathbf{set}}(t) = \mathcal{R}_z\left(\gamma_1, \gamma_2\right).\boldsymbol{k}_{\mathbf{eff}}^{\boldsymbol{\theta}}(t) &= \begin{pmatrix} -\cos\gamma_1 & -\sin\gamma_2 & 0 \\ \sin\gamma_1 & -\cos\gamma_2 & 0 \\ 0 & 0 & 1 \end{pmatrix} \cdot \begin{pmatrix} k_x^\theta(t) \\ k_y^\theta(t) \\ k_z^\theta(t) \end{pmatrix} \\ &= \begin{pmatrix} -\cos\gamma_1 k_x^\theta(t) - \sin\gamma_2 k_y^\theta(t) \\ \sin\gamma_1 k_x^\theta(t) - \cos\gamma_2 k_y^\theta(t) \\ k_z^\theta(t) \end{pmatrix} = \begin{pmatrix} k_x^{\mathrm{set}}(t) \\ k_y^{\mathrm{set}}(t) \\ k_z^{\mathrm{set}}(t) \end{pmatrix}.\end{aligned} \tag{4.28}$$

The angles $\gamma_{1,2}$ meant to express the change of basis from (g_x, g_y, z) to (m_1, m_2, z) are defined with respect to the axes x_c and y_c in order to keep them between 0 and 90° for technical reasons, which is why the rotation matrix has been adapted to angles $\pi + \gamma_{1,2}$ which can flip the sign of the cos and sin functions.

Angular setpoints for the control of the tip-tilt mirror

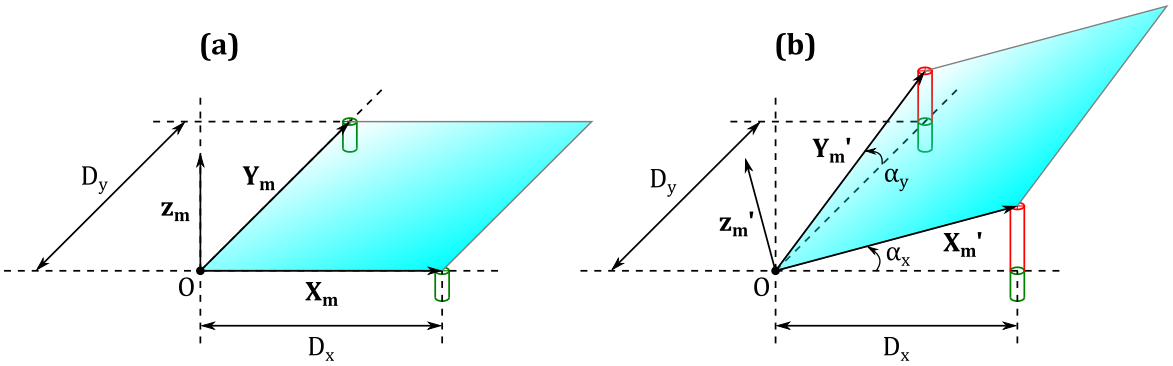

Figure 4.12: Schematic representation of the tip-tilt platform actuation along two orthogonal motion axes. Though each axis is comprised of two piezo-electric actuators, their displacements following a given command are symmetric thus only one actuator per axis is shown for clarity, the blue parallelogram equating to a quarter of the reference mirror. The orientation of the reference is depicted (a) at rest and (b) for two distinct angular setpoints $\alpha_{x,y}$. Green cylinders illustrate the length of the actuators at rest while red cylinders represent the displacement induced by the actuation order. O pictures the center of the mirror, assimilated to the center of rotation neglecting the lever arm of the tip-tilt stage d_m for the simplicity of the drawing.

Once we have determined the projections of the setpoint wave vector ensuring a stable orientation in the laboratory frame, we still need to calculate the corresponding commands to be sent to the tip-tilt platform. Specifically, two instructions are required as the mirror rotating stage features two rotation axes, supposed orthogonal in this section (neglecting the slight orthogonality defect found in section 2.4 for simplicity). As shown in figure 2.9, the electrical connections between the electrodes of a given axis ensure a symmetric operation, hence the reasoning can be limited to an operation

scheme based on one piezo-electric actuator per axis as illustrated in figure 4.12, showing the equivalent of a quarter of the reference mirror.

Denoting $\boldsymbol{X_m}$ and $\boldsymbol{Y_m}$ the vectors joining the center of the mirror with the contact point between the piezo-actuators and the mirror of respectively the first and second axes of the tip-tilt platform, we can first define their values at rest assuming associated horizontal distances D_x and D_y; this yields $\boldsymbol{X_m} = (0, 0, D_x)^T$ and $\boldsymbol{Y_m} = (0, 0, D_y)^T$. This situation is described in figure 4.12 (a). The resulting vector describing the normal to the mirror Z_m can thus be put under the form:

$$\boldsymbol{Z_m} = \boldsymbol{X_m} \times \boldsymbol{Y_m} = \begin{pmatrix} D_x \\ 0 \\ 0 \end{pmatrix} \times \begin{pmatrix} 0 \\ D_y \\ 0 \end{pmatrix} = \begin{pmatrix} 0 \\ 0 \\ D_x D_y \end{pmatrix}. \tag{4.29}$$

Normalizing this vector, we can connect it to the axes of the inertial frames defined in figure 4.1:

$$\frac{\boldsymbol{Z_m}}{\|\boldsymbol{Z_m}\|} = \boldsymbol{z_m} = (0, 0, 1)^T \tag{4.30}$$

reminding that when the mirror is at rest with its normal aligned with the mechanical accelerometer's measurement axis, the assertion $\boldsymbol{z_m} \equiv \boldsymbol{z_c}$ is true.

Now, in order to switch the tip-tilt's axes to angular positions α_x and α_y along the axes $\boldsymbol{X_m}$ and $\boldsymbol{Y_m}$ respectively, the vectors defined above will be modified according to:

$$\boldsymbol{X'_m} = \begin{pmatrix} D_x \\ 0 \\ D_x \tan(\alpha_x) \end{pmatrix} \quad ; \quad \boldsymbol{Y'_m} = \begin{pmatrix} 0 \\ D_y \\ D_y \tan(\alpha_y) \end{pmatrix} \tag{4.31}$$

as depicted in figure 4.12 (b). In this configuration, the normal to the mirror is carried by the vector:

$$\boldsymbol{Z'_m} = \boldsymbol{X'_m} \times \boldsymbol{Y'_m} = \begin{pmatrix} D_x \\ 0 \\ D_x \tan(\alpha_x) \end{pmatrix} \times \begin{pmatrix} 0 \\ D_y \\ D_y \tan(\alpha_y) \end{pmatrix} = \begin{pmatrix} -D_x D_y \tan(\alpha_x) \\ -D_x D_y \tan(\alpha_y) \\ D_x D_y \end{pmatrix}. \tag{4.32}$$

The norm of this vector amounting to $\|\boldsymbol{Z'_m}\| = D_x D_y \sqrt{1 + \tan^2(\alpha_x) + \tan^2(\alpha_y)}$, we reach the final expression:

$$\boldsymbol{z'_m} = \frac{1}{\sqrt{1 + \tan^2(\alpha_x) + \tan^2(\alpha_y)}} \begin{pmatrix} -\tan(\alpha_x) \\ -\tan(\alpha_y) \\ 1 \end{pmatrix} = \begin{pmatrix} z_m^{(1)} \\ z_m^{(2)} \\ z_m^{(3)} \end{pmatrix}. \tag{4.33}$$

For small angles $\alpha_{x,y} \ll 1$ rad, we have $\tan^2(\alpha_{x,y}) \approx \alpha_{x,y}^2 \ll 1$ and we can thus neglect the normalization factor.

In practice, the tip-tilt platform is constantly powered up and takes default setpoint angles $\alpha_{1,2}^0$ expressed in milliradians to be aligned with the collimator and mechanical accelerometer, corresponding to the position called "at rest". The commands sent to the tip-tilt device $\alpha_{1,2}^{\text{set}}$, expressed in milliradians as well, will thus be relative to the default setpoint angles and we can write the relations with the absolute angular positions:

$$\begin{cases} \alpha_x = \alpha_2^0 - \alpha_2^{\text{set}} \\ \alpha_y = \alpha_1^{\text{set}} - \alpha_1^0 \end{cases} \tag{4.34}$$

with $\alpha_{x,y}$ in milliradians and the signs set by definition of the platform's axes' directions. The subscripts x, y have been changed to $1, 2$ to avoid the confusion between the angular position *along* an axis, used for the demonstration, and the actual rotation *around* an axis taken as a command by the tip-tilt controller. Furthermore, the new subscripts $1, 2$ are used to match the tip-tilt platform's motion axes $m_{1,2}$ used in chapter 2 and in figure 4.11 as well. The transverse components of the mirror's normal can finally be written as follows:

$$\begin{cases} z_m^{(1)} = -\tan\left(\alpha_2^0 - \alpha_2^{\text{set}}\right) z_m^{(3)} \\ z_m^{(2)} = -\tan\left(\alpha_1^{\text{set}} - \alpha_1^0\right) z_m^{(3)} \end{cases}. \tag{4.35}$$

We can finally deduce the expression of the angular commands which need to be communicated to the piezo-electric actuators:

$$\begin{cases} \alpha_2^{\text{set}} = \alpha_2^0 + \arctan\left(\dfrac{z_m^{(1)}}{z_m^{(3)}}\right) \\ \alpha_1^{\text{set}} = \alpha_1^0 - \arctan\left(\dfrac{z_m^{(2)}}{z_m^{(3)}}\right) \end{cases} \tag{4.36}$$

where the ratio inside the arc-tangent function ensures the normalization of the axes. This feature is interesting reminding that $\boldsymbol{k}_{\mathbf{eff}}^{\mathbf{set}}(t) = \boldsymbol{k}_{\mathbf{eff}}^{\boldsymbol{\theta}}(t) = \boldsymbol{k}_{\mathbf{eff}}(t) = k_{\text{eff}}\boldsymbol{z_m} = k_{\text{eff}}\boldsymbol{z_c}$ at rest. Hence, the same reasoning which has been established above for the normal to the mirror $\boldsymbol{z_m}$ can be directly applied to the vector $\boldsymbol{k}_{\mathbf{eff}}^{\mathbf{set}}(t)$ which progresses in the same manner. Consequently, the angular setpoints transmitted to the tip-tilt controller and resulting from the calculation performed by the FPGA are the following:

$$\begin{cases} \alpha_2^{\text{set}}(t) = \alpha_2^0 + \arctan\left(\dfrac{k_x^{\text{set}}(t)}{k_z^{\text{set}}(t)}\right) \\ \alpha_1^{\text{set}}(t) = \alpha_1^0 - \arctan\left(\dfrac{k_y^{\text{set}}(t)}{k_z^{\text{set}}(t)}\right) \end{cases} \tag{4.37}$$

4.3.2 Implementation of the real-time rotation compensation: synchronization and timing constraints

The fiber-optic gyroscopes mounted on the vacuum chamber output a 32-bit digital signal with a resolution of ≈ 0.3 nrad/s and a dynamic range of 667 mrad/s $\simeq 38$ °/s. At each acquisition from the FOGs, the transverse rotation components $\Omega_x(t)$ and $\Omega_y(t)$ are communicated to the FPGA board at a rate of 1 kHz.

Regarding the timings, all of the calculations described in the previous subsection are performed quasi-continuously. Each signal is updated at every clock cycle at a frequency $f_{\text{FPGA}} = 100$ MHz. For the variables which need to be modified at a specific moment though, it is possible to implement trigger signals propagating throughout the calculation and conditioning the assignation of a new value to a given data bus. This is the case for the effective wave vector of the laser, updated every time the mirror is effectively rotated, or the tip-tilt stage's commands which must be transmitted at a precisely known instant.

Specifically, the communication of the tip-tilt commands $\alpha_{1,2}^{\text{set}}$ must be carefully triggered as the rotation pattern and the performances of the tip-tilt stage will condition the efficiency of the compensation system. The most naive way to correct for the reference mirror's motion would be to apply the scheme outlined above at every reception of the FOGs signals, i.e. every millisecond, in order to have a rigorous tracking of the rotation vector's evolution. Such implementation is picture in figure 4.13 with green dots on the top graph representing the measurements of the gyroscopes at 1 kHz and the green curve on the bottom diagram depicting the evolution of the mirror's angle $\alpha(t)$. The problem raised by this method comes from the performance of the piezo-actuated rotating stage, in particular its settle time. In section 2.4, we observed a settling time amounting to 5 to 6 ms which is five times slower than the gyroscopes' acquisition rate. In this configuration, even though the tilt steps performed by the piezo-electric actuators have lower amplitudes, there is a significant latency in their response which will result in a considerable pointing error at the beginning of the next Raman pulse. Thus, it appears necessary to limit at maximum the frequency at which the commands are sent to the tip-tilt controller, and to leave enough time to the platform to stabilize.

To this end, an intuitive solution consists in performing a single tilt jump between two successive light pulses as illustrated by the blue steps in figure 4.13. This technique requires to find a trade-off minimizing the steady-state error of the platform's response, which depends on its settling time, and maximizing the accuracy of the transmitted

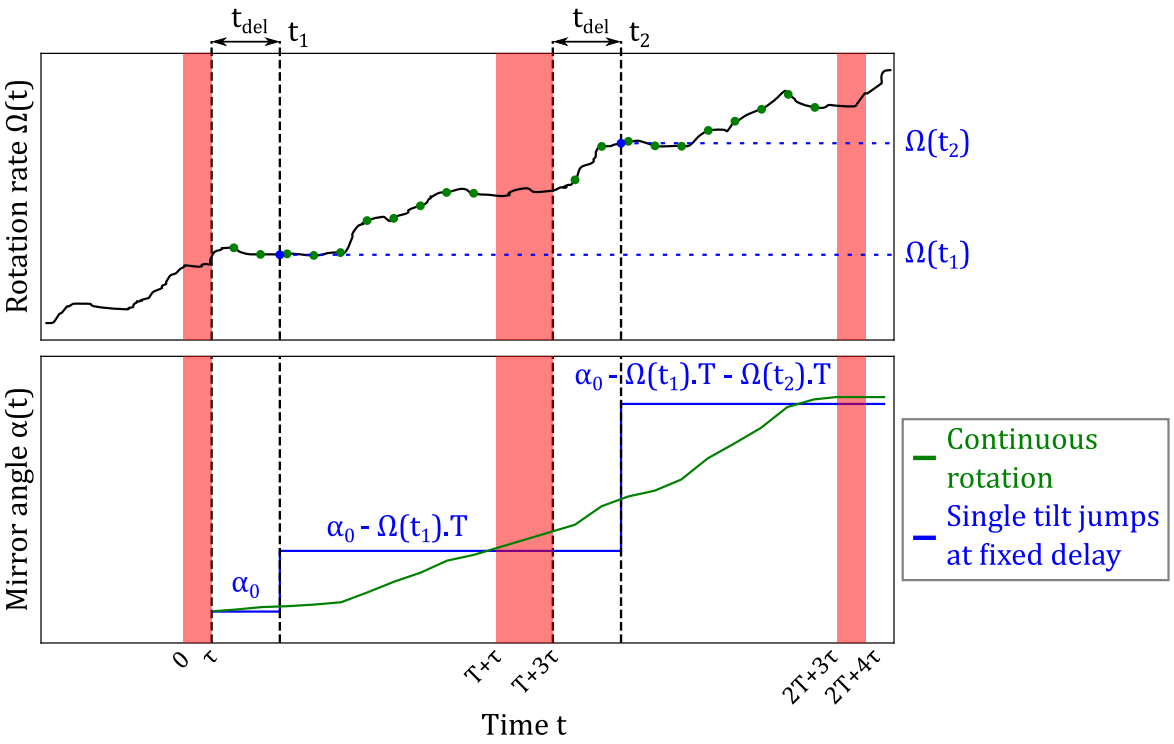

Figure 4.13: Timing diagram of the rotation rate $\Omega(t)$ measured by the gyroscopes (top) and of the mirror's angle $\alpha(t)$ (bottom). On the top graph, the black line represents the real rotation rate experienced by the apparatus, green dots display the measurements of the gyroscopes at 1 kHz and blue dots denote the measurements selected in the context of our single tilt jumps compensation scheme. As for the reference mirror's tilt angle, the green curve illustrates an ideal compensation with an integration of the rotation rate at the FOG acquisition rate, which is incompatible with our tip-tilt platform due to the settling time. The blue steps exhibit the behavior of the reference mirror with two tilt jumps at a fixed delay t_{del} after the two first Raman pulses. The overall linear tendency of the rotation rate throughout the interferometer, supported by the coarsely quadratic evolution of the mirror's angle in the case of a continuous rotation, illustrates the assumption made that we operate our instrument under angular velocities at most linear on these timescales.

command by taking the average value of the rotation rate. With respect to the first parameter, it seems natural that the sooner the mirror is rotated, the longer time it has to converge towards and stabilize at its final position. On the other hand, assuming angular velocities evolving at most linearly, then the mean values will be found exactly in-between two successive pulses at $t = \tau + T/2$ and $t = 3(\tau + T/2)$. Considering interrogation times $T \leqslant 10$ ms, this does not necessarily leave enough time for the tip-tilt stage to be stable, especially for large tilt amplitudes. For this reason, the delay separating the rotation of the reference mirror from the end of the previous Raman

pulse was adapted to the interrogation time as follows:

$$t_{\text{del}} = \begin{cases} T/256 & \text{for } T < 5 \text{ ms} \\ T/32 & \text{for } 5 \leqslant T < 8 \text{ ms} \\ T/4 & \text{for } T \geqslant 8 \text{ ms} \end{cases} . \tag{4.38}$$

Thus, the reference mirror will undergo two tilt jumps at times $t_1 = \tau + t_{\text{del}}$ and $t_2 = 3\tau + T + t_{\text{del}}$, setting the time origin $t = 0$ at the beginning of the interferometer. At these two instants, the latest calculated angular setpoints are converted in the floating-point format and transmitted to the controller of the piezo-actuated tip-tilt stage. Simultaneously, the effective wave vector of the laser $\boldsymbol{k}_{\mathbf{eff}}$ is updated by taking the value of the latest rotated wave vector $\boldsymbol{k}_{\mathbf{eff}}^{\boldsymbol{\theta}}$.

It is now possible to detail the evolution of the stabilized laser wave vector throughout the atom interferometer, and especially at the instant of each light-matter interaction. We will write $\boldsymbol{k}_{\mathbf{eff}}^{(i)}$ the effective wave vector at the i^{th} atom-light interaction and assume a wave vector initially aligned with the mechanical accelerometer on the z axis of the rotating frame $\boldsymbol{k}_{\mathbf{eff}}^{(1)} = (0, 0, k_{\text{eff}})^T$. Thus at the moment of the second and third Raman pulses, the stabilized wave vector can be expressed:

$$\boldsymbol{k}_{\mathbf{eff}}^{(2)} = \frac{1}{2} \begin{pmatrix} 2\Omega_y(t_1) T k_{\text{eff}} \\ -2\Omega_x(t_1) T k_{\text{eff}} \\ \left[2 - (\Omega(t_1)T)^2\right] k_{\text{eff}} \end{pmatrix} = \begin{pmatrix} k_x^{(2)} \\ k_y^{(2)} \\ k_z^{(2)} \end{pmatrix} \tag{4.39}$$

$$\boldsymbol{k}_{\mathbf{eff}}^{(3)} = \frac{1}{2} \begin{pmatrix} [2 - (\Omega_y(t_2)T)^2] k_x^{(2)} + \Omega_x(t_2)\Omega_y(t_2) T^2 k_y^{(2)} + 2\Omega_y(t_2) T k_z^{(2)} \\ \Omega_x(t_2)\Omega_y(t_2) T^2 k_x^{(2)} + [2 - (\Omega_x(t_2)T)^2] k_y^{(2)} - 2\Omega_x(t_2) T k_z^{(2)} \\ -2\Omega_y(t_2) T k_x^{(2)} + 2\Omega_x(t_2) T k_y^{(2)} + [2 - (\Omega(t_2)T)^2] k_z^{(2)} \end{pmatrix} . \tag{4.40}$$

This method of compensation works under the assumption that the rotation rate of the sensor head is constant between two pulses of the interferometer. From the measurements of the gyroscopes, we find that for our typical experimental conditions, the coefficient of variation - defined as the ratio of the standard deviation over the mean - of the sensor head's angular velocity during the interferometers is below 5% for more than 90% of the data points.

4.3.3 Performance of the rotation compensation system

After establishing a clear operating scheme for the compensation of the carrier's rotations, it appears necessary to estimate the performance of the system and in particular to analyze the residual rotation rate resulting from the various sources of

error yielding an imperfect compensation. In particular, we will focus on the difference between the average rotation rate between two successive pulses and the angular velocity value used by the real-time system for the compensation, before scrutinizing the interrogation time-dependent error arising from the responses of the piezo-actuators pairs.

Average rotation rate accuracy

The first effect which is prone to degrading the performance of the reference mirror's stabilization is the choice of a specific rotation rate measurement Ω_0 at a fixed instant t_0. This compensation scheme would yield a rotation of the mirror exactly balancing the one of the instrument only in the case of an angular velocity remaining constant between two Raman pulses. Considering constant angular accelerations, then the error made will lie in the time difference between the instant we enable the rotation of the mirror t_0 and the moment midway through two Raman pulses (separated by $T/2$ from the previous and next pulses), where the instantaneous rotation rate equals its mean value over the interrogation time $\overline{\Omega}$. In practice, the motion of the carrier is random and the rotation pattern constantly varies from constant to linear and, in some cases, even quadratic evolution of the angular velocity.

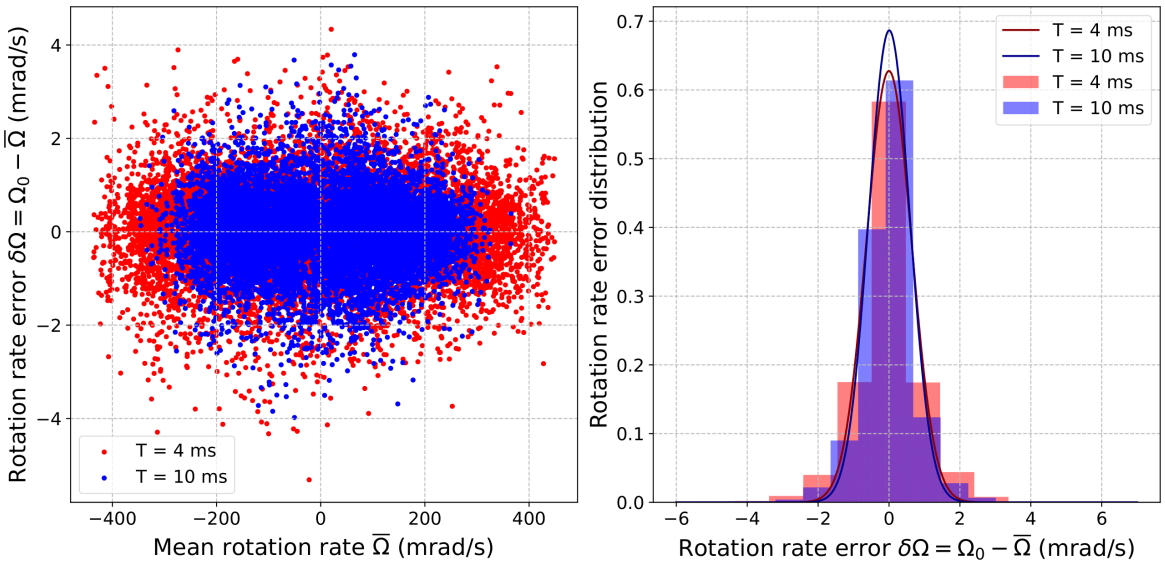

Figure 4.14: Analysis of the error made on the average rotation rate between two successive Raman pulses by taking a single measurement separated by t_{del} from the end of the previous pulse, at two interrogation times $T = 4$ ms (red) and $T = 10$ ms (blue). These errors are calculated for each rotation of the mirror, with one point corresponding to half an interferometer, and shown on the left graph versus the average angular velocity $\overline{\Omega}$. The right plot displays the histograms corresponding to the distribution of these discrepancies which are Gaussian fitted in darker solid lines.

To analyze this effect, we have recorded the measurements of the fiber-optic gyro-

scopes streamed at 1 kHz and synchronized with the experimental sequence, in order to retrieve the error made on the rotation rate $\delta\Omega = \Omega_0 - \overline{\Omega}$ with $\Omega_0 = \Omega(t_0)$. The results of this study, which was carried out for different interrogation times and in various rotation regimes, are exhibited in figure 4.14 where each point corresponds to half an interferometer. The histograms on the right-hand side reveal a very similar Gaussian distribution centered on $\delta\Omega = 0$ regardless of the interrogation time, proving that this imperfection in the compensation scheme is uncorrelated to the interrogation time nor to the rotation pattern or amplitude. Thus, if this defect may produce phase noise at the output of the interferometer, it is unlikely to generate a systematic phase shift. Moreover, it can be observed that the error on the angular velocity mostly remains within ±4 mrad/s even for rotation rates over 400 mrad/s, which is a satisfying behavior. Specifically, as far as the contrast preservation is concerned, a 1% error on the angular velocity will hardly be noticeable at all and regarding the phase correction, two distinct angular velocities of the chamber Ω and mirror Ω_m are involved in the model established. Thus, the high frequency streaming of the gyroscopes allows us to exploit independently the mean value of the instrument's rotation rate and the exact measurement transmitted to the reference by the real-time compensation system.

Steady-state error and stability of the piezo-electric actuators' feedback loop

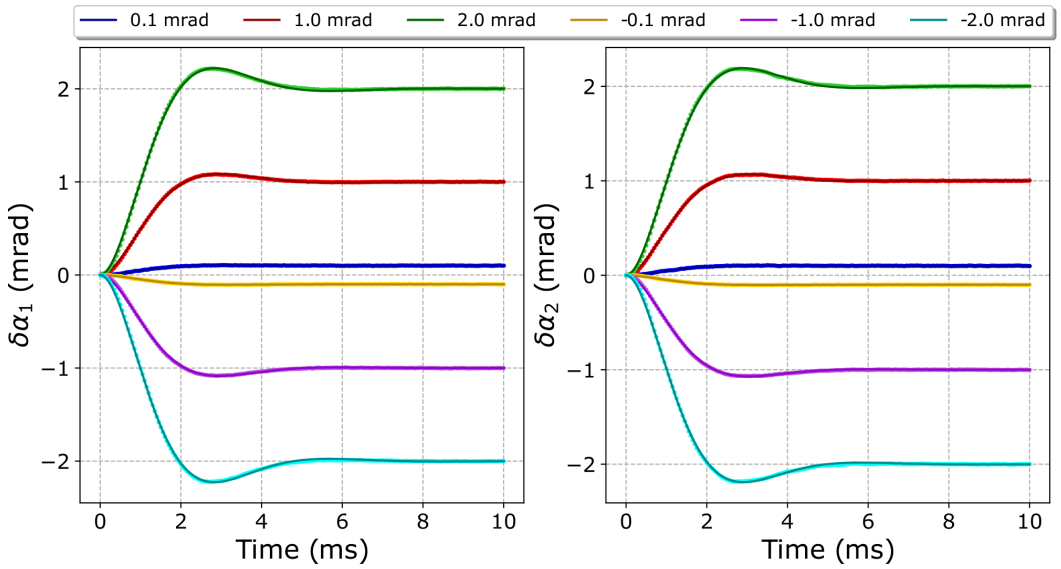

Figure 4.15: Second order fitting of the two motion axes' response to step angular setpoints $\delta\alpha_i$ of amplitude $U = \pm 0.1$ mrad, $U = \pm 1.0$ mrad and $U = \pm 2.0$ mrad. Light colored dots depict the measurements from the strain gauges while dark colored curves illustrate the result of the second order system response fit to these experimental data.

The second parameter which is likely to contribute to the pointing error during the

rotation of the reference mirror is the piezo-actuated tip-tilt stage itself. The settling time and steady state error of the two pairs of actuators were evaluated in section 2.4 but the latter parameter was measured at long times after the stabilization. Now, we want to determine precisely at what point of the piezo-electric actuators' stroke the next light pulse occurs, i.e. what is the error made on the actual angular position of the reference mirror with respect to the setpoint received by the tip-tilt stage. First, strain gauges measurements were recorded and analyzed as displayed in figure 4.15 in order to retrieve the characteristics of a second order system. Indeed, the underdamped response $y(t)$ of the actuators to a step setpoint $u(t)$ on a given axis can be fitted with the following function:

$$y(t) = K_s U \left(1 - \exp(-\xi\omega t)\left[\cos\left(\omega t\sqrt{1-\xi^2}\right) + \frac{\xi}{\sqrt{1-\xi^2}}\sin\left(\omega t\sqrt{1-\xi^2}\right)\right]\right) \quad (4.41)$$

with the step setpoint $u(t) = U$ for $t \geqslant 0$ and 0 otherwise, K_s the static gain of the system, ω its natural frequency and ξ its damping factor.

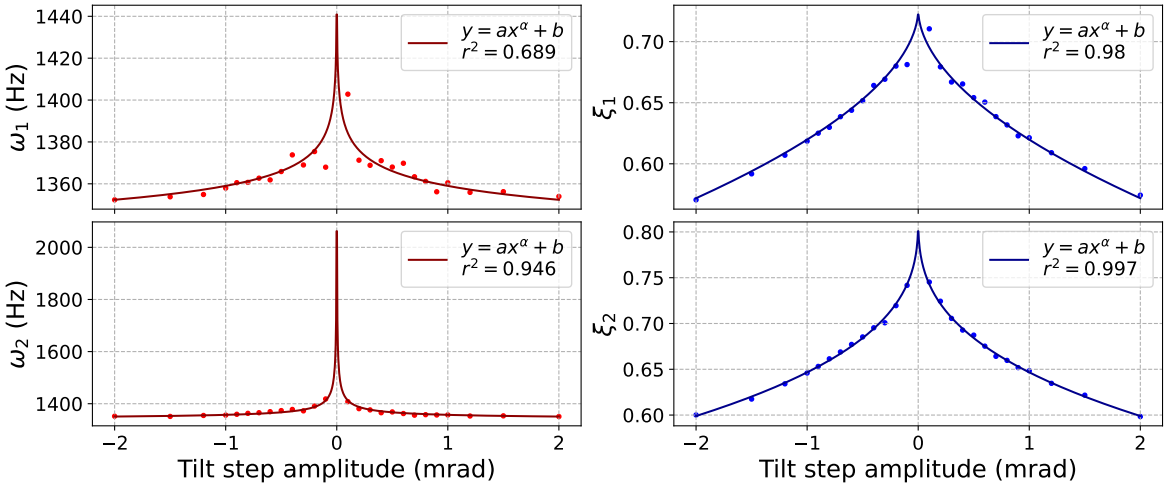

Figure 4.16: Evolution of the natural frequency (left) and damping factor (right) of a second order system's underdamped response for the first (top) and second (bottom) motion axes of the tip-tilt platform. The values of these parameters were obtained by fitting the signal from the strain gauges with equation 4.41 for step setpoints ranging from -2 to $+2$ mrad. The differences between the two axes are mostly marginal, apart from the fitted evolution of the natural frequencies significantly diverging for very small tilt step amplitudes. This effect occurring mostly for angular setpoints $|\delta\alpha_i| \leqslant 0.2$ mrad, we can reasonably neglect it.

This equation was used to fit the response of the two motion axes for angular setpoints varying from -2 to $+2$ mrad in steps of 100 µrad, enabling us to extract the evolution of the three relevant parameters. The steady state gains remained fairly constant regardless of the setpoint, and were set to $K_{s1} = 1.000407$ and $K_{s2} = 1.000468$. The evolution of the other parameters is displayed in figure 4.16 with the natural

frequencies $\omega_{1,2}$ on the left and the damping factors $\xi_{1,2}$ on the right. The subscripts $1, 2$ denote the motion axes of the tip-tilt platform. The behavior of these characteristics was further fitted with an empirical model as $y = ax^{\alpha} + b$, in order to be able to reproduce the response of each axis under any angular setpoint. With such a detailed analysis of the temporal response of the motion axes, we are now able to model the angular position of the mirror at any time and for any setpoint comprised between -2 and $+2$ mrad, which will be helpful in order to compare the actual orientation of the mirror when the light pulse occurs with the expected one.

During a sequence of atom interferometry, the strain gauges of the tip-tilt platform's motion axes are not streamed and we only have access to the final values of the setpoints and measured positions at the end of the sequence. The two setpoints and actual positions are thus extrapolated in the constant rotation rate approximation to $\delta\alpha_{1,2}^{\text{final}} \approx 2\delta\alpha_{1,2}^{\text{step}}$. The setpoints of the two axes are fed to the model established previously to estimate the actual position of the piezo-electric actuators at the beginning of the next pulse $t_{\text{pulse}} = T - t_{\text{del}} - t_{\text{com}} - t_{\text{lat}}$ with t_{del} the delay detailed in the previous subsection, t_{com} the time for the data bus to be communicated from the FPGA board to the tip-tilt controller and t_{lat} the latency separating the reception of the setpoint and the start of the actuator's motion (see appendix C). The effective rotation of the mirror can be retrieved from the oriented norm of the two axes' motion through the expression:

$$\delta\alpha_{\text{eff}} = \text{sign}(\delta\alpha_2) * \sqrt{\delta\alpha_1^2 + \delta\alpha_2^2} \Rightarrow \Omega_{\text{eq}} = \frac{\delta\alpha_{\text{eff}}}{\text{T}}. \tag{4.42}$$

From this point, we can distinguish the angular setpoints $\alpha_{1,2}^{\text{set}}$ and the actual angular positions measured by the strain gauges $\alpha_{1,2}^{\text{act}}$ and employ either of them in equation 4.42. This way, we can isolate the different sources of error such as the rotating stage itself (with an angular position not matching the setpoint) or a prior error already present in the transmitted setpoint for instance.

Figure 4.17 displays the two relevant types of error mentioned above. For the actual tilt jumps performed by the two motion axes at the beginning of the next Raman pulse $\delta\alpha_{1,2}^{\text{act}}(t_{\text{pulse}})$, they are calculated using the appropriate setpoint amplitudes and the second order underdamped response modeling with the setpoint-dependent parameters displayed in figure 4.16. The parameter Ω_{act} denoting the rotation rate equivalent to this tilt jump is then determined using equation 4.42. In a similar manner, the equivalent rotation rate associated to the angular setpoints Ω_{set} is obtained through the application of equation 4.42 to the setpoints $\delta\alpha_{1,2}^{\text{set}}(t_{\text{pulse}})$ directly, assuming $\delta\alpha_{1,2}^{\text{final}} \approx 2\delta\alpha_{1,2}$. The difference between these two quantities $\Omega_{\text{act}} - \Omega_{\text{set}}$ provides information on the incorrect position of the piezo-actuators at the instant of the next pulse with regard to the

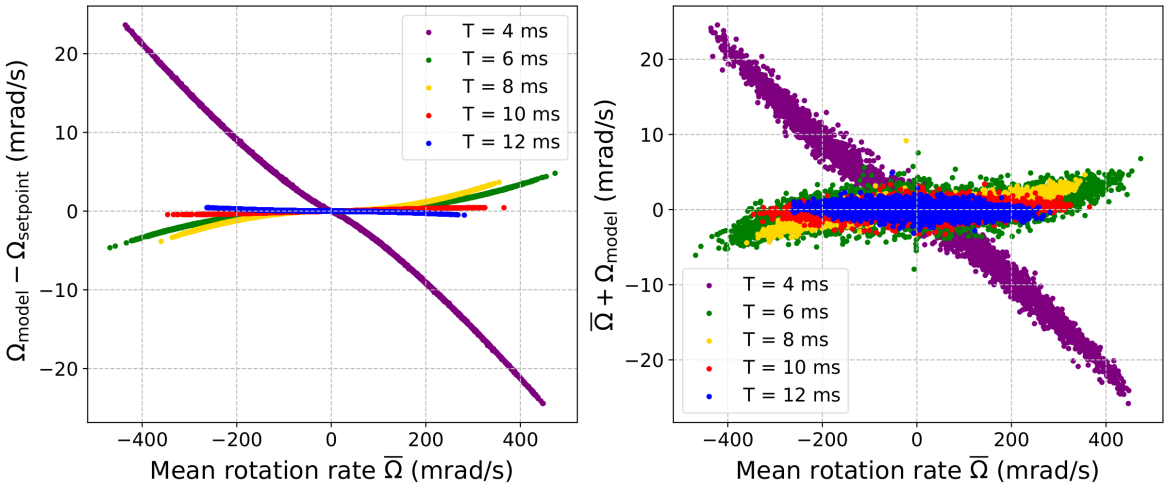

Figure 4.17: Evolution of the error made on the equivalent rotation rate Ω_{model} calculated using equations 4.41 and 4.42 with the signal from the two strain gauges versus the average rotation rate $\overline{\Omega}$ measured by the gyroscopes. The value modeled from the strain gauges measurements Ω_{model} is compared to the rotation rate resulting from the angular setpoints $\Omega_{setpoint}$ in order to evaluate the error due to the actuators' settling time specifically (left). On the right-hand side, the equivalent rotation rate Ω_{model} is directly compared to the mean angular velocity $\overline{\Omega}$ to estimate the overall pointing error of the tip-tilt stage.

setpoint they were given, directly related to an insufficient settling time, as exhibited in figure 4.17 (left). The results of this study are in good agreement with what could be expected, with a huge pointing error at $T = 4$ ms and still a significant error at $T = 6$ ms and $T = 8$ ms. The similarities in the actuators' behavior for the last two interrogation times mentioned is due to the difference in their respective correction delays defined in equation 4.38. As for the larger interrogation times above 10 ms, we observe a good agreement in the angular positions and setpoints regardless of the setpoint amplitude, denoting a satisfying steady state error of the two motion axes for settling times above 7.5 ms.

In figure 4.17 (right), the rotation rate Ω_{act} was added to the average rotation rate $\overline{\Omega}$ obtained from the gyroscopes' measurements in order to investigate the accumulated effects of the tip-tilt insufficient settling time described in the previous paragraph, and the setpoint error illustrated in figure 4.14. The result is fairly consistent, with error amplitudes similar to the ones in figure 4.17 (left) and a thickening of the lines translating the noise coming from the setpoint error. What can be concluded from this analysis is that the pointing error is dominated by the tip-tilt settling time at high rotation rates, and that it remains in the reasonable limit of 2 to 3% for interrogation times above $T = 8$ ms. If this can be a non-negligible source of phase noise when applying the phase correction, as it is difficult to estimate accurately the error made on the mirror's orientation, empirical results show that reducing the delay time t_{del} between

the previous pulse and the mirror's rotation induces a significant error on the estimation of the mean rotation rate, more critical for the contrast retrieval. Ultimately, it appears counter-productive to perform atom interferometers with a stabilized reference mirror at interrogation times below $T = 6$ ms, at least with the chosen piezo-actuated tip-tilt platform, since the pointing error is rapidly diverging due to the insufficient time let to the piezo-electric actuators to stabilize.

4.3.4 Fringes reconstruction on a rotating atom interferometer with stabilized reference mirror

Contrast recovery with the real-time stabilization of the reference mirror

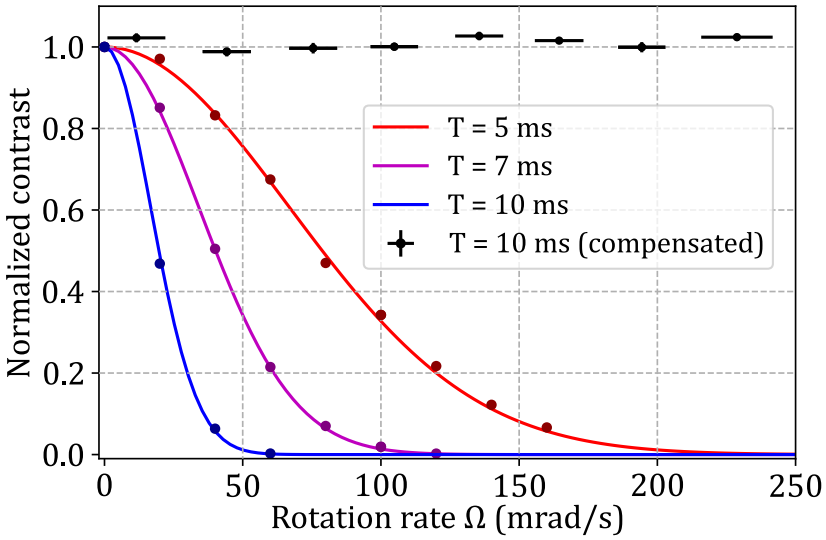

Figure 4.18: Illustration of the exponential decay of the interference pattern's normalized visibility for interrogation times $T = 5$ ms (red), $T = 7$ ms (purple) and $T = 10$ ms (blue). The dots represent experimental data and the straight lines are based on equation 1.78 for a cloud temperature $\mathcal{T} = 3.6$ µK. Black dots demonstrate the contrast of atomic interference fringes with the compensation system enabled at $T = 10$ ms. Black horizontal lines depict the standard deviation of the rotation rate on a given range of rotation rates as it cannot be precisely controlled on the manual rotary platform.

Figure 4.18 displays the evolution of the contrast of the atomic interference fringes in various relevant situations in order to demonstrate the efficiency of the real-time rotation compensation system. To coherently compare the different sets of data, the contrast is evaluated beforehand in static so that a reference value is determined in each situation, i.e. for each interrogation time and with the stabilization scheme enabled or not. Consequently, data are recorded while the apparatus is undergoing rotations and the resulting measured contrast is divided by the static reference value, yielding a normalized value only influenced by the angular motion. The initial tilt angles of the

sensor head are $\theta_{x,z} = 0°$ so that the contrast inhomogeneities related to the atomic cloud falling out of the Raman laser do not play part in this study.

The uncompensated case was already discussed in section 4.2. As for the compensated case, data were recorded at $\theta_z = 0°$ with the sensor head placed on the rotary platform, scanning the angle θ_x between $-10°$ and $+10°$ at speeds $|\Omega| \leqslant 250$ mrad/s. Since the rotation table is not automated, the angular velocity and acceleration cannot be precisely controlled and vary from a run to another, as well as within an interferometric sequence. For this reason, the results were filtered and sorted in arbitrary ranges of rotation rates, narrow enough and containing enough data points so that the interferometric fringes can be fitted to retrieve the contrast. In some cases, it is possible that the contrast of the fringes produced by a rotating interferometer with a stabilized mirror exceeds the static one, yielding a normalized contrast above 1. This effect is less related to the angular velocity or to the real-time compensation system than it is to the tilt-dependent contrast discrepancies, therefore we will not focus on this part. In figure 4.18, black dots stand for the contrast of the atomic interference pattern at $T = 10$ ms and are placed at the center of each range of rotation rate mentioned above while horizontal black lines denote the standard deviation of the angular velocity in each of these intervals. This analysis demonstrates that for the targeted interrogation time of $T = 10$ ms, which should allow interferometric measurements up to 50 mrad/s, the real-time compensation scheme stabilizing the orientation of the reference mirror extended the measurement range up to at least $|\Omega| = 250$ mrad/s with no noticeable degradation of the fringes' amplitude.

Correction of the rotating hybrid accelerometer's output phase

The rotation compensation scheme has proven effective to maintain the contrast over a vast range of angular velocities and at interrogation times that are suitable for the targeted range of sensitivity. Nevertheless, the interferometric phase remains to be taken care of as the individual motion of the reference mirror around the center of rotation of the tip-tilt stage introduces specific phase shifts, detailed in table 4.1.

Figure 4.19 represents the fringes reconstruction process for a rotating atom interferometer with an active compensation on the reference mirror. The sensor head is placed on the rotary platform which is manually operated around its x axis with the tilt angle θ_z set at 0° for all the runs. Hence, the sensor head will only undergo rotations along its x axis as well, measured by a single fiber-optic gyroscope. Throughout the performed interferometers, the tilt angle θ_x arbitrarily varies between 0 and 30° and the rotation rate Ω_x remains in the range ±250 mrad/s as depicted in figure 4.19 (a). Each

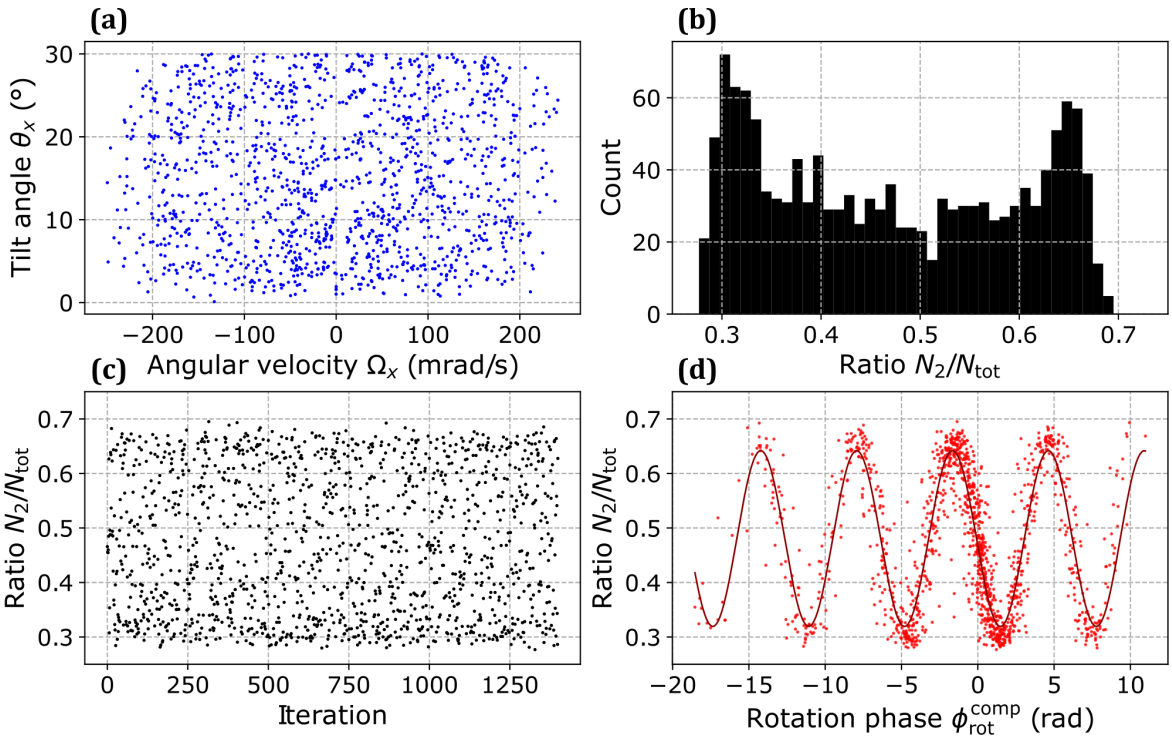

Figure 4.19: Fringes reconstruction on a Mach-Zehnder atom interferometer undergoing arbitrary rotations with a real-time stabilization of the reference mirror's orientation. (a) Distribution of the tilt angles $\theta_x \in [0, 30]°$ and angular velocities $\Omega_x \in [-250, 250]$ mrad/s for each run. (b) Histogram of the measured population ratios disclosing a bimodal distribution, which denotes a sine-like behavior. (c) Measured population ratios at the output of each matter-wave interferometer with a constant phase offset $\phi_{las} = \pi/2$ applied on the laser at the third Raman pulse, ensuring no other parameter than the rotation phase are scanned. (d) Same population ratios plotted as a function of the rotation phase in the compensated case ϕ_{rot}^{comp} (see table 4.1). The plain darker line depicts a sinusoidal fit to the data points, yielding a signal-to-noise ratio equal to 5.4.

dot corresponds to a distinct interferometric measurement associated with a couple of mean values (θ_x, Ω_x). The detection of the population N_2 in the upper ground state $|F = 2\rangle$ and the total population N_{tot} allows us to measure the population ratio, the histogram of which is depicted in figure 4.19 (b). This diagram features a bimodal distribution, characteristic of a sine-like signal and demonstrating the conservation of the contrast with the real-time rotation compensation system. Indeed, since the different runs are performed at random rotation rates, the exponential decay of the contrast at high angular velocities would have yielded a Gaussian distribution centered on the mean ratio $P_0 \approx 0.48$. For all the runs considered, a constant phase offset equal to $\pi/2$ is applied on the laser before the third Raman pulse ensuring no other parameter than the rotation phase are scanned, though the $\pi/2$ value is not critical as the large variations of the rotation phase do not allow us to stay on the linear part of the fringes and maximize the sensitivity of the measurement. Figure 4.19 (c) presents

the measured ratio at the output of each atom interferometer, showing once again the contrast recovery without any evidence of interference fringes yet.

From these data, no information on the phase of the central fringe can be retrieved and no acceleration measurement is possible. To remove the influence of the rotations which heavily scramble the interference pattern, it is thus necessary to calculate the rotation phase $\phi_{\text{rot}}^{\text{comp}}$ specific to each data set. This phase is defined as the opposite of the output phase of the interferometer $\Delta\Phi^{\text{comp}}$ where the phase associated to the classical bias $\phi_{\text{bias}} = k_{\text{eff}} b_z T^2$ was suppressed beforehand using the closed-loop fringe tracking algorithm to limit at most the variation of parameters unrelated to the rotations. It can be formulated:

$$\phi_{\text{rot}}^{\text{comp}} = \phi_{\text{bias}} - \Delta\Phi^{\text{comp}} \tag{4.43}$$

hence gathering all the phase contributions exclusively related to the rotations of the instrument and reference mirror. As for the experimental conditions, we know that the sensor head is rotated around the x axis which allows us to write $a_x = 0$ m/s^2, $v_x = 0$ m/s and $\Omega_y = \Omega_{\text{my}} = 0$ mrad/s. For clarity, the notations will be simplified as $\theta \equiv \theta_x$, $\Omega \equiv \Omega_x$ and $\Omega_m = \Omega_{\text{mx}}$. This allows us to write a first simplified expression, still under the assumption of constant angular velocities:

$$\begin{aligned}\phi_{\text{rot}}^{\text{comp}} = k_{eff} T^2 \Big[&- 2(v_y + a_y T)\delta\Omega - a_y \Omega_m T + \left\{ z_0^{\text{CA}} - y_0 \Omega^2 T (2\Omega + 3\Omega_m) \right\} \Omega^2 \\ &- \left\{ 2 z_0^{\text{MA}} + d_m + 3T \left(v_z + v_{\text{rec}} - y_0 \Omega_m \right) \right\} \Omega_m^2 - 3 v_z T \delta\Omega^2 \Big].\end{aligned} \tag{4.44}$$

Subsequently, we decide to restrict the model to phase shifts at most quadratic in rotation rate and interrogation time, as the higher order contributions are negligible before these. This allows us to further simplify the equation by removing the terms related to the initial transverse coordinate y_0. Eventually, writing $v_{\text{rec}} = \hbar k_{\text{eff}}/m$ and considering that the sensor head is attached to the rotary table with no translation allowed during the runs, we can explicit the inertial components of the atomic cloud at the beginning of the interferometer for a measurement on the z axis of the science chamber:

- $a_y = -g \sin(\theta)$;
- $v_y = -g.TOF. \sin(\theta)$;
- $v_z = -g.TOF. \cos(\theta)$.

The expressions of the velocity components are valid under the assumption that the angle θ remains constant during the free-falling time of the atoms before the

interferometer TOF, thus neglecting the composition of motions between the different inertial frames. We finally reach a convenient rotation phase shift only dependent on measurable parameters:

$$\begin{aligned}\phi_{\text{rot}}^{\text{comp}} = k_{eff}T^2\Big[&2g\sin(\theta)(TOF+T)\delta\Omega + g\sin(\theta)T\Omega_m + 3g\cos(\theta)TOF.T\delta\Omega^2 \\ &+ z_0^{CA}\Omega^2 - \left\{2z_0^{MA} + d_m - 3T\left(g\cos(\theta)TOF + \frac{\hbar k_{\text{eff}}}{m}\right)\right\}\Omega_m^2\Big].\end{aligned} \tag{4.45}$$

Several contributions to this phase shift let appear the tilt angle of the experiment $\theta = \theta_x$, which is naturally varying when an angular velocity is applied to the rotary table. However, as it was explained in the previous section, we consider it constant and thus take the average value over the atom interferometer.

The initial distance between the mirror surface and the atomic cloud z_0^{MA} and the initial distance between the mechanical accelerometer's proof mass and the atomic cloud z_0^{CA} have been determined in section 4.2. Though the dependence in the inclination of the Raman laser beam makes little difference, we still take it into account and remind their expressions below:

$$z_0^{\text{MA}}(\theta) = 129.7\text{ mm} - \frac{1}{2}g\cos(\theta)TOF^2. \tag{4.46}$$

$$\begin{aligned}z_0^{\text{CA}}(\theta) &= 75.9\text{ mm} + z_0^{\text{MA}}(\theta) \\ &= 205.6\text{ mm} - \frac{1}{2}g\cos(\theta)TOF^2.\end{aligned} \tag{4.47}$$

Ultimately, the rotation rate $\Omega = \Omega_x$ is calculated by taking the average value of the measurements of the FOG on the x axis over the whole interferometer. As for the rotation rate of the mirror, it corresponds to the mean value of the two measurements transmitted to the tip-tilt controller:

$$\Omega_m = -\frac{\Omega(t_1) + \Omega(t_2)}{2} \tag{4.48}$$

with $t_1 = \tau + t_{\text{del}}$ and $t_2 = T + 3\tau + t_{\text{del}}$. Furthermore, to tackle a prospective error made on the reference mirror's angular velocity, a correction coefficient ε was associated to the terms dependent on Ω_m as $\Omega_m' = (1+\varepsilon)\Omega_m$. This coefficient is estimated empirically by minimizing the phase noise σ_ϕ of the atomic fringes when fitting a sine wave to the experimental points. Rigorously speaking, the equation used to reconstruct

the interferometric fringes under compensated rotations is thus the following:

$$\phi_{\text{rot}}^{\text{comp}} = k_{eff}T^2\Big[2g\sin(\theta)(TOF+T)\delta\Omega + g\sin(\theta)T(1+\varepsilon)\Omega_m + 3g\cos(\theta)TOF.T\delta\Omega^2 + z_0^{CA}\Omega^2 - \left\{2z_0^{MA} + d_m - 3T\left(g\cos(\theta)TOF + \frac{\hbar k_{\text{eff}}}{m}\right)\right\}[(1+\varepsilon)\Omega_m]^2\Big] \tag{4.49}$$

where the residual rotation rate is now equal to $\delta\Omega = \Omega + (1+\varepsilon)\Omega_m$.

After estimating all the experimental parameters, the rotation phase $\phi_{\text{rot}}^{\text{comp}}$ is calculated for all the runs performed using equation 4.49 and the population ratios measured at the output of each interferometer (visible in figure 4.19 (c)) are displayed as a function of this rotation phase. The result of this operation, exhibited in figure 4.19 (d), demonstrates the validity of our theoretical model for the phase shift of a rotating interferometer with active compensation of the reference mirror. In comparison with the raw data, we can clearly observe a sinusoidal pattern in the phase distribution of the population ratios indicating that we have successfully reconstructed the atomic fringes. Furthermore, when fitting a cosine function to the experimental data, it results in a contrast $C = 32\%$ which is consistent with the value obtained in static and a signal-to-noise ratio $SNR = 5.4$. This parameter is calculated as the ratio of the contrast and the phase noise $SNR = C/\sigma_\phi$, the latter representing the standard deviation of the residuals between the measured ratios P_i and the fitted ratios $\tilde{P}_i$ as:

$$\sigma_\phi = \sqrt{\frac{1}{N}\sum_{i=1}^{N}\left(P_i - \tilde{P}_i\right)^2} \tag{4.50}$$

with N the total number of experimental points. The value of the SNR is directly related to the sensitivity to acceleration σ_a through the equation:

$$\sigma_a = \frac{1}{k_{\text{eff}}T^2}\frac{2}{SNR} \tag{4.51}$$

yielding a sensitivity $\sigma_a = 23.6$ µg/shot. The factor 2 on the numerator comes from our definition of the contrast.

As mentioned above, these results were obtained while minimizing the phase noise through the free parameter ε applied to the equivalent rotation rate of the mirror Ω_m. This process yielded a correction coefficient $\varepsilon = -1.3\%$, which could correspond to an insufficient amplitude in the displacement of the piezo-electric actuators or a marginal Coriolis phase shift associated with the classical accelerometer's measurement as discussed in subsection 4.3.5.

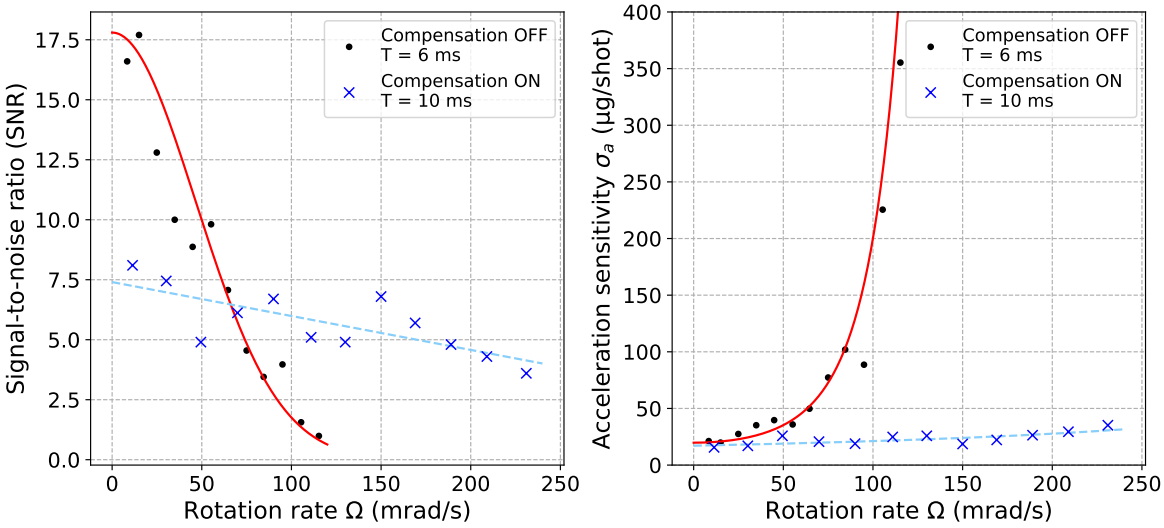

Figure 4.20: Comparison of the performances of the rotating interferometer using the fringes reconstruction process with and without mechanical compensation on the reference mirror. (Left) Evolution of the signal-to-noise ratio with the angular velocity with (blue crosses) and without (black dots) the stabilization of the reference mirror. The red curve is a theoretical prediction of the SNR drop in the uncompensated case with a cloud temperature $\mathcal{T} = 3.6$ µK, a constant phase noise and a static value $SNR_0 = 17.8$. The light blue dotted line depicts a linear fit to the measured SNR with the real-time rotations compensation. (Right) Corresponding acceleration sensitivity converted from the SNR values using equation 4.51, both for experimental measurements (black dots and blue crosses), theoretical prediction (red curve) and fit to the experimental points (light blue dotted line).

Figure 4.20 displays the evolution of the rotating interferometer's performance with the mechanical stabilization of the reference mirror in the laboratory frame (blue crosses), overlapped with the results in the uncompensated case already presented in figure 4.7. As we can see on the left-hand graph, the signal-to-noise ratio obtained when the compensation scheme is enabled is lower than in the uncompensated case at low rotation rates but remains fairly stable while increasing the angular velocity, despite a slight overall decline. What is interesting when turning this parameter into an acceleration sensitivity, which has more physical meaning, is that the performance of the rotating accelerometer with the compensation of the reference mirror's rotation is consistently better than in the uncompensated case for all the angular velocity ranges, mostly due to the larger interrogation time. Furthermore, a linear fit to the experimental points exhibits a fairly low influence of the rotation rate on the sensitivity to accelerations, namely:

$$\frac{d\sigma_a}{d\Omega} = (59.6 \pm 16.3)\frac{\mu g}{\text{rad/s}} \tag{4.52}$$

with a static sensitivity equal to $\sigma_a^0 = (16.2 \pm 2.2)$ µg/shot. These results demonstrate the robustness of the technique implemented and the promising outcomes of on-field

applications of atom interferometers with a rotation compensation scheme.

As it can be interesting to put these results in regard of other operating situations, interferometric measurements performed the same day on a static instrument returned average contrast $C \approx 33$ and signal-to-noise ratio $SNR \approx 24$. This corresponds to a sensitivity $\sigma_a^{\text{static}} = 5.3$ µg/shot which represents a degradation of the average performance of the rotating interferometer over the whole angular velocity range by a factor 4.5, but we still need to determine the limiting parameters and key factors of improving. Indeed, the effect of the rotation cannot be completely uncorrelated from other sources of noise such as vibrations or contrast inhomogeneities.

4.3.5 Current limitations and improvement prospects for the rotating atom interferometer

Restricted performance of the classical-quantum hybridization under strong vibrations

Apart from the rotations of the sensor head and reference mirror, the main factor which can reduce the sensitivity of the interferometer to the acceleration of the atoms relative to the reference mirror is the presence of exacerbated vibrations. In particular when performing measurements on the rotary platform, the weight of the sensor head above the rotation axis and of the counterweight below (both amounting to approximately 100 kg) induce strong vibrations that are directly transmitted to the whole instrument. Even though the real-time hybridization with the mechanical accelerometer helps mitigating the sensitivity of the measurement to these vibrations, it remains limited by the classical sensor's bandwidth and intrinsic noise.

In our hybridization scheme, the sensitivity of the interferometer to vibrations is determined by two main factors. In addition to the pass-band of the interferometer's transfer function, defined by the cycling time, interrogation time and pulse duration, the delay set on the acquisition of the classical accelerometer's signal for the real-time hybridization defines the frequency band where the vibrations will be compensated for by phase shifting the signal of the interferometer. This delay was adjusted in static, where specific vibrations from the environment and resonances of the mechanical structure were critical in the $20 - -30$ Hz band, but we observe large resonance peaks in the acceleration spectrum of the rotating accelerometer in the $50 - -60$ Hz range as displayed in figure 4.21 (a). Unfortunately, the acquisition delay of the classical accelerometers cannot be extended at will to tackle higher frequency vibrations, as a too large value eventually leads to a loss of correlation between the classical and the

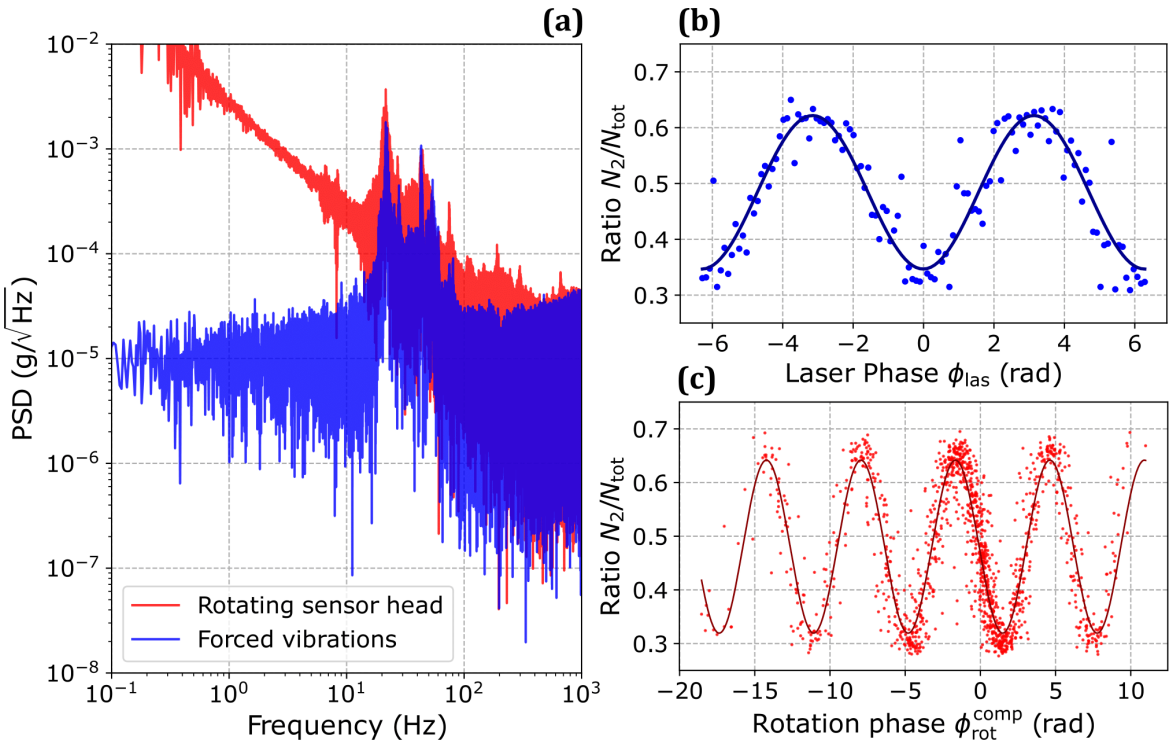

Figure 4.21: Comparison of the atom interferometer's performances under rotations and forced vibrations. (a) Overlapped spectra of the z axis classical accelerometer under (red) rotations of the three-axis platform at $|\Omega| \leqslant 250$ mrad/s and (blue) forced vibrations produced by a neoprene-tipped hammer. (b) Atomic fringes under forced vibrations on a static sensor head with experimental points in light blue and a cosine fit in dark blue, yielding $C = 0.27$ and $SNR = 6.2$ at $T = 10$ ms. (c) Reconstructed atomic fringes on a sensor head rotating at $|\Omega| \leqslant 250$ mrad/s with $\theta_z = 0°$ and $\theta_x \in [0, 30]°$ with experimental points in light red and a cosine fit in dark red, yielding $C = 0.32$ and $SNR = 5.4$ at $T = 10$ ms.

quantum inertial sensors.

In order to reproduce the vibration spectrum obtained in the presence of rotations, several attempts were made until we reached similar noise amplitudes at the critical frequencies exhibited by the rotating accelerometer's spectrum. The best results were obtained when gently tapping the rotary platform with a neoprene-tipped hammer while atom interference fringes were recorded. Figure 4.21 summarizes the result of this study, with the overlapped accelerometer's spectra under rotations (red) and forced vibrations (blue) appearing on the left and the corresponding fringes exhibited on the right. The acceleration spectrum for the rotating sensor head corresponds to a fraction of the runs displayed in figure 4.21 (c), for a rotation rate $|\Omega_x| \leqslant 250$ mrad/s. In the case of forced vibrations, the sinusoidal fit to the experimental points returned a contrast $C = 0.27$ for a signal-to-noise ratio $SNR = 6.2$. Considering a contrast $C' = 0.32$, as in the rotating case, and an equal phase noise σ_ϕ yields $SNR' = C'/\sigma_\phi = 7.4$. This operation allows us to compare both performances in similar configurations as

the reduced contrast is most likely related to the laser power or polarization rather than the vibrations or rotations themselves. In any case, we observe a signal-to-noise ration strongly limited by the vibration noise even when the instrument is not rotating, demonstrating that the real-time rotation compensation system for contrast recovery as well as the theoretical model for the phase reconstruction do not significantly inhibit the sensitivity to accelerations of our sensor.

Amplitude noise induced by the tilt-dependent fringes contrast

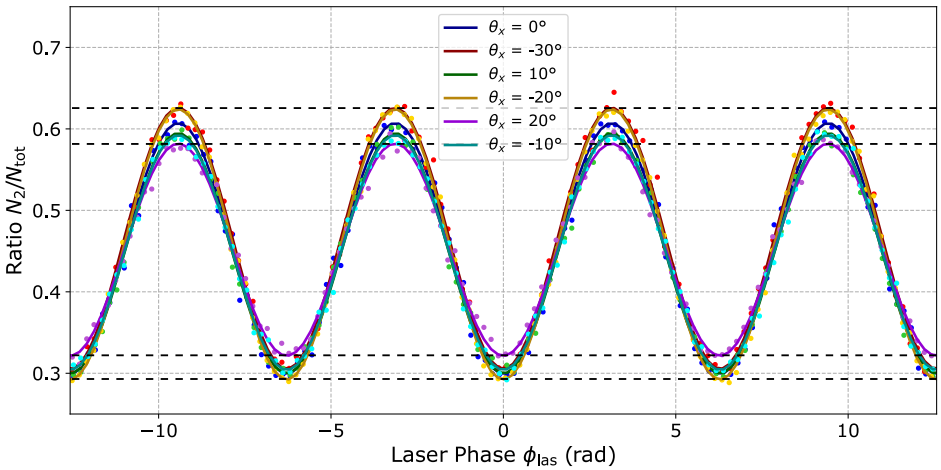

Figure 4.22: Atomic fringes recorded on a static sensor head at $T = 10$ ms. Each run corresponds to a tilt angle $\theta_x \in [-30, +20]°$ in steps of 10°. The black dashed lines illustrate the amplitude noise related to the tilt angle of the sensor head.

The second specificity to our experiment which can constrain the performance of the interferometer in rotation is related to the Rabi frequency inhomogeneities, arising from an atomic cloud free-falling in an inclined Gaussian Raman laser as described in section 3.2. For a given tilt angle θ_x of the sensor head, the trajectory of the atoms scanning the intensity profile of the Gaussian laser beam alters the pulse duration verifying the $\pi/2$ and π conditions throughout the interferometer. Due to this, the efficiency of the second and third Raman pulses are reduced with respect to the first one, causing a decrease in the contrast of the atomic fringes. Furthermore, the difficulty to implement a rigorously symmetric detection system producing consistent measurements in such a wide range of orientations also plays part in the amplitude noise of the atomic fringes, related to the contrast C and the population ratio offset P_0. These effects are exhibited in figure 4.22 where the contrast of atomic fringes is strongly dependent on the tilt angle θ_x of the Raman beam. These data were recorded before the detection system was adjusted, while a drastic contrast drop occurred between $\theta_x = 20°$ and $\theta_x = 30°$. Hence, both the detection system alignment and the intensity profile of the laser beam constitute ways of improving the robustness of the rotating hybrid accelerometer, by adding photodetectors and adapting the selected area depending on the tilt angle on

the one hand, and implementing flat-top laser collimators or top-hat beam shapers on the other hand [Mielec et al. 2018].

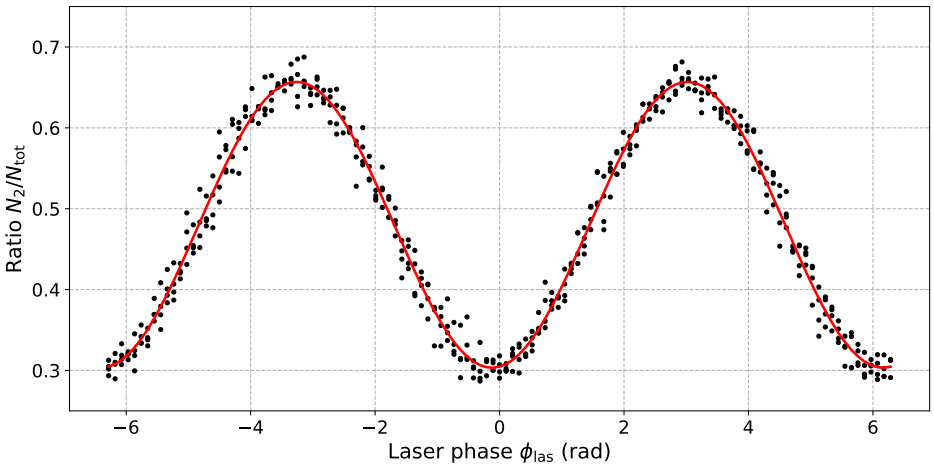

Figure 4.23: Atomic fringes acquired on a static sensor head at $T = 10$ ms. Black dots correspond to the overlapping of four different runs where θ_x varied from 0° to 30° in steps of 10°. The red curve displays a cosine fit to the concatenated experimental data, yielding a contrast $C = 0.35$ and a signal-to-noise ratio $SNR = 20.9$.

Contrary to static runs where the contrast C and the populations ratio offset P_0 can be evaluated individually, producing comparable signal-to-noise ratios, it is no longer possible when performing matter-wave interferometers on a rotating apparatus. For non-null angular velocities, the inclination of the Raman laser beam varies throughout a given interferometer but also from one measurement to the other. This feature finally results in amplitude noise on the interference pattern which is complex to separate from the phase noise when analyzing data and induces a deterioration of the instrument's sensitivity to accelerations. Figure 4.23 illustrates this issue with four concatenated sets of atomic fringes, acquired between 0° and 30°. This range of tilt angles is the same scanned for the dynamic runs presented in this section, as it corresponds to the scope where the contrast is the most stable. Nevertheless, when a cosine function is fitted to these four data sets altogether (red curve), we can observe a decrease in the SNR due to this amplitude noise visible on top and bottom of the red curve's extrema. This fit yields a signal-to-noise ratio equal to $SNR = 20.8$ while each run analyzed individually returns a SNR ranging between 25 and 26. This issue does not appear to be the major hindrance in figure 4.23 because the detection system was adjusted to produce a fairly constant fringes visibility in the chosen range of tilt angles, but it could become much more significant when scanning a wider angular range as part of onboard measurements for instance.

Improvement of the real-time rotations compensation for a constant angular acceleration

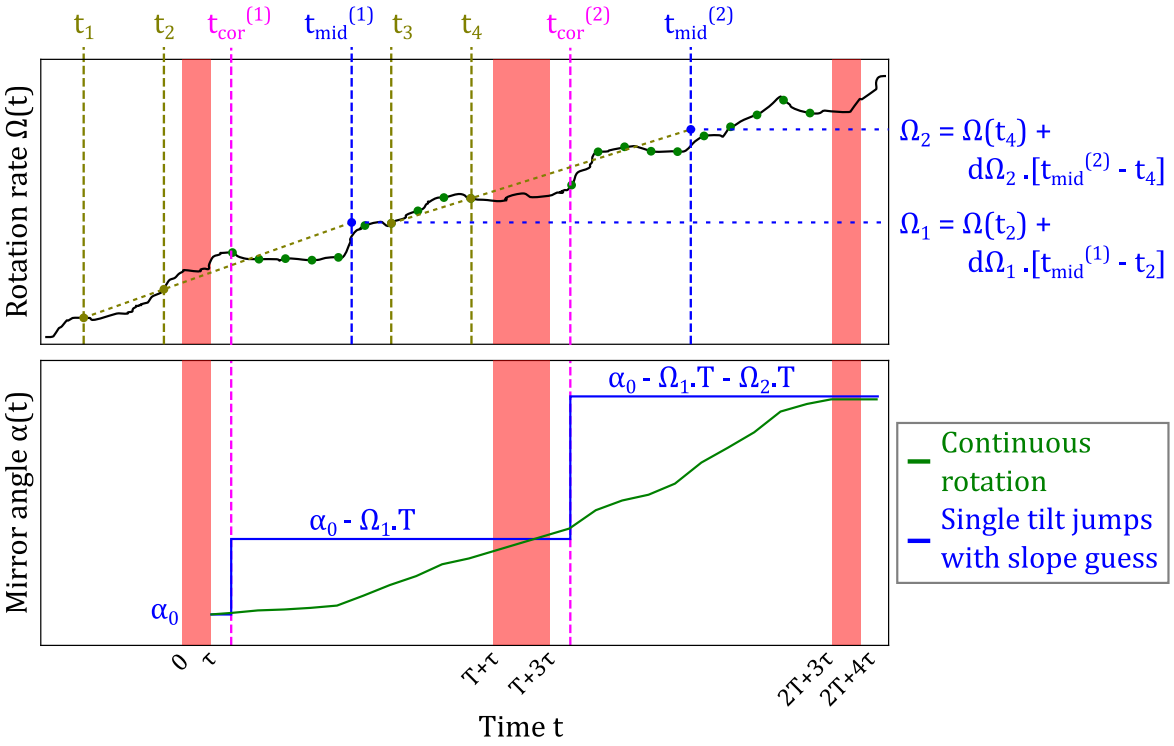

Figure 4.24: Timing diagram of the rotation rate $\Omega(t)$ measured by the gyroscopes (top) and of the mirror's angle $\alpha(t)$ (bottom) for a mean rotation rate estimation algorithm. On the top graph, the black line represents the real rotation rate experienced by the apparatus, green dots display the measurements of the gyroscopes at 1 kHz and blue dots denote the estimated average value of the angular velocity. Comparing two angular velocities measured before a Raman pulse, we can determine the angular acceleration used to assess the mean rotation rate (supposedly midway through the two Raman pulses for a rotation rate at most linear). As for the reference mirror's tilt angle, the green curve illustrates an ideal compensation with an integration of the rotation rate at the FOG acquisition rate, which is incompatible with our tip-tilt platform due to the settling time. The blue steps exhibit the behavior of the reference mirror with two tilt jumps at a short fixed delay after each first Raman pulses. The overall linear tendency of the rotation rate throughout the interferometer, supported by the coarsely quadratic evolution of the mirror's angle in the case of a continuous rotation, illustrates the assumption made that we operate our instrument under angular velocities at most linear on these timescales.

Alternatively to the compensation scheme described in subsection 4.3.2 and implemented on our experiment, an upgrade version was contemplated. Recording two isolated values of the rotation rate at times t_1 and t_2 and proceeding with the calculations make the experiment sensitive to the noise of the gyroscopes, in addition to restricting the utmost performance of the compensation system due to the trade-off on the choice of the correction times t_1 and t_2. However, it is possible to record two values of the angular velocity $\Omega(t_{1,3})$ and $\Omega(t_{2,4})$ prior to each Raman pulse in order to

determine the slope characterizing the local variation of the rotation rate:

$$\begin{aligned}\frac{d\Omega_1}{dt} &\approx \frac{\Omega(t_2)-\Omega(t_1)}{t_2-t_1}\\ \frac{d\Omega_2}{dt} &\approx \frac{\Omega(t_4)-\Omega(t_3)}{t_4-t_3}\end{aligned} \tag{4.53}$$

as depicted in figure 4.24 where $d\Omega_{1,2}/dt$ is written $d\Omega_{1,2}$ for simplicity. If we still consider a rotation rate varying at most linearly with the time, its mean value between the two first and the two last Raman pulses will be found midway through at times $t^1_{\text{mid}} = \tau + T/2$ and $t^2_{\text{mid}} = 3(\tau + T/2)$ respectively. The assumed mean values are thus calculated using the following expressions:

$$\begin{aligned}\Omega_1 &= \Omega(t_2) + \frac{d\Omega_1}{dt}\left[t^1_{\text{mid}} - t_2\right] = \Omega(t_2) + \frac{\Omega(t_2)-\Omega(t_1)}{t_2-t_1}\left[\tau + \frac{T}{2} - t_2\right]\\ \Omega_2 &= \Omega(t_4) + \frac{d\Omega_2}{dt}\left[t^2_{\text{mid}} - t_4\right] = \Omega(t_4) + \frac{\Omega(t_4)-\Omega(t_3)}{t_4-t_3}\left[3\left(\tau + \frac{T}{2}\right) - t_4\right].\end{aligned} \tag{4.54}$$

Hence, the correction of the reference mirror's orientation can be simply calculated using the rotation angles $\theta_{1,2} = -\Omega_{1,2}T$ and following the same procedure as described above.

The major advantage offered by this technique is that it allows us to evaluate the average value of the rotation rate before the Raman pulse so that the motion of the piezo-electric actuators can be initiated right after the light-matter interaction (at times $t^{1,2}_{\text{cor}}$ in figure 4.24, typically in the order of 10 µs). By doing so, we get rid of the trade-off on the correction time by having a better estimation of the average rotation rate in addition to leaving more time to the tip-tilt platform to stabilize. Nevertheless, the efficiency of this solution is based on the strong assumption of an angular velocity varying at most linearly, which is not necessarily the case. For an evolution at least quadratic or inflection points happening in between two light pulses, then the slope guessing may assess an average rotation rate very distant from the actual one, leading to an incorrect rotation of the reference mirror. Additionally, it remains unclear at what times the measurements should be recorded for the slope estimation, as a too short interval may yield a slope defined by the noise of the gyroscopes but a too long interval would average out several rotation patterns of the carrier, also leading to orientation errors. An implementation of this compensation scheme on the experiment was attempted, taking a 4 ms time interval before the first and second Raman pulses, but it did not show any evidence of an improvement or deterioration of the performances in addition to an increased consumption of the FPGA board's logical elements and resources. For these reasons, the compensation scheme used to

acquire the data presented in the following of this chapter was set back with the fixed time delay t_{del}. Though, with a good knowledge on the pattern of a given carrier's motion and specifically the amplitude, shape and period of its rotations, it might be advantageous to switch back to this slope estimation algorithm which would be more robust to strong angular accelerations for instance.

Correction coefficient ε related to the mirror's rotation

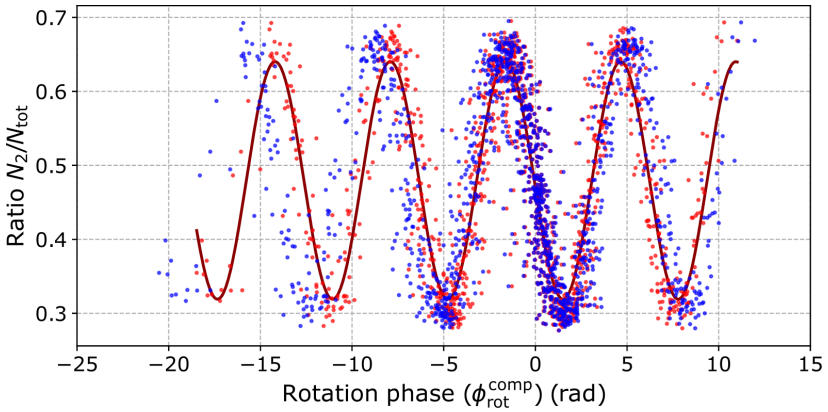

Figure 4.25: Atomic fringes corresponding to the runs displayed in figure 4.19 (red) with an empirical correction of the reference mirror's angular velocity $\varepsilon = -1.3\%$ and (blue) without correction. The dark red solid curve displays the fit to the experimental points, fairly similar in both case which is why only the fit with the correction was displayed. As the rotation phase $\phi_{\mathrm{rot}}^{\mathrm{comp}}$ and thus the rotation rates $\overline{\Omega}$ and Ω_m increase, we can observe the match between the fitting function and the blue points deteriorating, suggesting a dilatation of the atomic fringes in the non-corrected case.

As mentioned above, an empirical correction factor ε was added to the rotation of the mirror to minimize the phase noise σ_ϕ when fitting a cosine function to the reconstructed experimental points. The results are superimposed in figure 4.25 with an optimal correction $\varepsilon = -1.3\%$ in red and no correction applied in blue. The red points as well as the dark red curve resulting from a fit are the same data as presented in figure 4.19. What can be observed in this figure is that, as the rotation phase $\phi_{\mathrm{rot}}^{\mathrm{comp}}$ and thus the rotation rates $\overline{\Omega}$ and Ω_m increase, the uncorrected experimental points do not match the fitting function anymore and their relative phase difference keeps increasing. Such behavior indicates a dilatation of the atomic fringes which is often related to a problem in the scale factor of the accelerometer.

Considerable efforts have been put in eliminating the potential sources of error influencing this mismatch with the theoretical model, and a characterization of the tip-tilt yielding a systematic pointing error below 1% of uncertainty - which is inferior to the uncertainty on the optical characterization described in section 2.4 - is difficult.

For this reason, the tip-tilt stage is the privileged origin of this effect and the correction was specifically associated with the equivalent rotation rate of the mirror.

However, another theory could relate this effect to an error in the scale factor of the fiber-optic gyroscope for instance, misleading us on the estimation of the instrument's angular velocity and inducing a systematic error in the rotation of the mirror. This scale factor was calibrated before it was delivered, but in the absence of an automated platform enabling well-controlled, accurate angular velocities, it appears difficult to estimate the veracity of this hypothesis. Additionally, scale factor drifts related to the temperature variations or parasitic magnetic fields — as the fiber-optic gyroscopes are not shielded — also remain uncharacterized.

Furthermore, we have considered a residual Coriolis acceleration measured by the mechanical accelerometer. Regarding the latter, it was stated at the beginning of this chapter that no Coriolis acceleration should be sensed by the classical inertial sensor as the electro-mechanical elements implemented in the device should prevent the proof-mass from moving freely in the frame of the accelerometer's case. It is possible to imagine that for high enough angular velocities, this assumption does not hold anymore and the relative displacement between the accelerometer's body and its proof mass induces the measurement of a systematic, residual Coriolis acceleration.

In order to determine which of these hypotheses is valid, we have tried to apply this correction coefficient to the average rotation rate $\overline{\Omega}$ in the uncompensated case as the mirror is not rotating independently in this configuration. Though, the reconstruction of the atomic fringes in the absence of rotations compensation requires lower angular velocities and shorter interrogation times which reduces the importance of the rotation-induced phase shifts. Furthermore, without stabilizing the reference mirror, the rotation phase ϕ_{rot} is strongly dominated by the Coriolis effect related to the motion of the atomic cloud and other effects have a small impact difficult to observe. Nevertheless, estimating this empirical optimization of the phase noise yields a very close correction coefficient ($\varepsilon = +1.2\%$, reminding it is applied on the average rotation rate $\overline{\Omega}$ which has a sign opposite to that of the mirror's angular velocity Ω_m in the compensated case). This correction induces a very marginal improvement of the signal-to-noise ratio, from 8.63 to 8.71, hence it appears difficult to designate this effect as the source of the difference observed between the theoretical model and experimental data. As it is also difficult to reach an uncertainty at the 1% level on the optical characterization of the tip-tilt stage, it is at this time impossible for us to provide an unequivocal explanation and this study will require further investigation.

Conclusion

The operation of the fully hybridized accelerometer under high, arbitrary angular velocities has been established. In regard to the theoretical model, the closed-loop hybridization scheme has imposed a completion of the output phase shift of a rotating matter-wave interferometer determined in sections 1.3 and 1.4. Indeed, this algorithm consists in subtracting the measurement of the atom interferometer from the classical acceleration signal in order to isolate and correct for the latter's bias, but the mechanical sensor's motion also becomes non-trivial under non-negligible rotation rates. In particular, considering the trajectory of the classical accelerometer has led to a modification of the lever arm participating in the centrifugal phase shifts and a suppression of the instrument's center of rotation influence at the first order.

Thereafter, the models of both the exponential decay in the interference fringes visibility and the rotation-induced systematic phase shifts scrambling the output phase of the interferometer have been validated on the experimental apparatus described in chapter 2, allowing us to reconstruct the atomic fringes and retrieve an acceleration signal for angular velocities $|\Omega| \leqslant 80$ mrad/s ≈ 4.6 °/s at an interrogation time $T = 6$ ms, enabling a sensitivity $\sigma_a \approx 41.2$ µg/shot. If this represents a compelling result as it is the first demonstration of an atomic accelerometer in such noisy conditions, the loss of contrast strongly restricts the accessible experimental parameters to low angular velocities and short interrogation times and needs to be addressed first and foremost.

Based on the fact that the contrast loss is the consequence of the rotation of the wave vector of the Raman transition, a real-time rotation compensation system was designed. It consists in the mechanical stabilization of the reference mirror's orientation in the laboratory frame for the duration of the interferometer by applying to this mirror a rotation opposed to that of the science chamber. After detailing the FPGA-based algorithm, its implementation and performance on the hybrid instrument were evaluated. The compensation system successfully enhanced the measurement range of the hybrid accelerometer to a satisfying interrogation time $T = 10$ ms and a wide range of arbitrary angular velocities $|\Omega| \leqslant 250$ mrad/s ≈ 14.3 °/s by maintaining the visibility of the interference pattern with no deterioration. Moreover, the model of the output phase shift for a rotating compensated hybrid accelerometer was corroborated by the reconstruction of the atomic fringes using the same experimental parameters as stated above, yielding a consistent sensitivity $\sigma_a \leqslant 35$ µg/shot over the whole operating range.

In summary, this study represents the first realization of an atom interferometer-

based hybrid accelerometer capable of operating in a regime of strong vibrations and angular velocities and for a wide range of tilt angles through its correlation with high-performance fiber-optic gyroscopes. The theoretical model yielding the output phase shift of an hybrid accelerometer under strong rotations, with and without an independent rotation of the reference mirror, validates our general approach on a rotating atom interferometer and the successful reconstruction of the atomic fringes substantiates the relevance and robustness of our hypotheses, regarding both the experimental parameters and operating conditions. Ultimately, the factors of degradation in the hybrid accelerometer's performance yield very consistent results in the same environment, regardless of the presence of rotations of the instrument. These outcomes constitute a promising prospective in the application of strapdown atomic inertial sensors for measurements onboard a rotating vehicle.

Conclusion and prospects

Cold-atom inertial sensors based on matter-wave interferometers such as atomic accelerometers or gyroscopes stand out among the most mature quantum technologies. The growing interest in such sensors providing an absolute measurement of inertial components has led to remarkable developments yielding unrivaled sensitivity, stability and accuracy, and the successful technological transfer of atomic gravimeters even pushed the boundaries of field quantum gravity sensing to an industrial level [Ménoret et al. 2018; Antoni-Micollier et al. 2022]. However, various challenges remain to be addressed in the quest of truly mobile quantum inertial sensing, including multi-axis measurements and operation in harsh environments requiring a certain resilience to strong regimes of vibrations and rotations.

Three-axis hybrid quantum-classical accelerometer

This PhD work falls within the scope of the iXAtom project aiming at building a new generation of high-end inertial sensors based on the hybridization of classical accelerometers and gyroscopes with matter-wave interferometers. When I arrived in the laboratory, the experimental setup for the three-axis hybrid accelerometer had already been assembled and characterized in quasi-static configuration leading, shortly after, to the demonstration of a fifty-fold improvement on the stability of the gravitational acceleration norm's measurement as compared to a triad of classical accelerometers [Templier et al. 2022]. Our hybridization scheme, relying on atomic interferometry to calibrate the bias of classical sensors and use the latter's corrected signal as the sensor's output, enables for a bias-free tracking of the acceleration components while providing a high bandwidth and a large dynamic range.

Regarding the performances, this hybrid accelerometer demonstrated a sensitivity equal to 22 µg/$\sqrt{\text{Hz}}$ and an uncertainty of 5.8 µg on the reconstruction of the acceleration vector. For comparison, the static characterization of a transportable gravimeter yielded a sensitivity of 0.8 µg/$\sqrt{\text{Hz}}$ and an acurracy of 0.17 µg [Bidel et al. 2023]. The sensitivity on our measurement is primarily limited by the dead times imposed by the sequencer used and could thus be drastically improved by designing a new electronic control system avoiding this technical issue. Concerning the accuracy, it is by the scale factor error related to the Doppler compensation scheme using phase-discontinuous frequency jumps. With a higher-resolution direct digital synthesizer, a new compensation scheme

based on frequency chirps with arbitrary slope variations — according to the rotations of the instrument — could be contemplated to substantially reduce the uncertainty on this systematic phase shift. Furthermore, the characterization of so far undetermined systematic effects such as the wavefront distortion, as well as the refinement of other effects and misalignments calibration protocol, would also allow further improving this aspect. Ideally, it would be beneficial to gain between one and two orders of magnitude on these two characteristics of the hybrid accelerometers triad.

Rotating atom interferometer for acceleration measurement

My contribution to this project has been predominantly dedicated to the study and correction of rotations at unprecedented levels for an atomic accelerometer, including the characterization and installation of the fiber-optic gyroscopes and piezo-actuated tip-tilt mirror. The programming of the FPGA-based rotation compensation system, acquiring the signals of the gyroscopes and converting them in real time into angular setpoints for the stabilization of the reference mirror's orientation, has occupied a significant share of my work. The implementation of this rotation compensation has enabled maintaining a constant visibility of the atomic interference pattern over a wide range of arbitrary angular velocities, up to fifteen degrees per second - corresponding to five thousand Earth's rotation rates. Furthermore, the comprehensive theoretical model established for the rotating atom interferometer's output phase shift, taking into account the hybridization of the matter-wave interferometer with classical accelerometers as well as a possible independent rotation of the reference mirror, has permitted the measurement of rotation components transverse to the laser beam by correlating the atom interferometer with two high-end fiber-optic gyroscopes, yielding a hybrid gyroscope able to operate in an extensive range of tilt angles. Ultimately, the reconstruction of the atomic fringes under random, strong vibrations and angular velocities in addition to large variations of the tilt angle provides access to the pursued acceleration measurement and paves the way for truly mobile applications of multi-axis quantum inertial sensors operating in a strapdown configuration. Moreover, this represents a promising solution for achieving accurate acceleration measurements in situations where weight and volume are critical, for example in submarines for navigation or ocean floor mapping purposes, where cumbersome vibrations-isolation and gyro-stabilization platforms cannot be permitted.

The long-term objective is naturally to reach similar performances with this mobile sensor experiencing strong rotations and accelerations as the ones achieved in static, which implies to suppress as much rotation- and vibration-induced phase noise as possible to reach the utmost performances of the interferometer given our experimental parameters. By increasing the size and optimizing the intensity profile of the laser

beams, an increase in the interrogation time could also be contemplated in order to further increase the sensitivity on the measurement of the acceleration components. Ultimately, in regards to the operating conditions, being able to measure acceleration components under rotation rates up to 15 °/s appears to be a satisfying outcome with respect to typical motions of marine carriers. As for the tilt angle range of the experiment, it could be enhanced by putting efforts in conceiving a more symmetric detection — which was not prioritized so far — and a larger, flat-top intensity profile of the laser beams to reach a reasonable range of 50 – 60° with a constant visibility of the atomic fringes.

Enhancing the resilience of the quantum sensor in harsh environments

As mentioned in chapter 4, strong high-frequency vibrations represent the most critical issue which needs to be addressed in order to retrieve the acceleration information out of the output of the hybrid inertial sensor. The current implementation of the hybridization algorithm with the navigation-grade accelerometers attached to each reference mirror offers a limited compensation bandwidth and if it proved to be crucial below forty hertz, there remains a broad spectrum where vibrations are insufficiently compensated for - typically up to one hundred hertz with our experimental parameters. In order to overcome this obstacle, the first action which will be undertaken consists in a thorough characterization of the accelerometers currently installed on the science chamber, including an estimation of their acquisition noise to be compared with the intrinsic performances of the sensors as well as an analysis of their frequency behaviors on a shaker. If these studies reveal that the current devices are inadequate for our specifications in the higher frequencies, it might be interesting to replace them with similar sensors providing higher-performance or to consider other technologies such as seismometers or optical accelerometers to provide a complementary measurement in the real-time hybridization scheme.

On another note, the rotation of the interrogation laser in the frame of the science chamber induces a misalignment between the classical and quantum measurement axes which can deteriorate the correlation between the two sensors, in particular the compensation of vibrations. After a rotation of the reference mirror, the vibrations sensed by the classical device along the considered axis will contain an irrelevant component in the plane of the reference mirror, in addition to losing information about the effective wave vector's projection onto other axes. With a mechanical structure sufficiently rigid, it is possible to use the classical accelerometers attached to the other reference mirrors in order to account for this projection of the laser beam onto different axes, but this is difficult to guarantee in practice. An alternative solution consists in

replacing each single-axis accelerometer by three-axis instruments at the back of each reference mirror. However, regardless of their positions, the mechanical sensors which are not aligned with the rotation axis will also be sensitive to different projections of the centrifugal acceleration which should be subtracted from their output signal, otherwise the calculation of the mirror rotation's contribution to the total phase shift would be inaccurate. For this reason, such solution appears difficult to conciliate with the closed-loop hybridization scheme as it is and further consideration is required.

In terms of motion simulation devices, the rotational platform used to carry out the experiments presented in this thesis is the same described in [Templier 2021]. It is a manually operated apparatus requiring an appropriate counterweight for every change on the science chamber - in our case approximately one hundred kilograms on both sides of the rotation axis - which puts substantial frictions on the rotation axis, thus inducing high vibrations. These vibrations strongly limit our performances and are difficult to discriminate from the effects induced by the rotation of the instrument, while the manual operation of the platform makes difficult to reproduce constant or precise rotation rate regimes. The replacement of this table with a fully automated, six-axis hexapod enabling frictionless, complex and well-controlled movements should help resolve both these issues in the short-term, allowing to push further the study of rotating atom interferometers and improve the performance of the fringes reconstruction for acceleration sensing.

Another major hindrance to the strapdown implementation of the proposed hybrid accelerometer lies in the strong dependence of the atomic measurement on the tilt angle of the sensor head. First, the finite size of the laser beams fundamentally limits the achievable interrogation times at high inclinations and thus the utmost sensitivity of our interferometer. Furthermore, an asymmetric detection also induces differences in the population ratio measurements at distinct tilt angles of the interrogation laser, yielding variations of the contrast and amplitude noise on the atomic fringes. Currently, three photodiodes are installed on the science chamber and the most appropriate one is selected given an orientation of the sensor head. In the future, an improved detection scheme where the signals of all the photodiodes are balanced according to the configuration could improve the robustness of the measurement to extreme tilt angles and drastic variations in the laser orientation. Besides, the Gaussian profile of the laser intensity scanned by the transverse component of the motion of the atomic cloud induces inhomogeneous Rabi frequencies and systematic light shifts which substantially harm the accuracy of the quantum inertial sensor. Implementing top-hat beam collimation would enhance the operation dynamic range of the atomic accelerometer in addition to improving its absolute accuracy.

Ultimately, once the rotation compensation system is implemented on the three measurement axes, an important characterization related to the calibration of the triad's misalignments will be required. Indeed, the protocol proposed in chapter 3 allowed gaining an order of magnitude on the uncertainty on the acceleration norm's measurement but this effect remains a major limitation of the multi-axis hybrid sensor's accuracy. Currently, the estimation of the systematic phase shifts associated with each independent atom interferometer limits the confidence on the axes' misalignments and further characterizations are required to provide a more comprehensive model of the sensor's accuracy, notably on the phase shift associated with the wavefront distortions. Moreover, it must be considered that the vibrations, rotations and temperature fluctuations experienced onboard a vehicle will be on a different level from the conditions under which the calibration was performed in the past, and the independent rotations of each reference mirror in the context of the rotations compensation system may further degrade the stability of these misalignments. To curb this effect, efforts are - and will need to be - put in the choice of the materials used for the vacuum chamber and the assembly of all the components constituting the instrument, in particular classical inertial sensors, laser collimators and photodetectors, in order to achieve the most rigid structure possible.

Real-time operation of the hybrid inertial measurement unit for mobile applications

In the context of mobile acceleration measurements, it is important that the cycling rate of the experiment is optimized so as to increase the sensitivity of the acceleration measurement, in addition to reaching a stable value faster. In the context of the hybrid accelerometer, the acquisition rate is not a problem as the five kilohertz signals of the mechanical accelerometers are utilized as the output. However, the tracking of the atomic signals required to correct for the classical biases plays an important part in the achievable performances and the sequential operation along the three axes as well as the flipping of the momentum recoil direction tend to quickly increase the cycle time. Furthermore, as presented in chapter 2, the electronic control system used on this experiment needs to reload the sequence from the CPU to the FPGA sequencer between each shot, adding an approximately one second dead time which dramatically reduces the repetition rate of the quantum triad. On this aspect, the development of a dedicated sequencer as well as the realization of a new laser source are currently examined. These two improvements of the setup should allow us to suppress unnecessary dead times in addition to retrieving shorter MOT durations, thus further reducing the effective cycle time of the experiment up to a factor five.

As for the rotations correction system, while the stabilization of the reference mirror's orientation is performed throughout the interferometer to maintain the contrast of the atomic fringes, the reconstruction of the interference pattern with the determination of the rotation-induced phase shifts is currently performed by post-processing the data with the high-frequency streaming of the classical gyroscopes and accelerometers. The mid-fringe lock algorithm was implemented to enable the tracking of the acceleration components, but the rotation phase scanned by the tilt angle and angular velocity of the sensor head can rapidly induce fringe hopping preventing any long-term measurement to be performed. With the aim of combining the fringe-tracking algorithm with the rotations compensation scheme, it is necessary to find a way to correct for the rotation phase in a similar manner to the double-hybridization algorithm between the classical and quantum accelerometers, where the correlation phase including the vibration phase shift is fed back to the laser a few microseconds before the last Raman pulse. An attempt to calculate an overall correlation phase related to both rotations and vibrations within the real-time algorithm was made, unfortunately the computational resources of the FPGA board utilized on the experiment turned out to be insufficient. Here as well, the new sequencer currently being developed should help overcoming this technical limitation and allow for an operation of the hybrid accelerometers' triad truly in real time.

Eventually, some strategies to further miniaturize the whole apparatus are ongoing with notably the development of a multi-axis atom accelerometer utilizing a magnetic trap on an atomic chip hybridized with a microfabricated grating chip. This technology should enable the magneto-optical trapping of the atoms with a single laser beam, making use of the orders diffracted by the grating chip. Furthermore, this new sensor head could allow performing simultaneous multi-axis Raman interferometry [Barrett et al. 2019], which would help address most of the cycling time limitations and reach a higher short-term sensitivity.

Appendix A

Complemented phase shift for a three-dimension, linear rotation rate

A.1 Generalized atomic phase shift

In chapter 1, I developed the calculation of the atomic phase shift $\Phi_{\text{at}}^{\text{comp}}$ related to the motion of the atomic cloud in the frame of the science chamber rotating at an angular velocity $\boldsymbol{\Omega}$ considering a compensation of this rotation on the reference mirror $\boldsymbol{\Omega_m}$.

Acceleration term	**Notation**	**Associated phase shift expression**
Relative (translational)	ϕ_{relative}	$k_{\text{eff}} T^2 a_z$
Mirror's rotation	$\phi_{\text{rotation}}^{\text{mirror}}$	$k_{\text{eff}} T^3 \left[a_x \Omega_{\text{my}} - a_y \Omega_{\text{mx}}\right]$
Residual Coriolis	ϕ_{Coriolis}	$2k_{\text{eff}} T^2 \left[\left(v_x + a_x T\right) \delta\Omega_y - \left(v_y + a_y T\right) \delta\Omega_x\right]$
Centrifugal (chamber)	$\phi_{\text{centrifugal}}^{\text{chamber}}$	$k_{\text{eff}} T^2 \Omega^2 \left[z_0 + 2x_0 \Omega_y T - 2y_0 \Omega_x T\right]$
Centrifugal (mirror)	$\phi_{\text{centrifugal}}^{\text{mirror}}$	$k_{\text{eff}} T^2 \Omega_m^2 [- 2z_0^{\text{MA}} - d_m - 3T \left(v_z + v_{\text{rec}} + x_0 \Omega_{\text{my}} - y_0 \Omega_{\text{mx}}\right)]$
Other terms arising from composition of motion	$\phi_{\text{compo.}}$	$3k_{\text{eff}} T^3 \Big[- v_z \left(\delta\Omega_x^2 + \delta\Omega_y^2\right) + \left(x_0 \Omega_y - y_0 \Omega_x\right) \left(\Omega_x \Omega_{\text{mx}} - \Omega_y \Omega_{\text{my}}\right)\Big]$

Table A.1: Summary of the contributions to the phase shift of an atom interferometer undergoing opposed rotations of the laser input $\boldsymbol{\Omega}$ and retro-reflection mirror $\boldsymbol{\Omega_m}$, given up to the third order in interrogation time and rotation rate. The effective wave vector is oriented along $+\boldsymbol{u_z}$ at the instant of the first pulse

Table A.1 reminds the contributions to this phase shift, valid under the assumption of a constant angular velocity and a rotation axis comprised in the plane transverse to the effective wave vector of the laser, namely $d\boldsymbol{\Omega}/dt = \mathbf{0}$ and $\Omega_z = 0$. This study

yielded the following expression:

$$\Phi_{\text{at}}^{\text{comp}} = \phi_{\text{relative}} + \phi_{\text{rotation}}^{\text{mirror}} + \phi_{\text{Coriolis}} + \phi_{\text{centrifugal}}^{\text{chamber}} + \phi_{\text{centrifugal}}^{\text{mirror}} + \phi_{\text{compo}}. \tag{A.1}$$

where $\Omega^2 = \Omega_x^2 + \Omega_y^2$ and $\Omega_m^2 = \Omega_{\text{mx}}^2 + \Omega_{\text{my}}^2$, and writing $\delta\Omega_i = \Omega_i + \Omega_{\text{mi}}$ the residual rotation rate along the i axis of the science chamber.

Now, what we are interested in is the modification of this atomic phase shift in the case of a three-dimension rotation vector — considering $\Omega_z \neq 0$ — and for a non-null first derivative, implying an angular velocity at most linear with time (equivalent to a constant angular acceleration). In this case, all the contributions listed in table A.1 remain true considering $\Omega^2 = \Omega_x^2 + \Omega_y^2 + \Omega_z^2$ and $\Omega_m^2 = \Omega_{\text{mx}}^2 + \Omega_{\text{my}}^2 + \Omega_{\text{mz}}^2$. Naturally, to these terms must be added the phase shifts so far neglected and arising from three main sources, namely the chamber's and mirror's rotations along the z axis as well as the tangential acceleration related to the angular acceleration.

First, the phase shift associated with the rotation of the chamber around the z axis can be separated in two distinct expressions, namely a linear contribution of this rotation component:

$$\begin{aligned}\phi_{\Omega_z} = {} & k_{\text{eff}} T^2 \Omega_z \left[-x_0 \Omega_x - y_0 \Omega_y\right] \\ & + 3 k_{\text{eff}} T^3 \Omega_z \left[z_0 \left(\Omega_{\text{mx}} \Omega_y - \Omega_x \Omega_{\text{my}}\right) + v_x \left(\delta\Omega_x + \Omega_{\text{mx}}\right) + v_y \left(\delta\Omega_y + \Omega_{\text{my}}\right)\right]\end{aligned} \tag{A.2}$$

and a phase shift quadratic in Ω_z:

$$\phi_{\Omega_z^2} = k_{\text{eff}} T^2 \Omega_z^2 \left[-z_0 + 3T \left(x_0 \Omega_{\text{my}} - y_0 \Omega_{\text{mx}}\right)\right]. \tag{A.3}$$

If most of the terms appearing in these two expressions scale as T^3 and are mostly negligible, onboard applications where the yaw is added to the roll and pitch of the vehicle will require to consider at least the first-order centrifugal phase shift along the z axis containing the atomic cloud's initial position components:

$$\phi_{\text{centrifugal}}^{\text{z}} = -k_{\text{eff}} T^2 \Omega_z \left[x_0 \Omega_x + y_0 \Omega_y + z_0 \Omega_z\right]. \tag{A.4}$$

Additionally, since the rotations of the chamber along the z axis are now accounted for, the rotation of the mirror along this axis also induces interferometric phase shifts which can be separated as previously:

$$\begin{cases} \phi_{\Omega_{\text{mz}}} = k_{\text{eff}} T^2 \Omega_{\text{mz}} \left[\left(x_0 + 3 v_x T\right) \Omega_{\text{mx}} + \left(y_0 + 3 v_y T\right) \Omega_{\text{my}}\right] \\ \phi_{\Omega_{\text{mz}}^2} = k_{\text{eff}} T^2 \Omega_{\text{mz}}^2 \left[z_0^{\text{MA}} + d_m + \dfrac{3T}{2} v_{\text{rec}}\right]. \end{cases} \tag{A.5}$$

Here as well, we can isolate dominating contributions related to the initial position of the cloud which can be assimilated to a first-order centrifugal phase shift:

$$\phi^{\mathrm{mz}}_{\mathrm{centrifugal}} = k_{\mathrm{eff}} T^2 \Omega_{\mathrm{mz}} \left[x_0 \Omega_{\mathrm{mx}} + y_0 \Omega_{\mathrm{my}} + \left(z_0^{\mathrm{MA}} + d_m \right) \Omega_{\mathrm{mz}} \right]. \tag{A.6}$$

If the atom interferometer is rotation invariant around the axis of the effective wave vector of the Raman laser, it is important to remind that the rotation component Ω_{mz} denotes the rotation of the mirror around the z axis of the sensor head. Hence, after a first rotation of the reference mirror in the rotating frame of the science chamber, the wave vector of the laser is no longer aligned with the z axis considered and the phase shifts developed above should be taken into account. Incidentally, this rotation of the reference mirror around the z axis is effectively applied when utilizing the generalized three-dimension rotation matrix presented in appendix B to drive the tip-tilt stage.

Ultimately, considering angular velocities no longer constant but instead varying (at most) linearly with time will induce a tangential acceleration related to the angular acceleration, producing a phase shift as follows:

$$\begin{aligned} \phi_{\mathrm{tangential}} = & - k_{\mathrm{eff}} T^2 \dot{\Omega}_x \left[y_0 + v_y T + z_0 T \left(2\delta\Omega_x + \Omega_{\mathrm{mx}} \right) \right] \\ & + k_{\mathrm{eff}} T^2 \dot{\Omega}_y \left[x_0 + v_x T - z_0 T \left(2\delta\Omega_y + \Omega_{\mathrm{my}} \right) \right] \\ & + k_{\mathrm{eff}} T^3 \dot{\Omega}_z \left[x_0 \left(2\delta\Omega_x + \Omega_{\mathrm{mx}} \right) + y_0 \left(2\delta\Omega_y + \Omega_{\mathrm{my}} \right) \right]. \end{aligned} \tag{A.7}$$

A.2 Evolution of the classical phase shift

On another note, the generalization of the rotation to three dimensions with a non-null angular acceleration also affects the equivalent phase shift related to the classical accelerometer as the latter is sensitive to driving accelerations — including tangential acceleration in addition to the centrifugal term. Furthermore, the composition of motions also induces other contributions arising from the rotation along the z axis. Similarly to the logic applied in chapter 1, we use the sensitivity function formalism to calculate the phase shift associated with the classical measurement, which yields:

$$\Phi_{\mathrm{cl}} = k_{\mathrm{eff}} T^2 \left[a_z + b_z + \left(z_0^{\mathrm{cl}} + v_z^{\mathrm{cl}} T \right) \Omega^2 \right] \tag{A.8}$$

$$- k_{\mathrm{eff}} T^2 \Omega_z \left[\left(x_0^{\mathrm{cl}} + v_x^{\mathrm{cl}} T \right) \Omega_x + \left(y_0^{\mathrm{cl}} + v_y^{\mathrm{cl}} T \right) \Omega_y + \left(z_0^{\mathrm{cl}} + v_z^{\mathrm{cl}} T \right) \Omega_z \right] \tag{A.9}$$

$$+ k_{\mathrm{eff}} T^2 \left[\left(x_0^{\mathrm{cl}} + v_x^{\mathrm{cl}} T \right) \dot{\Omega}_y - \left(y_0^{\mathrm{cl}} + v_y^{\mathrm{cl}} T \right) \dot{\Omega}_x \right] \tag{A.10}$$

where we recognize the simplified model established in chapter 1 on the first row, taking $\Omega^2 = \Omega_x^2 + \Omega_y^2 + \Omega_z^2$, the Ω_z-dependent second-order phase shifts on the second

row and the contributions of the angular acceleration on the third row. Similarly to the assumption made previously, we can consider that the proof mass of the classical accelerometer has no relative velocity in the frame of the sensor's case, reducing the previous formula as:

$$\Phi_{\mathrm{cl}} = k_{\mathrm{eff}} T^2 \left[a_z + b_z + z_0^{\mathrm{cl}} \Omega^2 - \Omega_z \left(x_0^{\mathrm{cl}} \Omega_x + y_0^{\mathrm{cl}} \Omega_y + z_0^{\mathrm{cl}} \Omega_z \right) + x_0^{\mathrm{cl}} \dot{\Omega}_y - y_0^{\mathrm{cl}} \dot{\Omega}_x \right]. \quad \text{(A.11)}$$

Similarly to the phase shift at the output of the hybrid accelerometer calculated in chapter 4 as $\Delta\Phi = \Phi_{\mathrm{cl}} - \Phi_{\mathrm{at}}^{\mathrm{comp}}$, we observe that some contributions to the atomic phase shift involving the position of the atomic cloud relative to the center of rotation are partially compensated by the classical measurement. Specifically, the centrifugal and tangential terms dependent on the coordinates x_0, y_0 and z_0 are the same as in the classical phase shift with the components x_0^{cl}, y_0^{cl} and z_0^{cl}. This observation results in a cancellation of the instrument's center of rotation at the first order and a simplification of the additional phase terms computed in this appendix when calculating the hybrid accelerometer's output phase shift.

Appendix B

Rotation matrix for a three-dimension rotation compensation

In order to perform onboard acceleration measurements with the hybrid accelerometer in a strapdown configuration, it is required to account for the three components of the rotation vector. Appendix A details how the atomic and classical phase shifts at the output of the interferometer are impacted by a rotation component along the z axis, neglected in our operating conditions. However, the atomic phase shift lets appear a third component of the mirror's rotation as well, which can be applied only by adapting the rotation compensation algorithm as well. Furthermore, if the first iteration of the reference mirror's real-time stabilization scheme does not account for the rotation along the z axis of the rotating frame attached to the instrument — as it is initially aligned with the effective wave vector of the laser —, this is no longer the case for the subsequent rotations of the mirror and can induce, in addition to parasitic phase shifts, an insufficient recovery of the atomic fringes' contrast.

We remind that a rotation vector $\boldsymbol{\theta}(t) = \theta(t)\,\boldsymbol{N}(t)$ can be defined by its angle $\theta(t) = \sqrt{\theta_x^2(t) + \theta_y^2(t) + \theta_z^2(t)}$ and axis $\boldsymbol{N}(t) = (N_x(t), N_y(t), N_z(t))^T$ where $N_i(t) = \theta_i(t)/\theta(t)$ for $i = x, y, z$. The generalization of the transverse rotation matrix given in equation 4.24 to the three dimensions case is given below:

$$\mathcal{R}(\theta(t)) = \begin{pmatrix} N_x^2(1-C)+C & N_xN_y(1-C)-N_zS & N_xN_z(1-C)+N_yS \\ N_xN_y(1-C)+N_zS & N_y^2(1-C)+C & N_yN_z(1-C)-N_xS \\ N_xN_z(1-C)-N_yS & N_yN_z(1-C)+N_xS & N_z^2(1-C)+C \end{pmatrix} \tag{B.1}$$

where $C = \cos(\theta(t))$ and $S = \sin(\theta(t))$, and the time dependence on the rotation axis' components has been omitted for simplicity. Considering rotation rates in the order of 10^{-1} rad/s and a typical interrogation time $T = 10^{-2}$ s, we can use the small angles

approximation and build the real-time rotation matrix used in practice:

$$\mathcal{R}_{\mathrm{RT}}(\theta(t)) = \frac{1}{2}\begin{pmatrix} 2-\theta_y^2(t)-\theta_z^2(t) & \theta_x(t)\theta_y(t)-2\theta_z(t) & \theta_x(t)\theta_z(t)+2\theta_y(t) \\ \theta_x(t)\theta_y(t)+2\theta_z(t) & 2-\theta_x^2(t)-\theta_z^2(t) & \theta_y(t)\theta_z(t)-2\theta_x(t) \\ \theta_x(t)\theta_z(t)-2\theta_y(t) & \theta_y(t)\theta_z(t)+2\theta_x(t) & 2-\theta_x^2(t)-\theta_y^2(t) \end{pmatrix}. \quad \text{(B.2)}$$

Using this rotation matrix, one then only needs to follow the logic developed in chapter 4 and summarized in figure 4.10 in order to achieve a three-dimension stabilization of the effective wave vector of the laser in the non-rotating frame of the laboratory.

Appendix C

Technical details of the FPGA implementation

C.1 Delay of the tip-tilt setpoints communication

In chapter 4, the modeling of the response of each piezo-electric actuators pair as an underdamped second-order system allowed us to characterize the pointing error related to their respective settling times. In order to have a very accurate estimation of the reference mirror's orientation precisely at the start of the next Raman pulse, it is important to quantify the delays intervening before the start of the actuators' motion.

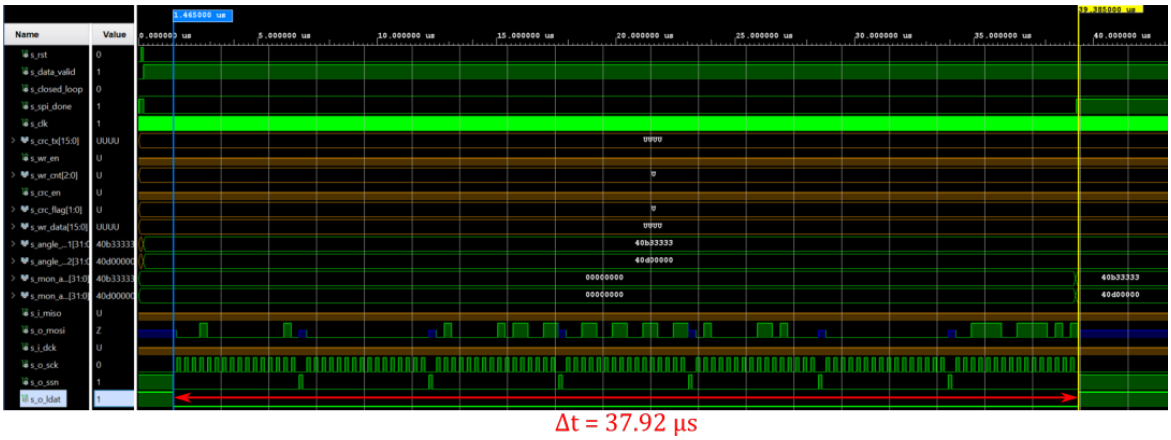

Figure C.1: Simulation of the transmission of a data bus containing the two angular setpoints from the FPGA board to the controller of the tip-tilt stage. The whole data packet is transmitted while the data-latch signal *s_o_ldat* (last row) is low, and we can observe that the monitoring inputs (displayed on the two rows above the *s_i_mosi* signal) are updated with the setpoint values transmitted after the following rising edge of the *s_o_ldat* signal.

The first relevant parameter is the time t_{del} separating the end of a Raman pulse and the transmission of a data bus, which is set within the Hardware Description Language (HDL) code implemented in the FPGA board and defined by equation 4.38. After this time, the data bus needs to be transmitted using the Serial Peripheral Interface (SPI) protocol, which will induce a supplementary delay t_{com}. Using the Vivado Design

Suite software used to program the Xilinx FPGA chip, it is possible to perform a digital simulation of the SPI communication of a data bus from the beginning of the transmission to the update of the external device's registers. This simulation, displayed in figure C.1, exhibits a delay $t_{\text{com}} = 37.92 \approx 38$ µs for the transmission of a single data packet with the 100 MHz FPGA clock.

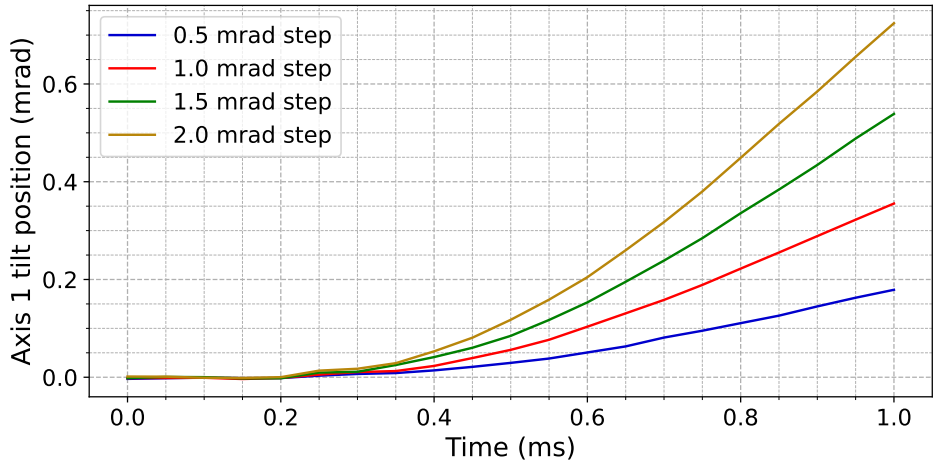

Figure C.2: Expansion on the first millisecond of the axis 1 strain gauge signal displayed in figure 2.13, demonstrating a $t_{\text{lat}} = 200$ µs delay between the reception of the command and the start of the piezo-electric actuators' motion.

Furthermore, from the study of the settling time conducted with the PIMikroMove software which produced the results shown in figure 2.13, we can retrieve the latency t_{lat} of the piezo-actuators. Figure C.2 displays an expansion of the strain gauge signal during the first millisecond and yields a $t_{\text{lat}} = 200$ µs latency between the reception of the command and the movement of the rotation axis. Nevertheless, the optical characterization of the tip-tilt response displayed in figure 2.14 revealed an approximately 500 µs delay between the update of the FPGA registers and the actual start of the mirror's rotation. Neglecting the propagation of the data bus — as the theoretical propagation velocity of an electromagnetic wave in a cable amounts to 2.10^8 m/s — and deducting the specific delays calculated in this section, this leaves 262 µs for the angular setpoints to be processed within the controller of the tip-tilt stage, including the conversion from digital to an analog high voltage, which appears to be a reasonable assumption.

C.2 Data format, dynamic range and resolution

Throughout the calculations performed by the HDL code implemented in the FPGA board, data are processed using the NQM fixed point format consisting in 1 sign bit, $(N-1)$ integer bits weighting $(2^{N-2}...2^0)$ and M fractional bits weighting $(2^{-1}...2^{-M})$.

The resolution on such signals propagating between the logical elements then amounts to $2^{-\mathrm{M}}$, in the appropriate unit and multiplied by prospective scale factors applied on the signal. For instance, a rotation rate measurement with a prior scale factor of 3.10^{-7} mrad/count expressed in the $32Q0$ integer format will have a resolution of 0.3 nad/s. Furthermore, the multiplication of two signals formatted as N_1QM_1 and N_2QM_2 produces a signal in the format $(N_1 + N_2)Q(M_1 + M_2)$, which can rapidly lead to very long data buses of 64 bits, 128 bits, etc. with an unnecessarily high resolution. For this reason, and because the rotation compensation scheme is mostly comprised of products, the resulting signals are regularly rescaled. Two methods are achievable: if the required dynamic range on a signal can be estimated and is lower than $(2^{\mathrm{N}-1} - 1)$, then it is possible to truncate the most significant bits (MSB). If it presents the advantage of preserving the resolution on the digital signal, it comes at the risk of saturating the data bus and getting a false value on a given parameter if the measurement overcomes the new limit set. On the other hand, truncating the least significant bits (LSB) will never corrupt the information itself but will systematically reduce the resolution as removing X LSBs will alter the lowest measurable signal from 2^{-M} to $2^{-(M-X)}$. Hence, this second option will be preferred in most cases.

As for the filling of the rotation matrix, using the trigonometric functions' Taylor expansion yields units inconsistencies depending on the terms with the dimension of a constant, an angle or a squared angle. This effect can alter the NQM format of the data buses, which can no longer be summed or subtracted anymore. For this reason, the factor 2 must be in the same NQM format and have the same prior scale factor as the angle it is multiplied with, so that the result has the same dimension as a product of angles. Following this reasoning, the constant 2 appearing in the diagonal terms needs as well to be in the same NQM format with the same scale factor as the previous result so that all the terms of the matrix are homogeneous. This way, all the elements can be identically rescaled in order to carry out the following calculations.

To conclude on the data format, as there are specific scale factors associated with the laser wave vector's components $\mathcal{S}_{\mathrm{k}}$ and with the rotation matrix elements $\mathcal{S}_{\mathcal{R}}$, every multiplication will induce a change in the scale factor applied on the resulting corrected wave vector $\boldsymbol{k}_{\mathbf{eff}}^{\boldsymbol{\theta}}$. In practice, at the n^{th} application of the rotation matrix, the corrected wave vector will be assigned a scale factor $(\mathcal{S}_{\mathcal{R}})^n . \mathcal{S}_{\mathrm{k}}$. To prevent this aspect to limit the dynamic range or resolution on our signals by saturating the data buses or forcing regular rescalings, a built-in Intellectual Property (IP) module was used for the conversion of the vector $\boldsymbol{k}_{\mathbf{eff}}^{\mathbf{set}}$ components into angular setpoints $\alpha_{1,2}^{\mathrm{set}}$. Indeed, the Vivado software on which the programming of the FPGA board is realized features a library of IP modules designed by the Xilinx company, and one module in

particular implements the Coordinate Rotation Digital Computer (CORDIC) algorithm for calculating basic trigonometric functions, in this case the arc-tangent. In addition to performing the calculation in parallel thus at a reasonably high speed, it presents the advantage of taking two parameters as an input and to calculate the arc-tangent of their ratio. This characteristic ensures that no matter the absolute scale factor assigned to the setpoint wave vector $\boldsymbol{k}_{\mathbf{eff}}^{\mathbf{set}}$, as long as it remains the same for all the components, it will eventually cancel out. Furthermore, the CORDIC IP module outputs a convenient phase signal expressed in $3Q29$ radians, independent from any prior scale factor propagating through the calculations. Ultimately, as the controller of the tip-tilt platform requires angular setpoints in the floating point format, a final IP block converting the angular setpoints $\alpha_{1,2}^{\text{set}}$ from the fixed-point to the single-precision floating-point notation was implemented before the transmission from the FPGA board to the tip-tilt controller. According to the IEEE 754 standard, the single-precision floating-point format (also called *binary32*) uses 1 sign bit s_0, 8 exponent bits $e_7...e_0$ and 23 fraction bits $f_{22}...f_0$ to represent a number N, following the expression:

$$N = (-1)^S.2^{(\mathrm{E}-127)}.\left(1+\sum_{i=0}^{22} f_{22-\mathrm{i}}2^{-i}\right) \tag{C.1}$$

with $E = (e_7...e_0)_2$ the value of the exponent and $S = s_0$ the value of the sign bit.

Bibliography

M. H. Anderson, J. R. Ensher, M. R. Matthews, C. E. Wieman, and E. A. Cornell. Observation of Bose-Einstein condensate in a dilute atomic vapor. *Science*, 269:198, 1995.

C. Antoine and C. J. Bordé. Exact phase shifts for atom interferometry. *Phys. Lett. A*, 306(5-6):277–284, 2003. doi: 10.1016/S0375-9601(02)01625-0. URL http://linkinghub.elsevier.com/retrieve/pii/S0375960102016250.

L. Antoni-Micollier, D. Carbone, V. Ménoret, J. Lautier-Gaud, T. King, F. Greco, A. Messina, D. Contrafatto, and B. Desruelle. Detecting volcano-related underground mass changes with a quantum gravimeter. *Geophysical Research Letters*, 49(13): e2022GL097814, 2022. doi: https://doi.org/10.1029/2022GL097814. URL https://agupubs.onlinelibrary.wiley.com/doi/abs/10.1029/2022GL097814.

A. Aspect, E. Arimondo, R. Kaiser, N. Vansteenkiste, and C. Cohen-Tannoudji. Laser Cooling below the One-Photon Recoil Energy by Velocity-Selective Coherent Population Trapping. *Phys. Rev. Lett.*, 61(7):826–829, 1988. doi: 10.1103/PhysRevLett.61.826. URL https://journals.aps.org/prl/abstract/10.1103/PhysRevLett.61.826.

B. Barrett, R. Geiger, I. Dutta, M. Meunier, B. Canuel, A. Gauguet, P. Bouyer, and A. Landragin. The Sagnac effect: 20 years of development in matter-wave interferometry. *C. R. Physique*, 15(10):875–883, 2014. doi: 10.1016/j.crhy.2014.10.009. URL http://linkinghub.elsevier.com/retrieve/pii/S1631070514001467.

B. Barrett, P. Cheiney, B. Battelier, F. Napolitano, and P. Bouyer. Multidimensional Atom Optics and Interferometry. *Phys. Rev. Lett.*, 122(4):043604, 2019. doi: 10.1103/PhysRevLett.122.043604. URL https://journals.aps.org/prl/abstract/10.1103/PhysRevLett.122.043604.

Q. Beaufils, J. Lefebve, J. G. Baptista, R. Piccon, V. Cambier, L. A. Sidorenkov, C. Fallet, T. Lévèque, and F. P. D. Santos. Rotation related systematic effects in a cold atom interferometer onboard a nadir pointing satellite. *npj Microgravity*, 9 (1):53, 2023. doi: 10.1038/s41526-023-00297-w. URL https://doi.org/10.1038/s41526-023-00297-w.

Y. Bidel, N. Zahzam, C. Blanchard, A. Bonnin, M. Cadoret, A. Bresson, D. Rouxel, and M. F. Lequentrec-Lalancette. Absolute marine gravimetry with matter-wave interferometry. *Nat. Commun.*, 9(1):627, feb 2018. doi: 10.1038/s41467-018-03040-2. URL http://www.nature.com/articles/s41467-018-03040-2.

Y. Bidel, N. Zahzam, A. Bresson, C. Blanchard, A. Bonnin, J. Bernard, M. Cadoret, T. E. Jensen, R. Forsberg, C. Salaun, S. Lucas, M. F. Lequentrec-Lalancette, D. Rouxel, G. Gabalda, L. Seoane, D. T. Vu, S. Bruinsma, and S. Bonvalot. Airborne absolute gravimetry with a quantum sensor, comparison with classical technologies. *Journal of Geophysical Research: Solid Earth*, 128(4):e2022JB025921, 2023. doi: https://doi.org/10.1029/2022JB025921. URL https://agupubs.onlinelibrary.wiley.com/doi/abs/10.1029/2022JB025921.

D. Boiron, C. Triché, D. R. Meacher, P. Verkerk, and G. Grynberg. Three-dimensional cooling of cesium atoms in four-beam gray optical molasses. *Phys. Rev. A*, 52: R3425, 1995. doi: 10.1103/PhysRevA.52.R3425. URL http://link.aps.org/doi/10.1103/PhysRevA.52.R3425.

K. Bongs, R. Launay, and M. A. Kasevich. High-order inertial phase shifts for time-domain atom interferometers. *Appl. Phys. B*, 84(4):599–602, 2006. doi: 10.1007/s00340-006-2397-5. URL http://link.springer.com/10.1007/s00340-006-2397-5.

B. Canuel, F. Leduc, D. Holleville, A. Gauguet, J. Fils, A. Virdis, A. Clairon, N. Dimarcq, C. J. Bordé, A. Landragin, and P. Bouyer. Six-Axis Inertial Sensor Using Cold-Atom Interferometry. *Phys. Rev. Lett.*, 97(1):010402, 2006. doi: 10.1103/PhysRevLett.97.010402. URL http://link.aps.org/doi/10.1103/PhysRevLett.97.010402.

Ch. J. Bordé. Atom Interferometry With Internal State Labelling. *Phys. Lett. A*, 140:10, 1989. doi: doi:10.1016/0375-9601(89)90537-9. URL http://www.sciencedirect.com/science/article/pii/0375960189905379.

P. Cheinet. *Conception et réalisation d'un gravimètre à atomes froids*. Theses, Université Pierre et Marie Curie - Paris VI, Mar. 2006. URL http://www.theses.fr/2006PA066561. Thèse de doctorat dirigée par Tuckey, Philip Laser et matière Paris 6 2006.

P. Cheinet, B. Canuel, F. P. Dos Santos, A. Gauguet, F. Yver-Leduc, and A. Landragin. Measurement of the sensitivity function in a time-domain atomic interferometer. *IEEE Transactions on Instrumentation and Measurement*, 57:1141–1148, 2008. doi: 10.1109/TIM.2007.915148. URL https://doi.org/10.1109/TIM.2007.915148.

Y.-J. Chen, A. Hansen, G. W. Hoth, E. Ivanov, B. Pelle, J. Kitching, and E. A. Donley. Single-Source Multiaxis Cold-Atom Interferometer in a Centimeter-Scale Cell. *Phys. Rev. Applied*, 12(1):014019, 2019. doi: 10.1103/PhysRevApplied.12.014019. URL https://link.aps.org/doi/10.1103/PhysRevApplied.12.014019.

S. Chu, L. Hollberg, J. E. Bjorkholm, A. Cable, and A. Ashkin. Three-dimensional viscous confinement and cooling of atoms by resonance radiation pressure. *Phys. Rev. Lett.*, 55:48–51, Jul 1985. doi: 10.1103/PhysRevLett.55.48. URL https://link.aps.org/doi/10.1103/PhysRevLett.55.48.

J. F. Clauser. Ultra high sensitivity accelerometers and gyroscopes using neutral atom matter wave interferometry. *Physica B & C*, 151:262, 1985.

J. Dalibard and C. Cohen-Tannoudji. Laser cooling below the Doppler limit by polarization gradients: simple theoretical models. *J. Opt. Soc. Am. B*, 6(11):2023, 1989. doi: 10.1364/JOSAB.6.002023. URL http://josab.osa.org/abstract.cfm?URI=josab-6-11-2023.

L. de Broglie. Radiations—Ondes et quanta (Radiation—Waves and quanta). *C. R. Acad. Sci. (Paris)*, 177:507, 1923.

D. Döring, J. E. Debs, N. P. Robins, C. Figl, P. A. Altin, and J. D. Close. Ramsey interferometry with an atom laser. *Opt. Express*, 17(23):20661–20668, Nov 2009. doi: 10.1364/OE.17.020661. URL https://opg.optica.org/oe/abstract.cfm?URI=oe-17-23-20661.

B. Dubetsky. Full elimination of the gravity-gradient terms in atom interferometry. *Applied Physics B*, 125:187, 2019. doi: 10.1007/s00340-019-7300-2. URL https://doi.org/10.1007/s00340-019-7300-2.

I. Dutta, D. Savoie, B. Fang, B. Venon, C. L. Garrido Alzar, R. Geiger, and A. Landragin. Continuous cold-atom inertial sensor with 1 nrad/sec rotation stability. *Phys. Rev. Lett.*, 116:183003, 2016. doi: 10.1103/PhysRevLett.116.183003. URL https://link.aps.org/doi/10.1103/PhysRevLett.116.183003.

A. Einstein. Über einen die erzeugung und verwandlung des lichtes betreffenden heuristischen gesichtspunkt. *Annalen der Physik*, 322(6):132–148, 1905. doi: https://doi.org/10.1002/andp.19053220607. URL https://onlinelibrary.wiley.com/doi/abs/10.1002/andp.19053220607.

R. Geiger, A. Landragin, S. Merlet, and F. Pereira Dos Santos. High-accuracy inertial measurements with cold-atom sensors. *AVS Quantum Science*, 2(2):024702, 06

2020. ISSN 2639-0213. doi: 10.1116/5.0009093. URL https://doi.org/10.1116/5.0009093.

P. Gillot, B. Cheng, S. Merlet, and F. Pereira Dos Santos. Limits to the symmetry of a mach-zehnder-type atom interferometer. *Phys. Rev. A*, 93:013609, 2016. doi: 10.1103/PhysRevA.93.013609. URL https://link.aps.org/doi/10.1103/PhysRevA.93.013609.

T. L. Gustavson, P. Bouyer, and M. A. Kasevich. Precision Rotation Measurements with an Atom Interferometer Gyroscope. *Phys. Rev. Lett.*, 78(11):2046–2049, 1997. doi: 10.1103/PhysRevLett.78.2046. URL http://link.aps.org/doi/10.1103/PhysRevLett.78.2046.

T. Hänsch and A. Schawlow. Cooling of gases by laser radiation. *Optics Communications*, 13(1):68–69, 1975. ISSN 0030-4018. doi: https://doi.org/10.1016/0030-4018(75)90159-5. URL https://www.sciencedirect.com/science/article/pii/0030401875901595.

M. Kasevich and S. Chu. Measurement of the gravitational acceleration of an atom with a light-pulse atom interferometer. *Appl. Phys. B*, 54:321, 1992.

M. Kasevich, D. S. Weiss, E. Riis, K. Moler, S. Kasapi, and S. Chu. Atomic velocity selection using stimulated raman transitions. *Phys. Rev. Lett.*, 66:2297–2300, May 1991. doi: 10.1103/PhysRevLett.66.2297. URL https://link.aps.org/doi/10.1103/PhysRevLett.66.2297.

M. A. Kasevich and S. Chu. Atomic Interferometry Using Stimulated Raman Transitions. *Phys. Rev. Lett.*, 67(2):181, 1991. doi: 10.1103/PhysRevLett.67.181. URL http://link.aps.org/doi/10.1103/PhysRevLett.67.181.

S.-Y. Lan, P.-C. Kuan, B. Estey, P. Haslinger, and H. Müller. Influence of the Coriolis Force in Atom Interferometry. *Phys. Rev. Lett.*, 108(9):090402, 2012. doi: 10.1103/PhysRevLett.108.090402. URL http://link.aps.org/doi/10.1103/PhysRevLett.108.090402.

J. Lautier, L. Volodimer, T. Hardin, S. Merlet, M. Lours, F. Pereira Dos Santos, and A. Landragin. Hybridizing matter-wave and classical accelerometers. *Appl. Phys. Lett.*, 105(14):144102, 2014. doi: 10.1063/1.4897358. URL http://scitation.aip.org/content/aip/journal/apl/105/14/10.1063/1.4897358.

J. Le Gouët, T. E. Mehlstäubler, J. Kim, S. Merlet, A. Clairon, A. Landragin, and F. Pereira Dos Santos. Limits to the sensitivity of a low noise compact atomic

gravimeter. *Appl. Phys. B*, 92:133–144, 2008. doi: 10.1007/s00340-008-3088-1. URL http://link.springer.com/article/10.1007/s00340-008-3088-1.

A. Lenef, T. D. Hammond, E. T. Smith, M. S. Chapman, R. A. Rubenstein, and D. E. Pritchard. Rotation sensing with an atom interferometer. *Phys. Rev. Lett.*, 78:760–763, Feb 1997. doi: 10.1103/PhysRevLett.78.760. URL https://link.aps.org/doi/10.1103/PhysRevLett.78.760.

T. Lévèque, A. Gauguet, F. Michaud, F. Pereira Dos Santos, and A. Landragin. Enhancing the Area of a Raman Atom Interferometer Using a Versatile Double-Diffraction Technique. *Phys. Rev. Lett.*, 103(8):080405, 2009. doi: 10.1103/PhysRevLett.103.080405. URL http://link.aps.org/doi/10.1103/PhysRevLett.103.080405.

A. Louchet-Chauvet, T. Farah, Q. Bodart, A. Clairon, A. Landragin, S. Merlet, and F. Pereira Dos Santos. The influence of transverse motion within an atomic gravimeter. *New J. Phys.*, 13(6):065025, 2011. doi: 10.1088/1367-2630/13/6/065025. URL http://stacks.iop.org/1367-2630/13/i=6/a=065025?key=crossref.1bc1455280673a2642ced74d41cfaf0a.

V. Ménoret. *Accéléromètre à atomes froids aéroporté pour un test du principe d'équivalence*. PhD thesis, Université Paris-Sud - Paris XI, 2012. URL https://tel.archives-ouvertes.fr/tel-00747538/.

V. Ménoret, P. Vermeulen, N. Le Moigne, S. Bonvalot, P. Bouyer, A. Landragin, and B. Desruelle. Gravity measurements below 10^{-9} g with a transportable absolute quantum gravimeter. *Sci. Rep.*, 8:12300, 2018. doi: 10.1038/s41598-018-30608-1. URL https://www.nature.com/articles/s41598-018-30608-1.

N. Mielec, M. Altorio, R. Sapam, D. Horville, D. Holleville, L. A. Sidorenkov, A. Landragin, and R. Geiger. Atom interferometry with top-hat laser beams. *Applied Physics Letters*, 113(16):161108, 2018. doi: 10.1063/1.5051663. URL https://doi.org/10.1063/1.5051663.

K. Moler, D. S. Weiss, M. Kasevich, and S. Chu. Theoretical analysis of velocity-selective Raman transitions. *Phys. Rev. A*, 45:342–348, 1992. doi: 10.1103/PhysRevA.45.342. URL http://link.aps.org/doi/10.1103/PhysRevA.45.342.

F. Oon and R. Dumke. Compact active vibration isolation and tilt stabilization for a portable high-precision atomic gravimeter. *Phys. Rev. Appl.*, 18:044037, Oct 2022. doi: 10.1103/PhysRevApplied.18.044037. URL https://link.aps.org/doi/10.1103/PhysRevApplied.18.044037.

C. Overstreet, P. Asenbaum, and M. A. Kasevich. Physically significant phase shifts in matter-wave interferometry. *American Journal of Physics*, 89(3):324–332, 2021. doi: 10.1119/10.0002638. URL https://doi.org/10.1119/10.0002638.

W. D. Phillips and H. Metcalf. Laser Deceleration of an Atomic Beam. *Phys. Rev. Lett.*, 48:596, 1982.

J.-C. Radix. Accéléromètres inertiels. *Techniques de l'ingénieur Grandeurs mécaniques*, base documentaire : TIB407DUO.(ref. article : r1930), 2000. doi: 10.51257/a-v3-r1930. URL https://www.techniques-ingenieur.fr/base-documentaire/mesures-analyses-th1/grandeurs-mecaniques-42407210/accelerometres-inertiels-r1930/.

S. Rosi, A. Burchianti, S. Conclave, D. S. Naik, G. Roati, C. Fort, and F. Minardi. Λ-enhanced grey molasses on the D2 transition of Rubidium-87 atoms. *Sci. Rep.*, 8(1):1301, 2018. doi: 10.1038/s41598-018-19814-z. URL http://dx.doi.org/10.1038/s41598-018-19814-z.

A. Roura, W. Zeller, and W. P. Schleich. Overcoming loss of contrast in atom interferometry due to gravity gradients. *New Journal of Physics*, 16(12):123012, dec 2014. doi: 10.1088/1367-2630/16/12/123012. URL https://dx.doi.org/10.1088/1367-2630/16/12/123012.

V. Schkolnik, B. Leykauf, M. Hauth, C. Freier, and A. Peters. The effect of wavefront aberrations in atom interferometry. *Applied Physics B: Lasers and Optics*, 120:311–316, 2015. doi: 10.1007/s00340-015-6138-5. URL https://doi.org/10.1007/s00340-015-6138-5.

D. Steck. *Quantum and Atom Optics*. 2007. URL https://books.google.fr/books?id=bc9TMwEACAAJ.

P. Storey and C. Cohen-Tannoudji. The Feynman path integral approach to atomic interferometry. A tutorial. *J. Phys. II*, 4:1999, 1994.

A. Sugarbaker, S. M. Dickerson, J. M. Hogan, D. M. S. Johnson, and M. A. Kasevich. Enhanced Atom Interferometer Readout through the Application of Phase Shear. *Phys. Rev. Lett.*, 111(11):113002, 2013. doi: 10.1103/PhysRevLett.111.113002. URL http://link.aps.org/doi/10.1103/PhysRevLett.111.113002.

S. Templier. *Three-axis Hybridized Quantum Accelerometer for Inertial Navigation*. Theses, Université de Bordeaux, 2021. URL https://theses.hal.science/tel-03296219.

S. Templier, J. Hauden, P. Cheiney, F. Napolitano, H. Porte, P. Bouyer, B. Barrett, and B. Battelier. Carrier-suppressed multiple-single-sideband laser source for atom cooling and interferometry. *Phys. Rev. Appl.*, 16:044018, Oct 2021. doi: 10.1103/PhysRevApplied.16.044018. URL https://link.aps.org/doi/10.1103/PhysRevApplied.16.044018.

S. Templier, P. Cheiney, Q. d'Armagnac de Castanet, B. Gouraud, H. Porte, F. Napolitano, P. Bouyer, B. Battelier, and B. Barrett. Tracking the vector acceleration with a hybrid quantum accelerometer triad. *Science Advances*, 8(45):eadd3854, 2022. doi: 10.1126/sciadv.add3854. URL https://www.science.org/doi/abs/10.1126/sciadv.add3854.

D. Wineland and H. Dehmelt. Proposed $10^{14}\delta\nu < \nu$ laser fluorescence spectroscopy on ti^{+} mono-ion oscillator. In *Bulletin of the American Physical Society*, volume 20, page 637, 1975.

Y.-y. Xu, X.-B. Deng, H. Zhou, K. Qi, X.-K. Chen, H.-Q. Luo, M.-K. Zhou, X.-C. Duan, and Z.-K. Hu. Measuring the effective height for atom gravimeters by applying a frequency jump to Raman lasers. *Rev. Sci. Instrum.*, 92(6):063202, 2021. URL https://doi.org/10.1063/5.0047996.

J. Yang, W. Wu, Y. Wu, and J. Lian. Improved iterative calibration for triaxial accelerometers based on the optimal observation. *Sensors*, 12(6):8157–8175, 2012. doi: 10.3390/s120608157. URL https://www.mdpi.com/1424-8220/12/6/8157.

Y. Zhao, X. Yue, F. Chen, and C. Huang. Extension of the rotation-rate measurement range with no sensitivity loss in a cold-atom gyroscope. *Phys. Rev. A*, 104:013312, Jul 2021. doi: 10.1103/PhysRevA.104.013312. URL https://link.aps.org/doi/10.1103/PhysRevA.104.013312.